Group 9 tris-chelate complexes as candidates to detect PVED in molecules

Quentin Gaydon

A thesis submitted to McGill University in partial fulfillment of the requirements of the degree of Doctor of Philosophy

Department of Chemistry

McGill University, Montreal

April 2022

This thesis is dedicated to my family.

Abstract

In nature, chiral biological molecules such as amino acids and sugars are predominantly observed as one of the enantiomers: L-amino acids and D-sugars. This observation has been termed biological homochirality. Several hypotheses have been proposed to explain this phenomenon. One of these is the existence of a small energy difference between the enantiomers, Parity Violation Energy Difference (PVED), a consequence of the weak interaction not conserving parity.

A difficult task has been to determine PVED in molecules: the effects of parity violation have been observed in atoms and PVED has been calculated theoretically for molecules. Several spectroscopic techniques have been proposed to measure PVED however none of these have been able to experimentally measure PVED in molecules. Unfortunately, many lightweight molecules have been considered; we now know that PVED scales with Z^6 indicating that molecules with heavy atoms should be preferred. Chiral molecules which are stable towards racemization are also preferred.

Neutral tris-chelate complexes of group 9 metals are prime candidates to measure PVED in molecules: they are chiral, possess a heavy atom at the center of symmetry, are easily prepared, can be optically resolved, and believed to be inert towards racemization. Some are known to be volatile.

In this thesis the synthesis, spectroscopy, and fluxional behaviour of tris-chelate complexes of cobalt, rhodium, and iridium with two different sets of ligands are discussed: a tropolonate derivative, 1,4-isopropyltropolone or hinokitiol (hino), and a small dithiocarbamate ligand, $[S_2CNH_2]^-$. Discussion of the synthesis and spectroscopic properties of the new complexes is complemented with an analysis of the mechanisms of racemization and their activation barriers, determined experimentally and computationally. Unexpectedly low barriers were determined for $Co(hino)_3$ and $Rh(hino)_3$ of 14.2 kcal/mol and 18.2 kcal/mol. A comparison of the structural distortions of the ground state geometry of $Rh(S_2CNH_2)_3$ to other known tris-dithiocarbamate complexes of rhodium, tris(dibenzyldithiocarbamato)rhodium(III) and tris(diethyldithiocarbamato)rhodium(III) suggests low barriers of around 16 kcal/mol. New Ru(II) and Os(II) complexes with both complexes are synthesized and structurally characterized.

The fluxional behaviour of the tropolonate complexes is also extended to Ru(II) and Os(II) complexes of the $MXL(CO)(PPh_3)_2$ type (X=H,Cl, M=Ru, Os) where an activation barrier of 22.5 kcal/mol is determined for the osmium complex.

Finally, the coordination chemistry of several fluorothiophosphate ligands is studied: while tris-chelate complexes of cobalt with $[S_2PF_2]^-$ have been reported to be volatile, very little is known about them in terms of structural features and spectroscopy, and they have been largely forgotten in the literature. To that end several complexes with $[S_2PF_2]^-$, $[S_5P_2F_2]^{2-}$ and $[S_3PF]^{2-}$ ligands with a variety of different metals are analyzed. The coordination of fluorodithiophosphate $[S_2PF_2]^-$ with Ru(II) d^6 results in three complexes with bidentate ligands, which are readily characterized by NMR, FTIR and X-ray diffraction: $RuH(CO)(S_2PF_2)(PPh_3)_2$, $RuCl(CO)(S_2PF_2)(PPh_3)_2$ and $Ru(S_2PF_2)_2(PPh_3)_2$. The latter bis-chelate complex $Ru(S_2PF_2)_2(PPh_3)_2$ is easily carbonalyated affording cis and trans complexes of $Ru(CO)(\eta^1\text{-}S_2PF_2)(\eta^2\text{-}S_2PF_2)(PPh_3)_2$.

The coordination of $[S_5P_2F_2]^{2-}$ and $[S_3PF]^{2-}$ to late transition metals results in a variety of coordination modes including simple bis-chelates with zinc, a trinuclear complex with cadmium and an octanuclear cluster complexes with copper. This rich diversity in the coordination modes of this ligand are simplified in the case d^8 square planar complexes of nickel, palladium and platinum, as well as in a binuclear d^6 ruthenium complex where only coordination as the fluorotrithiophosphate S_3PF^{2-} is observed.

Résumé

Les molécules chirales présentes dans la nature, telles que les acides aminés et les sucres sont principalement observées comme un seul énantiomère : les acides aminés-L et les sucres-D. Ce problème a été nommé homochiralité biologique. Plusieurs hypothèses ont été émises quant à l'origine de ce phénomène. Parmi elles, l'existence d'une petite différence d'énergie entre les énantiomères d'une molécule, la Différence d'Énergie de Violation de Parité (PVED) a été proposée. Elle est une conséquence des interactions faibles qui ne conservent pas la parité.

Une tâche difficile a été de mesurer la PVED dans des molécules : elle a été démontrée de manière expérimentale dans des atomes et calculée de manière théorique dans des molécules. Plusieurs techniques spectroscopiques ont été suggérées afin de mesurer la PVED mais aucune n'a permis pour l'instant de déterminer la PVED expérimentalement dans des molécules. Malheureusement, beaucoup de molécules légères ont été utilisées : nous savons maintenant que PVED augmente avec Z^6, prouvant que des molécules avec des atomes lourds sont nécessaires. De plus, des molécules chirales inertes à la racémisation sont préférées.

Des complexes neutres tris-chélates de métaux du groupe 9 sont de bons candidats pour mesurer PVED dans des molécules : ils sont chiraux, possèdent un atome lourd au centre de symétrie, sont faciles à synthétiser, peuvent être optiquement résolus et sont supposés être inertes à la racémisation. Certains complexes sont même volatiles.

Dans cette thèse, nous discuterons tout d'abord de la synthèse, la spectroscopie et le comportement dynamique de complexes tris-chélates du cobalt, rhodium et iridium avec deux types de ligands : un dérivé de la tropolone, 1,4-isopropyltropolone ou hinokitiol, et un petit dithiocarbamate $[S_2CNH_2]^-$. La discussion de la synthese et de la spectroscopie des mouveaux complexes est agrémentée d'une analyse des mécanismes d'isomerisation et des barrières d'activation, mesurées experimentallement et théoriquement. Des valeurs étonnamment basses on été déterminées pour $Co(hino)_3$ et $Rh(hino)_3$, de 14.2 kcal/mol et 18.2 kcal/mol. Une comparaison des données structurelles de $Rh(S_2CNH_2)_3$ à celles de deux autres complexes connus de rhodium, tris(dibenzyldithiocarbamato)rhodium(III) and tris(diethyldithiocarbamato)rhodium(III) indiquent des barrières basses d'environ 16 kcal/mol. De nouveaux complexes de Ru(II) et Os(II) sont synthétisés et charactérisés structurellement. Le

comportement dynamique de l'hinokitiol est aussi étendu dans des complexes de Ru(II) et Os(II) du type $MXL(CO)(PPh_3)_2$, (X=H,Cl, M=Ru, Os) où une barrière d'activation de 22.5 kcal/mol est calculée.

Finalement, la chimie de coordination de ligands fluorothiophosphates est étudiée: bien que des complexes de cobalt contenant $[S_2PF_2]^-$ soient connus pour être volatiles, très peu d'informations à leur sujet sont connues et ils ont été largement abandonnés dans la littérature. A cette fin, des complexes des ligands $[S_2PF_2]^-$, $[S_5P_2F_2]^{2-}$ et $[S_3PF]^{2-}$ avec une variété de métaux sont analysés. La coordination de $[S_2PF_2]^-$ au Ru(II) d^6 résulte dans trois complexes facilement charactérisables par RMN, IRTF et DRX: $RuH(CO)(S_2PF_2)(PPh_3)_2$, $RuCl(CO)(S_2PF_2)(PPh_3)_2$ and $Ru(S_2PF_2)_2(PPh_3)_2$. Ce dernier est facilement carbonylé pour donnerdes complexes cis et trans de $Ru(CO)(\eta^1\text{-}S_2PF_2)(\eta^2\text{-}S_2PF_2)(PPh_3)_2$.

La coordination de $[S_5P_2F_2]^{2-}$ et $[S_3PF]^{2-}$ à des métaux de transition tardifs résulte en une variété de modes de coordination, incluant un simple bis-chélate de zinc, un agrégat trinucléaire de cadmium et un agrégat octanucléaire de cuivre. Cette riche variété de modes de coordination est simplifiée avec des complexes d^8 à géométrie plane carrée de nickel, palladium et platinum ainsi que dans un complexe bimétallique de Ru(II) où seule la coordination de fluorotrithiophosphate S_3PF^{2-} est observée.

Acknowledgments

I would like to thank all the people who have made the last six years an unforgettable experience.

I would first like to thank my supervisor, Prof. Scott Bohle: it has been a pleasure to learn about inorganic chemistry from you. I greatly appreciate the interesting conversations, valuable input, and support over the years.

I would like to thank all the members of the Bohle group I have had the pleasure of working with: Dr. Ivor Wharf, Dr. Cassidy VanderSchee, Dr. Benita Kapuku, Dr. Danae Guerra, Dr. David Kuter, Harrison Cassidy, Philip Karagoerghis, Leo Hall, and Ambre Lambert. Although we have all worked on very different topics, I enjoyed the conversations and input. I thank the undergraduate students I have had the pleasure of mentoring: Gregory, Colin, Basil and Joanna.

I would like to thank Dr. Robin Stein and Dr. Tara Sprules for their tremendous help with the setup and design of NMR experiments without which much of this thesis would not have been possible. I would also like to thank Dr. Alexander Wahba and Dr. Hatem Titi for their help with mass spectroscopy and low temperature X-ray diffraction.

I would like to thank all the close friends who have kept my mind off work when necessary: Aidan, Allen, Ilias, Klaudiusz, Alex, Alex, Wanlei, Tommy, Philippe, and Julien.

Finally, I would like to thank my family for their support and encouragement since I've started my PhD. I am especially grateful to my sister, Elisabeth and to my parents, Bertrand and Hilde.

Contribution of Authors

The author has conducted the synthesis of the complexes as well as spectroscopic characterization, VT-NMR experiments, crystal structures and other work described in this thesis. The work was done under the supervision of Prof. Scott Bohle.

Chapter 3: Ian J. Bohle has helped in the synthesis of the complex $Ru(hino)_2(PPh_3)_2$.

Table of Contents

List of Schemes

List of Figures

List of Tables

List of Abbreviations

Abbreviation	Definition
Å	Angstrom
Acac	Acetylacetonate
AU	Atomic Units
B3LYP	Becke-3-parameter-Lee-Yang-Parr
Bipy	Bipyridine
CCD	Charge Coupled Device
cm^{-1}	Inverse centimeters
COSY	Correlation spectroscopy
Cp	Cyclopentadiene
CPL	Circularly Polarized Light
CSP	Chiral Stationary Phase
DBU	1,8-Diazabicyclo[5.4.0]undec-7-ene
DCM	Dichloromethane
DFT	Density Functional Theory
DHF	Dirac Hartree Fock
DMSO	Dimethylsulfoxide
DSC	Differential Scanning Calorimetry
Dtc	Dithiocarbamate
En	Ethylenediamine
EPR	Electron Paramagnetic Resonance
e.s.d.	Estimated standard deviation
ESI-MS	Electrospray Ionization Mass Spectrometry
EtOAc	Ethyl acetate
EtOH	Ethanol
Fac	Facial
FTIR	Fourier Transform Infrared
FWHM	Full Width Half Maximum
H_2O	Water
Hino	Hinokitiol
HMBC	Heteronuclear multiple bond correlation spectroscopy
HSQC	Heteronuclear single quantum coherence spectroscopy
Hz	Hertz
IR	Infrared
kcal/mol	Kilocalories per mole
kJ/mol	Kilojoules per mole

MeOH	Methanol
Mer	Meridional
MHz	Megahertz
mL	Milliliter
MS	Mass Spectrometry
Nm	Nanometers
NOESY	Nuclear overhauser effect spectroscopy
NMR	Nuclear Magnetic Resonance
N^nPr_4	Tetra-n-propylammonium
ORTEP	Oak Ridge Thermal Ellipsoid Plot Program
Phen	Phenanthroline
Ppm	Parts per million
PVED	Parity Violation Energy Difference
PXRD	Powder X-ray Diffraction
TGA	Thermo Gravimetric Analysis
THF	Tetrahydrofuran
UV-Vis	Ultraviolet Visible
VT-NMR	Variable Temperature Nuclear Magnetic Resonance
XRD	X-ray diffraction

Chapter 1: Origins of Biological Homochirality and Determination of Parity Violation Energy Difference in Molecules

The origin of life is a fascinating tale which has spurred many theories. Since the discovery of chirality by Louis Pasteur in 1848[1,2], its importance in biology has been well established: it plays a key role in the development of life to where it stands today. One of the most intriguing topics is the origin of biological homochirality: in this chapter we will discuss theories relating to this matter. Most of our attention will be focused on one of them: parity violation in chiral molecules as the origin of biological homochirality. First, important concepts relating to chirality specifically in the case of metal tris-chelates will be reviewed.

1.1 Chirality in tris-chelate complexes

1.1.1 Geometrical definitions

Chiral molecules consist of two enantiomers, which are non-superimposable mirror images of each other. In terms of their geometry, chiral molecules are asymmetric and do not possess any improper rotations (S_n) and therefore no planes of symmetry or inversion centers. When more than one chiral center is present, diastereomers can also form: they are stereoisomers but, in some cases, there will be enantiomers.

The nature of the ligand affects the symmetry elements in the complex: here symmetric bidentate ligands are defined as those with a C_2 axis while dissymmetric ligands are those without any rotation symmetry such as those possessing two different donor atoms. The symmetry operations of tris-chelate complexes with symmetric bidentate ligands include a C_3 axis and three C_2 axes, with the complexes having D_3 symmetry (Figure 1.1). The enantiomers formed are described as Δ or Λ. The picture is more complex in the presence of dissymmetric bidentate ligands. Depending on the relative positions of the ligands, two geometrical isomers may form: the fac isomer in which the three ligands are related by C_3 symmetry though no C_2 axes are present or the mer isomer where no elements of symmetry are present in the structure. Both the fac and mer

isomers exist as Δ or Λ enantiomers giving to a total of four stereoisomers: Δ-fac, Δ-mer, Λ-fac and Λ-mer. (Figure 1.2)

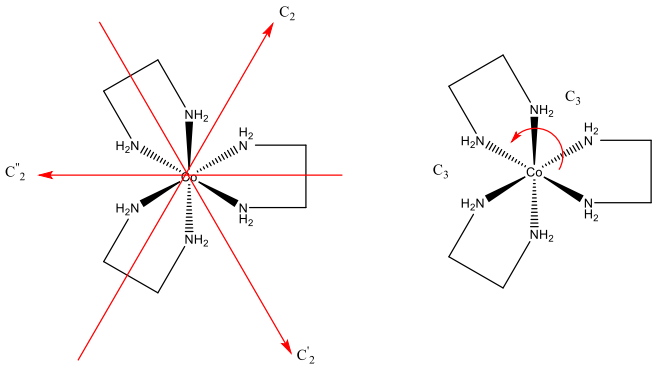

Figure 1.1: Chirality and symmetry operations in Λ-$[Co(en)_3]^{3+}$

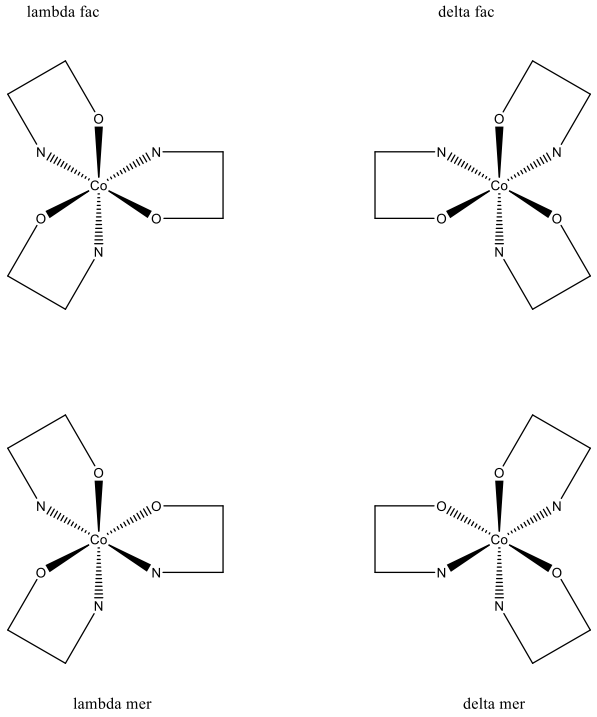

Figure 1.2: Stereoisomers in tris-chelate complexes with asymmetric bidentate ligands

1.1.2 Separation of enantiomers

Enantiomers of chiral molecules are characterized by identical physical and chemical properties, and widely perceived as being equienthalpic, however they differ in the way they interact with other chiral molecules and with polarized light. When synthesized a 50:50 mixture of the two

enantiomers, the racemic mixture is formed. The separation of enantiomers is an important task for many different applications: for example, enantiomers of a certain drug may have different applications. In the case of transition metal complexes, several methods have been used to achieve this goal. The most common method relies on chiral chromatography employing a chiral stationary phase (CSP), which will preferentially interact with one of the enantiomers more strongly. The CSP consists of a chiral complex bound to an achiral phase such as silica. Examples of CSPs include amino acids,[3-5] polysaccharides,[6-9] cyclodextrin[10-13] or crown ethers[14-16] to name a few. While liquid chromatography is the most common technique used,[17-21] supercritical fluid chromatography has also been successful.[22] Capillary electrophoresis has also shown success in the separation of enantiomers of tris-chelate complexes.[23,24]

An alternative method is crystallization using a chiral resolving agent. In this scenario, a resolved chiral molecule may form covalent[25] or non-covalent[26] interactions with one of the enantiomers of the compound of interest. Choosing a correct solvent or combination of solvent will result in the crystallization of the new binary complex, while the other enantiomer remains in solution. While this method is not as labour intensive as chromatography, it requires finding the correct chiral resolving agent for the compound of interest and a correct solvent combination. One of the most well known applications of this method with tris-chelate complexes involves the resolution of tris-ethylenediamine cobalt(III) chloride with tartaric acid.[27] Subsequently, cobalt tris-acetylacetonate $Co(acac)_3$ was successfully optically resolved using dibenzoyltartaric acid [28]

One last method involves synthesis of the desired compound by substitution from a resolved starting material. This method requires the prior resolution of the starting material from known methods. Very few reports of this resolution method have been made: for example tris-(diethyldithiocarbamate)cobalt(III) was obtained by substitution from previously resolved disodium ethylenediaminetetraacetate cobalt(III).[29] Knowledge of the substitution mechanism is important in understanding whether optical resolution will be successful in this case.

1.1.3 Racemization and mechanisms of inversion of stereochemistry

Racemization is an important concept when dealing with chiral compounds: it describes the conversion of an enantiomerically pure sample into the racemic mixture.

Racemization occurs via mechanisms by which one enantiomer is converted to the other. In the case of tris-chelate complexes, two such mechanisms are possible: mechanisms with bond breaking and mechanisms without bond breaking.[30] Mechanisms without bond breaking are further divided into two mechanisms: the Bailar twist[31] and Ray Dutt mechanism.[32] In their study of the electronic properties of $[Fe(bipy)_3]^{2+}$ and its potential use in dye-sensitized solar cells, Jakubikova *et al*. proposed an alternative twisted Bailar twist mechanism with a C_{3h} intermediate with remarkably lower energy than its D_{3h} counterpart.[33] This mechanism was termed the dancing Bailar twist. In the case of asymmetric ligands, fac-mer isomerization may also occur via these same mechanisms.

The first type of mechanism involves the rupture of a metal-ligand bond, twisting around the other bond and formation of the new metal-ligand bond (Scheme 1.1). This mechanism results in the formation of a five-coordinate intermediate with either trigonal bipyramidal or square pyramidal geometry.[30] In complexes with symmetrical ligands, the opposing enantiomer is formed. In complexes with dissymmetric ligands such as those presented in Figure 1.2, depending on the intermediate, fac-mer isomerization will occur either with or without inversion of stereochemistry.[33]

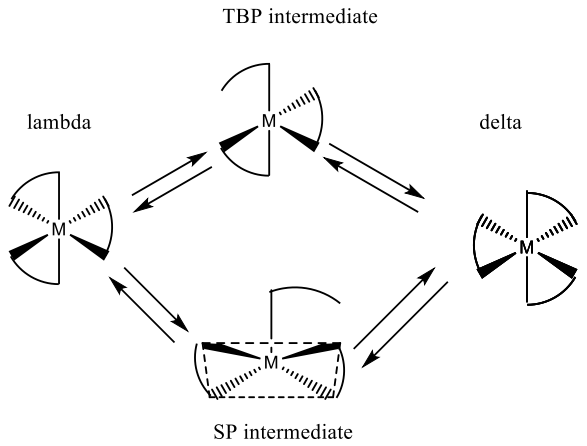

Scheme 1.1: Mechanism of inversion of stereochemistry with bond breaking

The Bailar twist mechanism involves a rotation of one of the faces in the star of David representation along the C_3 axis of the molecule (Scheme 1.2). This results in the formation of a trigonal prismatic intermediate with D_{3h} symmetry. The Ray Dutt mechanism is described as a rhombic twist mechanism with formation of a C_{2v} intermediate (Scheme 1.3). Bailar twist mechanisms in dissymmetric complexes will result in inversion of stereochemistry but no fac-mer isomerization while the Ray Dutt mechanism will give both.[34]

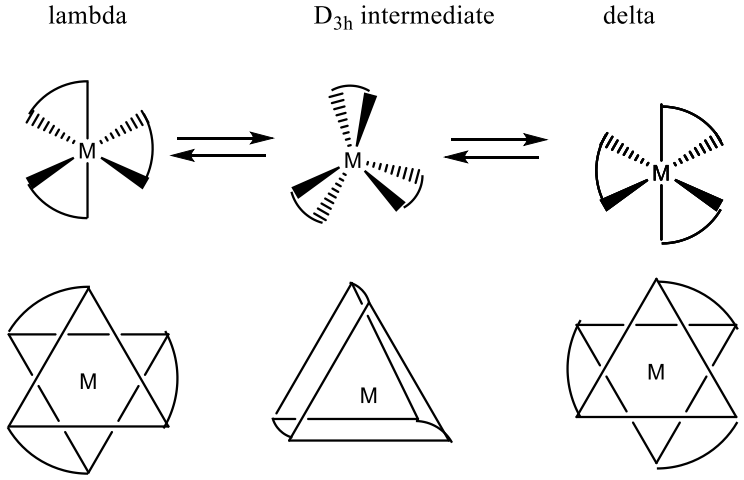

Scheme 1.2: Bailar twist mechanism

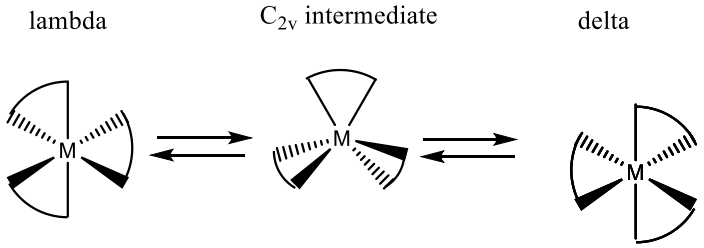

Scheme 1.3: Ray Dutt Mechanism

An important parameter to consider when determining which of the Bailar twist and Ray Dutt mechanism is the most likely to occur is the normalized bite, or the ratio of the distance between donor atoms of the same ligand and the metal-ligand bond length. The distortion to a D_{3h} intermediate in the case of the Bailar twist are preferred when the normalized bite is smaller than 1.5. Conversely, a value larger than 1.5 is preferred for the Ray Dutt mechanism.[35]

1.1.4 Structural parameters relating to distortion of octahedral geometry

While the ideal tris-chelate geometry is octahedral with D_3 symmetry, it is often the case that such a complex, adopts a slightly distorted geometry in its ground state. Several important parameters which quantify the degree of distortion of a tris-chelate complex away from ideal D_3 geometry are described here, namely the bite angle, twist angle, pitch angle and polar angle. The degree of distortion is strongly related to the activation barrier of the inversion of stereochemistry: it is observed that more distorted complexes will have lower activation barriers. It is therefore crucial to analyze this distortion when investigating racemization of tris-chelate complexes: this will be discussed again throughout this thesis.

The most straightforward parameter is the bite angle, the angle formed between the metal and donor atoms of the ligand. The twist angle is the projection of the bite angle onto the plane perpendicular to the C3 axis. The polar angle is the angle between the M-L bonds and the C3 axis. The pitch angle is the angle formed by the plane of the chelate ring and the C3 axis.

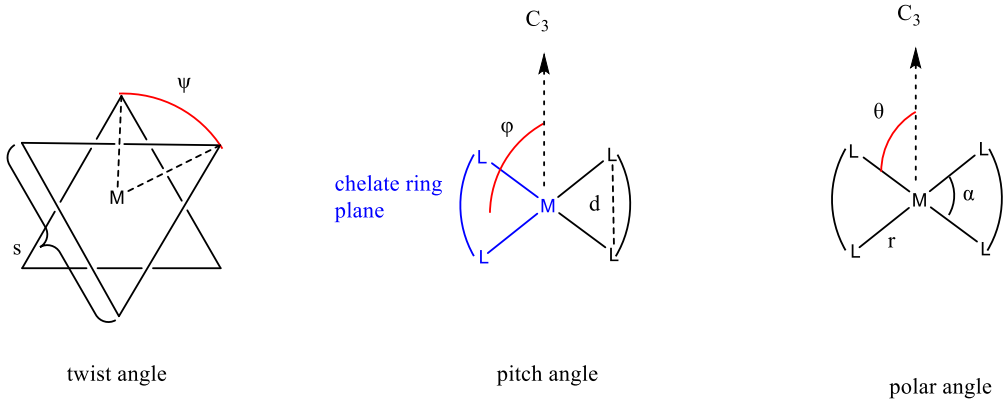

Figure 1.3: Representation of the twist angle, polar angle and pitch angle

The equations relating the different parameters are the following, where α is the bite angle, θ is the polar angle, φ is the twist angle and ψ is the pitch angle.

$$\cos\left(\frac{\alpha}{2}\right) = \sin(\theta)\cos\left(\frac{\varphi}{2}\right)$$

$$\sin\left(\frac{\alpha}{2}\right) = \frac{\cos(\theta)}{\cos(\psi)}$$

$$s = \sqrt{3}rsin(\theta)$$

$$\cos(\psi) = \frac{h}{d}$$

In ideal D_3 geometry, the values of the bite angle, twist angle and pitch angle are respectively 90°, 60° and 35.3°. Distorted complexes will typically have lower values for all three with ideal D_{3h} geometry having twist and pitch angles of 0°.

In this section, important considerations when studying chirality have been discussed. Overall, chirality is an essential characteristic in many structures not limited to transition metal complexes, with a wide variety of applications. Importantly, it is present in biological molecules and is therefore essential to many biological functions.

1.2 Definition of Homochirality

In biology, the building blocks of biological macromolecules are chiral: this includes the amino acids in proteins, nucleic acids in DNA and RNA and sugars in biomass/carbohydrates. It is observed that other than achiral glycine, all of the other 19 amino acids exist exclusively in the L form. Similarly, carbohydrates are exclusively found in the D form.[36] Biological homochirality is the term used to describe the observation that these molecules mostly exist in nature as one enantiomer: some D-amino acids are present in bacteria, however.

The observation that L-amino acids are present in enantiomeric excesses does not limit itself to amino acids on earth. Amino acid residues in concentrations of 10-60ppm were for example found in the Murchison meteorite.[37,38] Five biological amino acids were identified in the meteorite: alanine, proline, leucine, aspartic acid, and glutamic acid. All of these amino acids showed a preference towards the L enantiomer, with D/L ratios of concentrations varying between 0.166 for leucine and 0.682 for alanine. Additionally, preferences of the L enantiomer were also observed for non biological amino acids such as isovaline, α-methylisoleucine and α-

methylalloisoleucine.[39-41] Unlike on Earth where the amino acids exist predominantly as the L enantiomer, the amino acids from the Murchison meteorite showed preference for the L enantiomer but the D enantiomer was still present.

Two important questions must be raised from these observations.[42] First, what is the cause of the preference of one enantiomer? Since amino acids in meteorites have the same preference for the L- enantiomer, extraterrestrial causes can be considered. Second, how did this initial imbalance amplify to the extent that is biological homochirality? We will briefly discuss some mechanisms of amplification of chirality and then focus our attention on the origin of molecular asymmetry.

1.3 Processes of amplification of enantiomeric excesses

Several hypotheses exist concerning these amplification processes relying on the chemical and physical properties of chiral compounds. In 1953 Charles Frank proposed the Frank model where homochirality originates from autocatalysis.[43] The concept is that one enantiomer of a chiral compound may catalyze its own production while the reaction between two enantiomers results in the deactivation of the enantiomers. In the case of a mixture with a small enantiomeric excess, this will lead to the amplification of the enantiomeric excess as shown in Figure 1.4. At the time the model was proposed, no autocatalytic reactions had been observed and much research was focused on finding such an example.

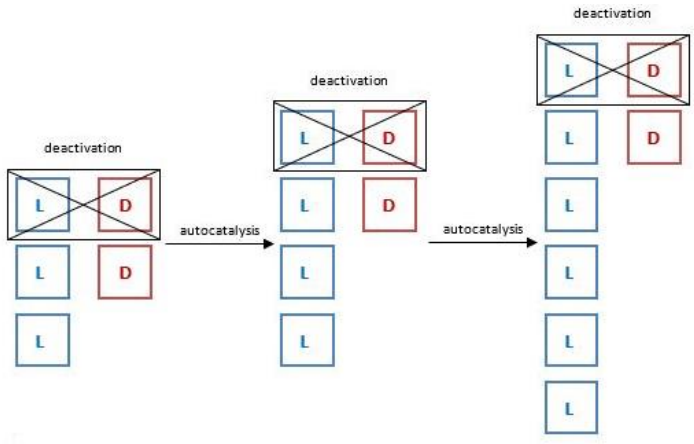

Figure 1.4: Frank model of chiral amplification

In 1995, Soai and coworkers reported an autocatalytic reaction, the alkylation of pyrimidyl aldehydes with dialkylzincs, in which the product in low enantiomeric excess catalyzes its own formation giving a product in 90% enantiomeric excess.[44,45] Several mechanisms have been proposed. The most likely, involving the formation of homochiral and heterochiral dimers was suggested by Blackmond and Brow. [46,47] While the homochiral dimers catalyze the production of the product in one handedness, the heterochiral dimer is inactive. This provides the two main criteria for the Frank model: each enantiomer catalyzes its own production while reaction between both enantiomers results in their deactivation.

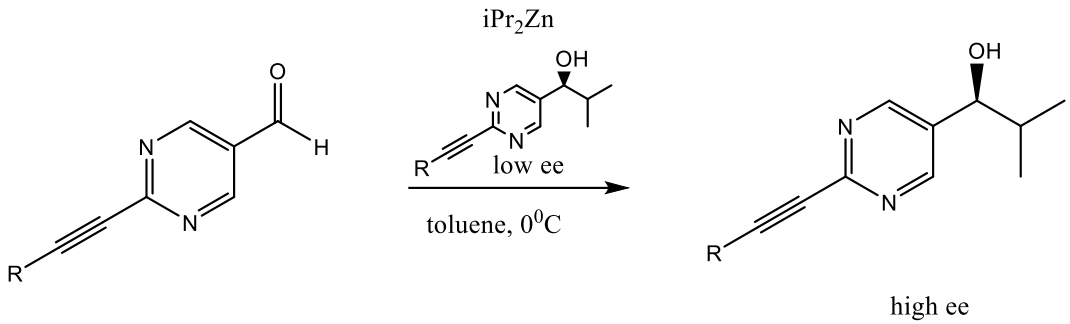

Scheme 1.4: Example of the Soai reaction

This reaction is a good example of how autocatalysis can be used to generate homochiral systems however it does not prove the origin of biological homochirality, due to the likely absence of dialkylzincs in the early stages of evolution of life on earth. Additionally, the final product was obtained in very high enantiomeric excess (>99.5%): while this is an exceedingly high enantiomeric excess, it is not enantiopure.

Autocatalysis can be observed in crystallization processes as well. Symmetry breaking during crystallization of inorganic compounds was first noted by Kondepudi[48,49] in the case of sodium chlorate $NaClO_3$. While the molecule itself is not chiral, crystallization results in chiral crystals. Crystallization of the compound in an aqueous solution without any mechanical effects resulted in the expected 50:50 mixture of D-$NaClO_3$ and L-$NaClO_3$. On the other hand, crystallization with stirring resulted in a mixture with 99.7% of one of the enantiomers. Later Viedma was able to obtain 100% enantiomeric purity by stirring sodium chlorate with glass beads in a saturated solution.[50,51] Noorduin *et al.* extended this technique to chiral molecules including biologically

relevant molecules such as amino acids and demonstrated the viability of the process on an industrial scale, suggesting potentially using this method to obtain enantiomerically pure drugs.[52,53] The mechanism of deracemization involves several phenomena: the larger crystals are continuously ground by the glass beads inducing the formation of smaller crystals which are dissolved into the solution. The smaller crystals then aggregate to the larger crystals of the same chirality resulting in the formation of crystals of single handedness.[54] Preferential formation of one of the enantiomers can be controlled under the influence of circularly polarized light.[55,56]

1.4 Origin of small differences in enantiomeric excesses of chiral molecules

The examples presented above are used to explain the amplification of enantiomeric excess leading to homochirality, however they do not explain the origin of the small enantiomeric excess before amplification. Theories regarding this origin in enantiomeric differences fall under two categories: chance and deterministic mechanisms.[57]

1.4.1 Chance mechanisms

Chance mechanisms require an event with 50/50 chance of producing either the L or D enantiomer of a chiral molecules. One such example includes asymmetric adsorption onto inorganic substances such as quartz. Crystallization of quartz affords enantiomorphic crystals which have first been used in 1935 for the resolution of chiral cobalt complexes such as $Co(en)_3Cl_3$ by adsorption.[58] Bonner later observed that D-quartz preferentially adsorbs D-alanine while L-quartz preferentially adsorbs L-alanine.[59] Random samples from quartz from various locations all amounted to an equal distribution of D-quartz an L-quartz. Therefore, although large enantiomeric excesses may be observed locally, the overall distribution of chiral molecules adsorbed on quartz gives a 50/50 mixture of the enantiomers.[60] This example illustrates a major caveat with chance mechanisms: while local enantiomeric excesses may be observed, since there is a 50% chance of the opposite event happening elsewhere, the probability of it being the cause of homochirality is quasi null. Chance mechanisms have been generally discarded in favour of deterministic mechanisms.

1.4.2 Deterministic mechanisms

Deterministic mechanisms require an external physical process which may interact with chiral molecules resulting in the preferential formation of one enantiomer. Two main deterministic phenomena were proposed: circularly polarized light (CPL) and parity violation.

1.4.2.1 Circularly Polarized Light

Circularly Polarized Light originates from astronomical sources and may be either right or left-handed. Its interaction with chiral molecules may cause an imbalance in enantiomeric excesses. Feringa described three processes by which irradiation with circularly polarized light may result in enantiomeric excesses. In the first, photodestruction, irradiation with CPL results in the destruction of one of the enantiomers while the other is unaffected. In the second process, photoresolution, one of the enantiomers is excited and the excited state then undergoes racemization. This will result in the accumulation of the other enantiomer. Finally, the third process is asymmetric photosynthesis in which irradiation with CPL results in the formation of a chiral complex from a prochiral one.[61] Examples of these types of mechanisms have been observed in the photodestruction of pyrimydil alkanol[62] or leucine,[63] photoresolution of liquid crystals,[64,65] and asymmetric photosynthesis of tartaric acid[66] and hexahelicene.[67]

Overall, several advantages of CPL as a source of homochirality are present:

- various sources of CPL are known including stellar radiation and may explain the presence of enantiomeric excesses of amino acids in the Murchison meteorite
- from the examples listed above, it is known that CPL may induce enantiomeric excesses in organic molecules including amino acids with values close to those observed in the Murchison meteorite.
- mechanisms of amplification of enantiomeric excesses by autocatalysis are known, as discussed in section 1.3.

Bonner has drawn several criticisms of CPL as an origin of biological homochirality:[57] Exposure to CPL on Earth is rather negligible. Additionally, exposure to right or left-handed CPL varies

with time of day, climatic events, or perhaps even irregular terrain. These criticisms do not apply however, if the origin of chiral imbalance is extraterrestrial.

In addition to CPL, results from the MeerKat telescope suggest synchtron radiation measured throughout the galaxy is polarized and may play a similar role.

1.4.2.2 Parity Violation

Unlike circularly polarized light, which is an external agent, parity violation is intrinsic to atoms and molecules. From the perspective of most chemists, it is widely accepted that enantiomers of a chiral molecule have identical energies, physical and chemical properties and only differ by their ability to rotate polarized light. This is inconsistent with theoretical physics which predicts that parity can be violated causing an imbalance in the energies of enantiomers of chiral molecules.

Parity is a transformation which changes the sign of the spatial coordinates of an object, according to the equation P(x,y,z) = (-x,-y,-z). As such, parity transforms an object into its mirror image which relates it to chirality. Until 1956 it was believed that all physical interactions conserve parity. While this is true for most interactions, it is not the case for weak nuclear interactions: weak nuclear interactions are interactions between sub-atomic particles causing radioactive decay.[68] In 1956, Wu studied the beta decay in an isotope of cobalt, cobalt-60, at near absolute zero temperatures. The unstable cobalt-60 isotope is converted into a stable nickel-60 isotope with the emission of gamma rays.[69] It was observed that 60% of gamma rays were emitted in one direction and 40% in the other (Figure 1.5). If parity was conserved in the experiment, then there should have been an equal chance of decay occurring in both directions. The importance of this experiment awarded the authors with a Nobel prize in physics in 1957.

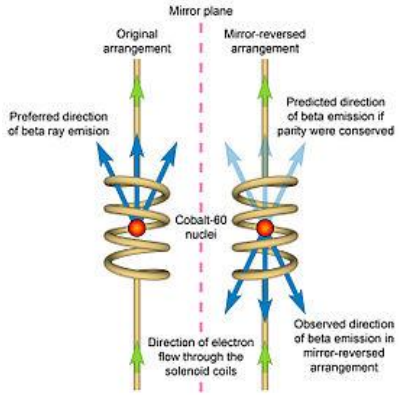

Figure 1.5: Parity violation in the beta decay of Co-60. Copied from public access: https://de.wikipedia.org/wiki/Wu-Experiment

It is now widely accepted that the weak nuclear interaction does not conserve parity.[70] In his lectures, Feynman describes the relationship between space and time reversal: any reversal in spatial coordinates must be met with time reversal.[71] Therefore, violation of spatial parity will also involve violation of time reversal: this time dependence is often omitted when discussing chirality from a chemistry point of view as they relate to very short time frameworks. The effect of parity violation has important consequences for both atoms and molecules.

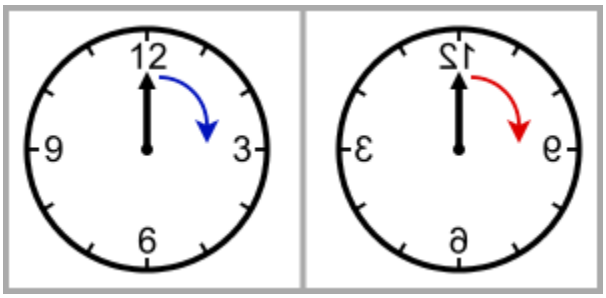

Figure 1.6: Space and time violation

1.5 Parity violation in atoms

Parity violation effects in atoms originate from the exchange of Z^0 bosons between electrons and quarks in the nucleus.[72] In order to measure parity violating effects in atoms, the mass of the Z^0 boson and the electronic structure of the atom must be accurately known. Uncertainties in atomic structure vary between 1 and 10% depending on the atom.[73]

In heavy atoms, where there is a larger contribution of the exchange of bosons between electrons and quarks, the effects of parity violation are amplified: atoms with high atomic number Z are preferred in parity violation measurements. The best evidence of parity violation in atoms comes from cesium vapours, determined by Wod *et al.* in 1995.[74] Uncertainty arising from the atomic structure of cesium is only 1%, making cesium a good candidate for determination of Parity Violation in atoms. This low atomic structure uncertainty arises from the presence of only one valence electron. In heavy atoms such as cesium, transitions which would normally be forbidden can be observed. In cesium, the forbidden $^{6}S_{1/2}$->$^{7}S_{1/2}$ transition could be measured by using a spin-polarized atomic beam. This transition is amplified due to parity violation: it causes a mixing of P state into the ^{6}S and ^{7}S states resulting in a parity-violating transition. This measurement gave an amplitude for the forbidden transition of -1.5935(36) mV/cm and was the first example of parity violation being measured in atoms. This falls within the 1% experimental precision required for such experiments.

Several attempts to measure parity violation effects in atoms were made with different atoms. The amplitudes of forbidden $^{1}S_{0}$->$^{3}D_{1}$ (408nm) transition in ytterbium[75] as well as transitions at 1279nm for lead,[76] 1279nm ($^{6}P_{1/2}$->$^{7}P_{1/2}$) for thallium[77,78] and 876nm for bismuth[79] were also determined. The amplitudes of the corresponding transitions were of the same order of magnitude as the amplitude determined for the transition in cesium. However, none of these have obtained the 1% experimental precision required for these experiments. Therefore, the only unambiguous determination of parity violation effects in atoms comes from atomic cesium.

1.6 Parity violation in molecules

A consequence of the parity violation in the weak interaction is that the enantiomers of chiral molecules will have a very small difference in energy, contrary to traditional beliefs.[80] As discussed by Rein et al., Fermi coupling of the weak nuclear interaction with the electron cloud results in asymmetry in intramolecular interactions. This has consequences for energies such as the molecular binding energies which differ for both enantiomers.[80]

Traditionally, it is believed that each enantiomer of a chiral moleculecorresponds to a minimum in its potential energy surface with identical energies resulting in a reaction enthalpy for the stereomutation equal to 0. Due to parity violation effects resulting from the weak force, the energies of the ground states become unequal: while one of the enantiomers sees an increase in energy of E_{PV}, the opposing enantiomer will see a decrease of $-E_{PV}$. This will in turn result in a non-zero reaction enthalpy. This difference in the energies of the ground states, ΔE_{PV}, is the Parity Violation Energy Difference, PVED.

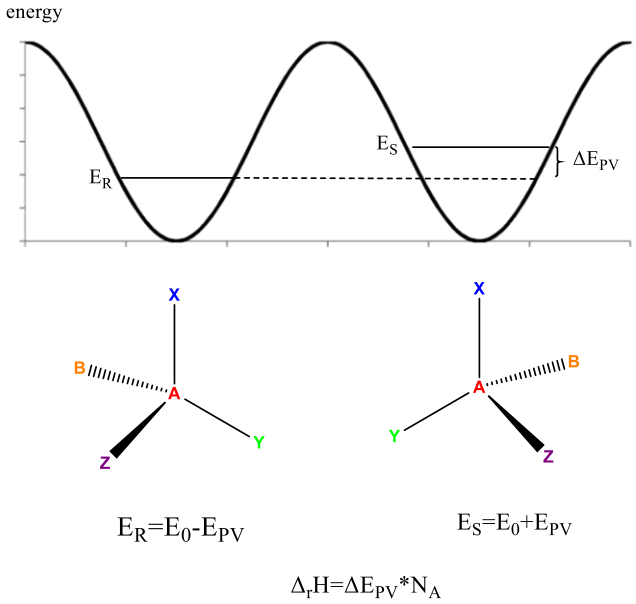

Figure 1.7: PVED in chiral molecules

Yamagata was the first to suggest Parity Violation followed by chiral amplification processes as the origin for biological homochirality in 1966.[81] The relationship between PVED and homochirality has since been the object of several reviews,[82-86] of which we highlight the influential review by Quack.[87] The very small magnitude of Parity Violating Energy of the order of 10^{-17} eV for chiral biomolecules has often been seen as one of the main arguments against PVED: such small differences, even after millions of years of evolution cannot be amplified to the extent of biological homochirality.[88,89]

Theoretical and experimental determination of ΔE_{PV} has drawn considerable attention especially in the 90's-early 2000's. We present here several attempts at determining PVED in molecules both theoretically and experimental.

1.6.1 Theoretical calculations of PVED in molecules

Modern calculations of parity violation energy ΔE_{PV} make use of four-component relativistic time-dependent Dirac Hartree Fock (DHF) calculations. Time-dependent calculations are essential here to account for the time component of parity violation in the weak interaction. Relativistic pseudopotentials are used for the heavier elements[90] while the lighter elements are described by augmented correlation consistent triple zeta Gaussian basis sets.[91] The main component of the Parity Violation Hamiltonian H_{PV} using DHF calculations is:[92]

$$H_{PV} = \frac{G_F}{2\sqrt{2}} \sum_i^n Q_{w,n} \gamma_i^5 \rho_n(r_i) \qquad \textbf{(1)}$$

With the various parameters being the Fermi coupling constant G_F, the pseudoscalar chirality operator γ^5, the weak charge on the nucleus Q_w and the particle density ρ_n. The total parity violation energy E_{PV} is the expectation value of H_{PV} giving:

$$E_{PV} = \frac{G_F}{2\sqrt{2}} \sum_i^n Q_{w,n} M_{PV}^n \qquad \textbf{(2)}$$

where M_{PV}^n is the contribution of each atom.

The first chiral molecule proposed to measure PVED was tetrahedral CHFClBr.[93] As will be discussed later this was also the first molecule for which experimental attempts have been used to determine PVED in molecules. Later, Schwerdtfeger used several tetrahedral atoms with increasingly heavy atoms, including Se, W and Re.[94-96] Recently, Mirzaeva has calculated PVED using a metal organic framework $[Zn_2(C_8H_4O_4)_2.C_6H_{12}N_2]$.[97]

Molecule	**Calculated $\lvert\Delta E_{PV}\rvert$**	**Reference**
CHFClBr	9.12×10^{-18} a.u.	93
SeOClI	2.38×10^{-15} a.u.	94
NWHClI	2.08×10^{-14} a.u.	95
$Re(\eta^5\text{-Cp*})(=O)(CH_3)Cl$	8.28×10^{-14} a.u.	96
$[Zn_2(C_8H_4O_4)_2.C_6H_{12}N_2]$.	4.94×10^{-16} a.u.	97

Table 1.1: Calculated PVED values for selected complexes

An alternative method to determining PVED theoretically was described by Schwerdtfeger *et al.*: rather than measuring the total parity violation energy E_{PV}, differences in vibrational frequencies in the range 820-1100cm^{-1}.[94-96] The chosen range correspond to the range of the CO_2 laser proposed for such experiments.[98] One limitation of this method is the requirement that the molecules have a vibrational transition in that specific range. Table 1.2 compares the values found by this method including the stretching mode of interest.

Molecule	Stretching mode	$\Delta\nu_{PV}^{0\rightarrow1}$ (calculated)
CHFClBr	C-F	3.64x10^{-19} a.u.
SeOClI	Se-O	1.67x10^{-17} a.u.
NWHClI	N-W	1.07x10^{-16} a.u.
Re(η^5-Cp*)(=O)(CH_3)Cl	Re-O	1.96x10^{-16} a.u.

Table 1.2: Theoretical determination of differences in vibrational frequencies of selected complexes in the range 820-1100cm^{-1}

There are two main observations from the data collected in Table 1.1 and Table 1.2 which gives information on how to proceed in order to experimentally determine PVED in molecules. First of all, the scale of calculated ΔE_{PV} is unsurprisingly very small: therefore, any experimental technique designed towards determining PVED in molecules must be precise enough to account for such small differences in energy.

The second observation is that ΔE_{PV} increases in the molecules with atoms having higher atomic number Z. As a matter of fact, it was demonstrated that ΔE_{PV} scales with Z^5 [99]: it was then deemed essential that any molecule used to determine PVED in molecules must contain at least one heavy atom, preferably as the chiral center or in close proximity to it. This dependence on atomic number is similar to what is observed in atoms.

Laerdahl and Schwerdtfeger determined ΔE_{PV} for H_2X_2 where X=O,S,Se,Te and Po.[99] This was the first example of an increase in ΔE_{PV} values with increasing Z going down the periodic table. Mirzaeva observed the same behaviour with zinc, cadmium, and mercury in the metal organic framework discussed previously.[100] Equation (2) reveals that each atom has a contribution to

ΔE_{PV}. Combining this with knowledge that ΔE_{PV} scales with Z^5 indicates that increasing the number of heavy atoms in a molecule would be favourable in determining PVED in molecules.

More relevant to the topic of biological homochirality is the importance of measuring PVED in biomolecules. Mason and Tranter have calculated differences in energies of 10^{-20}a.u. for amino acids, glyceraldehyde, and deoxyribose.[101-103] This was increased to 10^{-17} a.u. for thiosubstituted analogues of DNA.[104] While the presence of heavier sulphur in thiosubstituted DNA analogues has increased the value of PVED, the absence of heavier elements severely limits the potential of calculating PVED in biomolecules.

1.6.2 Experimental determination of PVED in molecules

We have seen that PVED has been theoretically calculated for several different molecules and has been determined experimentally in heavy atoms. In this section we will discuss several experimental techniques aimed at determining PVED in molecules.

1.6.2.1 Vibrational spectroscopy

Measuring the total PVED can be more difficult experimentally. The first option proposed by a consortium of chemists and physicists called the Paris consortium was to measure the difference in vibrational frequencies between the enantiomers. In this case, parity violation contributes to a change in molecular potential causing the difference in the vibrational frequencies. This was attempted using a CO_2 laser and the vibrational frequencies were measured in the range 870-1100cm^{-1} corresponding to the tuning range of the laser. The first molecule to be used was CHFClBr: it is a small chiral molecule and can be synthesized by decarbonylation reaction of strychnine salts.[98,105] While values were proposed for the differences in vibrational frequencies, for CHFClBr the experimental precision of 8Hz was 3000 times larger than the predicted difference in frequency. The same consortium then focused their attention towards chiral oxorhenium complexes bearing tridentate sulphur-containing ligands as well as ones containing trispyrazylborate and ephedrine, Figure 1.7[105] These are readily synthesized starting from the rhenium precursors, $TpRe(O)Cl_2$ and $Re(O)Cl_2(PPh_3)_2$. The complexes were easily resolved via chiral HPLC. One major disadvantage of these complexes is their stability upon heating:

degradation of the complexes above 150 °C was observed. An alternative chiral rhenium containing system involved derivatives of methyltrioxorhenium: these are known to be thermally stable as well as having low sublimation temperatures.[106] Quack first proposed the use isotopically chiral methyltrioxorhenium, $(CH_3)Re(^{16}O)(^{17}O)(^{18}O)$.[107] A better derivative with two oxygens replaced by a sulfur and selenium complex was proposed which would significantly enhance PVED as isotopic chirality only has a minimal effect on PVED. In 2011, using a similar experimental setup as described previously, the Re=O stretching frequency of methyltrioxorhenium was found at 959 cm^{-1}. While this result proves the experimental setup may be successfully applied to chiral derivatives of methyltrioxorhenium, there has so far not been any attempts to use this technique on the molecules presented in Figure 1.7 in order to measure PVED.[108]

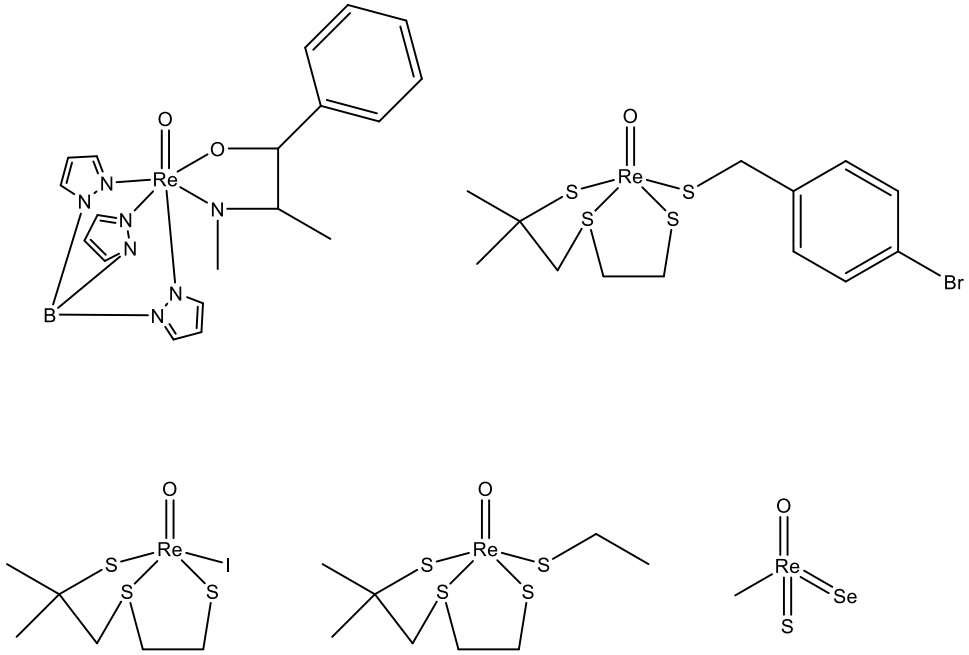

Figure 1.8: Proposed chiral oxorhenium complexes for PVED measurements using vibrational spectroscopy

Vibrational spectroscopy has been sparsely used since: in 2019 Cournol *et al.* proposed an experimental setup which could achieve a resolution of 0.1Hz, an increase of three orders of magnitude compared to the experiment with CFHClBr:[109] a cold beam of the species of interest was first obtained by cooling in cryogenic cell at 4K and quantum cascade lasers were used to

obtain the desired frequency. The experimental setup was successfully applied to an achiral rhenium precursor, methyltrioxorhenium. Work on using this experiment on chiral molecules is still underway: one proposed molecule was the uranium(VI) complex NUHFI on the condition that it be easily synthesized first. This compound would exhibit very large PVED as uranium is the atom with the highest atomic number available, other than the in-laboratory synthesized actinides. Two other examples are the acetylacetonate tris-chelates, $Ru(acac)_3$ and $Os(acac)_3$. These complexes can be readily synthesized and are thermally stable, however the M-O vibrational bands are not within the required range for the experiment. While C-O frequencies are, their differences in shifts between the enantiomers will not be as large due to the dependence on Z^5.[110]

1.6.2.2 Nuclear spectroscopy

Other than vibrational spectroscopy, several new methods have been proposed to measure PVED in molecules. Nuclear spectroscopy methods such as Mössbauer and NMR have been proposed although not as common as vibrational spectroscopy. The first mention of Mossbauer spectroscopy was made by Kesthelyi in 1995 on the ^{193}Ir complex tris(1,2-ethanediamine)iridium(III).[111] However the experimental details were lacking, and no Mossbauer spectra were shown. In 2000, Lahamer provided a more detailed description of the application of Mossbauer spectroscopy to determine PVED in the enantiomers of the tris-chelate iron salt $Fe(phen)_3.Sb_2(S_4O_2H_6)_2$.[112] The complex was easily prepared by substitution of chloride in $FeCl_2.6H_2O$ with phenantroline. Potassium antimonyl (+)-tartrate and Potassium antimonyl (-)-tartrate were used to obtain l- $Fe(phen)_3.Sb_2(S_4O_2H_6)_2$ and d- $Fe(phen)_3.Sb_2(S_4O_2H_6)_2$. In the experimental setup, the ^{57}Fe nucleus was excited from the I=1/2 to I=3/2 state using ^{57}Co as the radioactive source at room temperature. The difference in shifts between the enantiomers resulted in an energy difference of $1.9x10^{-10}$eV, close to the calculated PVED of 10^{-11} eV for the complex. The authors have proposed that the difference in shifts were not due to PVED but possibly solid-state effects of the antimony salts. It was concluded that while the experiment was promising, more work was required. Additionally, it was proposed to use $Sn(phen)_3^{2+}$ instead of the iron analog to increase PVED 70-fold.

Barra was the first to propose the use of NMR to determine PVED experimentally in 1986 by laying out the theory.[113,114] Only in 2017 was it realized experimentally for the first time by Eills *et al.*[115] While enantiomers are expected to yield the same NMR spectra, when taking parity violation effects into account, interactions of the NMR active nuclei with the chiral weak force result in different environments leading to a small difference in NMR chemical shifts. Unfortunately, line broadening often overshadows the expected very small differences in chemical shifts. To overcome this problem, Eills *et al.* increased the concentration of an enantiopure solvent to the NMR tube. Non-covalent interactions with the compound of interest, here 1-phenylethanol, produces diastereomers with different chemical shifts from which parity violation effects can be determined. ^{13}C-NMR spectra on an 850MHz spectrometer were obtained since parity violation effects are negligible in ^{1}H-NMR.

So far, this his been the only example of the application of NMR spectroscopy to measuring PVED in molecules. An upper limit of 1.8mHz for the parity violating difference in chemical shift was observed, far exceeding the expected 10^{-8}-10^{-6}Hz. This experiment was designed as a proof of principle rather than an accurate determination of PVED in molecules. NMR-active nuclei of heavy elements such as ^{195}Pt or ^{207}Pb should greatly enhance differences in chemical shifts due to parity violation compared to ^{13}C used in the experiment.

1.6.2.3 Rotational spectroscopy

One of the most recent developments proposed by Schnell to measure PVED is using rotational microwave spectroscopy.[116] Microwave spectroscopy requires obtaining molecules in the gas phase therefore more volatile compounds are preferred. One candidate molecule for microwave spectroscopy measurements was a rhenium complex proposed by Medcraft, $CpRe(CH_3)(CO)(NO)$.[117] A rotational spectrum was obtained for the complex, however some problems persisted. Rhenium has two abundant isotopes, rhenium-185 (37%) and rhenium-187 (63%). The presence of two commonly occurring isotopes complicates the spectrum. Additionally, some internal motion independent from the rest of the molecule such as rotation of the Me bond and Cp bond complicates the spectrum even further. Parity violation would cause a change in rotational constants in the same order of magnitude as the changes in vibrational

frequencies used in the previous method. The results showed that the rhenium complex was a good candidate for microwave spectroscopy however the PVED has not yet been measured.

1.6.2.4 Crystallization

Several reports claiming to detect PVED by crystallization have been made. Kesthelyi proposed that crystallization of complexes with heavy atoms would be able to detect PVED. They reported enantiomeric excesses in the crystallization of racemic mixtures of tris(1,2-ethanediamine)cobalt(III), and tris(1,2-ethanediamine)iridium(III).[118] Similarly, Shinitzky observed that solubility differences between D and L- tyrosine lead to an enantiomeric excess of L-tyrosine by crystallization.[119] The attribution of these phenomena to PVED was strongly criticized by Lahav *et al.* mainly on the grounds that the authors did not account for impurities which may cause in imbalance in enantiomeric excesses.[120]

Finally, several methods have been described but not yet applied experimentally, including optical rotation[121,122] or via Bose-Einstein condensation.[123]

1.6.2.5 Conclusion

Since the introduction of the theory that parity violation in molecules is the origin of homochirality, many attempts have been made to experimentally measure PVED in molecules using a variety of high resolution spectroscopic methods. The sobering conclusion is that, even after decades of work in the field, not a single experiment has yet been able to unambiguously measure PVED in molecules. As a consequence, few groups have to decided to pursue this path.

1.7 What makes a good candidate molecule?

One of the possible reasons why parity violation has not been measured is due to the difficulty of finding a suitable candidate molecule.

A certain number of criteria must be met in order for a candidate molecule to be considered: it must be chiral, resolvable, and obtainable in enantiopure form. It must be available in large enough quantities to run measurements. Volatile molecules may be preferred for some experiments namely microwave spectroscopy.

One of the most important factors is the presence of a heavy atom preferably at the center. Tables 1.1 and 1.2 show the increase either in total PVED or in the difference in vibrational frequencies when a heavy atom is present by an order of magnitude of 1000. It has been previously determined that PVED scales with the atomic number to the power 5. Therefore, the presence of a heavy atom in the molecule is not only important but critical in determining accurately parity violation in molecules. This is also important regarding the problem of homochirality: since amino acids are small molecules without any heavy atoms, their PVED would be too small to be measured. A metal complex containing a heavy atom is a much more viable candidate for the measurement of PVED in molecules.

Finally, an important consideration in finding molecules for PVED detection is their stability against racemization: when optically resolved, the enantiomers must not revert back to the racemic form. We have noticed that many discussions of PVED in molecules seem to omit this critical point.

1.8 Rationale and Objectives

In section 1.7 we have discussed the criteria required for a molecule to be a good candidate for PVED detection in molecules. From this knowledge, we have concluded that neutral tris-chelate complexes of group 9 d^6 metals (Co, Rh and Ir) fulfill many of these criteria. In section 1.1 we have discussed the chirality of such complexes and seen how two enantiomers, Δ and Λ exist. We have also seen that several methods have been successfully used to optically resolve transition metal complexes including tris-chelate complexes. We turn our attention to neutral complexes since charged species may be more difficult to obtain in the gas phase. Many of these complexes are simple to synthesize and in good yields.

These complexes, especially with the heavier elements rhodium and iridium, have been accepted to be stereochemically rigid with high barriers of interconversion between the enantiomers.[124,125] In section 1.1.3 and 1.1.4 we have discussed mechanisms by which tris-chelate complexes invert stereochemistry as well as related structural parameters. As discussed previously, the d^5 tris-

chelate complexes $Ru(acac)_3$ and $Os(acac)_3$ were suggested as tris-chelate complexes viable for PVED measurements using vibrational spectroscopy.[110]

In this thesis we will be interested in the application of group 9 d^6 tris-chelate complexes as potential candidates to measure PVED in molecules. We will investigate complexes with different ligands, namely tropolonates and dithiocarbamates, and focus on their fluxional behaviour, and mechanisms of inversion of stereochemistry. In Chapter 2 we will discuss the synthesis, spectroscopy and dynamic NMR behaviour first of tris-chelate complexes of cobalt, rhodium and iridium of a tropolonate derivative, hinokitiol as well as potential kinetic lability. Based on the results from this chapter we will then discuss the dynamic behaviour of several Ru(II) and Os(II) complexes with the same ligand in Chapter 3. While the complexes studied are not tris-chelates, they help give a better insight into the fluxionality of complexes of this tropolone derivative. This may also have important consequences for the biochemistry of hinokitiol.

In chapter 4 we will focus our attention to a different class of ligands, dithiocarbamates, in particular the smaller parent dithiocarbamate $[S_2CNH_2]^-$. Since very little organometallic chemistry has been done with this particular ligand, we will discuss the synthesis of some Ru(II) complexes in order to get a better understanding of its bonding to metals. We will then discuss the synthesis of tris-chelate complexes of group 9 metals and compare their structural parameters to those of other known dithiocarbamate complexes in order to assess its fluxional behaviour, in the same vein as in Chapter 2.

Finally, in Chapters 5, 6 and 7, we will also be interested in studying a very rare class of ligands, fluorodithiophosphates, in particular $[S_2PF_2]^-$, $[S_5P_2F_2]^{2-}$ and $[S_3PF]^{2-}$. These are ligands of which the organometallic chemistry is still virtually unknown. We will present some of the first examples of crystal structures of such complexes and give a detailed analysis of their spectroscopy: this includes several Ru(II) complexes of $[S_2PF_2]^-$, as well as a wide range of complexes with different metals and different coordination in the case of $[S_5P_2F_2]^{2-}$ and $[S_3PF]^{2-}$.

1.9 References

1. Pasteur, L: Sur les Relations qui Peuvent Exister Entre la Forme Crystalline, la Composition Chimique et le Sens de la Polarization Rotatoire *Ann. Chim. Phys. Sér.*, **1848**, *3* 24, 442–459
2. Gal, J.: Pasteur and the Art of Chirality, *Nat. Chem.*, **2017**, *9*, 604–605
3. Gil-Av, E.; Feibush, B.: Resolution of Enantiomers by Gas Liquid Chromatography with Optically Active Stationary Phases. Separation on Packed Columns, *Tetrahedron Lett.*, **1967,** *35*, 3345-3347
4. Frank, H.; Nicholson, G.; Bayer, J. E.: Chiral Polysiloxanes for Resolution of Optical Antipodes, *Angew. Chem. Int. Ed. Engl.*, **1978**, *17*, 363-365
5. Schurig, V.: Gas Chromatographic Separation of Enantiomers on Optically Active Metal-Complex-Free Stationary Phases. New Analytical Methods (24) *Angew. Chem. Int. Ed. Engl.*, **1984**, *23*, 747-765
6. Xie, S.; Yuan, L.: Recent Development Trends for Chiral Stationary Phases Based on Chitosan Derivatives, Cyclofructan Derivatives and Chiral Porous Materials in High Performance Liquid Chromatography. *J. Sep. Sci.*, **2019**, *42*, 6–20.
7. Yashima, E.: Polysaccharide-Based Chiral Stationary Phases for High-Performance Liquid Chromatographic Enantioseparation., *J. Chromatogr. A*, **2001**, *906*, 105–125.
8. Tang, S.; Bin, Q.; Chen, W.; Bai, Z.-W.; Huang, S.H.: Chiral Stationary Phases Based on Chitosan Bis(methylphenylcarbamate)-(isobutyrylamide) for High-Performance Liquid Chromatography., *J. Chromatogr. A*, **2016**, *1440*, 112–122
9. Shen, J.; Wang, F.; Bi, W.; Liu, B.; Liu, S.; Okamoto, Y.: Synthesis of Cellulose Carbamates Bearing Regioselective Substituents at 2,3- and 6- Positions for Efficient Chromatographic Enantioseparation, *J. Chromatogr. A*, **2018**, *1572*, 54–61.
10. Bressolle, F.; Audran, M.; Pham, T.-N.; Vallon, J.-J.: Cyclodextrins and Enantiomeric Separations of Drugs by Liquid Chromatography and Capillary Electrophoresis: Basic Principles and New Developments., *J. Chromatogr. B Biomed. Appl.*, **1996**, *687*, 303–336.

11. Xiao, Y.; Ng, S.C.; Tan, T.T.Y.; Wang, Y.: Recent Development of Cyclodextrin Chiral Stationary Phases and Their Applications in Chromatography., *J. Chromatogr. A,* **2012**, *1269*, 52–68.
12. Chen, X.J.; Yang, G.L.; Xu, X.D.; Sheng, J.J.; Shen, J.: Preparation and Chromatographic Evaluation of β-cyclodextrin Derivative CSPs Bearing Substituted Phenylcarbamate Groups for HPLC., *J. Liq. Chromatogr. Relat. Technol.*, **2016**, *39*, 647–657.
13. Zhou, J.; Yang, B.; Tang, J.; Tang, W.: A Cationic Cyclodextrin Clicked Bilayer Chiral Stationary Phase for Versatile Chiral Separation in HPLC., *New J. Chem.*, **2018**, *42*, 3526–3533.
14. Sousa, L.R.; Sogah, G.D.Y.; Hoffmann, D.H.; Cram, D.J.: Host-Guest Complexation. 12. Total Optical Resolution of Amine and Amino Ester Salts by Chromatography., *J. Am. Chem. Soc.,* **1978**, *100*, 4569–4576.
15. Hyun, M.H.: Liquid Chromatographic Enantioseparations on Crown Ether-Based Chiral Stationary Phases., *J. Chromatogr. A,* **2016**, *1467*, 19–32.
16. Hyun, M.H.: Development of HPLC Chiral Stationary Phases Based on (+)-(18-Crown-6)-2,3,11,12-Tetracarboxylic Acid and Their Applications., *Chirality*, **2015**, *27*, 576–588.
17. Yoneda, H.:Stereochemical Aspects of Optical Resolution of Octahedral Metal Chelates by Liquid Chromatography, *J. Liq, Chromatogr*, **1979**, *2*,1157-1178,
18. Kobayashi, H.; Matsuzawa, H.; Kaizu, Y.; Ichida, A.: Resolution and Circular Dichroism of the Optical Isomers of Tris(2,4-pentanedionato)ruthenium(III), *Inorg. Chem.,* **1987**, *26*, 4318-4323
19. Sun, P.; Krishnan, A.; Yadav, A.; Singh, S.; MacDonnell, F. M.; Armstrong, D. W.; Enantiomeric Separations of Ruthenium(II) Polypyridyl Complexes Using High-Performance Liquid Chromatography (HPLC) with Cyclodextrin Chiral Stationary Phases (CSPs), *Inorg. Chem.,* **2007**, *46*, 10312–10320
20. Chen, X. M.; Okamoto, Y.; Yano, T.; Otsuki, J.: Direct Enantiomeric Separations of tris(2-phenylpyridine) Iridium(III) Complexes on Polysaccharide Derivative-Based Chiral Stationary Phases, *J. Sep. Sci.,* **2007**, *30*, 713–716

21. Yamazaki, S.; Yukimoto, T.; Yoneda, H.: Chromatographic Study of Optical Resolution : III. Separation of Isomers of Facial Tris(minoacidato)Cobalt(III) Complexes with D-Tartrate and Antimony D-Tartrate Solutions, *J. Chromatogr. A.*, **1979**, *175*, 317-324
22. Coughlin, F. J.; Westrol, M. S.; Oyler, K. D.; Byrne, N.; Kraml, C.; Zysman-Colman, E.; Lowry, M. S.; Bernhard, S.: Synthesis, Separation, and Circularly Polarized Luminescence Studies of Enantiomers of Iridium(III) Luminophores, *Inorg. Chem.*, **2008**, *47*, 2039-2048
23. Shelton, C. M.; Seaver, K. E.; Wheeler, J. F.; Kane- Maguire, N. A. P.: Application of Capillary Electrophoresis for the Assessment of Enantiomeric Purity of α-Diimine Transition Metal Complexes, *Inorg. Chem.*, **1997**, *36*, 1532-1533
24. Harris, J. E.; Desai, N.; Seaver, K. E.; Watson, R. T.; Kane-Maguire, N. A. P.; Wheeler, J. F.; Chiral Separations of Transition Metal Complexes Using Capillary Zone Electrophoresis, *J. Chromatogr. A*, **2001**, *919,* 427–436
25. Carmona, M.; Rodríguez, R.; Passarelli, V.; Lahoz, F. J.; García-Orduña, P.; Carmona, D.: Metal as Source of Chirality in Octahedral Complexes with Tripodal Tetradentate Ligands, *J. Am. Chem. Soc*., **2018**, *140*, 912−915
26. Jakobsen, V. B.; O'Brien, L.; Novitchi, G.; Müller-Bunz, H.; Barra, A. L.; Morgan, G. G.: Chiral Resolution of a Mn^{3+} Spin Crossover Complex, *Eur. J. Inorg. Chem.*, **2019**, 4405–4411
27. Broomhead, J. A.; Dwyer, F. P.; Hogarth, J. W.: Resolution of the Tris(Ethylenediamine)Cobalt(III) Ion., *Inorg. Synth.*, **1960**, *VI.*, 183–186
28. Drake, A. F.; Gould, J. M.; Mason, S. F.; Rosini, C.; Woodley, F. J.: The Optical Resolution of Tris(pentane-2,4-dionato)Metal(III) Complexes, *Polyhedron*, **1983**, 2, 537-538
29. Gahan, L. R.; Hughes, J. F.; O'Connor, M. J.; Oliver, P. J.: Optically Active Tris(dithiocarbamato)Cobalt(III) Chelates. Preparation and Assignment of Absolute Configuration, *Inorg. Chem.*, **1979**, *18*, 933-937
30. Pignolet L.H., Dynamics of Intramolecular Metal-Centered Rearrangement Reactions of Tris-Chelate Complexes, *Top. Chr. Chem*., **1975**, 56,91-137

31. Bailar, J. C.: Some Problems in the Stereochemistry of Coordination Compounds: Introductory Lecture, *J. Inorg. Nucl. Chem.*, **1958**, *8*, 165-175
32. Ray, P.; Dutt, N. K.: Kinetics and Mechanism of Racemization of Optically Active Cobaltic Trisbiguanide Complex, *J. Indian Chem. Soc.*, **1943**, *20*, 81-92
33. Ashley, D. C.; Jakubikova, E.: Ray-Dutt and Bailar Twists in Fe(II)-Tris(2,2′-bipyridine): Spin States, Sterics, and Fe–N Bond Strengths., *Inorg. Chem.*, **2018**, *57*, 5585−5596.
34. N. Serpone and D. G. Bickley, Kinetics and Mechanisms of Isomerization and Racemization Processes of Six Coordinate Chelate Complexes, *Progr. Inorg. Chem.*, **1972**, *17*, 391-559
35. Rodger A., Johnson B. F. G., Which Is More Likely: The Ray-Dutt Twist or the Bailar Twist?, *Inorg. Chem*., **1988**, *27*, 3061-3062
36. Blackmond D. G., The Origin of Biological Homochirality., *Cold Spring Harb. Perspect. Biol.*, **2010**, *2*, a002147
37. Kvenvolden, K. A.; Lawless, J.; Pering, K.; Peterson, E.; Flores, J.; Ponnamperuma, C.; Kaplan, I. R.; Moore, C.: Evidence for Extraterrestrial Amino-Acids and Hydrocarbons in the Murchison Meteorite., *Nature.*, **1970**, *228*, 923–926
38. Meierhenrich, U. J.; Bredehöft, J. H.; Jessberger, E. K.; Thiemann, W. H. P.: Identification of Diamino Acids in the Murchison Meteorite. *PNAS*., **2004**, *101*, 9182–9186.
39. Engel, M. H.; Nagy, B.: Distribution and Enantiomeric Composition of Amino Acids in the Murchison Meteorite. *Nature*, **1982**, *296*, 837–840
40. Bada, J. L.; Cronin, J. R.; Ho, M. S.; Kvenvolden, K. A.; Lawless, J. G.; Miller, S. L.; Oro, J.; Steinberg, S.: On the Reported Optical Activity of Amino Acids in the Murchison Meteorite, *Nature.*, **1983**, *301*, 494–496
41. Cronin, J. R.; Pizzarello, S.: Enantiomeric Excesses in Meteoritic Amino Acids., *Science.*, **1997**, *275*, 951–955.
42. Cronin, J.R.; Pizzarello, S. Amino Acid Enantiomer Excesses in Meteorites: Origin and Significance., *Adv. Space Res.*, **1999**, *23*, 293–299

43. Frank, F. C.: On Spontaneous Asymmetric Synthesis, *Biochim. Biophys. Acta*, **1953**, *11*, 459–463
44. Soai K, Shibata T, Morioka H, Choji K.: Asymmetric Autocatalysis and Amplification of Enantiomeric Excess of a Chiral Molecule, *Nature.*, **1995**, *378*, 767–768.
45. Shibata T, Morioka H, Hayase T, Choji K, Soai K.: Highly Enantioselective Catalytic Asymmetric Automultiplication of Chiral Pyrimidyl Alcohol, *J. Am. Chem. Soc.*, **1996**, *118*, 471–472.
46. Blackmond, D. G.: Autocatalytic Models for the Origin of Biological Homochirality, *Chem. Rev.*, **2020**, *120*, 4831−4847
47. Hawbaker, N. A.; Blackmond, D. G.: Energy Threshold for Chiral Symmetry Breaking in Molecular Self-Replication, *Nat. Chem*., **2019**, *11*, 957-962
48. Kondepudi, D. K., Kaufman R. J.; Singh, N.: Chiral Symmetry Breaking in Sodium Chlorate Crystallization, *Science*, **1990**, *250*, 975–976
49. Kondepudi, D. K.; Asakura, K.: Chiral Autocatalysis, Spontaneous Symmetry Breaking, and Stochastic Behavior, *Acc. Chem. Res.*, **2001**, *34*, 946–954
50. Viedma, C.: Chiral Symmetry Breaking During Crystallization: Complete Chiral Purity Induced by Nonlinear Autocatalysis and Recycling, *Phys. Rev. Lett.*, **2005**, *94*, 065504
51. Viedma, C.: Chiral Symmetry Breaking and Complete Chiral Purity by Thermodynamic-Kinetic Feedback Near Equilibrium: Implications for the Origin of Biochirality, *Astrobiology*, **2007**,*7*, 312-319
52. Noorduin, W. L.; Izumi, T.; Millemaggi, A.; Leeman, M.; Meekes, H.; Van Enckevort, W. J. P.; Kellogg, R. M.; Kaptein, B.; Vlieg, E.; Blackmond, D. G.: Emergence of a Single Solid Chiral State from a Nearly Racemic Amino Acid Derivative., *J. Am. Chem. Soc.*, **2008**, *130*, 1158–1159
53. Noorduin, W. L.; van der Asdonk, P.; Bode, A. A. C.; Meekes, H.; van Enckevort, W. J. P.; Vlieg, E.; Kaptein, B.; van der Meijden, M. W.; Kellogg, R. M.; Deroover, G.: Scaling up Attrition-Enhanced Deracemization by Use of an Industrial Bead Mill in a Route to Clopidogrel (Plavix), *Org. Process Res. Dev.*, **2010**, *14*, 908–911.

54. Noorduin, W. L; van Eckenvoort, W. J. P.; Meekes, H.; Kaptein, B.; Kellogg, R. M.; Tully, J. C.; McBride, M.; Vlieg, E.: The Driving Mechanism Behind Attrition-Enhanced Deracemization, *Angew. Chem. Int. Ed*., **2010**, *49*, 8435 –8438
55. Noorduin, W. L. ; Bode, A. A. C.; Van der Meijden, M.; Meekes, H.; van Etteer, A. F.; van Enckevort, W. J. P.; M.Christianen, P. C.; Kaptein, B.; Kellogg, R. M.; Rasing, T.; Vlieg, E.: Complete Chiral Symmetry Breaking of an Amino Acid Derivative Directed by Circularly Polarized Light, *Nat. Chem.*, **2009**, *1*, 729-732
56. Engwerda, A. H. W.; van Schayik, P.; Jagtenberg, H.; Meekes, H.; Rutjes, F. P. J. T.; Vlieg E.: Deracemization of a Racemic Compound by Using Tailor-Made Additives, *Chem.Eur.J*., **2018**, *24*, 2863 –2867
57. Bonner, W. A.: The Origin and Amplification of Biomolecular Chirality, *Orig Life Evol Biosph.*, **1991**, *21*, 59-111
58. Tsuchida, R.; Kobayashi, M.; Nakamura, A.: Asymmetric Adsorption of Complex Salts on Quartz, *J. Chem. Soc. Japan*, **1935**, *56*, 1339
59. Bonner, W. A.; Kavasmaneck, R R.; Martin, F. S.; and Flores, J. J.: Asymmetric Adsorption by Quartz: A Model for the Prebiotic Origin of Optical Activity, *Orig Life Evol Biosph*, **1975**, *6*,367.
60. Klabunovskii, E.; Thiemann, W.: The Role of Quartz in the Origin of Optical Activity on Earth, *Orig Life Evol Biosph.*, **2000**, *30*, 431–434
61. Feringa, B. L.; van Delden, R. A.: Absolute Asymmetric Synthesis: The Origin, Control, and Amplification of Chirality, *Angew. Chem. Int. Ed.*, **1999**, *38*, 3418-3438
62. Kawasaki, T.; Sato, M.; Ishiguro, S.; Saito, T.; Morishita, Y.; Sato, I.; Nishino, H.; Inoue, Y.; Soai, K.: Enantioselective Synthesis of Near Enantiopure Compound by Asymmetric Autocatalysis Triggered by Asymmetric Photolysis with Circularly Polarized Light, *J. Am. Chem. Soc.*, **2005**, *127*, 3274–3275
63. Flores, J. J.; Bonner, W. A.; Massey, G. A.: Asymmetric Photolysis of (RS)-Leucine with Circularly Polarized Ultraviolet Light, *J. Am. Chem. Soc.*, **1977**, *99*, 3622–3625

64. Choi, S. W.; Izumi, T.; Hoshino, Y.; Takanishi, Y.; Ishikawa, K.; Watanabe, J.; Takezoe, H.: Circular-Polarization-Induced Enantiomeric Excess in Liquid Crystals of an Achiral, Bent-Shaped Mesogen, *Angew.Chem.*, **2006**, *118*, 1410–1413
65. Suarez, M.; Schuster, G. B.: Photoresolution of an Axially Chiral Bicyclo[3.3.0]octan-3-one: Phototriggers for a Liquid-Crystal-Based Optical Switch, *J. Am. Chem. Soc.*, **1995**, *117*, 6732-6738
66. Tenney L. D., Ackerman, J.: Asymmetric Synthesis. III.1 Experiments Toward a Total Asymmetric Synthesis of Tartaric Acid, *J Am. Chem. Soc*, **1945**, *67*, 486-489
67. Moradpour, A.; Nicoud, J. F.; Balavoine, G.; Kagan, H.; Tsoucaris, G.: Photochemistry with Circularly Polarized Light.The Synthesis of Optically Active Hexahelicene, *J. Am. Chem. Soc*., **1971**, *93*, 2353-2354
68. Schwinger, J. S.: A Theory of the Fundamental Interactions, *Ann. Phys. (N.Y.)*, **1957**, *2*, 407-434
69. Wu, C. S.; Ambler, E.; Hayward, R. W.; Hoppes, D. D.; Hudson, R. P.: Experimental Test of Parity Conservation in Beta Decay., *Phys. Rev.*, **1957**, *105*, 1413–1415
70. Kobayashi, M.; Maskawa, T.: CP-Violation in the Renormalizable Theory of Weak Interaction, *Prog. of Theor. Phys*., **1973**, *49*, 652–657
71. Feynman, R.; Leighton, R.; Sands, M.; Hafner, E.: The Feynman Lectures on Physics; Vol. I, AAPT, **1965**
72. Bouchiat, M. A.; Bouchiat, C.; Parity Violation in Atoms, *Rep. Prog. Phys.*, **1997**, *60*, 1351-1396
73. Ginges, J. S. M.; Flambaum, V. V.: Violations of Fundamental Symmetries in Atoms and Tests of Unification Theories of Elementary Particles, *Phys. Rep.*, **2004**, *397*, 63-154
74. Wood, C. S.; Bennett, S. C.; Cho, D.; Masterson, B. P.; Roberts, J. L.; Tanner, C. E.; Wieman, C. E.; Measurement of Parity Nonconservation and an Anapole Moment in Cesium, *Science*, **1997**, *275*, 1759-1763
75. DeMille, D.: Parity Nonconservation in the $6s^2 {}^1S_0 \rightarrow 6s5d\,{}^3D_1$ Transition in Atomic Ytterbium, *Phys. Rev. Lett.*, **1995**, *74*, 4165-4168

76. Meekhof, D. M.; Vetter, P. A.; Majumder, P. K.; Lamoreaux, S. K.; Fortson, E. N.: High-Precision Measurement of Parity Nonconserwing Optical Rotation in Atomic Lead, *Phys. Rev. Lett.*, **1993**, *71*, 3442-3445
77. Vetter, P. A.; Meekhof, D. M.; Majumder, P. K.; Lamoreaux, S. K.; Fortson, E.N.: Precise Test of Electroweak Theory from a New Measurement of Parity Nonconservation in Atomic Thallium, *Phys. Rev. Lett.*, **1995**, *74*, 2658-2661
78. Drell, P. S.; Commins, E. D.: Parity Nonconservation in Atomic Thallium, *Phys Rev A.*, **1985**, *32*, 2196-2210
79. Macpherson, M. J. D.; Zetie, K. P.; Warrington, R. B.; Stacey, D. N.; Hoare, J. P.: Precise Meas«ement of Parity Nonconserving Optical Rotation at 876 nm in Atomic Bismuth., *Phys Rev. Lett.*, **1991**, *67*, 2784-2787
80. Rein D. W.: Some Remarks on Parity Violating Effects of Intramolecular Interactions, *J. Mol. Evol.*, **1974**, *4*, 15-22
81. Yamagata, Y.: A Hypothesis for the Asymmetric Appearance of Biomolecules on Earth., *J. Theor. Biol.*, **1966**, *11*, 495-498
82. Bonner, W. A.: Parity Violation and the Evolution of Biomolecular Homochirality., *Chirality*, **2000**, *12*, 114-126.
83. Fitz, D.; Reiner, H. ; Plankensteiner, K.; Rode, B. M. : Possible Origins of Biohomochirality., *Curr. Chem. Biol.*, **2007**, *1*, 41-52.
84. MacDermott, A. J.: The Ascent of Parity-Violation: Exochirality in the Solar System and Beyond., *Enantiomer*, **2000**, *5*, 153-168.
85. MacDermott, A. J. Perspectives and Concepts: Biomolecular Significance of Homochirality: The Origin of the Homochiral Signature of Life. *In Comprehensive Chirality*, E. M. Carreira, H. Y., Ed.; Elsevier: Amsterdam, **2012**, *8*, 11−38
86. Keszthelyi, L., Origin of the Homochirality of Biomolecules., *Q. Rev. Biophys.*, **1995**, *28*, 473-507
87. Quack, M.: How Important is Parity Violation for Molecular and Biomolecular Chirality?" *Angew. Chem. Int. Ed.*, **2002**, *41***,** 4618-4630.

88. Chandrasekhar, S.: Molecular Homochirality and the Parity-Violating Energy Difference. A Critique with New Proposals., *Chirality*, **2008**, *20*, 84-95.
89. Chandrasekhar, S.: The Origins of Molecular Homochirality: A Critique of Current Theories. Is It Really Possible to Amplify the Parity-Violating Energy Difference (PVED)? Possible Implications for the Racemic Compound-Conglomerate Dichotomy., *Chem. Prepr. Server, Org. Chem.*, **2004**, 1-13
90. Peterson, K. A.; Figgen, D.; Goll, E.; Stoll, H.; Dolg, M.: Systematically Convergent Basis Sets with Relativistic Pseudopotentials. II. Small-Core Pseudopotentials and Correlation Consistent Basis Sets for the Post-d Group 16–18 elements, *J. Chem. Phys.*, **2003**, *119*, 11113-11123
91. Kendall, R. A.; Dunning Jr., T. H.; Harrison, R. J.: Electron Affinities of the First-Row Atoms Revisited. Systematic Basis Sets and Wave Functions, *J. Chem. Phys*., **1992**, *96*, 6796-6806
92. Blundell, S. A.; Sapirstein, J.; Johnson, W. R.: High-Accuracy Calculation of Parity Nonconservation in Cesium and Implications for Particle Physics, *Phys. Rev. D*, **1992**, *45*, 1602–1623
93. Crassous, J.; Chardonnet, C.; Saue, T.; Schwerdtfeger, P.: Recent Experimental and Theoretical Developments Towards the Observation of Parity Violation (PV) Effects in Molecules by Spectroscopy, *Org. Biomol. Chem.*, **2005**, *3*, 2218-2224
94. Figgen, D.; Schwerdtfeger, P.: SeOClI: A Promising Candidate for the Detection of Parity Violation in Chiral Molecules, *Phys. Rev. A.*, **2008**, *78*, 012511
95. Figgen, D.; Schwerdtfeger, P.: NWHClI: A Small and Compact Chiral Molecule with Large Parity-Violation Effects in the Vibrational Spectrum, *Angew. Chem. Int. Ed.* **2010**, *49*, 2941 –2943
96. Schwerdtfeger, P.; Bast, R.: Large Parity Violation Effects in the Vibrational Spectrum of Organometallic Compounds, *J. Am. Chem. Soc*. **2004**, *126*, 1652-1653.
97. Mirzaeva, I. V.; Kozlova, S. G.: Computational Estimation of Parity Violation Effects in a Metal-Organic Framework Containing DABCO., *Chem. Phys. Lett.*, **2017**, *687*, 110-115.

98. Darquié, B.; Stoeffler, C.; Shelkovnikov, A.; Daussy, C.; Amy-Klein, A.; Chardonnet, C.; Zrig, S.; Guy, L.; Crassous, J.; Soulard, P.; Asselin, P.; Huet, T. R.; Schwerdtfeger, P.; Bast, R.; Saue, T.: Progress Toward the First Observation of Parity Violation in Chiral Molecules by High-Resolution Laser Spectroscopy, *Chirality*, **2010**, *22*, 870–884
99. Laerdahl, J. K.; Schwerdtfeger, P.: Fully Relativistic Ab Initio Calculations of the Energies of Chiral Molecules Including Parity-Violating Weak Interactions, *Phys. Rev. A*, **1999**, *60*, 4439-4453
100. Mirzaeva, I. V.; Kozlova, S. G.: Parity Violating Energy Difference for Mirror Conformers of DABCO Linker Between Two M^{2+} Cations (M = Zn, Cd, and Hg)., *J. Chem. Phys.*, **2018**, *149*, 214302
101. Mason, S. E.; Tranter, G. E.: The Parity-Violating Energy Difference Between Enantiomeric Molecules, *Mol. Phys.*, **1984**, *53*, 1091-1111
102. Tranter, G. E.: Preferential Stabilization of the D-Sugar Series by the Parity-Violating Weak Interactions, *J. Chem. Soc. Chem. Commun.*, **1986**, *6*, 60-61
103. MacDermott, A. J.; Tranter, G. E.: The Search for Large Parity-Violating Energy Differences Between Enantiomers, *Chem. Phys. Lett.*, **1989**, *163*, 1-4
104. MacDermott, A. J. ; Tranter, G. E. ; Trainor, S. J.: The Search for Large Parity-Violating Energy Differences Finds Fruit in Thiosubstituted DNA Analogues., *Chem. Phys. Lett.*, **1992**, *194*, 152-156
105. Crassous, J.; Collet, A.: The Bromochlorofluoromethane Saga, *Enantiomers.*, **2000**, *5*, 429-438
106. De Montigny, F.; Bast, R.; Severo Pereira Gomes, A.; Pilet, G.; Vanthuyne, N.; Roussel, C.; Guy, L.; Schwerdtfeger, P.; Saue, T.; Crassous, J.: Chiral Oxorhenium(V) Complexes as Candidates for the Experimental Observation of Molecular Parity Violation: a Structural, Synthetic and Theoretical Study, *Phys. Chem. Chem. Phys.*, **2010**, *12*, 8792–8803
107. Quack, M.: Structure and Dynamics of Chiral Molecules, *Angew Chem Int Ed Engl*, **1989**, *28*, 571–586

108. Stoeffler, C.; Darquie, B.; Shelkovnikov, A.; Daussy, C.; Amy-Klein, A.; Chardonnet, C.; Guy, L.; Crassous, J.; Huet, T. R.; Soularde, P.; Asselin, P.: High Resolution Spectroscopy of Methyltrioxorhenium: Towards the Observation of Parity Violation in Chiral Molecules, *Phys. Chem. Chem. Phys*., **2011**, *13*, 854–863

109. Cournol, A.; Manceau, M.; Pierens, M.; Lecordier, L.; Tran, D. B. A.; Santagata, R.; Argence, B.; Goncharov, A.; Lopez, O.; Abgrall, M.; Le Coq, Y.; Le Targat, R.; Álvarez Martinez, H.; Lee, W. K.; Xu, D.; Pottie, P. E.; Hendricks, R. J.; Wall, T. E.; Bieniewska, J. M.; Sauer, B. E.; Tarbutt, M. R.; Amy-Klein, A.; Tokunaga, S. K.; Darquié, B.: A New Experiment to Test Parity Symmetry in Cold chiral Molecules Using Vibrational Spectroscopy., *Quantum Electron.*, **2019**, *49*, 288-292

110. Fiechter, R. M.; Haase, P. A. B.; Saleh, N; Soulard, P.; Tremblay, B.; Havenith, R. W. A.; Timmermans, R. G. E.; Schwerdtfeger, P.; Crassous, J.; Darquie, B.; Pasteka, L. F.; Borschevsky, A.: Towards Detection of the Molecular Parity Violation in Chiral $Ru(acac)_3$ and $Os(acac)_3$, arXiv:2111.05036

111. Keszthelyi, L.: Possibilities to Measure the Parity-Violating Energy Difference, *J. Biol. Phys*., **1994**, *20*, 241-245

112. Lahamer, A. S. ; Mahurin, S. M.; Compton, R. N.; Hounse, D.; Laerdahl, J. K.; Schwerdtfeger, P.: Search for a Parity-Violating Energy Difference between Enantiomers of a Chiral Iron Complex., *Phys. Rev. Lett.*, **2000**, *85*, 4470-4473.

113. Barra, A. L.; Robert, J. B.; Wiesenfeld, L.: Parity Non-Conservation and NMR Observables. Calculation of Tl Resonance Frequency Differences in Enantiomers, *Phys. Lett. A*, **1986**, *115*, 443–447

114. Barra, A. L.; Robert, J. B.: Parity Non-Conservation and NMR Parameters, *Mol. Phys*., **1996**, *88*, 875–886

115. Eills, J.; Blanchard, J. W.; Bougas, L.; Kozlov, M. G.; Pines, A.; Budker, D.: Measuring Molecular Parity Nonconservation Using Nuclear Magnetic-Resonance Spectroscopy, *Phys. Rev. A*, **2017**, *96*, 042119

116. Schnell, M.; Küpper, J.: Tailored Molecular Samples for Precision Spectroscopy Experiments, *Faraday Discuss*., **2011**, *150*, 33 – 49.

117. Medcraft C., Wolf R., Schnell M., High-Resolution Spectroscopy of the Chiral Metal Complex [CpRe(CH_3)(CO)(NO)]: A Potential Candidate for Probing Parity Violation, *Angew. Chem. Int. Ed.*, **2014**, *53*, 11656-11659

118. Szabó-Nagy, A.: Keszthelyi, L.: Demonstration of the Parity-Violating Energy Difference Between Enantiomers, *PNAS*, **1999**, *96*, 4252-4255

119. Shinitzky, M.; Nudelman, F.; Barda, Y.; Haimovitz, R.; Chen, E.; Deamer, D. W.: Unexpected Differences Between D- and L-Tyrosine Lead to Chiral Enhancement in Racemic Mixtures, *Orig Life Evol Biosph.*, **2002**, *32*, 285-297

120. Lahav, M.; Weissbuch, I.; Shavit, E.; Reiner, C.; Nicholson, G. J.; Schurig, V.: Parity Violating Energetic Difference and Enantiomorphous Crystals-Caveats; Reinvestigation of Tyrosine Crystallization, Orig. Life Evol. Biosph., **2006**, *36*, 151-170.

121. MacDermott, A. J.; Hegstrom, R. A.: A Proposed Experiment to Measure the Parity-Violating Energy Difference Between Enantiomers from the Optical Rotation of Chiral Ammonia-Like "Cat" Molecules., *Chem. Phys.*, **2004**, *305*, 55-68.

122. Gonzalo, I.; Bargueno, P.; Perez de Tudela, R.; Miret-Artes, S.: Towards the Detection of Parity Symmetry Breaking in Chiral Molecules., *Chem. Phys. Lett.*, **2010**, *489*, 127-129.

123. Bargueno, P.; Perez de Tudela, R. ; Miret-Artes, S. ; Gonzalo, I.: An Alternative Route to Detect Parity Violating Energy Differences Through Bose-Einstein Condensation of Chiral Molecules., *Phys. Chem. Chem. Phys.*, **2011**, *13*, 806-810.

124. Palazzotto, M. C; Duffy, D. J.; Edgar, B. L.; Que, L., Jr.; Pignolet, L.M., Dynamic Stereochemistry of Tris-Chelate Complexes. Tris(dithiocarbamato) Complexes of Iron, Cobalt, and Rhodium, *J. Am. Chem. Soc.*, **1973**, *95*, 4537-4545

125. Eaton S. S., Hutchison J. R., Holm R. H., Muetterties E. L., Intramolecular Rearrangement Reactions of Tris-Chelate Complexes. III. Analysis of the Rearrangements of Tris(a:-isopropenyl- and -isopropyltropolonato) aluminum (III) and -cobalt(III). Examples of Stereochemically Nonrigid Aluminum (III) and Cobalt (III) Complexes, *J. Am. Chem. Soc.*, **1972**, *94*, 6411-6426

Chapter 2: Fluxional Behaviour of Group 9 d^6 Tris-chelate Complexes of Hinokitiol

2.1 Preface

O,O-donor ligands provide stable tris-chelate complexes with group 9 d^6 metals which makes them ideal in PVED research. Acetylacetone is one of the most studied ligands: complexes of it are known with every metal and $Co(acac)_3$ has been successfully resolved in a facile manner. The major drawback are the very poor yields in the syntheses of $Rh(acac)_3$ and $Ir(acac)_3$ as was reported first by Sargeson and then Bennett. This is partly due to coordination of one of the ligands via the carbon rather than the oxygens.

To overcome this problem, we have focused our attention towards a different O,O donor ligand. Tropolone and its derivatives have been used as ligands, though not to the same extent as acetylacetone. Most of the early work on the subject was done by Griffiths. 1,4-isopropyltropolone or hinokitiol is one example: it has the advantage of being a natural product part of the wider thujaplicin family present in the bark of the red cedar tree. It is therefore readily available.

In this chapter we present the synthesis of tris-chelate complexes of cobalt, rhodium and iridium of hinokitiol. The dynamic behaviour of the complexes is investigated by variable temperature NMR. The work presented in this chapter was published as Gaydon Q.; Bohle D. S., Separation of Isomers and Mechanism of Inversion of Stereochemistry of Group 9 d6 Tris-Chelate Complexs of Hinokitiol, *Inorg. Chem*. **2021**, *60*, 13567.

2.2 Abstract

Tris-chelate complexes of Co(III), Rh(III) and Ir(III) with 4-isopropyltropolone (hinokitiol or β-thujaplicin) form by substitution of carbonate and chloride ligands from group 9 trivalent metal salts. The new complexes are neutral, readily soluble in most organic solvents and brightly coloured with strong charge transfer bands. The fac isomer of $Co(hino)_3$ and $Rh(hino)_3$ were isolated from the mixture by fractional recrystallization from ethanol. The remaining mixtures were respectively enriched by 5/3 and 4.4/3 for the mer isomer.The ^{1}H-NMR data shows that the complexes exhibit remarkable stereochemical lability which is unusual for diamagnetic d^6 group 9 metals, with rotational barriers for of 14.2 and 18.2kcal/mol found for the inversion of stereochemistry of $Co(hino)_3$ and $Rh(hino)_3$. The low activation barriers as well as the analysis of some key structural parameters suggests the inversion of stereochemistry occurs via a trigonal twist (Bailar) mechanism. Facile substitution of a single hinokitiol ligand in the cobalt complex with ethylenediamine to form $[Co(en)(hino)_2]Cl$ also indicates the tris-chelates are substitutionally and configurationally labile.

2.3 Introduction

The origin of homochirality in biology is a longstanding unresolved problem.[1,2] One hypothesis for its origin is the existence of a small energy difference between the enantiomers of two chiral molecules due to Parity Violation Energy Difference (PVED).[3] Although PVED is responsible for the observed breakdown in the Laporte selection rules in heavy atoms,[4] it has not been experimentally observed in molecules yet.[5-8] A corollary of molecular PVED is that heavy metal catalyzed reactions may generate products with non-zero enantiomeric excess. Part of the difficulty in detecting molecular PVED is in finding a suitable candidate molecule for such measurements. We believe several criteria are optimal for such a candidate: it must be stable, volatile to allow for PVED measurements in the gas phase, resolvable, available in large scale, contain at least one heavy atom and be inert towards racemization. Group 9 d^6 tris chelate complexes of monoanions fulfill most of these criteria: they are neutral, stable complexes which

are often stereochemically inert: some examples of the metallotrischelated complexes are resolvable into enantiomers.[9-11]

Hinokotiol, or 4-isopropyltropolone, is a well-known natural product extracted from the heart wood of the red cedar tree. Although it is readily available, its biological and ligating properties have been surveyed but much of its fundamental chemistry needs further attention.[12-14] Recently we have synthesized several osmium and ruthenium complexes of hinokitiol and have studied the unusual fluxional behaviour of some of these complexes.[15] Tris-chelate complexes of hinokitiol are less common: only the iron complex has been synthesized previously.[16] Because of the availability of hinokitiol, tris-chelate complexes of d^6 group 9 complexes of hinokitiol may be a good choice for PVED measurements.

The hinokitiols are part of a family of mono isopropylated derivatives of tropolone: α, β and γ-isopropyltropolone. Recently, Grillo *et al.* reported the use of the tris-chelate iron complex of hinokitiol as an iron transporter.[16] In 1972, Muetterties *et al.* reported surprising stereochemical lability of Co(III) and Al(III) complexes of α-isopropyltropolone, but the Rh(III) complex does not show fluxionality in tetrachloroethane up to 140°C.[17] To our knowledge, this is one of the few examples of such facile behaviour for Co(III) tris-chelate complexes. For the rhodium complex there is an important solvent dependence, described herein, which may account for this observation.

In this chapter we present the synthesis of three new compounds: the cobalt, rhodium, and iridium tris-chelate complexes of hinokitiol and an ethylenediamine derivative of cobalt. A detailed analysis of their vibrational frequencies will also be presented. Dynamic NMR studies are used to determine if similar behaviour to that presented by Muetterties *et al.* is observed for the isomerization in the β-isomer. Possible racemization mechanisms are analyzed with density functional theory on its intermediates and transition states. Finally, the substitution reaction of $Co(hino)_3$ with ethylenediamine show facile substitution of one of the hinokitiol ligands.

2.4 Results and discussion

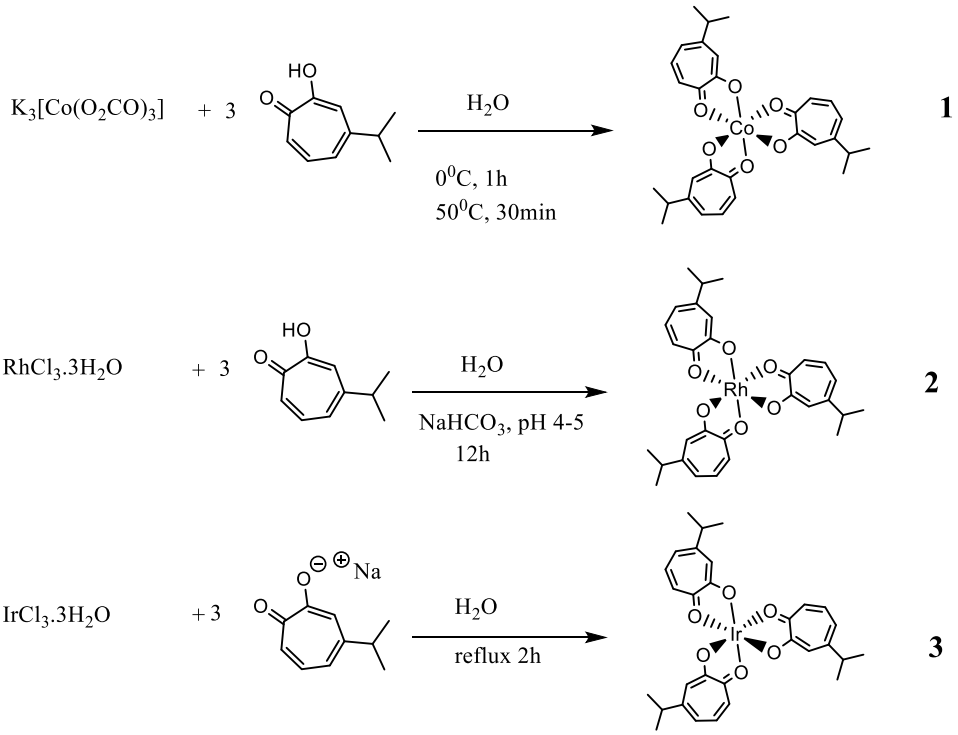

The tris-chelates Co(hino)$_3$ (complex **1**), Rh(hino)$_3$ (complex **2**) and Ir(hino)$_3$ (complex **3**) were synthesized as shown in equations 1-3. Co(hino)$_3$ was obtained by first forming $K_3[Co(CO_3)_3]$ at 0 ˚C and then adding the hinokitiol ligand. Rh(hino)$_3$ was obtained by heating $RhCl_3.3H_2O$ to reflux with hinokitiol while Ir(hino)$_3$ was prepared by heating at reflux the sodium salt Na(hino) and $IrCl_3.3H_2O$ in water. Under these conditions, the product precipitated out of solution. The complexes are air stable and have good solubility in most organic solvents and are readily purified by recrystallization from chloroform/petroleum ether for complex **1** and acetone/water for complexes **2** and **3**. Mass spectroscopy confirms the formation of the desired products.

As tris-chelates, the complexes can either be Δ or Λ enantiomers while the presence of the 4-isopropyl group results in either fac or mer conformation. In the fac conformation, all three isopropyl groups are in the same environment while in the mer conformation, all three isopropyl groups are in a different environment. In total, two enantiomers of two isomers are present: lambda-fac, lambda-mer, delta-fac, and delta-mer. The diastereotopic nature of the methyl protons on the isopropyl groups additionally complicates the ^{1}H-NMR spectrum. This results in

the presence of two sets of doublets with equal integration value for the fac isomer and 6 sets of doublets with the same integration value for the mer isomer. ^{1}H-NMR data indicated the formation of the products as a mixture of both isomers. Integration of the peaks gave a 3 to 1 ratio of the mer over the fac isomer for all three complexes. As initially prepared, by precipitation from solutions upon formation, the product is a statistical distribution of fac/mer expected for such a mixture.

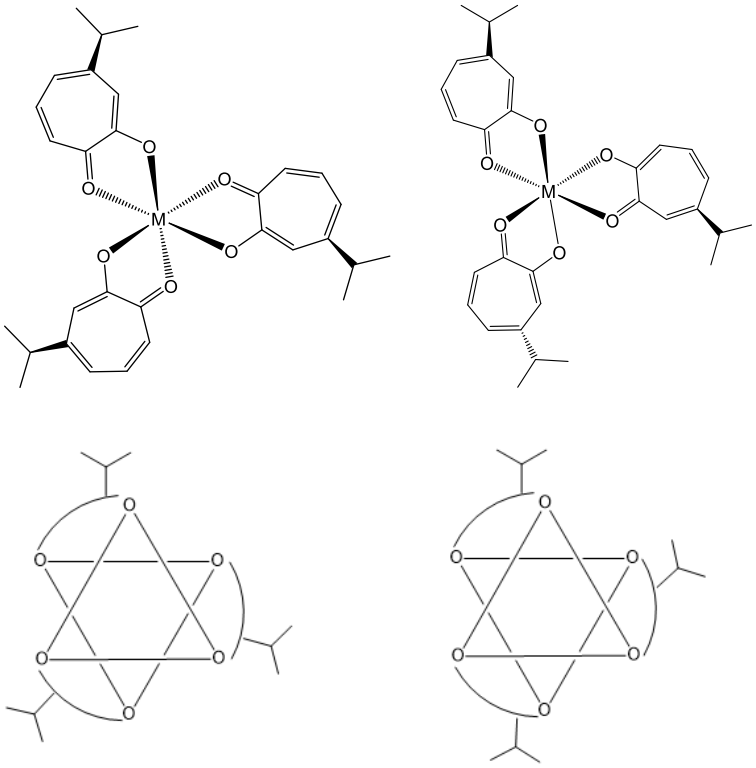

1 iPr environment	3 iPr environments
Fac	Mer

Figure 2.1: Possible isomers of λ-M(hino)$_3$ viewed down the top face with molecular structure above and star of David representation below

The lower solubility of the fac isomer in polar solvents such as ethanol or methanol allow for the subsequent isolation of pure fac isomer by fractional crystallization at -22 ˚C. The remaining solution consists of a mixture of the mer and fac isomers in a 5:1 mixture of the mer isomer over

the fac isomer for **1** and 4.4:1 for **2**. This represents a 5/3 and 4.4/3 effective enrichment of the mer isomer respectively. Suitable crystals of fac-Rh(hino)$_3$ were obtained for X-ray diffraction.

2.4.1 X-ray Crystallography

Rh1-O1	1.986(4)
Rh1-O2	1.998(4)
O1-C1	1.299(7)
O2-C2	1.296(6)
C1-C2	1.454(7)
O1-Rh1-O2	81.77(16)
O1-Rh1-O4	175.39(17)
O1-Rh1-O3	88.42(17)
O1-Rh1-O6	95.65(17)
O1-Rh1-O5	94.31(16)
Twist angle φ	45.3
Pitch angle ψ	28.7
Compression ratio	1.08

Table 2.1: Selected bond lengths(Å) and bond angles(°) of the 5-membered RhOCCO ring

C1-C2	1.454(7)	O1-C1-C2-O2	-2.93
C2-C3	1.398(8)	C1-C2-C3-C4	-1.41
C3-C4	1.405(9)	C2-C3-C4-C5	2.47
C4-C5	1.379(11)	C3-C4-C5-C6	2.41
C5-C6	1.358(13)	C4-C5-C6-C7	-4.71
C6-C7	1.407(11)	C5-C6-C7-C1	-0.41
C7-C1	1.382(8)	C6-C7-C1-C2	5.87
		C7-C1-C2-C3	176.74

Table 2.2: Selected bond lengths(Å) and torsion angles(°) of the hinokitiol chelate

Fac-Rh(hino)$_3$ crystallized from a DCM/methanol mixture as a racemic pair in the hexagonal non-centrosymmetric P6(3) space group. The absolute configuration of the structure could not be determined with a Flack parameter of 0.420, however we can confirm that only the fac isomer is present rather than a mixture of mer and fac isomers.

One methanol solvate, likely from the crystallization process, is present in the structure. The disorder in three sites did not allow for accurate determination of the hydrogen positions: these were omitted from the refinement.

The structure shared some features similar to those we reported in other hinokitiol containing complexes with osmium and ruthenium.[12] In particular, the long C1-C2 bond length and C-O bonds with a 1.5 bond order are consistent with the presence of two Lewis structures. The bond lengths in the 7-membered ring vary between 1.358(13) Å and 1.405(9) Å with the C1-C2 bond being significantly longer at 1.454(7) Å. The torsion angles on the 7-membered ring and O1-C1-C2-C1 close to 0° and 180° indicate the ligand is planar. No disorder of the isopropyl group either at its position or between other carbon ring positions is observed

Other noticeable features include short Rh-O bonds of less than 2 Å and bite angles of 81.77(16)°. The mean angle between different hinokitiol ligands of 92.8°, and trans angles of 175.39(17)° indicate a slight distortion of the octahedral geometry towards D_{3h} trigonal prismatic geometry. Finally, the values of the twist angle, pitch angle and compression ratio deviate significantly from their ideal D_3 geometry values. We find values of 45.3°, 28.7° and 1.08 respectively. With an exact or ideal D_3 geometry, these values would be 60°, 35° and 1.22. With D_{3h} symmetry, the twist and pitch angle are both 0°. This indicates that the geometry of the RhS_6 core of the complex is somewhere between D_3 and D_{3h} geometry. The presence of the isopropyls groups removes the possibility of C_2 perpendicular axes: therefore, the geometry of the entire complex is more accurately described as being distorted C_3. The lower value of the compression ratio indicates an elongated octahedral complex.

No other tris-chelate complexes of rhodium with tropolonate ligands have been reported in the literature. Of the group 9 d^6 triad, $Co(trop)_3$ has been structurally characterized by Doddrell *et al.*[18] The complex shared similar structural features with $Rh(hino)_3$. While the O-Co-O bite angle was significantly larger than O-Rh-O at 84.9°, the cobalt complex also deviates slightly from ideal octahedral geometry.

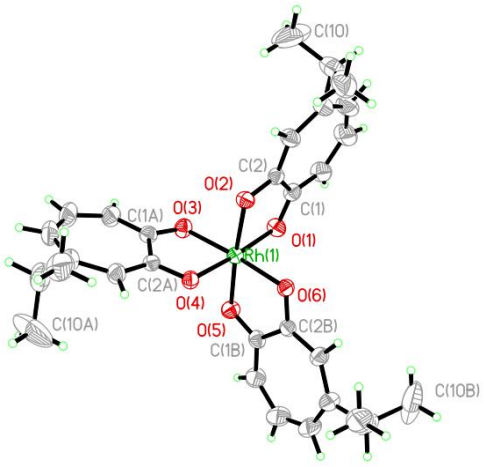

Figure 2.2: ORTEP plot for Rh(hino)$_3$ with 40% thermal elliposoids. The disordered methanol solvate is not included for clarity. Note that the hydrogens on the solvate have not been included in the refinement.

2.4.2 Dynamic ^{1}H-NMR data

These complexes may undergo two types of reactions: fac-mer isomerization and Δ-Λ inversion of stereochemistry. Variable temperature NMR experiments were used to follow these reactions and obtain the corresponding activation barriers.

The solvent dependency of the activation barriers is evident when comparing the spectra of the complexes in MeOD-d_4 compared to less polar solvents such as C_6D_6 or d_8-toluene. In MeOD-d_4, sharp peaks are present: a doublet for the methyl protons, a multiplet for the isopropyl proton, and a singlet, two doublets and a triplet for the aromatic protons. In C_6D_6 and d_8-toluene, the peaks are less well defined. This is especially visible for the methyl protons: one very broad peak (FWHM=0.037ppm) is observed for Co(hino)$_3$ while several broad peaks are observed for Rh(hino)$_3$ and Ir(hino)$_3$. This indicates that the activation barriers are lower in methanol than they are in less polar solvents. Possible hydrogen bonding, as well as the differing dielectric constants of the solvent affect the observed fluxionality.

2.4.3 Isomerization of M(hino)$_3$

Under the reaction conditions discussed previously, the products precipitate out of water as mixture of fac and mer isomers in a statistical distribution. Precipitation of the product out of

solution guarantees that fac-mer isomerization occurs during formation of the product is minimal prior to the isolation.

The activation barrier for the isomerization reaction can be determined by the evolution of the isopropyl methyl signals at 500 MHz. At room temperature a broad peak is observed. At higher temperatures, starting at 45 °C, a well resolved doublet is observed. As discussed later, the coalescence temperature for the inversion of stereochemistry of the fac isomer occurs at much lower temperature while inversion of stereochemistry of the mer isomer would lead to the formation of three doublets. We can therefore unambiguously attribute this behaviour to the fac-mer isomerization of $Co(hino)_3$. The broad peak observed at room temperature results from overlap of the signals from both isomers. From the data presented in Figure 2.3, using 45 °C as coalescence temperature, a rotational barrier for the isomerization of $Co(hino)_3$ equal to 16.6±0.4 kcal/mol is determined.

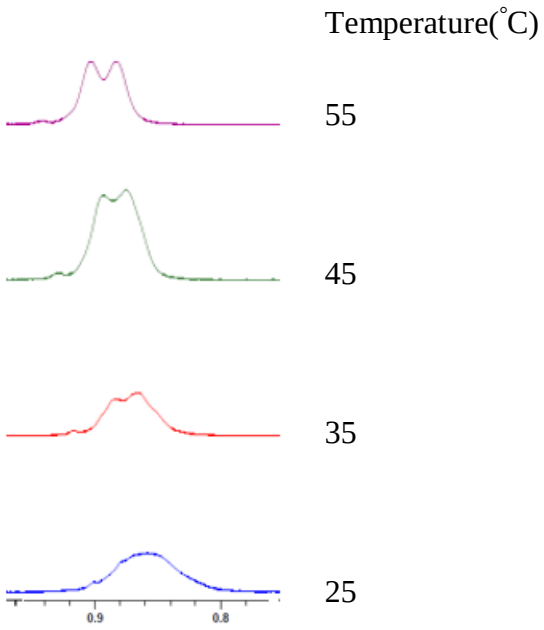

Figure 2.3: VT ^{1}H-NMR spectra of the proton the isopropyl methyl signal of $Co(hino)_3$ at 500 MHz in d_8-toluene

Similar behaviour can also be observed in the spectrum of $Rh(hino)_3$ and $Ir(hino)_3$ in at 800 MHz. Four doublets corresponding to the proton on carbon C5 are observed. When heating

$Rh(hino)_3$ at 75 °C, the doublets start to merge. While at 75 °C coalescence temperature has not yet been reached, the peaks start to merge, indicating that the coalescence temperature is close. Using 75 °C as coalescence temperature, the limit of our VT probe at 800MHz, a lower limit of the rotational barrier of 18.3±1 kcal/mol is obtained. When heating $Ir(hino)_3$ to 75 °C, the doublets corresponding to the mer isomer move slightly closer to the doublet corresponding to the fac isomers. Unlike with $Rh(hino)_3$, at 75 °C, the temperature is not close to coalescence indicating a higher barrier of isomerization for $Ir(hino)_3$.

Overall, the barrier for isomerization is highest for the iridium complex, then rhodium and finally cobalt. This is the expected trend: the metal-ligand bond strength increases in that order with complexes of the same ligands. This trend in metal-ligand bond strengths can be observed in the A_{1g} transition in the Raman spectra of $[Co(NH_3)_6]Cl_3$, $[Rh(NH_3)_6]Cl_3$, and $[Ir(NH_3)_6]Cl_3$: the transitions were found respectively at 500 cm^{-1}, 515 cm^{-1} and 527 cm^{-1} [19]. This fully symmetric M-N stretch for all six ligands will be determined by the product of the reduced masses and the force constants for each. Given that the reduced masses for these modes are almost constant across this triad, the observed increase for this triad clearly indicates that the force constants increase in the order $f_{Co}<f_{Rh}<f_{Ir}$.

2.4.4 Inversion of fac-M(hino)$_3$

Fac-$Co(hino)_3$ and fac-$Rh(hino)_3$ are readily isolated from the mixture of isomers by precipitation out of methanol. At room temperature, the ^{1}H-NMR spectrum of fac-$Co(hino)_3$ showed a single doublet in the isopropyl region, corresponding to the high temperature behaviour of the complex. The variable temperature NMR data presented in Figure 2.4 shows that at temperatures below -15 °C, two doublets appear corresponding to each of the diastereotopic methyl groups. Coalescence was reached at 5 °C. An activation barrier for the Δ-Λ inversion of fac-$Co(hino)_3$ of 14.2±0.2 kcal/mol was found with this coalescence temperature. Upon heating the sample at high temperatures past 45°C, the coalescence temperature for the fac-mer isomerization, and cooling back down to room temperature, only the signal corresponding to the fac isomer is present in solution. We conclude that under these conditions the fac isomer is more thermodynamically stable than the mer isomer.

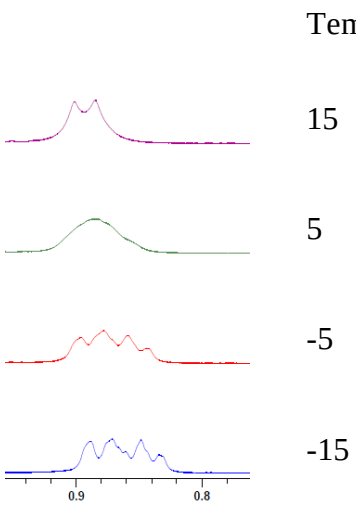

Figure 2.4: VT ^{1}H-NMR spectra for the isopropyl methyl groups at 400 MHz of the isolated fac isomer of Co(hino)$_3$ in d$_8$-toluene

In the case of rhodium, upon dissolution of the crystals used in the X-ray diffraction experiment in C_6D_6, the ^{1}H-NMR spectrum showed two doublets in the isopropyl region consistent with the presence of only the fac isomer. Additionally, the absence of disorder of the isopropyl groups in the diffraction proves only the fac-isomer is obtained. In d_8-toluene at higher temperatures, starting at 75 °C, a single doublet starts to emerge indicating that coalescence temperature is reached. This can be observed in the variable temperature NMR data presented in Figure 2.5. With a coalescence temperature of 75 °C, a rotational barrier for the inversion reaction of the fac isomer of 18.2±0.2 kcal/mol is calculated. Upon cooling to room temperature, the original product was recovered. No conversion or buildup of the mer isomer was observed.

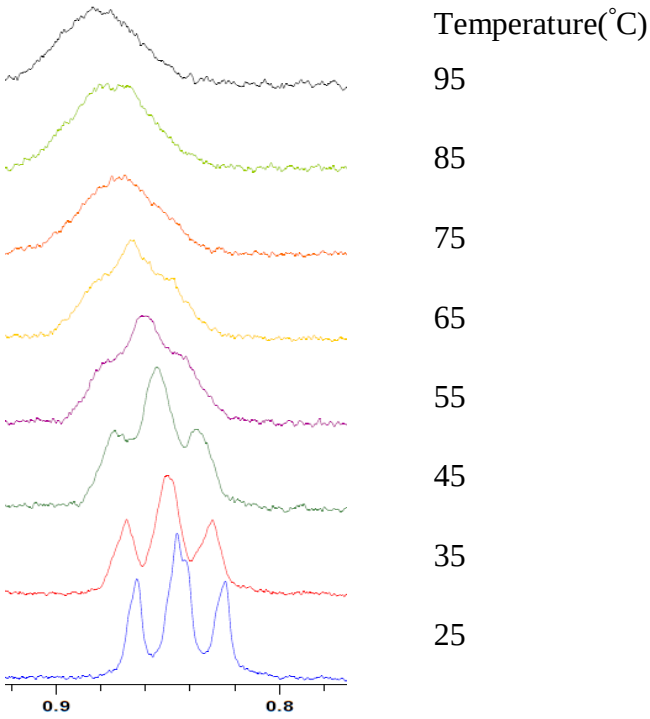

Figure 2.5: VT ^{1}H-NMR spectra of the methyl protons at 400 MHz of the isolated fac isomer of Rh(hino)$_3$ in d_8-toluene

Our results with rhodium stand in contrast with those made by Muetterties: in his paper the rhodium complex of 1-isopropyltropolone, α-hinokitiol, did not exhibit fluxionality up to 140 °C in tetrachloroethane-d_2 in a 100 MHz spectrometer.[17] In contrast, we observe Δ-Λ inversion of the fac isomer at 75 °C. One possible explanation could be that sterical hindrance has an effect on the fluxional behaviour of the complexes. Alternatively, solvent mediated chlorination may have influenced the prior results.

At 800 MHz, the ^{1}H-NMR spectrum of Rh(hino)$_3$ in d_8-toluene of the isolated fac isomer has two doublets in the isopropyl region with coupling constants of 6.9 Hz. In the spectrum of the mixture of isomers, due to overlap in this region, not all of the 6 other doublets corresponding to the mer isomer are visible. We have identified three of the six at 0.961 ppm (J=7.1 Hz), 0.9430 ppm (J=7.1 Hz) and 0.940 ppm (J=7.1Hz). Comparison of the isopropyl region of the isolated fac isomer and mixture of isomers is shown in Figure 2.6.

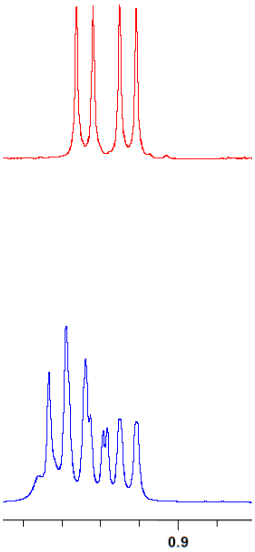

Figure 2.6: ^{1}H-NMR spectra of the methyl protons of the isolated fac isomer from crystallography and the mixture of isomers of Rh(hino)$_3$ prepared in the initial synthesis at 800 MHz in d$_8$-toluene

2.4.5 ^{1}H-NMR data of Ir(hino)$_3$

The ^{1}H-NMR spectrum of Ir(hino)$_3$ in C_6D_6 at 800MHz shows all 8 doublets in the isopropyl region. The integration and J coupling constant values of one of the doublets (0.5251 and 0.5160ppm) seem to indicate overlap of two doublets at that chemical shift. Using the values of the coupling constants and integrations we have assigned each doublet to either the fac or mer isomer.

Chemical shift (ppm)	Integration	J coupling constant (Hz)	Isomer
0.546	1	6.9	Fac
0.504	1	6.9	Fac
0.521	1	7.2	Mer
0.521	1	7.2	Mer
0.543	1	7.1	Mer
0.540	1	7.1	Mer
0.534	1	7.1	Mer
0.530	1	7.7	Mer

Table 2.3: Assignment of doublets to the corresponding isomer in the ^{1}H-NMR spectrum of Ir(hino)$_3$ in C_6D_6 at 800 MHz at 25 °C

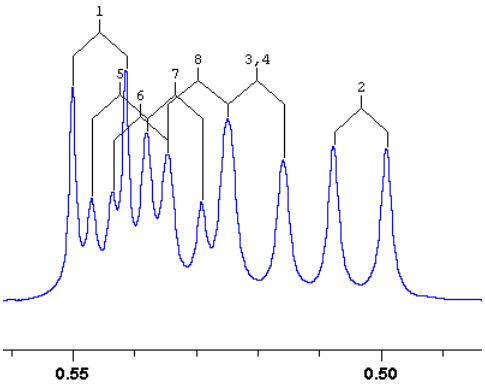

Figure 2.7: Isopropyl methyl doublets present in the 1H-NMR spectrum of Ir(hino)$_3$ in C_6D_6 at 800MHz at 25°C

At higher temperatures, the number of visible doublets in the isopropyl methyl region decreases. At room temperature, all 8 doublets can be distinguished while at 65 ˚C several peaks appear to have merged, reducing the number to only 5 doublets. Upon cooling to 25 ˚C, the original spectrum was restored. This is evidence that the more stereochemically rigid iridium complex also exhibits fluxional behaviour albeit with higher coalescence temperatures.

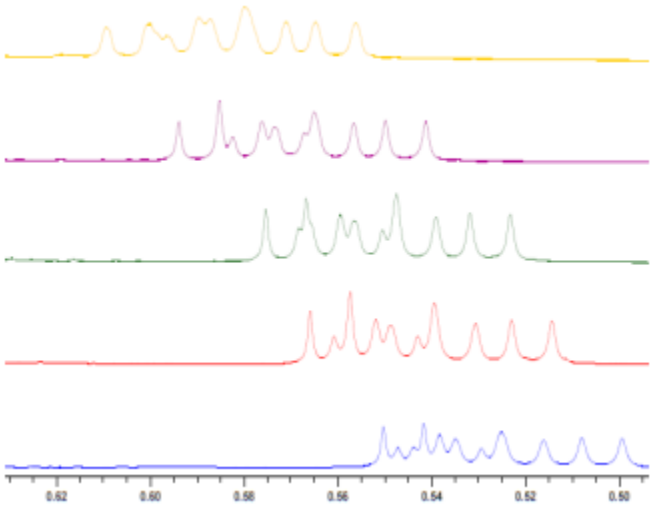

Temperature(^{0}C)	Number of discernable doublets
65	5
55	5
45	6
35	7
25	8

Figure 2.8: VT-NMR spectra of Ir(hino)$_3$ at 800MHz in C_6D_6 with temperature and number of discernable doublets

Metal	Ligand	Reference	Reaction	Solvent	Rotational barrier
Co	Hinokitiol	This study	Fac-Mer isomerization	Toluene-d_8	16.6±0.4 kcal/mol
			Fac delta-lambda inversion	Toluene-d_8	14.2±0.2 kcal/mol
Co	α-isopropyltropolone	17	Fac-mer isomerization	CD_2Cl_2	16.6±1.8 kcal/mol
			Fac delta-lambda inversion	CD_2Cl_2	14.3±0.7 kcal/mol
			Mer delta-lambda inversion	CD_2Cl_2	14.1±1.8 kcal/mol
Rh	Hinokitiol	This study	Fac-Mer isomerization	Toluene-d_8	>18.3±0.7 kcal/mol
			Fac delta-lambda inversion	Toluene-d_8	18.2±0.2 kcal/mol
Rh	α-isopropyltropolone	17		Tetrachloroethane-d_2	Stereochemically rigid up to high temperatures
Ir	Hinokitiol	This study		Toluene-d_8	Stereochemically rigid up to high temperatures

Table 2.4: Comparison of rotational barriers of hinokitiol complexes with other tropolonate complexes

Comparison of our results with the α-isopropyltropolone derivatives of cobalt shows several trends. In the case of $Co(hino)_3$, the barrier for the isomerization of 16.6 kcal/mol and inversion of stereochemistry of the fac isomer of 14.2 kcal/mol are in good agreement with that of the α-isopropyltropolone derivative. For both $Co(hino)_3$ and $Rh(hino)_3$, the barrier for isomerization reaction was higher than that of delta-lambda inversion reactions. Additionally, the barrier for inversion of stereochemistry is higher for the heavier element rhodium than it is for cobalt. Based on our results, $Ir(hino)_3$ stays stereochemically rigid up to higher temperatures.

Stereochemical inversion of tris-chelate complexes may occur via two different types of mechanisms, with or without cobalt-oxygen ligand bond breaking. In the case of a dissociative mechanisms, two different pathways are possible depending on the geometry of the 5-coordinate intermediate, which can be either square pyramidal or trigonal bipyramidal. According to theory outlined in a review by Pignolet *et al.*[20] and more recently by Cass *et al.*,[21] the bite angles and distorted octahedral geometry play a key role in understanding the possible mechanisms of inversion reactions. Complexes with smaller bite angles and an octahedral geometry distorted

towards D_{3h} symmetry invert stereochemistry nondissociatively via an intramolecular mechanism with low activation barriers. Complexes with larger bite angles and a near ideal D_3 geometry are more likely to invert stereochemistry via bond-breaking mechanisms and higher activation barriers.

This can be observed with tris-dithiocarbamate complexes which have been reported by Pignolet to go through fast intramolecular isomerization via a Bailar twist mechanism.[20] Tris-dithiocarbamate complexes are generally observed to have small bite angles around 73-76°.[22-24] On the other hand, tris-diketonate complexes have near perfect octahedral geometry with bite angles close to 90°. The tris-tropolonates are in a position between these two types of complexes. Based on our DFT calculations, the bite angle of $Co(hino)_3$ is 84.2°. This value is very close to the bite angle of $Co(trop)_3$ of 84.9° determined by Doddrell *et al.*.[18] The crystal structure of $Rh(hino)_3$ gave bite angles of 81.8° and a slight deviation from the octahedral geometry is observed based on the values of the twist angle, pitch angle and compression ratio. Based on these observations, it is very likely that the inversion of stereochemistry of the complexes presented occurs via an intramolecular mechanism.

Finally, an important consideration is the type of intramolecular mechanism which can occur, either a Bailar twist or a Ray Dutt mechanism. The Bailar twist forms a D_{3h} trigonal prismatic intermediate by twisting the chelates along their C_3 axis. The Ray Dutt mechanism forms a C_{2v} intermediate. The normalized bite, the ratio of the distance between the chelating atoms and the metal-ligand bond length gives information on the preferred mechanism. The Bailar twist is preferred when the normalized bite ratio is less than 1.5.[25-27] Based on DFT calculations, the normalized bite of $Co(hino)_3$ is 1.33. Based on the crystal structure, the normalized bite of $Rh(hino)_3$ is 1.30.

Overall, the structural parameters of $Co(hino)_3$ and $Rh(hino)_3$ as well as the lower barriers for the inversion of stereochemistry indicate that reaction occurs via a Bailar twist mechanism for both of the complexes.

2.4.6 Vibrational spectroscopy

The IR data feature several bands characteristic of the hinokitiol ligand. These include three strong bands in the range 1400-1600 cm^{-1}, one medium band in the range 1330 cm^{-1}-1351 cm^{-1} and one band at 1235 cm^{-1}-1236 cm^{-1}. The differences between the frequencies of the three complexes are small, less than 10cm^{-1}, with the exception of one band at 1351 cm^{-1} for **1**, 1334 cm^{-1} for **2** and 1330 cm^{-1} for **3**.

$Co(hino)_3$	$Rh(hino)_3$	$Ir(hino)_3$
2961m	2961m	2960m
2929w	2924w	2920w
2865w	2863w	2863w
1583vs	1584vs	1585.3vs
1571s	1567s	1571.8s
1429vs	1426s	1422s
1351m	1334m	1330m
1236m	1235m	1236m

Table 2.5: IR data of $Rh(hino)_3$ and $Ir(hino)_3$. All values given in cm^{-1}

The vibrational frequencies of the complexes were compared to the calculated frequencies of $Ni(trop)_2$ and $Co(trop)_3$ and $Co(hino)_3$ using DFT calculations using B3LYP functionals and aug-cc-pvtz basis sets. In an effort to describe these modes, each frequency was then assigned to a motion around the 5-membered MOCCO ring.

$Ni(trop)_2$ (calc)	$Co(trop)_3$ (calc)	$Co(hino)_3$ (calc)	$Co(hino)_3$	$Rh(hino)_3$	$Ir(hino)_3$	Mode
1552	1551	1544	1583s	1584vs	1585vs	Symmetric breathing
1506	1511	1511	1506s	1495s	1499s	Asymmetric breathing
1457	1453	1456	1429vs	1426s	1422s	O-M-O scissoring + Symmetric C-C stretching
1394	1400	1404	1351vs	1334m	1330m	O-M-O symmetric stretching + C-C scissoring
1289	1289	1274	1236m	1235m	1236m	O-M-O scissoring + Asymmetric C-C stretching

Table 2.6: Experimental data from KBr pellets at 25°C and theoretical results from B3LYP/aug-cc-pvtz in the gas phase. All values given in cm^{-1}

2.4.7 Theoretical considerations

Calculations (B3LYP/cc-pvtz) on the two fac/mer isomers of the Λ isomer enantiomers of $Co(hino)_3$ gave very small gas phase energy difference between the two. The energy of the fac

isomer with all three isopropyl groups in the same environment had an energy of -2997.925548 A.U. The energy of the mer isomer was -2997.925750 A.U, giving a small energy difference of 0.127 kcal/mol for the two isomers, indicating a small preference for the formation of the mer isomer. This is in contrast with the experimental results which indicated that the fac isomer was the more thermodynamically stable isomer. Discrepancies between these results may come from theoretical calculations being performed in a vacuum and highlights the importance of solvent effects on the stability of the isomers. This is certainly related to strong solvent effects observed in the dynamic NMR spectra. Small differences in the IR frequencies and intensities were also noticeable between the two isomers.

Fac Isomer		Mer Isomer	
Calculated Frequency	Intensity	Calculated Frequency	Intensity
1274.24	32.66	1274.48	38.21
1404.63	735.12	1404.14	714.08
1456.22	254.17	1456.25	198.26
1511.14	30.27	1511.05	27.58
1544.7	448.96	1544.68	457.07

Table 2.7: Comparison of calculated IR frequencies and intensities of the fac and mer isomer of λ-Co(hino)$_3$ using B3LYP/cc-pvtz

2.4.8 Electronic Spectroscopy

The compounds are brightly coloured: compound **1** is dark green, compound **2** is bright yellow and compound **3** is dark red. The UV-vis spectra show the presence of charge transfer bands respectively at 368 nm, 368 nm and 372 nm. A d-d transition at 619 nm was observed for the cobalt complex though none were visible for the rhodium and iridium complexes. No differences in the UV spectra were observed for the isolated fac isomers compared to the mixtures of isomers.

Complex	λ(nm)	log(ε)
Co(hino)$_3$	368	4.3
	619	2.4
Rh(hino)$_3$	368	4.3
Ir(hino)$_3$	372	4.2

Table 2.8: UV-Vis data of the complexes in methanol as a mixture direct from the preparation

2.4.9 Substitution of Co(hino)$_3$ with ethylenediamine

The results provided by the ^{1}H NMR data is a good indication of the stereochemical lability of the hinokitiol complexes studied. In order to determine if the same could be said about the kinetic lability of the complexes, Co(hino)$_3$ was dissolved in methanol and an excess of ethylenediamine was added to the solution. The UV-Vis of the solution was monitored over time. After 30 min the dark green solution faded into a light yellow colour and the d-d transition of the complex at 619 nm shifted to a shoulder around 500 nm. The change in the UV-Vis data is good evidence that substitution of at least one hinokitiol ligand occurred.

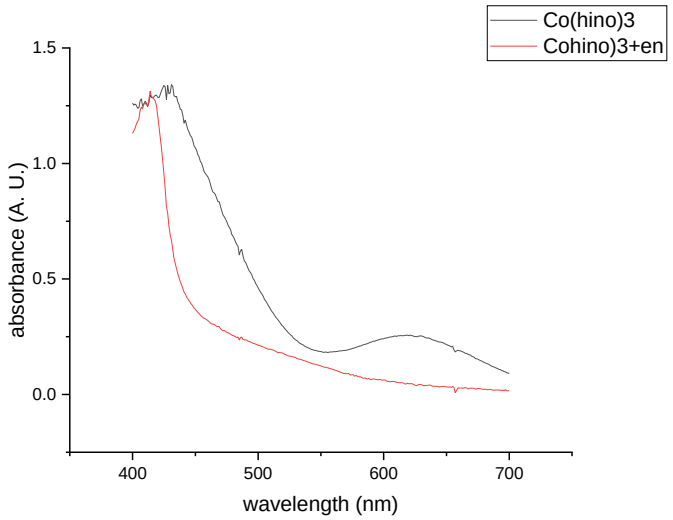

Figure 2.9: UV-Vis data of the reaction of Co(hino)$_3$ and ethylenediamine

The reaction was followed by ^{1}H-NMR spectroscopy. Upon addition of one equivalent of ethylenediamine to a solution of Co(hino)$_3$ in MeOD, an increase in the number of peaks present in the hinokitiol region of the spectrum within 5 min suggests formation of the free ligand, as well as formation of a new complex. Additionally, a new peak at 2.69 ppm corresponds to the coordinated ethylenediamine: the broad nature of the peak results from the inequivalence of the CH_2 protons leading to overlapping multiplets. Upon further addition of ethylenediamine (2 then 3 equivalents), no change in the spectrum is observable. This suggests that only one of the hinokitiol was substituted, leading to the formation of [Co(en)(hino)$_2$]$^+$.

The reaction of $Co(hino)_3$ with an excess (4 equivalents) of ethylenediamine was attempted in methanol. Ammonium chloride was then added to the mixture to provide the necessary counteranion. This gave an orange product with the same UV-Vis spectrum as shown in Figure 2.9. The ESI-MS spectrum in positive mode of showed a peak at 445m/z corresponding to the $[Co(en)(hino)_2]^+$ cation, confirming the results seen in the NMR experiment.

$[Co(en)(hino)_2]^+$ can exist as different geometrical isomers depending on the orientation of the two isopropyl groups, in addition to the delta and lambda enantiomers, Figure 2.10.

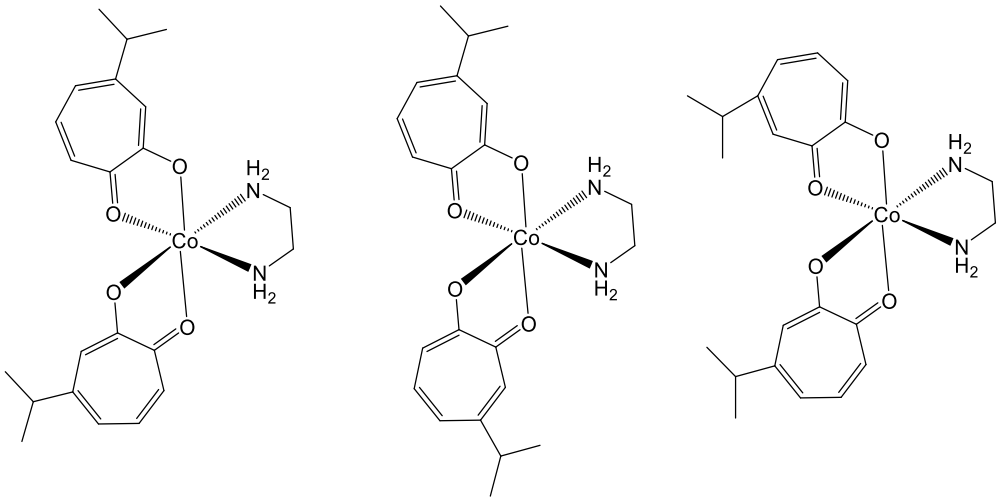

Isomer A Isomer B Isomer C

Figure 2.10: Geometrical isomers of the lambda enantiomer of $[Co(en)(hino)_2]^+$

The geometries of the isomers optimized using B3LYP-cc-pvdz basis sets gave very small energy differences between the three isomers in the gas phase.

Isomer	A	B	C
Energy (A.U.)	-2649.650591	-2649.650387	-2649.650499
Relative energy (kcal/mol)	0	0.12	0.06

Upon addition of five drops of C_6D_6 in an NMR tube containing the $[Co(en)(hino)_2]^+$ cation in MeOD-d_4, the sharp peaks present in the spectrum became much broader. When the reaction was carried out in an NMR tube in C_6D_6, an immediate colour change was observed and the NMR

spectrum showed a very broad peak in the isopropyl region. Comparison of the spectra in the isopropyl region is shown in Figure 2.11. This behaviour is similar to the one observed with the tris-chelate cobalt complex, showing the fluxional behaviour also extends to $[Co(en)(hino)_2]^+$.

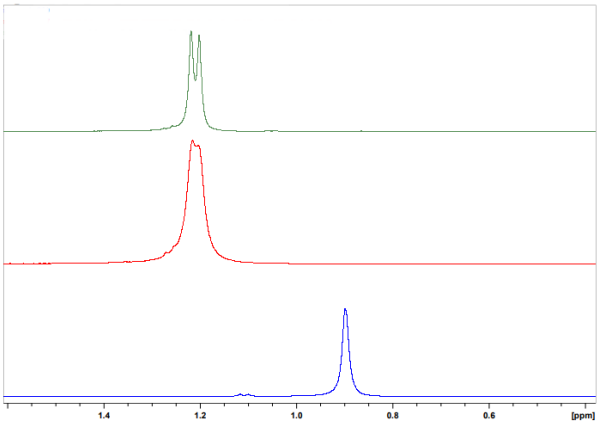

Solvent:

MeOD-d_4

MeOD-d_4+C_6D_6

C_6D_6

Figure 2.11: ^{1}H-NMR spectrum for the isopropyl methyl resonances of $Co(en)(hino)_2$ in different solvents at 400MHz

Finally, we measured the kinetics of the reaction of $Co(hino)_3$ with ethylenediamine in methanol. The reaction rates depend on the concentration of ethylenediamine as they increase with increased concentration. A plot of the reaction rates versus concentration of ethylenediamine shown in Figure 2.12 gives a linear dependence of the reaction rates in the pseudo first order regime, > 10 eq, with respect to the concentration of ethylenediamine.

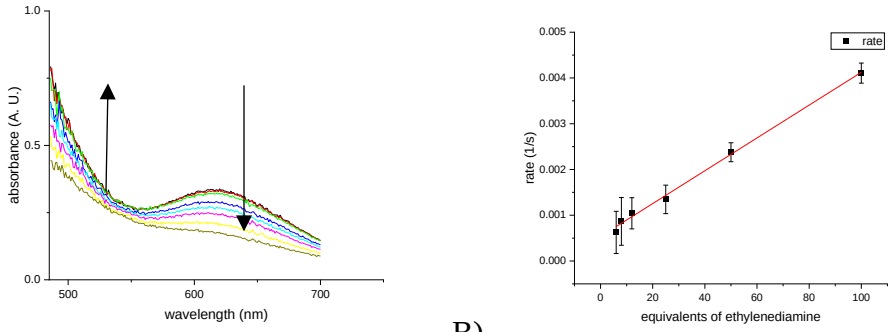

A) B)

Figure 2.12: A) Disappearance of $Co(hino)_3$ d-d transition at 624 nm monitored over time. B) Linear regression of the reaction rate constant vs. concentration of ethylenediamine. Standard deviations are used for the error bars.

The reaction mechanism likely occurs via a dissociative mechanism with the formation of a five-coordinate intermediate followed by addition of the incoming ethylenediamine ligand. The dependence of the reaction rates on the concentration of ethylenediamine suggests t hat the formation of the 5-coordinate intermediate happens fast while addition of the incoming ethylenediamine ligand would be the rate determining step.

2.5 Conclusion

Three new complexes of hinokitiol have been successfully synthesized. Unlike previously reported tris-chelate complexes of tropolone derivatives, our complexes show remarkable stereochemical lability even for the heavier elements, rhodium and iridium. Additionally, substitution of $Co(hino)_3$ with one ethylenediamine ligand is a rare example of a kinetically labile Co(III) complex. In the context of PVED measurements, tris-chelate complexes of hinokitiol would not be ideal candidates since stereochemically rigid complexes are required. The observed lability of these tropolonate derivative complexes may also have an impact on their bioinorganic chemistry and biochemical role in nature.

2.6 Experimental

The starting materials $CoCl_2.6H_2O$, $RhCl_3$, $IrCl_3$ and hinokitiol were purchased and Na(hino) was prepared by literature procedure[10]. IR spectra were measured on Bomem MB3000 FTIR spectrometer as KBr pellets. ^1H and ^{13}C NMR spectra were measured on a Bruker AVIIIHD 500 spectrometer at 22 °C at 500 MHz for ^1H, 131MHz for ^{13}C. UV-Visible spectra and kinetics measurements were obtained using an HP 8453 diode array spectrophotometer.

2.6.1 Synthetic Procedures

$Co(hino)_3$ (1): The procedure was adapted from a literature procedure[28]. $CoCl_2.6H_2O$ (100 mg) was dissolved in 5 mL of water and 0.15 mL of 30% H_2O_2 was then added to the solution. The solution was added to a solution of $KHCO_3$ (300 mg) in 10 mL of water at 0 °C. The solution was stirred for 1h, after which hinokitiol (207 mg) was added. The mixture was stirred for 30 min at 50 °C. The precipitate was filtered and washed with 3x10 ml of water. The precipitate was then recrystallized from chloroform/petroleum ether. The light green solid was obtained in 52% yield (130 mg) as a mixture of isomers. DSC: stable up to T=350°C IR(KBr): 2961.5m, 2929.5w, 2865.1w, 1583.7vs, 1563.2 vs, 1506.5s, 1429.3s, 1351.8s, 1236.0m , 1180.7m, 952.6w, 811.0m, 733.9m, 677.5m, 572.8m ^1H-NMR (MeOD-d_4): 7.57 (s, 1H) , 7.41 (t, 1H,J_{HH}=10.3Hz), 7.30 (d, 1H,J_{HH}=10.8Hz), 7.10 (d, 1H,J_{HH}=10.4Hz), 2.93 (m, 1H), 1.29 (d, 6H,J_{HH}=6.1Hz) ^{13}C-NMR (MeOD-d_4): 186.67, 186.20, 161.02, 137.72, 128.05, 127.24, 126.24, 38.84, 22.49 UV-Vis MeOH: 368nm (4.3), 619nm(2.4) MS(ESI-MS): 571.15m/z $[(CoO_6C_{30}H_{33})Na]^+$

Separation of fac and mer-$Co(hino)_3$

A solution of the mixture of fac and mer-$Co(hino)_3$ was dissolved in ethanol and kept at in the freezer -22 °C overnight. The green precipitate was filtered and washed with cold ethanol to afford fac-$Co(hino)_3$. ^1H-NMR (toluene-d_8, T=238.15K): 7.51 (s, 1H) 7.36 (d, 1H,J_{HH}=10.6Hz), 6.68 (t, 1H,J_{HH}=10.6Hz), 6.25 (d, 1H, J_{HH}=10.1Hz), 2.27 (m, 1H), 0.88 (d, 3H, J_{HH}=6.9Hz), 0.84 (d, 3H, J_{HH}=6.9Hz)

Rh(hino)$_3$ (1): $RhCl_3.3H_2O$ (85 mg, 0.32 mmol) was dissolved in water (10 mL) and 3.4 equivalents of hinokitiol (200 mg 1.1 mmol) was added to the solution. The pH of the solution was adjusted to the range 4-5 using 10% $NaHCO_3$ and the reaction was heated at reflux for 30 min. It was cooled down and the pH was readjusted to the range 4-5 and the reaction was left at reflux overnight. The reaction was cooled to room temperature and methanol (10 mL) was added to the solution causing the formation of a yellow precipitate. The precipitate was filtered and washed with water (3x10 mL) and then recrystallized from a 1:1 nixture of acetone/water giving Rh(hino)$_3$ as a mixture of isomers. Yield: 55 mg (25%) DSC: decomposition T=307˚C ΔH=35.64 J/g IR(KBr): 2961.5m, 2923.7w, 2863.4w, 1583.7vs, 1567.1vs, 1495.2s, 1426.8s, 1334.2m, 1233.0s , 1180.7m, 955.3w, 806.3m, 733.9m, 677.5m, 572. ^{1}H-NMR (MeOD-d$_4$): 7.48 (t, 1H, J_{HH}=10.3Hz), 7.41 (s, 1H), 7.30 (d, 1H,J_{HH}=10.8Hz), 7.09 (d, 1H,J_{HH}=10.4Hz), 2.89 (m, 1H), 1.21 (d, 6H,J_{HH}=6.1Hz) ^{13}C-NMR (MeOD-d$_4$): 187.28, 186.61, 159.25, 136.60, 128.49, 128.04, 127.25, 39.14, 23.62, UV-Vis (MeOH): 368 nm (4.3) MS(ESI-MS): m/z 615.12 $[(RhO_6C_{30}H_{33})Na]^+$

Separation of fac and mer-Rh(hino)$_3$

A solution of the mixture of fac and mer-Rh(hino)$_3$ was dissolved in ethanol and kept at in the freezer -22 ˚C overnight. The yellow precipitate was filtered and washed with cold ethanol to afford fac-Rh(hino)$_3$. ^{1}H-NMR (C_6D_6): 7.35 (s, 1H), 7.16 (d, 1H,J_{HH}=11.1Hz), 6.47 (t, 1H,J_{HH}=10.6Hz), 6.10 (d, 1H,J_{HH}=9.7Hz), 2.13 (m, 1H), 0.75 (d, 3H,J_{HH}=6.9Hz), 0.72 (d, 3H,J_{HH}=6.9Hz) X-ray diffraction crystals grown from DCM/methanol.

Ir(hino)$_3$ (2): $IrCl_3.3H_2O$ (100 mg, 0.28 mmol) and 4 equivalents of Na(hino) (250.8 mg, 1.32 mmol) were refluxed in water (10 mL) for 2 hours during which the solution turned dark red. Upon cooling red crystals of Ir(hino)$_3$ were filtered and washed with water (3x10 mL). The crystals were recrystallized from acetone/water. Yield:. 110 mg 57% DSC: decomposition T=285˚C ΔH=18.07 J/g IR: KBr(cm^{-1}): 2960.0m, 2919.9w, 2863.4 w, 1585.3vs, 1571.8vs, 1498.7s, 1422.2s, 1329.6m, 1225.0s , 1180.7w, 1092.1m, 1015.6w, 955.3w, 902.9vw, 798.3m, 733.9m, 677.5m, 576.9m UV-Vis: 372nm (4.2) ^{1}H-NMR (MeOD-d$_4$): 7.60 (t, 1H, J_{HH}=10.7Hz), 7.36 (s, 1H), 7.25 (d, 1H, J_{HH}=11.1Hz), 7.01 (d, 1H,J_{HH}=9.5Hz), 2.87 (m, 1H), 1.29 (d,

6H,J_{HH}=7.3Hz ^{13}C- NMR (MeOD-d_4): 187.30, 186.39, 158.10, 135.25, 129.85, 127.84, 126.75, 39.10, 22.01 MS(+p ESI-MS): m/z 682.20 [$(IrO_6C_{30}H_{33})$]$^+$

[Co(en)(hino)$_2$]Cl: $Co(hino)_3$ (100 mg) was dissolved in 10mL of methanol and 0.2 mL of ethylenediamine was added dropwise to the solution. The mixture was stirred for 30 min and ammonium chloride (10 mg) was added. The solvent was removed under vacuum. The red paste obtained was washed with water(2x10 mL) and toluene(10 mL). IR: KBr(cm^{-1}): 3509.0m, 3212.9m, 3084.15m, 2961.6m, 1583.7s, 1506.5.7s, 1429.3s, 1358.3m, 1242.1.0m , ^{1}H-NMR (MeOD-d_4). ^{1}H-NMR(MeOD-d_4): 7.10 (t, 1H, J_{HH}=10.5Hz), 7.03 (s, 1H), 6.88 (d, 1H, J_{HH}=10.9Hz), 6.88 (d, 1H,J_{HH}=9.7Hz), 2.80 (m, 5H), 1.21 (d, 6H,J_{HH}=6.7Hz) ^{13}C-NMR: 181.50, 181.02, 158.17, 136.16, 124.45, 123.25, 121.20, t44.63, 38.73, 22.98 UV-Vis: 425 nm (4.2) MS(+p ESI-MS): m/z 445.15 [$(CoO_4N_2C_{22}H_{30})$]$^+$

2.6.2 Kinetics

A stock solution of 25 mg of $Co(hino)_3$ in 25 mL of methanol was prepared. 3 mL of the stock solution was used for each run with varying amounts of ethylenediamine added: 6, 8, 12, 25, 50 and 100 equivalents. The temperature was kept constant at 25 °Cand the cuvette was shaken vigorously before starting the data collection. Each run was acquired over a time of 5000 s, with a cycle time of 10 s, increasing by 2% every 300 s. First order rate calculation types were used to calculate the rates and associated standard deviations.

2.6.3 Theoretical calculations

Density functional theory implemented on Gaussian16 with B3LYP functionals were used with cc-pvdz, cc-pvtz, and aug-cc-pvtz basis sets. Visualization of the normal modes was accomplished with Gauss-view which was used to generate the vectors shown in Table S2.1.

2.6.4 Crystallographic Methodologies

Crystals are mounted on glass fibers with epoxy resin or Mitogen mounts using Paratone-N from Hampton Research and single-crystal X-ray diffraction experiments are carried out with a BRUKER APEX-II D8 CCD diffractometer by using graphite-monochromated Mo Kα radiation

(λ = 0.71073 Å) the SHELX package[29] is used for integration of the intensity reflections, scaling, and absorption correction. Intrinsic phasing methods were used to solve the structures. Non-hydrogen atoms are located by difference Fourier maps and final solution refinements are carried out by full-matrix least-squares methods on F2 for all of the data. The hydrogen atoms are placed in calculated positions and were not refined.

2.7 References

1. Blackmond, D. G., The Origin of Biological Homochirality. *Cold Spring Harb. Perspect. Biol*., **2010**, *2*, a002147
2. Quack, M. On Biomolecular Homochirality as a Quasi-Fossil of the Evolution of Life., *Adv. Chem. Phys*., Vol 157; John Wiley & Sons: New York, **2002**; 249−290
3. Quack, M. How Important is Parity Violation for Molecular and Biomolecular Chirality? *Angew. Chem., Int. Ed*. **2002**, *41*, 4618−4630
4. Wood, C.S; Bennett, S.C; Cho, D.; Masterson, B.P.; Roberts, J.L.; Tanner, C.E.; Wieman, C.E.; Measurement of Parity Nonconservation and an Anapole Moment in Cesium, *Science*, **1997**, *275*, 1759-1763
5. Quack, M., Combined Multidimensional Anharmonic and Parity Violating Effects in CDBrClF, *J. Chem. Phys*.,**2003**, *119*, 11228.
6. Figgen, D;, Schwerdtfeger, P., NWHClI: A Small and Compact Chiral Molecule with Large Parity-Violation Effects in the Vibrational Spectrum, *Angew. Chem. Int. Ed*. **2010**, *49*, 2941 –2943.
7. Figgen, D.; Schwerdtfeger, P., SeOClI: A Promising Candidate for the Detection of Parity Violation in Chiral Molecules, *Phys Rev A***, 2008**, *78*, 012511
8. Schwerdtfeger, P.; Bast, R. *J*., Large Parity Violation Effects in the Vibrational Spectrum of Organometallic Compounds, *Am. Chem. Soc*.. ***2004***, *126*, 1652-1653.
9. Drake, A. F.; Gould, J. M.; Mason, S. F.; Rosini, C.; Woodley, F. J.: The Optical Resolution of Tris(pentane-2,4-dionato)metal(III) Complexes, *Polyhedron*, **1983**, *2*, 537-538
10. Gahan, L. R.; Hughes, J. G.; O'Connor, M. J.; Oliver, P. J.: Optically Active Tris(dithiocarbamato)cobalt(III) Chelates. Preparation and Assignment of Absolute Configuration, *Inorg. Chem.* **1979**, *18*, 933-937
11. Coughlin, F. J.; Westrol, M. S.; Oyler, K. D.; Byrne, N.; Kraml, C.; Ztsman-Colman, E.; Lowry, M. S.; Bernhard, S.; Synthesis, Separation, and Circularly Polarized

Luminescence Studies of Enantiomers of Iridium(III) Luminophores, *Inorg. Chem.*, **2008**, *47*, 2039-2048

12. Nomiya, K.; Onodera, K.; Tsukagoshi, K.; Shimada, K.; Yoshizawa, A.; Itoyanagi, T. A.; Sugie, A.; Tsuruta, S.; Sato, R.; Kasuga, N. C.: Syntheses, Structures and Antimicrobial Activities of Various Metal Complexes of Hinokitiol, *Inorg. Chim. Acta,* **2009**, *362*, 43 – 55
13. Nomiya, K.; Yoshizawa, A.; Tsukagoshi, K.; Kasuga, N. C.; Hirakawa, S.; Watanabe, J. Synthesis and Structural Characterization of Silver(I), Aluminium(III) and Cobalt(II) Complexes with 4-isopropyltropolone (Hinokitiol) Showing Noteworthy Biological Activities. Action of Silver(I)- Oxygen Bonding Complexes on the Antimicrobial Activities., *J. Inorg. Biochem.,* **2004**, *98*, 46–60
14. Chen, X.; Zhang, X.; Chen, J.; Yang, Q.; Yang, L.; Xu, D.; Zhang, P.; Wang, X.; Liu, J. Hinokitiol Copper Complex Inhibits Proteasomal Deubiquitination and Induces Paraptosis-like Cell Death in Human Cancer Cells., *Eur. J. Pharmacol*., **2017**, *815*, 147−155.
15. Gaydon Q.; Bohle I. J.; Bohle D. S.; Fluxionality in the Tropolone Hinokitiol Chelate, *Inorg. Chem.* **2021**, *60*, 3305–3313
16. Grillo. A. S.; SantaMaria, A. M.; Kafina, M. D.; Cioffi, A. G.; Huston, N. C.; Han, M.; Seo, Y. A.; Yien Y. Y.; Nardone C.; Menon, A. V.: Restored Iron Transport by a Small Molecule Promotes Absorption and Hemoglobinization in Animals, *Science,* **2017**, *356*, 608-616
17. Eaton, S. S.; Hutchison, J. R.; Holm, R. H.; Muetterties, E. L.; Intramolecular Rearrangement Reactions of Tris-Chelate Complexes. III. Analysis of the Rearrangements of Tris(a:-isopropenyl- and -isopropyltropolonato) aluminum (III) and -cobalt(III). Examples of Stereochemically Nonrigid Aluminum (III) and Cobalt (III) Complexes, *J. Am. Chem. Soc.*, **1972**, *94*, 6411-6426
18. Doddrell, D. M.; Bendall, M. R.; Healy, P. C.; Smith, G.; Kennard, C. H. L; Ralston, C. L; White, A. H., ^{59}Co and ^{13}C Nuclear Spin Relaxation Studies in Solutions of Symmetric, Bidentate Cobalt(III) Complexes. On the Mechanism of ^{59}Co Spin

Relaxation. Crystal Structure Determination of Tris(tropolonato)cobalt(III), *Aust. J. Chem.*, **1979**, *32*, 1219-1230

19. Nakamoto, K. Infrared and Raman Spectra of Inorganic and Coordination Compounds, Fourth Edition', *Wiley-lnterscience,* **1986**
20. Pignolet L.H., Dynamics of Intramolecular Metal-Centered Rearrangement Reactions of Tris-Chelate Complexes, *Top. Chr. Chem*., **1975**, 56, 91-137
21. Rzepa, H. S.; Cass, M. E.: In Search of the Bailar and Raŷ−Dutt Twist Mechanisms That Racemize Chiral Trischelates: A Computational Study of ScIII, TiIV, CoIII, ZnII, GaIII, and GeIV Complexes of a Ligand Analogue of Acetylacetonate., *Inorg. Chem.*, **2007**, *46*, 8024− 8031
22. Palazzotto, M. C.; Duffy, D. J.; Edgar, B. L.; Que, L., Jr.; Pignolet, L. H.: Dynamic Stereochemistry of Tris-Chelate Complexes. Tris(dithiocarbamato) Complexes of Iron, Cobalt, and Rhodium, *J. Am. Chem. Soc.,* **1973**, *95*, 4537-4545
23. Sinn, E.: Solvent Effects in Dithiocarbamate Complexes. Structures of Tris-pyrrolidinecarbodithioato) iron (III) -, -chromium(III)- and -iridium(III)-Hemibenzene. Direct Comparison of $3d^5$, $3d^3$, and $5d^6$ Coordinations, *Inorg. Chem*., **1976**, *15*, 369-375
24. Butcher, R. J.; Sinn, E.: Structural Effect of Adding Paired and Unpaired Electrons to Otherwise Identical Transition Metal Systems. Relation between the Magnetic and Structural Properties in Iron(III) Complexes, Observation of a New Intermediate Iron(III) Spin (S=3/2) State, and Structures of Benzene Solvated Tris(4-morpholinecarbodithioato--S,S')chromium(III), -iron(III), -cobalt(III), -rhodium(III), and -iridium(III) *J. Am. Chem. Soc.*, **1976**, *98*, 2440-2449
25. Raston, C. L.; White, A. H.; Willis, A. C.: Crystal Structure of Tris(dithiocarbamato)cobalt(III), *J. Chem. Soc., Dalton Trans.*, **1975**, 2429-2432
26. Rodger, A.; Johnson, B. F. G.; Which Is More Likely: The Ray-Dutt Twist or the Bailar Twist?, *Inorg. Chem*., **1988**, *27*, 3061-3062
27. Kane-Maguire, N. A. P.; Hanks, T. W.; Jurs, D. G.; Tollison, R. M.; Heatherington, A. L.; Ritzenthaler, L. M.; McNulty, L. M.; Wilson, H. M.: Synthesis, Characterization, and

Photobehavior of Δ- and Λ-fac-Tris((S)-tryptophanato)chromium(III), *Inorg. Chem*. **1995,** *34*, 1121-1124

28. Hulett, L. G.; Thornton, D. A.: Infrared Spectra of First Transition Series Metal Tropolonates, *Spectrochim. Acta 27A*,**1971**, 2089-2096
29. Sheldrick, G. M. SADABS, TWINABS; Siemens Industrial Automation, Inc.: Madison, WI, 1996

Chapter 3: Fluxionality in Ru(II) and Os(II) Complexes of Hinokitiol

3.1 Preface

In chapter 2, the synthesis of tris-chelate complexes of cobalt, rhodium, and iridium with hinokitiol resulted in complexes with surprising stereochemical lability with the low rotational barriers being easily determined from variable temperature NMR.

In order to gain a better understanding of this type of behaviour, complexes of hinokitiol in an even more stereochemically rigid system such as with Ru(II) and Os(II) must be investigated. Simple substitution of triphenylphosphine and chlorine ligands in $MH(CO)Cl(PPh_3)_3$ (M=Ru,Os) and $RuCl_2(PPh_3)_3$ has afforded many different complexes of ruthenium and osmium. The presence of inert bulky triphenylphosphines aids greatly in the crystallization of the complexes. The presence of ligands such as hydrides, triphenylphosphines and carbonyls give excellent spectroscopic handles with which to characterize the complexes.

In this chapter we present the synthesis of several Ru(II) and Os(II) complexes with hinokitiol. Crystal structures and spectroscopic characterizations are provided. Variable temperature NMR is used to determine possible rotational barriers in the same vein as with the tris-chelate complexes presented in Chapter 2.

The work presented in this chapter was published in Gaydon Q.; Bohle I. J.; Bohle D. S., Fluxionality in the Tropolone Hinokitiol Chelate, *Inorg. Chem*. **2021**, *60*, 3305

3.2 Abstract

Tropolonate complexes of Ru(II), Ru(III), and Os(II) with hinokitiol (β-thuljaplicin, or 4-isopropyltropolone) readily form by chloride and triarylphosphine substitution in $RuCl_2(PPh_3)_3$ and $MHCl(CO)(PR_3)_3$, M= Ru, R = Ph; Os; R = Ph, *p*-tolyl. The resulting colorful complexes have variable and strong charge transfer bands and have a surprising combination of stereochemical selectivity and lability. For the Os(II) d^6 examples the tropolone chelate has a fluxionality with a barrier of only 22.5 kcal/mol for the R = aryl examples, as determined by VT-^{31}P NMR. Chlorination with N-chlorosuccinimide results in $MCl(CO)(hino)(PPh_3)_2$, M = Ru, Os. Together, these results quantify the fluxionality of this important chelate which in turn has consequences for its biology.

3.3 Introduction

Ring anealled 1,2 –dioxo/oxo-hydroxo/ or dihydroxo ligands in complexes **A**-**D** are a rich family[1-6] of redox active chelates with exceptional importance in biology[7,8] and material science.[9,10] The catechol branch of this family, **C**, is particularly renowned both for its remarkable set of redox tautomers catechol ↔ semiquinione ↔ quinone forms, and has been described as dioxolenes in analogy with the dithiolenes.[11] In addition, the catechols have a rich role in the enterobactin type of polycatechol siderophores,[12] which have some of the highest iron binding constants in biology. As a consequence, considerable attention has been paid to the thermodynamics and kinetics of the iron release from **C**.[13,14] In addition to **C**, there are a wide range of coordinated chelate analogs of natural products with the tropolone ring,[15] found in complexes of type **D,** such as cholchiceine, **E**, and the hinokitiols, **F**, which are potential anticancer agents[16] in the case of **E** or as antifungal agents[16,17] for both **E** and **F**.

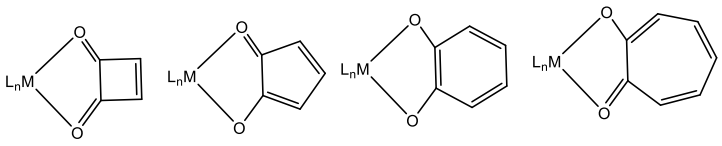

A B C D

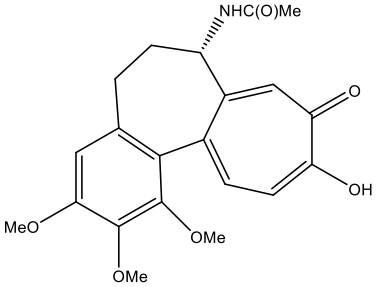

E Colchiceine

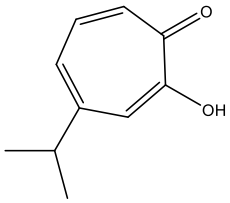

F Hinokitiol

Although the biological activity of **E** and **F** are not limited to their coordination complexes, their chelating tropolone moiety, **D**, has attracted sporadic research interest.[18,19] Beyond the simple observation[17] that the binding constants of **D** are variable, and often less than the related catecholate complexes **C**, the thermodynamics and kinetics of complex **D** formation remain unknown. In the course of our studies to detect parity violation energy differences,[20] PVED, in simple chiral chelate complexes, we have discovered a surprising lability in tropolonate d^6 M(III) complexes. While this fact limits their use in PVED research, they point to an underlying lability which may also have important roles in their material applications and in their biochemistry.

Herein we report: the synthesis of d^5 and d^6 second and third row transition metal complexes with Os(II), Ru(II) and Ru(III) which contain the conjugate base of hinokitiol(hino): OsX(hino)(CO)L_2 [X= H, Cl; L = PPh_3, P(*p*-tolyl)$_3$] RuH(hino)(CO)$(PPh_3)_2$, Ru(hino)$_2(PPh_3)_2$, and $RuCl_2$(hino)$(PPh_3)_2$. The colorful complexes are characterized by IR, UV-Vis, NMR, and EPR (for 1) and X-ray crystallography. Surprisingly, these complexes show marked fluxionality in the tropolonate ligand suggesting poorly recognized kinetic lability.

3.4 Results and Discussion

Chelation of hinokitiol with these group M(II) complexes occurs in the absence of base, in the case of **1**, or more rapidly in the presence of the noncoordinating base DBU. In the case of **1**, the reaction is performed in the open with the resulting isolating complex being the Ru(III) derivative **1**.

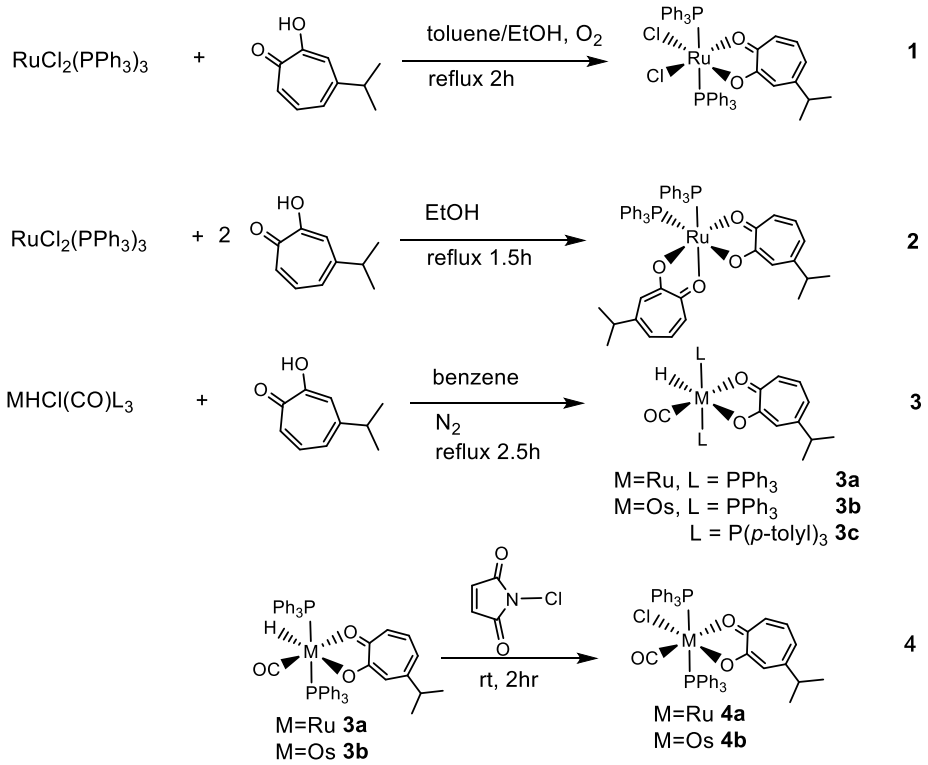

The new hinokitiol complexes are often deeply and brightly colored derivatives, eqs. 1-3, of $RuCl_2(hino)(PPh_3)_2$ (**1**), $Ru(hino)_2(PPh_3)_2$ (**2**), $RuH(CO)(hino)(PPh_3)_2$ (**3a**), and $OsH(CO)(hino)(PPh_3)_2$ (**3b**). Further, they are readily purified by recrystallization from dichloromethane/ethanol in the open with all but **3a** and **4a** being characterized by X-ray diffraction, Figures 3.1 and 3.2, and Tables S3.1-S3.3.

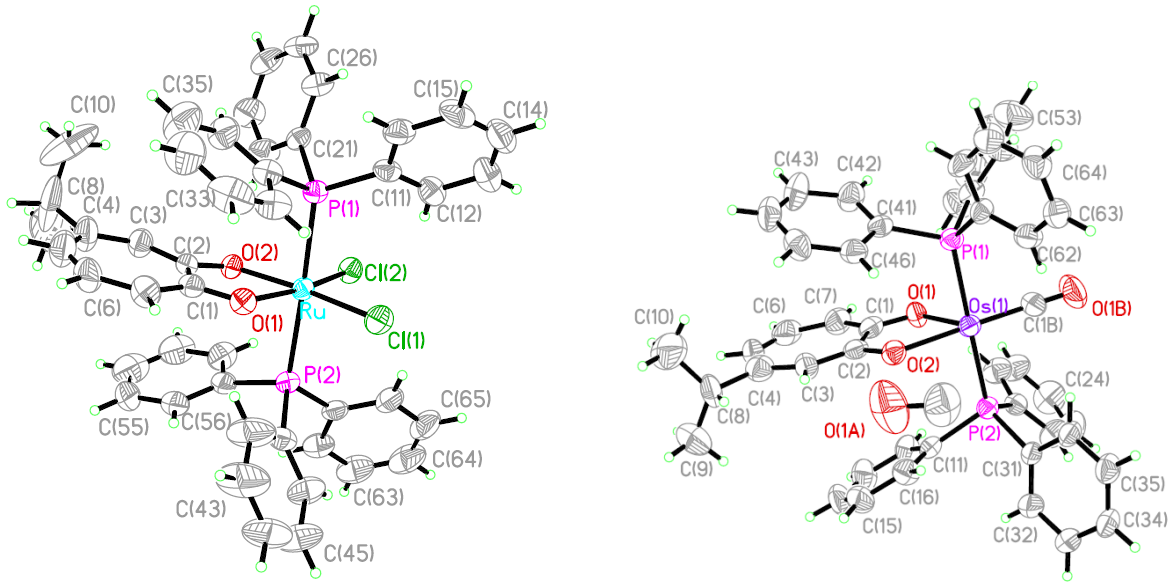

a) **b)**

Figure 3.1: ORTEP plots with thermal ellipsoids of a) $RuCl_2(hino)(PPh_3)_2$, 1; and b) $OsH(CO)(hino)(PPh_3)_2$, 3a. Thermal ellipsoids are shown with 45% probability.

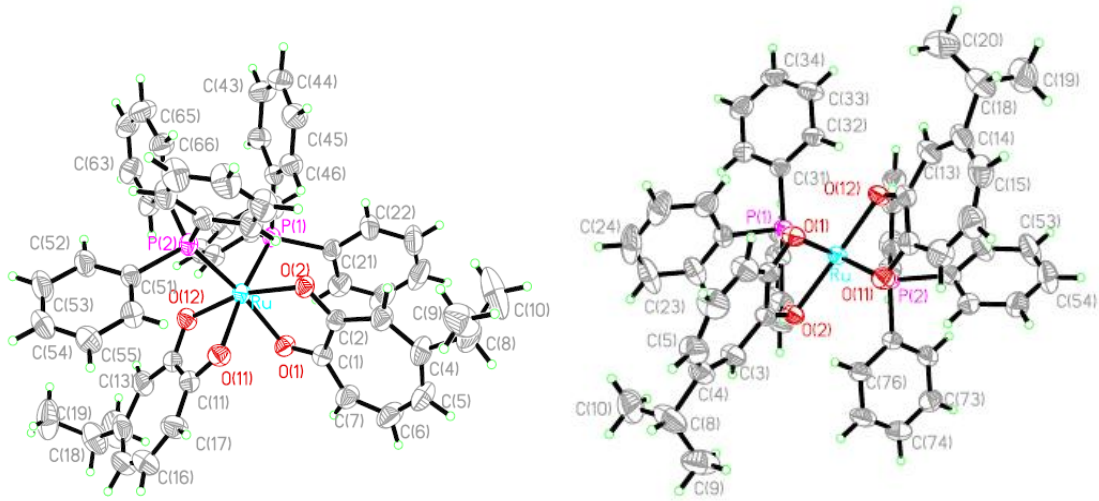

a) **b)**

Figure 3.2: ORTEP plots for $Ru(hino)_2(PPh_3)_2$, 2, viewed with respect to the non-crystallographic C_2 a) orthogonal to; and b) along or parallel with the C_2 axis with the two cis-PPh_3 in the rear.

$RuCl_2(hino)(PPh_3)_2$ **1** and $Ru(hino)_2(PPh_3)_2$ **2** were obtained by treating $RuCl_2(PPh_3)_3$ with either 1 or 2 equivalents of hinokitiol in toluene or ethanol at reflux with the specific conditions of stoichiometry and reaction conditions determining the product.

The solid-state structural characterization of the new complexes with X-ray diffraction has led to some surprising results in terms of the specific geometries at the metal and the hinokitiol ligand isopropyl orientation. Some 1639 entries of 1700 with $Ru(Os)(PPh_3)_2$ in the CCSD reveal the preponderance of group 8 bis triaryphosphine complexes have mutually *trans* triarylphospines This is of course the geometry found in complexes, **1**, **3b,c,** and **4a**. A variety of bis chelates such a benzoate,[21] acetoacetenato (acac),[22] and semicarbazoles[23] also adopt a *cis*-triarylphosphine as seen in **2**. The origins for this stereoselectivity for substituiton at the metal is most likely kinetically controlled, and it correlates with other substitution reactions for $RuCl_2(PPh_3)_3$.[24] A possible rationale is that chelate addition to the 14 electron species $RuCl_2(PPh_3)_2$ which results from triphenylphosphine dissociation, would lead to the observed product. Alternatively, chelate addition to the distorted geometry of the 16 electron $RuCl_2(PPh_3)_3$ ground state may be the determing factor. Aspects of the complicated reaction chemistry were laid out in Caulton's seminal spectroscopic characterization of the solution dynamics of $RuCl_2(PPh_3)_3$.[25] In addition to the stereospecificity for cis/trans chelation by tropolone the solid structure of all complexes also crystallize with a single nondisordered orientation of the hinokitiol isopropyl group. The solution structures of these complexes will be discussed below.

The IR and structural data illustrate the aromatic character of the chelated hinokitiol ligand. In the structural data for the hinokitiol ring, Table S3.1, there is no significant C-C bond length alteration, which supports aromatic delocalization within the ring, but the longer C(1)-C(2) bond lengths, which vary from 1.470(4) for **2** to 1.439(7) Å for **1**, are consistent with the contribution of the two Lewis structures **G** and **H.**

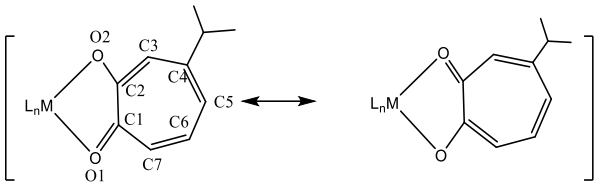

	1	2	2	3b	3c	4b
C1-O1	1.298(5)	1.281(4)	1.286(4)	1.271(11)	1.300(7)	1.297(7)
C2-O2	1.303(5)	1.294(3)	1.305(10)	1.288(8)	1.306(7)	1.314(7)
C1-C2	1.439(7)	1.470(4)	1.456(4)	1.447(12)	1.448(10)	1.443(8)
						1.460(8)
C2-C3	1.388(6)	1.406(4)	1.404(4)	1.433(14)	1.399(11)	1.393(8)
						1.393(9)
C3-C4	1.396(7)	1.391(5)	1.420(5)	1.413(17)	1.360(12)	1.385(9)
						1.377(10)
C4-C5	1.370(8)	1.392(5)	1.384(6)	1.373(16)	1.373(13)	1.379(10)
						1.377(11)
C5-C6	1.369(8)	1.366(5)	1.346(6)	1.362(16)	1.363(12)	1.393(6)
						1.425(11)
C6-C7	1.391(7)	1.384(5)	1.369(5)	1.379(13)	1.375(10)	1.396(8)
						1.373(10)
C7-C1	1.402(6)	1.401(4)	1.396(4)	1.386(12)	1.394(10)	1.407(8)
						1.408(8)

Table 3.1: Selected bond lengths (Å) for the tropolone chelate[a]
a. Orientation for common labelling scheme is shown in structure **G**.
b. Independent molecule in unit cell.

In addition to the structural data, the 1,2-dioxolene character of **D** is supported by the EPR spectrum for **1** which indicates a low spin *S*= ½ Ru(III) d^5 electronic structure which gives rise to an axial EPR spectrum at 9.2K, Fig. S3.1, with $g_{\|} = 1.82$ and $g_{\perp} = 2.33$. These values correspond well to similar known ruthenium(III) halotropolone complexes.[26,27]

The stereochemistry of the diamagnetic M(II) d^6 complexes **2** and **3** are well defined by a combination of ^{1}H and ^{31}P NMR spectroscopy with the solution spectra being consistent with

crystallographically observed structures in Figures 3.1-3.2. In particular, the bistropolone complex **2** crystallizes in a single habit in a centrosymmetric space group with the enantiomers related by an inversion center. While this is expected, what is surprising is that for this complex there is no solid state or solution evidence for the presence of other isomers: that is isomers with trans triphenylphosphines, or with another hinokitiol sidechain stereochemistry. This stereochemical integrity is expected and often observed for a Ru(II) d^6 coordinatively saturated complex.[28] Even upon standing in CD_2Cl_2 for two days at room temperature under nitrogen there is no build up of spectroscopic signatures of new triphenylphosphine containing complexes/isomers. All of these complexes are halogenated/decomposed by chloroform or larger excesses of NCS, however.

The inertness of **2** stands in stark contrast with the solid state and solution structure of **3b**. In the solid state the crystal structure of $OsH(CO)(hino)(PPh_3)_2$ has only one isomer, that with the isopropyl group being vicinal to the hydride. The longer Os-O bond trans to the hydride is a result of its stronger trans influence. In solution, both isomers are seen and dissolution of single crystals with a single geometry led to the same mixture. In order to have a better understanding of this apparent dynamic stereochemistry, variable temperature NMR was used to estimate the conversion barrier between the two isomers, Figure 3.3. The phosphorus NMR at room temperature in a 2:1 mixture of toluene-d_8/mesitylene shows two singlets at 22.49 ppm and 22.34 ppm corresponding to both isomers. At 80 $^{\circ}$C, the singlets merge indicating coalescence and at 100 $^{\circ}$C only one singlet is present.

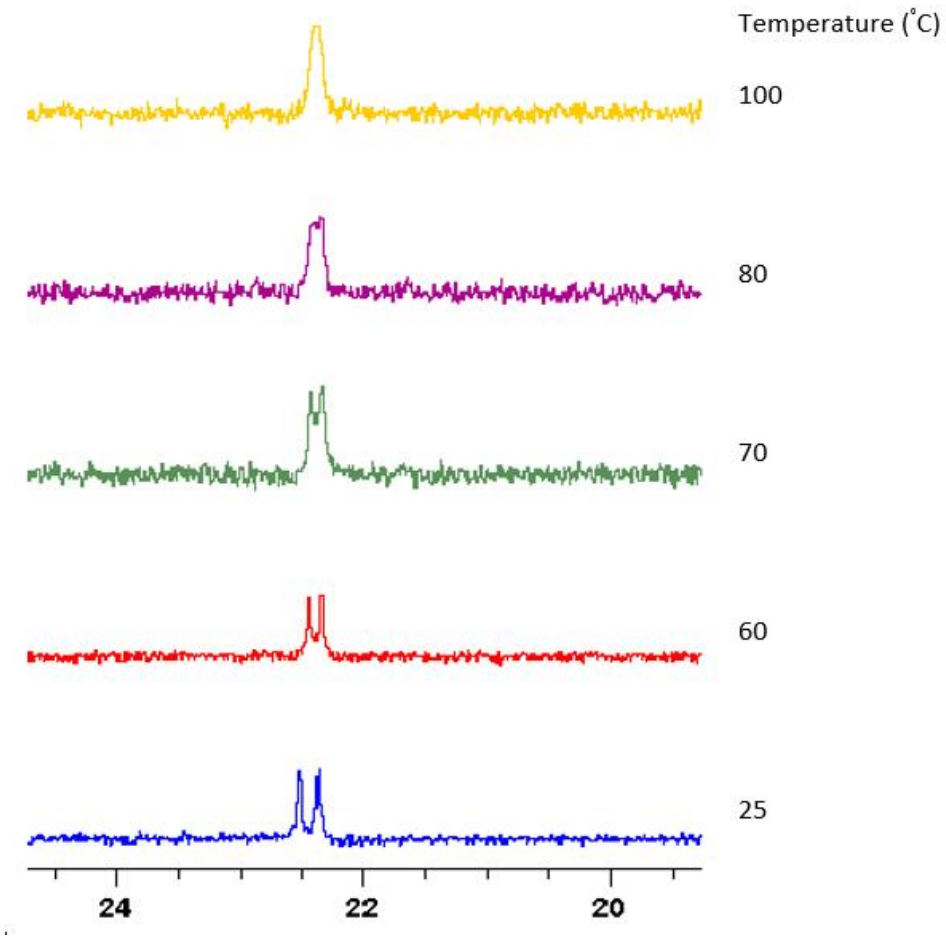

Figure 3.3: VT ^{31}P-NMR spectrum of OsH(CO)(hino)(PPh_3)$_2$ measured in a 2:1 toluene/mesitylene mixture at 162 MHz.

Complex 3a does not show the same fluxional behaviour. At room temperature, both isomers in the ^{31}P NMR were separated by 2.4 ppm which was reduced to 1.7 ppm upon heating to 95˚C. In order to understand more about the coalescence behavior of these types of complexes, additional examples were synthesized and characterized: the hydride was substituted for a chlorine for both Ru(II) and Os(II) and a different phosphine, tris p-tolylphosphine was made with osmium. The behavior of these complexes at room temperature and high temperature are shown in Table 3.2. All complexes have ^{31}P NMR resonances, $\Delta\delta$, whose difference in shift, $\Delta\delta = \delta A - \delta B$, decreases on heating. We interpret this $\Delta\delta$ decrease as being due to dynamics that are approaching the NMR time scale for interconversion. For the larger $\Delta\delta$, we are not able to heat

the sample to a temperature to attain fluxionality as found for 3b and 3c. Thus for **1**, **2**, and **4b**, the fluxionality is responsible for hino isomerization and the observed stereospecificity of their isopropyl group into a crystal with one stereochemistry. Coordinating solvents have markedly dependent fluxional behavior where weakly coordinating acetonitrile does little to perturb the fluxionality, while the more strongly coordinating DMSO promotes isomerization.

	Solvent	22˚C	95˚C
OsH(hino)(CO)(PPh_3)$_2$, 3b	Toluene/mesitylene	δ_A-δ_B=0.15 ppm	δ_A-δ_B=0 ppm coalescence at 80^{0}C Ea=90 kJ/mol
3b	Benzene	δ_A-δ_B=0.16 ppm	δ_A-δ_B=0.09 ppm (65^{0}C)
3b	Acetonitrile	δ_A-δ_B=0.08 ppm	δ_A-δ_B= 0.06 ppm (75^{0}C)
3b	DMSO	δ_A-δ_B=0 ppm	Not observed
OsH(hino)(CO)(P(p-tol_3))$_2$, 3c	Toluene/mesitylene	δ_A-δ_B=0.27 ppm	δ_A-δ_B=0 ppm coalescence at 95^{0}C Ea= 101 kJ/mol
OsCl(hino)(CO)(PPh_3)$_2$, 4b	Toluene/mesitylene	δ_A-δ_B=2.49 ppm	δ_A-δ_B=1.84 ppm
RuH(hino)(CO)(PPh_3)$_2$, 3a	Toluene/mesitylene	δ_A-δ_B=2.40 ppm	δ_A-δ_B=1.68 ppm
RuCl(hino)(CO)(PPh_3)$_2$, 4a	Toluene/mesitylene	δ_A-δ_B=2.40 ppm	δ_A-δ_B= 1.68 ppm

Table 3.2: Differences in the ^{31}P NMR Chemical Shifts of Isomers of Several Os(II) and Ru(II) Complexes at Room Temperature and at 95°C

The observed coalescence temperatures of 80 and 90 ˚C give energy barriers of 22.5 and 25.2 kcal/mol for isomer interconversion. In what is most likely a dissociative mechanism for this isomerization, chelate ring rupture leading to five coordinate intermediates is the most plausible. Oxygen dissociation from Os−O rupture is expected to be the rate-determining step in this isomerization, followed by a rotation around the remaining Os−O bond and then reformation of the six-coordinate complex (Scheme 3.1).

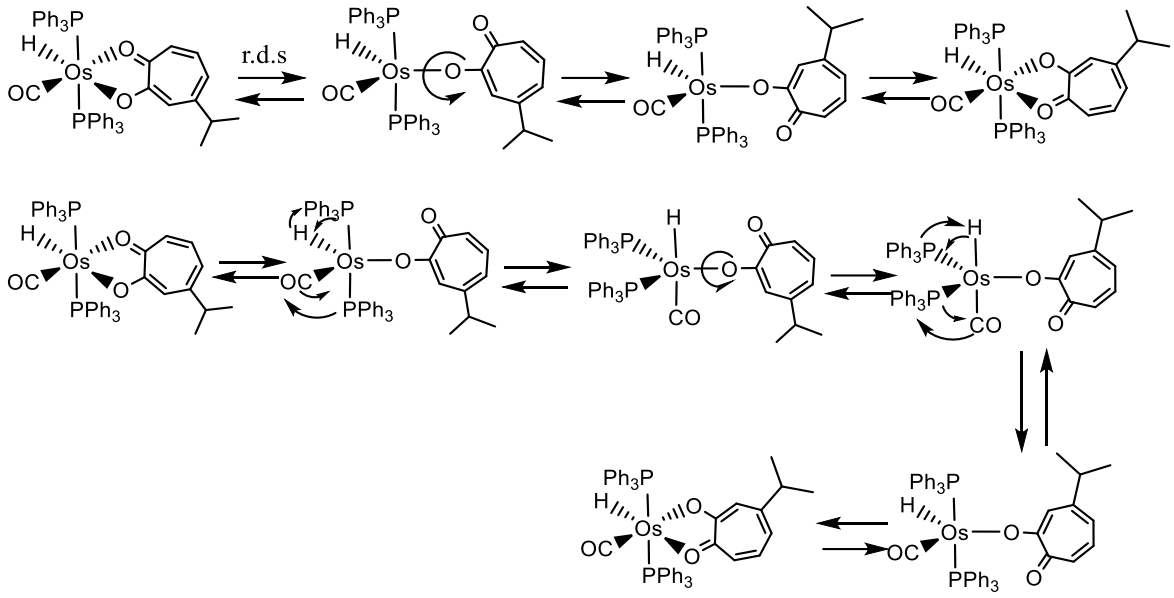

Scheme 3.1: Mechanism of inversion of the isomers of OsH(CO)(hino(PPh_3)$_2$ via a dissociative five coordinate intermediate

Regardless of the specific steps leading to isomer interconversion, the facile rupture of a chelating Os−O bond to generate the required five coordinate intermediate is unusual for an Os(II) d^6 18-electron complex, but has been suggested with osmium acetate complexes.[29] The inescapable conclusion is that the tropolone ligand has unusual lability. This has been noted before in M(tropolonate)$_3$ complexes whose dynamics do not fit with simple ground state considerations of chelate ring size and have been suggested to involve the low-lying excited states.[30] Our results with MX(CO)(hino)(L)$_2$ demonstrate that this fluxionality extends beyond D_3 symmetric complexes to those with a single tropolone chelate. The excited states responsible for this fluxionality can be tropolone-based as well as those delocalized over the M−L ensemble. Tropolones have a rich chemistry frequently involving tropelium cations,[31] as well as benzenoid intermediates.[15] The latter are the reverse of the carbene/benzenoid addition/rearrangement leading to many tropolones,[32] as well as the reverse of the formal oxidation/ring expansion found in the catechol interdiol oxygenases.

In an effort to trap intermediate I, **3b** was treated with an isocyanide, tmic, p-tolylsulfonylmethyl isocyanide, in toluene for 3 h at reflux. The resulting orange product was isolated in 36% yield

and has IR data consistent with isocyanide, hydride, carbonyl, tropolonate, and triphenylphosphine ligands. The electrospray mass spectrum of this product demonstrates the presence of starting material, 834.95 m/z, a large peak at 1104 m/z corresponds to a starting material complexed to tmic, that is, a complex with one isocyanide, carbonyl, hydride, tropolonate, and two triphenylphosphine ligands. Coordination of the isocyanide ligand to I would lead to such a product where the tropolonate ligand is now coordinated through only one oxygen. This is good evidence that the isomerization of complex 3b occurs via a dissociative mechanism. The complex formed in the reaction with the isocyanide may exist in three different isomers depending on the ligand trans to the incoming isocyanide.

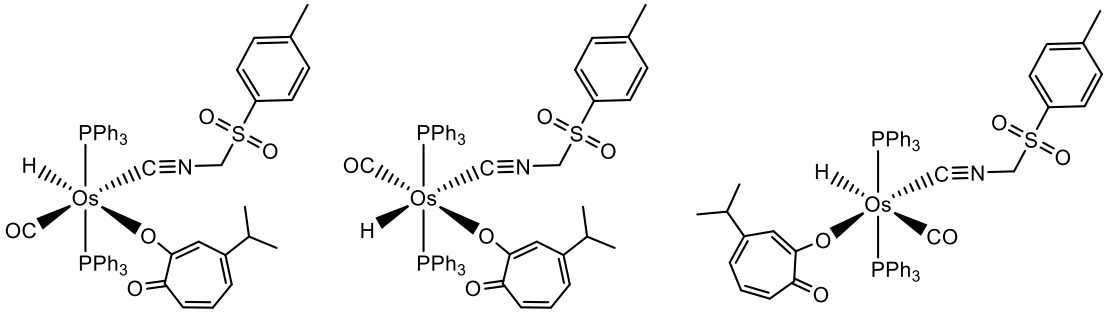

Isomer A Isomer B Isomer C

The observed lability in the hinokitioate ligand may be the origin of its role in mammalian iron mobilization and transport of iron described by Grillo *et al.*[8] This is in contrast with the generally described thermodynamic roles for the catechol siderophores which strongly bind and transport iron. The basis of the Burke ion transport model[8] is that chelates such as hinokitiol have a kinetic role whereby ligand lability correlates to rapid transport and uptake. Thus, in addition to lipid solubility, hinokitiol may play this role due to its facile fluxionality allowing for facile release and equilibration of the iron after transport. An important question this raises is the generality of these observation for other metals: as pointed out by Grillo *et al.*, other labile metals may share these same interactions with hinokitiol.

3.5 Conclusion

In conclusion, complexes with the tropolonate chelate represent an important fundamental class of coordination complexes with considerable practical and biological significance and potential. In common with the other dioxolene chelates tropolones strongly bind to a range of metals with a range of oxidation states. However, set against this thermodynamic robustness is the kinetic lability discovered here. Their lability stands in contrast with the catechol chelates and is an important aspect of tropolonate coordination chemistry in materials and bioinorganic chemistry which will contribute to their utilization in materials applications and modulate their biochemical roles in nature.

3.6 Experimental

The starting materials $OsHCl(CO)(PPh_3)_3$, $RuHCl(CO)(PPh_3)_3$, $RuCl_2(PPh_3)_3$, and $OsHCl(CO)(P(p\text{-tolyl})_3)_3$ were prepared by literature methods[33] or purchased. IR spectra were measured on Bomem MB3000 FTIR spectrometer as KBr pellets, and ^1H, $^{13}C\{^1H\}$, and $^{31}P\{^1H\}$ NMR spectra were measured on a Bruker AVIIIHD 500 spectrometer at 22 °C at 500 MHz for ^1H, 131 MHz for ^{13}C and 202 MHz for ^{31}P. UV−visible spectra were obtained using an HP 8453 diode array spectrophotometer.

3.6.1 Synthetic Procedures

$RuCl_2(hino)(PPh_3)_2$ (1): $RuCl_2(PPh_3)_3$ (0.2 g, 0.21 mmol) was dissolved in hot toluene (10 mL) in the open. Hinokitiol (1 equiv, 34 mg, 0.21 mmol) was dissolved in hot ethanol (10 mL) and added to the previous mixture, and the solution was heated at reflux overnight in the open. After cooling and concentration to 10 mL and addition of 10 mL of ethanol, a green precipitate, $RuCl_2(hino)(PPh_3)_2$, was collected. Yield: 76 mg (42%). DSC: decomposition T = 274.4°C. ΔH = 16.48 J/g. IR: KBr (cm^{-1}): 3058.2 w, 2961.7 w, 1583.2 m, 1563.2 m, 1499.5 m, 1480.1 m, 1428.8 vs, 1364.5 s, 1229.0 w, 1183.4 w, 1093.6 s, 1029.2 w, 951.9 w, 803.8 w, 745.9 m. (ESI-MS): m/z 882.09 $[(RuCl_2P_2C_{46}H_{41})Na]^+$. UV−vis CH_2Cl_2 λmax (log ε): 244 nm (4.6), 301 nm (4.3), 378 nm (3.9), 647 nm (2.3). Crystals suitable for X-ray diffraction were grown from dichloromethane/ethanol.

cis-$Ru(hino)_2(PPh_3)_2$ (2): $RuCl_2(PPh_3)_3$ (0.2 g, 0.21 mmol) and 3.3 equiv of hinokitiol (0.115 g, 0.7 mmol) were stirred in 20 mL of ethanol and 1 drop of DBU under nitrogen. This suspension was heated at reflux for 1.5 h during which time it turned a deep red. After cooling in an ice/salt bath, the product crystallized out of solution as deep red plates. Upon further concentration on a rotoevaporator, the crystal mass increased in volume and separated as large red needles which were separated by filtration and washing with ethanol and n-hexane. Analytical-grade crystals were obtained by recrystallization from dichloromethane/ethanol. Yield 0.143 g, 71% yield. DSC: irreversible decomposition. T = 261.9°C, ΔH = 12.2 J/g. UV−vis CH_2Cl_2 λmax (log ε): 490 nm (4.1), 384 nm (4.3), 331 nm (4.6). IR: KBr (cm^{-1}): 3058.1 w, 2955.2 w, 1576.6 m, 1493.2 m,

1422.2 s, 1357.8 m, 1229.0 w, 1183.9 w, 1093.6 m, 1016.4 w, 951.9 w, 797.5 m, 739.4 m. ^{1}H NMR $CDCl_3$: 6.91 (m, PPh_3, 30) 6.9 (s, 2H, CH), 6.72 (d, $^{3}J_{HH}$ = 11.1, 2H, CH), 6.45 (t, $^{3}J_{HH}$ = 10.3, 2H, CH), 5.98 (d, $^{3}J_{HH}$ = 11.05, 2H, CH), 2.27 (m, CH, 2). 0.93 (d, $^{3}J_{HH}$ = 6.9, 12H, CH_3). $^{31}P\{^{1}H\}$ NMR: $CDCl_3$, 58.41 s. $^{13}C\{^{1}H\}$: 187.23, 183.73, 155.02, 136.46, 136.31, 136.14, 134.64 (t, J_{CP} = 4.7), 128.20, 126.96 (t, J_{CP} = 4.6), 125.79, 124.41, 122.70, 39.69, 20.45. Crystals suitable for X-ray diffraction were grown from dichloromethane/ethanol. Anal. Calcd $C_{56}H_{54}P_2O_4Ru$: C 70.50%, H 5.71%. Found: C 70.74%, H 6.02%.

RuH(hino)(CO)$(PPh_3)_2$ (3a): RuHCl(CO)$(PPh_3)_3$ (0.309 g, 0.352 mmol), hinokitiol (164 mg, 0.49 mmol, 1.5 equiv), and 0.02 mL of DBU (1,8-diazabicycl[5.4.0]undec-7-ene) were heated to reflux in 20 mL of benzene under nitrogen. During this period, the initially colorless solution became a bright yellow color. After 2.5 h, heating was discontinued, and benzene was removed from the cooled solution to give a yellow/orange solid which was recrystallized from dichloromethane/ethanol to give deep orange yellow crystals. Filtration and washing with cold ethanol (2 × 10 mL) gave 0.233 mg of microcrystalline needles in 88% yield. DSC: Dec. 208°C. ΔH = −3.3 J/g. In solution, this corresponds to a mixture of two isomers in a 55:45 ratio as determined by by NMR spectroscopy. UV−vis CH_2Cl_2 λmax (log ε): 430 nm (4.1), 335 nm (4.3). IR: KBr (cm^{-1}): 3058.2 w, 2961.6 w, 1931.0 vs, 1912.2 s, 1586.0 m, 1563.9 m, 1493.6 m, 1480.9 m, 1429.29vs, 1358.4 m, 1235.5 w, 1183.9 w, 1094.2 m, 1022.9 w, 958.6 w, 798.2 m, 746.6s. NMR spectroscopy ($CDCl_3$): Major isomer (61%): ^{1}H −13.96 (t, $^{2}J_{HP}$ = 20.2 Hz, 1H, Ru−H), 1.09 (d, $^{3}J_{HH}$ = 7.2 Hz, 6H, CH_3), 2.36 (m, 1H, $CHCH_3$), 5.87 (s,1H, CH), 6.17 (d, $^{3}J_{HH}$ = 10.1 Hz, 1H, CH), 6.42 (d, $^{3}J_{HH}$ = 10.6 Hz, 1H, CH), 6.67 (t, $^{3}J_{HH}$ = 10.5 Hz, 1H, CH), 7.30 (m, PPh_3), 7.57 (m, PPh_3). Minor isomer (39%): 1H −14.18 (t, $^{2}J_{HP}$ = 19.8 Hz, 1H, Ru− H), 1.00 (d, $^{3}J_{HH}$ = 6.8 Hz, 6H, CH_3), 2.49 (m, 1H, $CHCH_3$), 6.17 (d, $^{3}J_{HH}$ = 10.1 Hz,1H, CH), 6.46 (s,1H, CH), 6.46 (t, $^{3}J_{HH}$ = 11.5 Hz, 1H, CH), 6.56 (d, $^{3}J_{HH}$ = 11.0 Hz, 1H, CH), 7.30,(m, PPh_3), 7.57 (m, PPh_3). 31P$\{^{1}H\}$ $CDCl_3$, major 26.76 (s), minor: 29.63 (s). $^{13}C\{^{1}H\}$: 182.35, 182.24, 182.03, 182.00, 156.34, 156.21, 134.55 (t, J_{CP} = 6.4 Hz), 134.53 (t, J_{CP} = 6.4 Hz), 133.84, 133.81, 133.68, 133.65, 133.52, 133.48, 129.39, 129.35, 127.75 (t, J_{CP} = 4.7 Hz), 125.77, 124.88, 124.80. 123.57, 121.56, 121.40, 38.63, 23.66. Anal. calcd $C_{41}H_{42}P_2O_3Ru$: C 69.03%, H 5.18%. Found: C 68.89%, H4.97%.

$RuCl(CO)(hino)(PPh_3)_2$ (4a): $RuH(CO)(hino)(PPh_3)_2$ (0.100 g, 0.11 mmol) and N-chlorosuccinimide (22 mg, 0.11 mmol) were stirred in 10 mL of DCM for 30 min. Next, 10 mL of ethanol was added to the solution. The DCM was subsequently removed, and an orange precipitate formed. Filtration and washing with cold ethanol (2 × 10 mL) gave 0.63 mg of product in 61% yield. DSC: Dec. 277°C. ΔH = 31 J/g. UV−vis CH_2Cl_2 λmax (log ε): 447 nm (2.8). IR: KBr (cm^{-1}): 3056.5 w, 2959.1 w, 1934.1 s, 1587.5 m, 1495.6 m, 1481.2 m, 1433.9 s, 1357.7 m, 1238.1 w, 1186.0 w, 1092.8 m, 957.6 w, 803.0 m, 745.2 s. Mixture of two isomers in a 50:50 ratio by NMR spectroscopy. NMR spectroscopy($CDCl_3$): Isomer A (50%): ^1H 1.07 (d, $^3J_{HH}$ = 6.8, 6H, CH_3), 2.48 (m, 1H, $CHCH_3$), 5.87 (s,1H,CH), 6.17 (d, $^3J_{HH}$ = 9.9 Hz,1H, CH), 6.56 (d, $^3J_{HH}$ = 10.9, 1H, CH), 6.67 (t, $^3J_{HH}$ = 10.5 Hz, 1H, CH), 7.30 (m, PPh_3), 7.57 (m, PPh_3). Isomer B (50%): ^1H 1.00 (d, $^3J_{HH}$ = 6.8, 6, CH3), 2.35 (m, 1H, $CHCH_3$), 6.03 (d, $^3J_{HH}$ = 11 Hz,1H, CH), 6.17 (d, $^3J_{HH}$ = 9.9 Hz,1H,CH), 6.43 (t, $^3J_{HH}$ = 11.5 Hz,1H,CH), 6.46 (s, 1H, CH), 7.30 (m, PPh_3), 7.57 (m, PPh_3). $^{31}P\{^1H\}$ $CDCl_3$: Isomer A: 30.22(s). Isomer B: 28.08(s). $^{13}C\{^1H\}$: 183.36, 182.97, 182.76, 182.16, 157.44, 156.17, 134.80 (t, J= 5.5 Hz), 131.12, 130.96, 130.76, 130.63, 129.75, 127.78 (t, J_{CP} = 4.6 Hz), 125.70, 125.44, 124.26, 124.12, 123.67, 38.58, 38.45, 23.55, 23.45. (ESI-MS): m/z 875.29 $[(RuClO_3P_2C_{47}H_{41})Na]+$.

$OsH(CO)(hino)(PPh_3)_2$ (3b): $OsHCl(CO)(PPh_3)_3$ (0.368 g, 0.35 mmol), hinokitiol (68 mg, 0.42 mmol), and 2 drops of diazobicycloundene (DBU) were heated to reflux in 25 mL of benzene under nitrogen. During this period, the initially colorless solution became a bright yellow color. After 5.5 h, heating was discontinued, and benzene was removed from the cooled solution to give a yellow/orange solid which was recrystallized from dichloromethane/ethanol to give deep orange yellow crystals. Filtration and washing with cold ethanol (2 × 10 mL) gave 0.290 mg of microcrystalline needles in 91% yield. DSC: Dec. 235 °C. ΔH = 20 J/g. UV−vis CH_2Cl_2 λmax (log ε): −430 nm (4.1), 333 nm (3.8). IR: KBr (cm^{-1}): 3051.9 w, 2961.6 w, 2098.9 w, 1886.3 s, 1588.0 m, 1499.9 m, 1473.8 m, 1429.3 s, 1358.2 m, 1235.5 w, 1183.9 w, 1087.9 m, 964.8 w, 810.3 m, 746.6 s. Mixture of two isomers in a 50:50 ratio by NMR spectroscopy. ^1H-NMR spectroscopy ($CDCl_3$): Isomer A (50%): ^1H −16.10 (t, $^2J_{HP}$ = 16.5 Hz, 1H, Os−H), 1.09 (d, $^3J_{HH}$ = 6.9, 6H, CH_3), 2.47 (m, 1H, $CHCH_3$), 5.96 (s, 1H, CH), 6.11 (d, $^3J_{HH}$ = 9.4 Hz, 1H, CH), 6.47 (d, $^3J_{HH}$ = 11.2, 1H, CH), 6.67 (t, $^3J_{HH}$ = 10.6 Hz, 1H, CH), 7.30 (m, PPh_3), 7.57 (m, PPh_3). Isomer B

(50%): ^{1}H −16.40 (t, $^{2}J_{HP}$ = 16.2, 1H, Os−H), 1.05 (d, $^{3}J_{HH}$ = 6.9, 6H, CH3), 2.40 (m, 1H, $CHCH_3$), 5.94 (d, $^{3}J_{HH}$ = 10.5 Hz, 1H, CH), 6.08 (d, $^{3}J_{HH}$ = 9.4 Hz, 1H, CH), 6.40 (s, 1H, CH), 6.54 (t, $^{3}J_{HH}$ = 10.6 Hz, 1H, CH), 7.30 (m, PPh_3), 7.57 (m, PPh_3). $^{31}P\{^{1}H\}$ $CDCl_3$: Isomer A: 21.69 (s). Isomer B: 21.62 (s). $^{13}C\{^{1}H\}$: 182.36, 182.04, 181.96, 181.56, 155.84, 134.75 (t, JCP = 4.4 Hz), 134.68 (t, JCP = 4.4 Hz), 134.353, 134.16, 133.94, 13.75, 133.63, 133.44, 129.45, 129.41, 127.72 (t, JCP = 4.6 Hz), 126.41, 125.44, 125.40, 124.02, 122.97, 38.74, 23.48, 23.44 u. Anal. calcd $C_{41}H_{42}P_2O_3Os$: C 62.24%, H 4.67%. Found: C 61.95%, H 4.72%. Crystals suitable for X-ray diffraction were grown from dichloromethane/methanol.

$OsH(CO)(hino)(P(p\text{-}tolyl)_3)_2$ (3c): $OsHCl(CO)(P(p\text{-}tolyl)_3)_3$ (0.120 g, 0.10 mmol), hinokitiol (38 mg, 0.23 mmol, 1.91 equiv), and 2 drops of DBU were heated to reflux in 10 mL of benzene under nitrogen for 2.5 h. During this period, the initially colorless solution became a deep orange yellow color. After 3 h at reflux, the solution was cooled, concentrated to 2 mL, and diluted with 10 mL of ethanol. This orange-yellow solution was cooled at −4 °C overnight, and the resulting orange crystalline mass filtered and washed with cold ethanol (5 mL) and hexanes gave 96 mg in 95% yield. This can be further purified by recrystallization from a dichloromethane/ethanol/water (20:20:1). DSC: Dec T > 300 ˚C. UV−vis CH_2Cl_2 λmax (log ε): −430 nm (4.1), 333 nm (3.8). IR: KBr (cm^{-1}): 3051.9 w, 2961.6 w, 2098.9 w, 1886.3 s, 1588.0 m, 1499.9 m, 1473.8 m, 1429.3 s, 1358.2 m, 1235.5 w, 1183.9 w, 1087.9 m, 964.8 w, 810.3 m, 746.6 s. Mixture of two isomers in a 71:29 ratio by NMR spectroscopy. NMR Spectroscopy($CDCl_3$): Isomer A (71%): ^{1}H −16.37 (t, $^{2}J_{HP}$ = 16.2 Hz, 1H, Os−H), 1.09 (d, $^{3}J_{HH}$ = 6.9, 6H, CH_3), 2.34 (s, 18H, CH_3), 2.48 (m, 1H, $CHCH_3$), 5.81 (d, $^{3}J_{HH}$ = 10.9 Hz, 1H, CH), 6.08 (d, $^{3}J_{HH}$ = 10.2, 1H, CH), 6.41 (s,1H,CH), 6.50 (t, $^{3}J_{HH}$ = 10.5 Hz, 1H, CH), 7.45 (m, $P(p\text{-}tol)_3$). Isomer B (29%): ^{1}H −16.41 (t, $^{2}J_{HP}$ = 16.9, 1, Os−H), 1.04 (d, $^{3}J_{HH}$ = 6.9, 6, CH_3), 2.26 (s, 18H, CH_3) 2.40 (m, 1H, $CHCH_3$), 5.98 (s, 1H, CH), 6.08 (d, $^{3}J_{HH}$ = 10.2 Hz, 1H, CH), 6.36 (d, $^{3}J_{HH}$ = 11.3 Hz, 1H, CH), 6.61 (t, $^{3}J_{HH}$ = 10.2 Hz, 1H, CH), 7.45 (m, $P(p\text{-}tol)_3$). $^{31}P\{^{1}H\}$ Isomer A: 20.70 (s). Isomer B: 20.52 (s). $^{13}C\{^{1}H\}$: 182.14, 181.75, 155.30, 134.65 (t, J_{CP} = 5.6 Hz), 131.02, 130.83, 130.78, 130.64, 130.59, 129.30, 129.25, 128.48, 126.55, 125.63, 125.35, 124.09, 121.95, 121.86, 38.67, 38.43, 23.41, 23.39, 21.33, 21.29. Crystals suitable for X-ray diffraction were grown from dichloromethane/ethanol. ESI-MS: m/z 1015.30 $[(OsO_3P_2C_{53}H_{54})Na]+$.

$OsCl(CO)(hino)(PPh_3)_2$ (4b): $OsH(CO)(hino)(PPh_3)_2$ (0.100g, 0.11 mmol) and N-chlorosuccinimide (22 mg, 0.11 mmol) were stirred in 10 mL of DCM for 30 min. First, 10 mL of ethanol was added to the solution. The DCM was subsequently removed, and an orange precipitate formed. Filtration and washing with 2 × 10 mL cold ethanol gave 0.63 mg of product in 61% yield. DSC: Dec. 258 °C, ΔH = 16 J/g. UV−vis CH_2Cl_2 λmax (log ε): 453 nm (3.3). IR: KBr (cm^{-1}): 3051.9 w, 2955.3 w, 1911.9 s, 1588.4 m, 1499.9 m, 1480.6 m, 1435.6 s, 1351.8 m, 1236.1 w, 1178.0 w, 1094.2 m, 959.1 w, 798.2 m, 740.1 s. Mixture of two isomers in a 50:50 ratio by NMR spectroscopy. NMR spectroscopy($CDCl_3$): Isomer A (50%): ^1H 1.07 (d, $^3J_{HH}$ = 6.9, 6H, CH_3), 2.45 (m, 1H, $CHCH_3$), 5.96 (s,1H,CH), 6.19 (d, $^3J_{HH}$ = 10.0 Hz,1H, CH), 6.41 (d, $^3J_{HH}$ = 10.9,1H,CH), 6.73 (t, $^3J_{HH}$ = 10.5 Hz,1H,CH), 7.32 (m, PPh_3), 7.57 (m,PPh_3). Isomer B (50%): ^1H 1.02 (d, $^3J_{HH}$ = 6.9, 6, CH3), 2.37 (m, 1H, $CHCH_3$), 6.14 (d, $^3J_{HH}$ = 11 Hz, 1H, CH), 6.19 (d, $^3J_{HH}$ = 10 Hz, 1H, CH),6.29 (s, 1H, CH), 6.56 (t, $^3J_{HH}$ = 10.5 Hz, 1H, CH), 7.30 (m, PPh_3), 7.57 (m, PPh_3). $^{31}P\{^1H\}$ $CDCl_3$: Isomer A: 7.65 (s). Isomer B: 5.44 (s). $^{13}C\{^1H\}$: 182.86, 182.49, 182.02, 181.38, 157.02, 155.86, 134.78 (t,J_{CP} = 5.3 Hz), 131.00, 130.88, 130.80, 130.69, 130.61, 130.50, 129.79, 127.82 (t, J_{CP} = 4.6 Hz), 125.99, 125.70, 125.13, 125.10, 124.43, 38.74, 38.56, 23.33, 23.29 Crystals suitable for X-ray diffraction were grown from dichloromethane/ethanol. (ESI-MS): m/z 965.17 $[(OsClO_3P_2C_{47}H_{41})Na]+$.

3.6.2 Crystallographic Methodologies

Crystals are mounted on glass fibers with epoxy resin or Mitogen mounts using Paratone-N from Hampton Research and single-crystal X-ray diffraction experiments are carried out with a BRUKER APEX-II D8 CCD diffractometer by using graphite-monochromated Mo Kα radiation (λ = 0.71073 Å) the SHELX package[34] is used for integration of the intensity reflections, scaling, and absorption correction. Intrinsic phasing and Patterson methods were used to solve the structures. Non-hydrogen atoms are located by difference Fourier maps and final solution refinements are carried out by full-matrix least-squares methods on F2 of all data. The hydrogen atoms are placed in calculated positions and were not refined. Efforts to locate the hydrides in 3b,c were hampered by large residual peaks and holes near the osmium which are associated with the residuals associated with absorption corrections.

3.7 References

1. Hall, L. A.; Williams, D. J. Complexes of Squaric Acid and its Monosubstituted Derivatives. *Adv. Inorg. Chem.* **2001**, *52*, 249-291.
2. West, R.; Niu, H. Y. New Aromatic Anions VI. Complexes of Croconate Ion with Some Divalent and Trivalent Metals. *J. Am. Chem. Soc.* **1963**, *85*, 2586-2588.
3. West, R.; Niu, H.Y.; Ito, M.: New Aromatic Anions V. The Synthesis of Diketocyclobutenediol and its Conversion to Octahydroxycyclobutane *J. Am. Chem. Soc.* **1963**, *85*, 2584-2586.
4. Pierpont, C. G. Studies on Charge Distribution and Valence Tautomerism in Transition Metal Complexes of Catecholate and Semiquinonate Ligands. *Coord. Chem. Rev.* **2001**, *216-217*, 99-125.
5. Demir, S.; Jeon, I.-R.; Long, J. R.; Harris, T. D. Radical Ligand-Containing Single-Molecule Magnets. *Coord. Chem. Rev.* **2015**, *289-290*, 149-176.
6. Tezgerevska, T.; Alley, K. G.; Boskovic, C. Valence Tautomerism in Metal Complexes: Stimulated and Reversible Intramolecular Electron Transfer Between Metal Centers and Organic Ligands. *Coord. Chem. Rev.* **2014**, *268*, 23-40.
7. Raymond, K. N.; Dertz, E. A.; Kim, S. S. Enterobactin: An archetype for Microbial Iron Transport. *Proc. Natl. Acad. Sci. U. S. A.* **2003**, *100*, 3584-3588.
8. Grillo, A. S.; Santamaria, A. M.; Kafina, M. D. ; Cioffi, A. G.; Huston, N. C.; Han, M.; Seo Y. A.; Yien Y. Y.; Nardone C.; Menon , A. V. Restored Iron Transport by a Small Molecule Promotes Absorption and Hemoglominization in Animals, *Science*, **2017**, *356*, 608-616
9. Ferrando-Soria, J.; Vallejo, J.; Castellano, M.; Martinez-Lillo, J.; Pardo, E.; Cano, J.; Castro, I.; Lloret, F.; Ruiz-Garcia, R.; Julve, M. Molecular Magnetism, Quo Vadis? A Historical Perspective From a Coordination Chemist Viewpoint. *Coord. Chem. Rev.* **2017**, *339*, 17-103.

10. Naumov, P.; Chizhik, S.; Panda, M. K.; Nath, N. K.; Boldyreva, E. Mechanically Responsive Molecular Crystals. *Chem. Rev. (Washington, DC, U. S.)* **2015**, *115*, 12440-12490.
11. Pierpont, C. G. Unique Properties of Transition Metal Quinone Complexes of the MQ3 Series. *Coord. Chem. Rev.* **2001**, *219-221*, 415-433.
12. Raymond, K. N.; Cass, M. E.; Evans, S. L. Metal Sequestering Agents in Bioinorganic Chemistry: Enterobactin Mediated Iron Transport in E. Coli and Biomimetic Applications. *Pure Appl. Chem.* **1987**, *59*, 771-778.
13. Harrington, J. M.; Mysore, M. M.; Crumbliss, A. L. The Kinetics of Dimethylhydroxypyridinone Interactions with Iron(III) and the Catalysis of Iron(III) Ligand Exchange Reactions: Implications for Bacterial Iron Transport and Combination Chelation Therapies. *Dalton Trans.* **2018**, *47*, 6954-6964.
14. Harrington, J. M.; Crumbliss, A. L. The Redox Hypothesis in Siderophore-Mediated Iron Uptake. *BioMetals* **2009**, *22*, 679-689.
15. Pietra, F. Seven-Membered Conjugated Carbo-and Heterocyclic Compounds. *Chem. Rev.* **1973**, *73*, 293-364.
16. Kurek, J.; Kwaśniewska-Sip, P.; Myszkowski, K.; Cofta, G.; Barczyński, P.; Murias, M.; Kurczab, R.; Śliwa, P.; Przybylski, P. Antifungal, Anticancer, and Docking Studies of Colchiceine Complexes with Monovalent Metal Cation Salts. *Chemical Biology & Drug Design* **2019**, *94*, 1930-1943.
17. Komaki, N.; Watanabe, T.; Ogasawara, A.; Sato, N.; Mikami, T.; Matsumoto, T. Antifungal Mechanism of Hinokitiol against Candida albicans. *Biological and Pharmaceutical Bulletin* **2008**, *31*, 735-737.
18. Muetterties, E.; Roesky, H.; Wright, C. Chelate Chemistry. V. Metal Chelates Based on Tropolone and its Derivatives. *Journal of the American Chemical Society* **1966**, *88*, 4856-4861.
19. Griffith, W. P.; Pumphrey, C. A.; Skapski, A. C. Tropolonato Complexes of Osmium, Iridium, Platinum, Molybdenum and Tungsten, and the X-Ray Crystal Structure of MoO_2trop_2. *Polyhedron* **1987**, *6*, 891-896.

20. Figgen D.; Koers A.; Schwerdtfeger, P., "NWHClI - A Small and Compact Chiral Molecule with Large Parity Violation Effects in the Vibrational Spectrum.". *Angew. Chem. Int. Ed* **2010**, *49*, 2941-2943.
21. Hiett, N. P.; Lynam, J. M.; Welby, C. E.; Whitwood, A. C.: Ruthenium Carboxylate Complexes as Easily Prepared and Efficient Catalysts for the Synthesis of β-oxopropyl Esters *J. Organomet. Chem.* **2011**, *696*, 378.
22. Nguyen H. H.; Hoang N. ; Abram U. Synthesis and Structures of Two Ruthenium Dibenzoylmethane Triphenylphosphine Mixed Ligand Complexes, *Transition. Met. Chem.* **2010**, *35*, 89
23. Mishra, D.; Naskar, S.; Drew, M. G. B.; Chattopadhyay, S. Y. *Polyhed.* **2005**, *24*, 1861.
24. Prater, B. E. New Isocyanide Complexes of Ruthenium(II) containing Triphenylphosphine, Triphenylarsine, and Triphenylstibine. *J. Organometal. Chem.* **1972**, *34*, 379-386.
25. Hoffman, P. R.; Caulton, K. G. Solution Structure and Dynamics of Five-Coordinate d^6 Complexes. *J. Am. Chem. Soc.* **1975**, *97*, 4221-4228.
26. Medhi, O. K.; Agarwala, U. Mixed Complexes of Ru(III) with Bromotropolonato Ion. *J. of Inorg. Nucl. Chem.*, **1980**, *42*, 1413-1416.
27. Le Guennic, B.; Floyd, T.; Galan, B. R.; Autschbach, J.; Keister, J. B. Paramagnetic Effects on the NMR Spectra of "Diamagnetic" Ruthenium(bis-phosphine)(bis-semiquinone) Complexes. *Inorg. Chem.* **2009**, *48*, 5504-5511.
28. Hill, A. F.: In *Comprehensive Organometallic Chemitry*, Wilkinson, G.; Stone, F. G. A.; Hegedus L. S., Ed; Elsevier: New York, 1996; Vol. 6, 299-440
29. Bolano, T.; Castarlenas, R.; Esteruelas, M. A.; Onate, E.: Hydride-Carbyne to Carbene Transformation in an Osmium-Acetate-Bis(triisopropylphosphine) System: Influence of the Coordination Mode of the Carboxylate and the Reaction Solvent, *Organometallics*, **2007**, *26*, 2037-2041
30. Palazzotto, M. C.; Duffy, D. J.; Edgar, B. L.; Que, L.; Pignolet, L. H. Dynamic Stereochemistry of Tris-Chelate Complexes. I. Tris(dithiocarbamato) Complexes of Iron, Cobalt, Rhodium, *J. Am. Chem. Soc*. **1973**, *95*, 4537−4545.

31. Kolomnikova, G. D.; Parnes, Z. N.: Tropenium Cations. *Russ. Chem. Rev.* **1967**, *36*, 735-756.
32. Closs, G. L.; Closs, L. E.: Dichlorocarbene Addition to Phenols. *J. Am. Chem. Soc.* **1961**, *83*, 599-611.
33. Collins, T. J.; Grundy, K. R.; Roper, W. R.: The Tris-(triphenylphosphine)osmium Zerovalent Complexes., *J. Organomet. Chem.* **1982**, *231*, 161−172
34. Sheldrick, G. M. SADABS, TWINABS; Siemens Industrial Automation, Inc.: Madison, WI, 1996.

Chapter 4: Organometallic Chemistry and Tris Chelate Complexes of the Parent Dithiocarbamate $[S_2CNH_2]^-$

4.1 Preface

It was concluded from chapters 2 and 3 that complexes of hinokitiol would not be good candidates for the detection of Parity Violation Energy Difference in molecules due to low activation barriers in both tris-chelate complexes of cobalt, rhodium and iridium, as well as in Ru(II) and Os(II) complexes. A new, more rigid class of ligands must therefore be investigated.

We have turned our attention to dithiocarbamates, $[S_2CNR_2]^-$ and more specifically, the smallest dithiocarbamate $[S_2CNH_2]^-$. The library of transition metal complexes of dialkyldithiocarbamates is immense but that of $[S_2CNH_2]^-$ is much more limited. A good understanding of the coordination chemistry to d^6 transition metals is required. Additionally, the potential volatility of these complexes would be an advantage in PVED measurements in the gas phase.

In this chapter, we present first a new synthesis of the ligand as well as two new ruthenium complexes in order to gain a better insight into the coordination chemistry of this ligand. We then describe the synthesis of tris-chelate complexes and investigate its stereochemical rigidity using variable temperature NMR, X-ray crystallography and DFT calculations in a manner similar to that described in chapter 2. A comparison of the tris-chelate complexes of $[S_2CNH_2]^-$ and hinotkiol is presented.

The work presented in this chapter was published in: Gaydon Q.; Bohle D. S., Coordination Chemistry of the Parent Dithiocarbamate $H_2NCS_2^-$: Organometallic Chemistry and Trischelates of Group 9 Metals, *Inorg. Chem*., **2022**, *61,* 4662

4.2 Abstract

Two tris-chelate complexes of cobalt and rhodium and two complexes of Ru(II) of dithiocarbamate, $[S_2CNH_2]^-$, were synthesized. The complexes were spectroscopically characterized by IR, NMR, UV-Vis, MS and structurally characterized by X-ray diffraction. The structural features of the rhodium complex were compared to other tris-chelate Rh(III) dithiocarbamate complexes and are characterized by a strong distortion away from ideal octahedral geometry. This was confirmed both experimentally by X-ray diffraction and theoretically using DFT calculations. The inversion barriers of $Rh(Bz_2dtc)_3$, $Ir(Bz_2dtc)_3$, and $Rh(Et_2dtc)_3$ were determined using VT-NMR in DMSO. These barriers were found to be surprisingly low for heavy group 9 elements of d^6 tris-chelate complexes: values of 16.7, 17.1 and 16.4 kcal/mol were calculated. By comparing structural features relating to this distortion, we are able to determine that the activation barrier for the inversion of stereochemistry of $Rh(H_2dtc)_3$ must have similarly low values. A modified version of the Bailar twist involving an intermediate with C_{3h} geometry was proposed as the mechanism of inversion.

4.3 Introduction

One hypothesis to explain the origin of homochirality in biology is the existence of a small difference in energy between the enantiomers of chiral biomolecules called Parity Violation Energy Difference (PVED).[1,2] The consequence of PVED can be experimentally observed in heavy atoms, since it is responsible for the observed breakdown in Laporte selection rules: forbidden S→S transitions were unambiguously observed in the gaseous atomic spectra of cesium[3] and with high accuracy for ytterbium, bismuth, lead and thallium.[4-7] The experimental determination of PVED in molecules has proved to be a challenge: several techniques using vibrational spectroscopy,[8-10] NMR[11] or Mössbauer spectroscopy[12] have been used without success. Recently, rotational spectroscopy in the gas phase has appeared as a suitable option for PVED measurements:[13] high resolutions can be achieved but this technique requires the molecules to be in the gas phase. While the nature of the experiment is essential, finding a suitable candidate molecule is equally as important. We have determined several criteria such a

molecule should meet: it must be chiral, available in sufficient scale, contain at least one heavy atom, be resolvable and inert towards racemization. Tris-chelate group 9 d^6 complexes fulfill many of these criteria.

Recently we studied the tris-chelate complexes of a tropolone derivative, 4-isopropyltropolone, as potential candidates for PVED measurements.[14] Using dynamic NMR studies as well as the determination of key structural parameters, we have concluded that the complexes have remarkable low temperature fluxional behaviour even with the heavier elements, rhodium and iridium. Because of the unusually low barriers, these molecules would not be suitable candidates for PVED measurements. We have decided to turn our attention towards smaller bidentate ligands with two sulfur donor atoms. Complexes with such ligands may be more suited for measurements in the gas phase and more stereochemically rigid.

One important class of bidentate S,S donor ligands are dithiocarbamates with the general formula $S_2CNR_2^-$. [15-17] Dialkyldithiocarbamates can be easily obtained by treating carbon disulfide with the corresponding secondary amine.[18-20] Complexes with dialkyldithiocarbamates have been extensively studied: complexes are known for every transition metal.[21-27] Among their general properties, good solubility in organic solvents, good thermal stability,[28-30] and vibrant colors are common characteristics. Some dithiocarbamate complexes with diethyldithiocarbamate have been reported to be volatile.[31,32]

The parent dithiocarbamate, ammonium dithiocarbamate, $S_2CNH_2^-$ (H,Hdtc) is the smallest possible dithiocarbamate ligand. While alkyl and aryl dithiocarbamates have received considerable attention, few examples of transition metals of H,Hdtc are known: Teske *et al.* have synthesized complexes of bismuth, chromium, copper, silver, and gold.[33] Among the possible tris-chelate d^6 complexes, only the cobalt complex has been structurally characterized by Raston and White.[34] We hypothesized that tris-chelate complexes of this small dithiocarbamate ligand may be good candidates for PVED measurements.

In our study of tris-chelate complexes of hinokitiol,[14] we have measured low barriers for the inversion of stereochemistry even for $Ir(hino)_3$, complex. This is important in the context of determining PVED since this means the molecules are not inert towards racemization. Along the

same vein, it is necessary to determine rotational barriers for the inversion of stereochemistry of tris-chelate complexes of H,Hdtc.

We present here several new d^6 complexes of H,Hdtc: tris-chelate complexes of cobalt and rhodium as well as two Ru(II) complexes. X-ray diffraction data is provided for all the complexes as well as a comparison with other dithiocarbamate complexes. Insight into the fluxionality of the rhodium tris-chelate complexes as well as the mechanisms of inversion of stereochemistry can be obtained by comparison parameters with other known rhodium tris-dithiocarbamate complexes as well as DFT calculations.

4.4 Results and Discussion

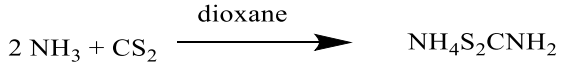

1

The ammonium salt of the parent dithiocarbamate, $NH_4S_2CNH_2$ **1** was prepared by treating carbon disulfide and ammonia in dioxane. IR and DSC spectra as well as PXRD patterns match those previously described.[35,36] Previous syntheses of the ligand reported the formation of either a yellow or off-white product, presumably due to the presence of NH_4HCS_2O, when the reaction is carried out in ethanol and left to stand for several days.[36] Our synthesis bypasses this issue by employing dioxane as a solvent which leads directly to colorless crystalline products rapidly and quantitatively. The ^{1}H-NMR spectrum of the ligand was obtained owing to little H/D exchange in deuterated DMSO. It is dominated by two singlets: the cation at 7.17 ppm and the dithiocarbamate peak at 7.40 ppm. Rapid H/D exchange of both sets of protons occurs in MeOD-d_4 as demonstrated by the absence of peaks in that solvent. A downfield singlet in the ^{13}C NMR at 218.29 ppm is observed. While this is expected for a dithiocarbamate, it is at slightly lower fields than other dithiocarbamate ligands, generally found around 205-215 ppm.[37] The vibrational spectrum has two sets of ν(N-H) for the cation and anion, and the anion modes reflect strong coupling of the N-H deformation modes with the carbon-nitrogen and carbon-sulfur stretching modes.

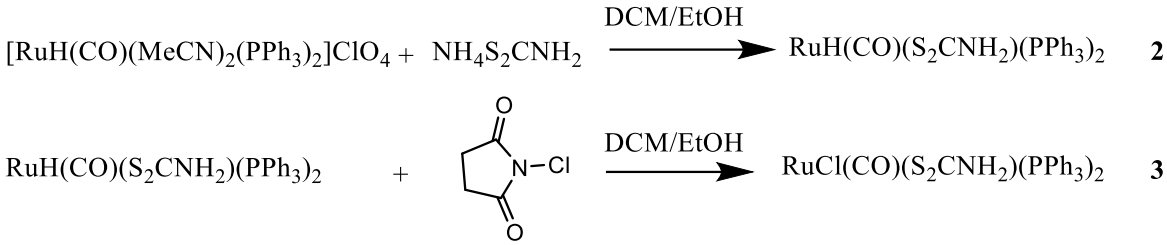

As with most dithiocarbamates, **1** forms a range of metal complexes with good stability, solubility, and spectroscopy. An initial foray into the coordination chemistry with **1** is its coordination in two organometallic ruthenium(II) carbonyl phosphine complexes, **2** and **3**. Substitution of the two labile acetonitrile ligands in $[RuH(NCMe)_2(CO)(PPh_3)_2]ClO_4$ returns the neutral pale yellow complex $RuH(CO)(S_2CNH_2)(PPh_3)_2$, **2**, as a single isomer with mutually trans triphenylphosphine ligands and bidentate dithiocarbamate ligands. This is confirmed by X-ray diffraction of a bisethanol solvate of **2**. Although the two nitrogen bound protons are inequivalent in **2**, only a single exchange broadened peak is observed in the ^1H NMR spectrum. Upon coordination to Ru(II) a noticeable downfield shift of the nitrogen bound protons of 0.6 ppm is observed. This peak undergoes rapid H/D exchange in solution with CD_3OD and gives a ^1H NMR spectrum with the triphenylphosphine and hydride peaks intact and unaltered. In addition to the Bronsted acidity of the N-H protons, in **2**, the metal bound hydride is readily chlorinated at ambient temperature with N-chlorosuccinimide to give the corresponding chloro complex, 3, in modest yield. X-ray diffraction of crystals of **3** indicate that the two triphenylphosphines have rearranged to a cis geometry, each trans to a sulfur, and with trans chloride and carbonyl, Figure 4.3. The ^{31}P-NMR spectrum in CD_2Cl_2 reveals only one peak at 36.80ppm indicates the cis-geometry is retained in solution and no cis-trans isomerization is present. Cis-triphenylphosphine complexes of Ru(II) have also been observed with acac,[38] bisbenzoate,[49] and bissemicarbazole.[40] These cis-triphenylphosphines were obtained during the substitution of $RuCl_2(PPh_3)_2$ rather than by chlorination of a hydride ligand. In our study of tropolonate complexes of Ru(II) and Os(II) derivatives,[41] chlorination of the hydride of trans-$RuH(CO)(trop)(PPh_3)_2$ did not change the geometry of the triphenylphosphines. The remarkable difference in Ru-S bond lengths between the complexes serves a good illustration of the trans influence of the CO, H^- and PPh_3 ligands. The significantly longer Ru-S1 bond length in **4** suggests it is predominantly trans to the hydride, but this increase is not reflected in the C-S

separation. The difference in Ru-S bond length of 0.027(1)Å in **2** and 0.020(1)Å in **3** suggests a symmetric bidentate binding mode A in Figure 4.1, as opposed to an asymmetric binding mode B. Previously described complexes with binding mode B report very high ΔM-S distances from 0.3 to 0.6Å. [42,43]

binding mode A binding mode B

Figure 4.1: possible bidentate binding modes of $[S_2CNH_2]^-$

Disorder in the CO position (70/30) is present in **2** while the Cl/CO positions were unambiguously determined in 3. The hydride in **2** is characterized by a triplet at -11.47 ppm ($^2J_{HP}$=20.5 Hz) in the ^{1}H-NMR spectrum. The position of the hydride could not be determined by X-ray diffraction, and it is omitted in the ORTEP diagram of **2** (Figure 4.2A). Chlorination of the hydride ligand and rearrangement of the triphenylphosphine ligands has some effect on the structural features of the dithiocarbamate ligand: while the S-C-S angles do not change, the C-N bond and one C-S bond in **2** are longer than the bond lengths in **3**. This change in bond length is not as clear in the IR spectrum where changes of less than 10 cm^{-1} are observed for the dithiocarbamate bands. In addition to these bands, CO stretches at 1926 cm^{-1} (**2**) and 1940 cm^{-1} (**3**) are observed. A unique ruthenium-hydride stretching band is not observed.

$RuH(CO)(S_2CNH_2)(PPh_3)_2$ 2		$RuCl(CO)(S_2CNH_2)(PPh_3)_2$ (3)		$NH_4S_2CNH_2$ (1)	
Bond	Length (Å)	Bond	Length (Å)	Bond	Length (Å)
Ru-S1	2.4950(10)	Ru-S1	2.4390(15)	N/A	
Ru-S2	2.5228(10)	Ru-S2	2.4195(15)		
C2-S1	1.701(4)	C1-S1	1.699(6)	C-S	1.723(2)
C2-S2	1.714(4)	C1-S2	1.698(6)		1.726(3)
C2-N1	1.312(7)	C1-N1	1.326(7)	C-N	1.331(2)
Ru-C1A	1.858(6)	Ru-C2	1.979(9)	N/A	
Ru-C1	1.872(13)				
Ru-P	2.3673(10)	Ru-P1	2.3985(15)	N/A	
	2.3513(9)	Ru-P2	2.3914(15)		
Angle	°	Angle	°	Angle	°
S1-Ru-S2	69.79(3)	S1-Ru-S2	71.82(5)	N/A	
S1-C2-S1	114.4(2)	S1-C2-S1	114.0(3)	S-C-S	121.9(1)
P1-Ru-P2	171.21(3)	P1-Ru-P2	106.84(5)	N/A	

Table 4.1: Selected bond lengths(Å) and bond angles(°) of $RuH(CO)(S_2CNH_2)(PPh_3)_2$, $RuCl(CO)(S_2CNH_2)(PPh_3)_2$ and $NH_4S_2CNH_2$[36]

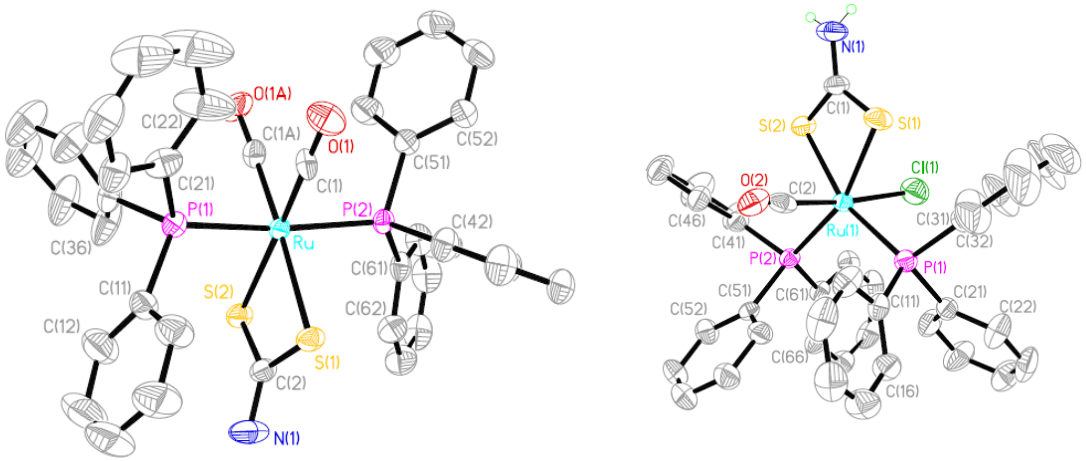

A) B)

Figure 4.2: ORTEP diagram of A) $RuH(CO)(S_2CNH_2)(PPh_3)_2$ (2) and B) $RuCl(CO)(S_2CNH_2)(PPh_3)_2$ (3) with 40% thermal ellipsoids. Solvates are omitted for clarity. Both disordered CO positions in 2 are shown.

Complexes **2** and **3** have high thermal stability: the DSC reveals high decomposition temperatures above 200°C for both complexes. They are stable in the solid state and do not show

signs of decomposition after being kept for several weeks at room temperature in the open. The combination of solubility, with the steric protection by the triphenylphosphine ligands, good thermal stability, and excellent spectroscopic handles in terms of the NMR and IR bands provides insight into the electronic character of the donor properties of **1** to d^6 transition metals. Comparison of the ν(CO) stretches of several $RuH(CO)L(PPh_3)_2$ complexes with varying donor atoms (Table 4.2) reveal the ν(CO) band of **3** on the lower end at 1926.5 cm^{-1}. This suggests increased electron density being donated to the metal by the dithiocarbamate ligand resulting in stronger π-backbonding and weakening of the CO bond compared to the other complexes.

L	ν(CO) (cm^{-1})	Reference
$S_2CNH_2^-$	1926.5	This work
HCO_2^-	1927.9	45
$H_3CCO_2^-$	1928.3	46
4-isopropyltropolone	1931.0	41
$S_2PF_2^-$	1936.5	
N-methylnitrosoguanidine	1937.0	47
$(EtO)PS_2^-$	1942.7	44

Table 4.2: Comparison of ν(CO) stretches in various $RuH(CO)L(PPh_3)_2$ complexes

$$CoCl_2.6H_2O + 3\ NH_4S_2CNH_2 \xrightarrow[r.t,\ 30min]{water} Co(S_2CNH_2)_3 + 3\ NH_4Cl \qquad \mathbf{4}$$

$$RhCl_3.H_2O + 3\ NH_4S_2CNH_2 \xrightarrow[60^0C,\ 3h]{water} Rh(S_2CNH_2)_3 + 3NH_4Cl \qquad \mathbf{5}$$

The tris-chelate complexes $Co(S_2CNH_2)_3$ and $Rh(S_2CNH_2)_3$ were synthesized by substitution of chloride ligands in $CoCl_2{\cdot}6H_2O$ and $RhCl_3{\cdot}H_2O$ with an excess of $NH_4S_2CNH_2$: $CoCl_2{\cdot}6H_2O$ was stirred for 30 min in water and $RhCl_3{\cdot}H_2O$ was refluxed for 3 hours. Both products subsequently precipitated out of solution. ESI-MS was used to confirm the identity of the products. The dark green compound **4** is characterized by d-d transitions at 486 nm and 661 nm while a charge transfer band at 446 nm is present for compound **5**. The DSC of the complexes reveal high decomposition temperatures, proving that the complexes have good thermal stability.

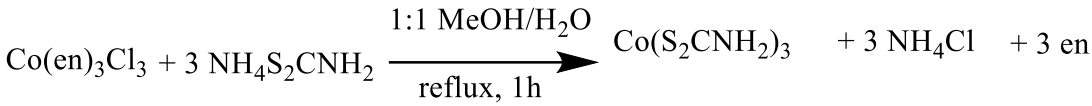

4

An alternative synthesis of **4** involves the substitution of the ethylenediamine ligands in $Co(en)_3Cl_3$ by heating for an hour in a 1:1 mixture of MeOH:H_2O at reflux. Comparison of the UV-Vis and IR spectra (Figure 4.3) of the green product that of **4** confirmed the substitution of all three ethylenediamine ligands.

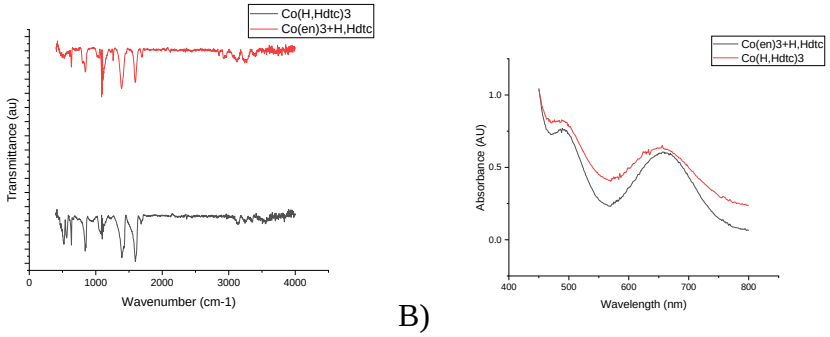

A) B)

Figure 4.3: Comparison of A) the IR spectrum and B) the UV-Vis spectrum of $Co(H_2dtc)_3$ and the product of the substitution reaction of $[Co(en)_3]Cl_3$ with $NH_4S_2CNH_2$. The values of transmittance in 3A were omitted due to scaling of the spectra for clarity.

In the absence of light however, the reaction did not occur. Similar light-induced substitution reactions have been observed by Kida *et al.* with the substitution of tris-ethylenediamine cobalt(III) with bis-(2-hydroxyethyl)-dithiocarbamate:[48] a mechanism with the formation of a dithiocarbamate radical was proposed.

Several attempts were made to synthesize the iridium complex of H,Hdtc using both $IrCl_3$ and K_2IrCl_6 as starting materials. Under several different experimental conditions, some of which are presented in Table S4.6, insoluble products were obtained. A strong band around 2000cm^{-1} was present in the IR spectra of some of the products formed in addition to the typical amino dithiocarbamate bands. Such bands may indicate the presence of a thiocyanide ligand as a decomposition product of the ligand or from a side reaction.

A structure of $Co(S_2CNH_2)_3$ was obtained with an improvement over the structure presented by Raston and White.[34] The final R_1 was improved to 2.5% from 5% and the bond lengths are more

accurate to one decimal place in the redetermined structure. Upon coordination to Co(III) and Rh(III), the ligands form tris-chelate complexes which exhibit strong distortion from ideal D_3 octahedral geometry: this can be seen in the very small bite angles and trans S-M-S angles. For the former, angles between 76.33(4)° and 76.61(4)° for **4** and between 73.59(5)° and 73.89(5)° deviate significantly from the ideal value of 90°. For the latter, trans angles of 166.84(5)°, 166.89(5)° and 168.12(5)° for **4** and 166.84(5)°, 166.89(5)° and 168.12(5)° for **5** are observed. The geometry of the complexes is better described as close to a D_{3h} trigonal prismatic geometry.[49] Other parameters relating to type of distortion and their relation to fluxionality will be discussed in more detail later. Another unusual type of distortion is observed for these complexes which has not been described by Raston and White in their structure of $Co(S_2CNH_2)_3$.

Bonds	Å	Difference	Bonds	Å	Difference
5		Experimental	**4**		
Rh-S1	2.3605(15)	0.0240(22)	Co-S1	2.2673 (12)	0.0126(17)
Rh-S2	2.3365(15)		Co-S2	2.2799(12)	
Rh-S3	2.3387(16)	0.010(21)	Co-S3	2.2750(12)	0.0087(16)
Rh-S4	2.3490(15)		Co-S4	2.2837(11)	
Rh-S5	2.3606(14)	0.0060(18)	Co-S5	2.2563(13)	0.0374(17)
Rh-S6	2.3546(15)		Co-S6	2.2937(11)	
5		Theoretical	**4**		
Rh-S	2.41290		Co-S	2.32305	0.00003
	2.41290			2.32302	
	2.41289			2.32277	0.00019
	2.41289			2.32296	
	2.41290			2.32304	0.00031
	2.41290			2.32272	

Table 4.3: Comparison of M-S bond lengths(Å) of 4 and 5 with calculated values(B3LYP/aug-cc-pvtz) on the bottom for each ligand. The pseudopotential methods used for the rhodium calculations are described in the experimental section.

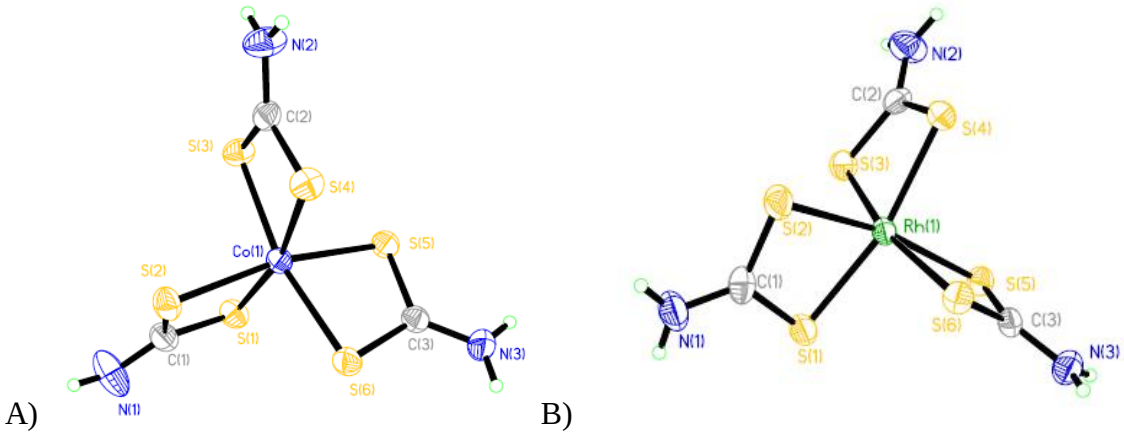

Figure 4.4: A) ORTEP diagram of A) newly determined structure of $Co(S_2CNH_2)_3$ and B) $Rh(S_2CNH_2)_3$ with 40% thermal elliposoids

An analysis of the metal-sulfur bond lengths reveals a distinct drop in symmetry characterized by each dithiocarbamate having a long M-S and a short M-S bond length (Table 4.3). The difference in bond lengths is accentuated in one of the ligands for both complexes. This results in one of the triangle faces having a smaller area than the other one and the complexes lose D_3 symmetry and are closer to C_3 symmetry. The differences in the bond lengths are more pronounced in the cobalt complex. The distorted nature of the octahedral complexes is present in their optimized ground state geometries calculated using B3LYP with aug-cc-pvtz basis sets and a relativistic pseudopotential used for the rhodium complex. Significantly, bite angles of 76.62° and trans angles of 167.50° for the cobalt complex and 74.21° and 167.21° for the rhodium complex were found. These geometric and angular values are in very good agreement with the experimentally determined values. For the cobalt complex the chelate asymmetry found in the experimental structure, by the difference in the metal-sulfur bond lengths, is also represented in the optimized ground state structures albeit with small differences in the case of cobalt structure and by nonsignificant differences for the rhodium complex. Part of the difference in these trends is due to the N---H---S hydrogen bonds which accompany the crystal packing in the experimental results. As shown in Figure 4.5C the close intramolecular hydrogen bonds most likely contribute to the chelate asymmetry. But as seen for the calculated structure for the cobalt complex this asymmetry persists in the gas phase isolated molecule. Hydrogen bonding patterns in the packed

structure between one sulfur in each dithiocarbamate complex to amine protons from adjacent complexes accentuates the inherent M-S bond length differences.

A) 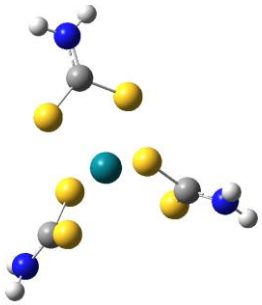 B) 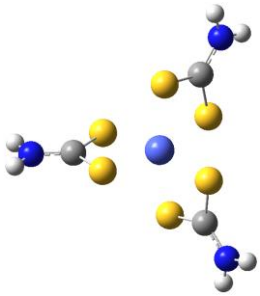

C) 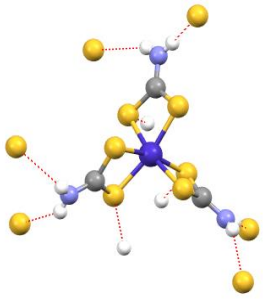

Figure 4.5: A) ground state geometry of $Rh(S_2CNH_2)_3$ using B3LYP cc-pvtz basis sets B) ground state geometry of $Co(S_2CNH_2)_3$ using B3LYP cc-pvtz basis sets and C) hydrogen bonding pattern in the structure of $Co(S_2CNH_2)_3$

The structural features of the dithiocarbamate ligands are not significantly altered between the different complexes: comparison of the bond lengths and angles related to the ligand are not statistically significant within the esd's (Figure 4.6). This is further suppported by very small differences in the IR frequencies, within 6-12 cm^{-1}. The structural features are also very similar to those observed for the ruthenium complex. We can conclude that while coordination of the dithiocarbamate ligands results in severe distortion of the MS_6 core, this is not amplified or represented in the coordinated ligand.

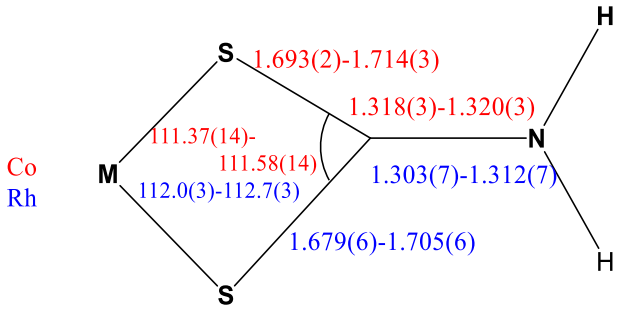

Figure 4.6: Comparison of bond lengths and angles relating to the dithiocarbamate ligand in $Co(S_2CNH_2)_3$ and $Rh(S_2CNH_2)_3$

A search in the Cambridge Crystallographic Database only revealed the structure of two tris-dithiocarbamate complexes of rhodium with diethyldithiocarbamate and dimorpholinedithiocarbamate.[50,51] In order to compare the structural features of $Rh(S_2CNH_2)_3$ with other dithiocarbamate complexes of rhodium, we have also structurally characterized $Rh(S_2CNMe_2)_3$ and $Rh(S_2CNBz_2)_3$. The structure of $Rh(S_2CNEt_2)_3$ was previously determined by Raston and White.[50]

A full comparison of the bond lengths and angles of the four rhodium complexes is presented in Table S4.10. Using all the data collected we can generalize our observations: the Rh-S_6 core of the complexes are characterized by short Rh-S bond lengths and small S-Rh-S bite angles as well as S-Rh-S trans angles: strong distortion to trigonal prismatic geometry is present in all of the complexes. An important observation is that the nature of the substituent groups on the dithiocarbamate ligands do not significantly alter the geometry of the nitrogen or the Rh-S bond lengths. The basicity of the amine does not seem to affect the donor capabilities of the sulfur atoms based on structural data alone although it has been reported that larger contribution from the thioureide resonance structure, with formal positive charge on the nitrogen, results in weaker field ligands.[15] A comparison of the UV-Vis data of $Co(S_2CNH_2)_3$, 662cm^{-1}, and $Co(S_2CNBz_2)_3$, 651cm^{-1}, reveals a small decrease in the energy of the d-d $^1A_1$->$^1T_1$ band. While this is consistent with the more basic tertiary amine dithiocarbamate being a stronger field ligand, the very small differences in energy confirm the observation that the nature of the amine substituent does not

strongly alter the donor capabilities of the ligand. Given the invariance of the charge transfer bands in the rhodium complexes there is little dependence of their transitions upon NR_2.

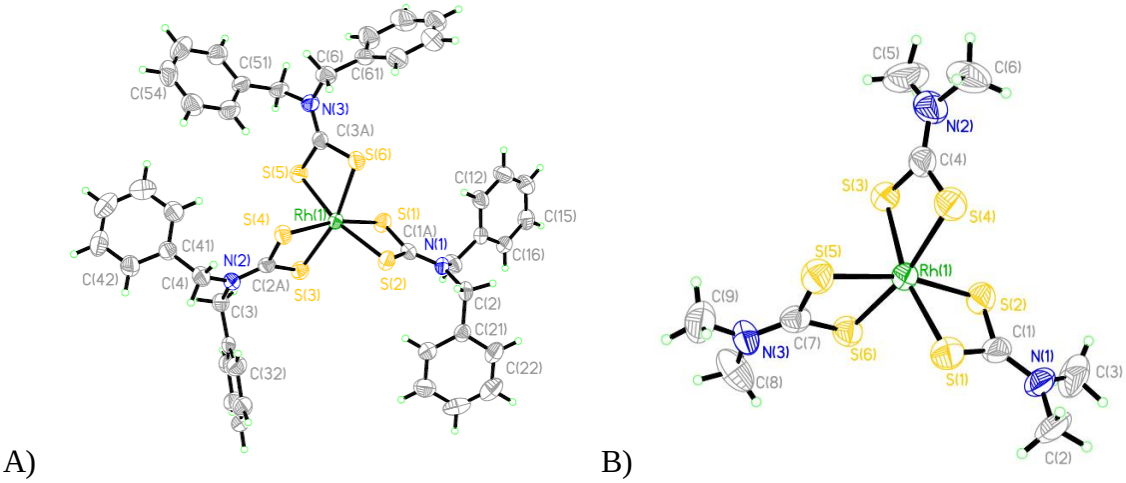

Figure 4.7: ORTEP diagrams of A) $Rh(S_2CNBz_2)_3$ and B) $Rh(S_2CNMe_2)_3$ with 40% thermal elliposoids. Solvated water in B is omitted for clarity

The complexes presented here are tris-chelate complexes with symmetric ligands which are synthesized as a racemic mixture of the Λ and Δ enantiomers. Inversion of stereochemistry between the two enantiomers may occur. The ^{1}H-NMR spectra in DMSO-d_6 of **4** and **5** both show a singlet peak for amine protons at high chemical shifts: 9.29 ppm for **4** and 9.36 ppm for **5**. Because the two hydrogens on the amine are equivalent, NMR-techniques do not allow us to determine the barriers for the inversion of stereochemistry of $M(S_2CNH_2)_3$. However, the diastereotopic benzylic and methylene protons of $Rh(Bz_2dtc)_3$ and $Rh(Et_2dtc)_3$ can be used to determine the activation barriers for racemization as in either enantiomer they are inequivalent but collapse into a single time averaged resonance upon heating to achieve racemization.

In a chiral environment such as the one presented here, the diastereotopic benzylic protons form a J_{AB} coupling pattern. If the complexes were highly fluxional, this pattern would coalesce into a singlet peak. Pignolet[52] presented NMR data obtained at 100 MHz in $CDCl_3$ of $Co(Bz_2dtc)_3$ and $Rh(Bz_2dtc)_3$ and observed a J_{AB} coupling pattern at 5.14 ppm and coupling constant of 15.3 Hz for both complexes. Additionally, it was reported that the rhodium complex was stereochemically rigid up to 200 °C in deuterated nitrobenzene.

The fluxional behaviour of the cobalt, rhodium, and iridium complexes of benzyldithiocarbamate was investigated first in deuterated toluene at low and high temperature with a field of 9.39798 Tesla corresponding to a 400 MHz spectrometer. The values of the J coupling constants and differences in chemical shift at 25 ˚C and 95 ˚C are presented in Table 4.4.

Complex	NMR field	Solvent	J_{AB} coupling constant (25˚C)	Chemical shift difference (25˚C)	J_{AB} coupling constant (95˚C)	Chemical shift difference (95˚C)	Ref
$Co(Bz_2dtc)_3$	100 MHz	$CDCl_3$	15.3 Hz	N/A	N/A	N/A	52
$Co(Bz_2dtc)_3$	400 MHz	Toluene-d_8	15.3 Hz	0.1611 ppm	14.9 Hz	0.1424 ppm	This study
$Rh(Bz_2dtc)_3$	100 MHz	$CDCl_3$	15.3 Hz	N/A	N/A	N/A	51
$Rh(Bz_2dtc)_3$	400 MHz	Toluene-d_8	15.2 Hz	0.1581 ppm	15.0 Hz	0.1480 ppm	This study
$Ir(Bz_2dtc)_3$	400 MHz	Toluene-d_8	15.2 Hz	0.1334 ppm	15.0 Hz	0.1208 ppm	This study

Table 4.4: J_{AB} coupling constants of benzylic protons of $Co(Bzdtc)_3$, $Rh(Bzdtc)_3$, and $Ir(Bzdtc)_3$ at 25 ^{0}C and 95 ^{0}C at 400 MHz

At room temperature and higher temperature, a J_{AB} coupling pattern is present consistent with the diastereotopic nature of the protons. At higher temperature, no significant change in the coupling constants or the chemical shifts are noticeable for all three complexes. At first glance, our results confirm those made by Pignolet.

This is remarkably different than the behaviour observed for the complexes in DMSO-d_6. In the case of cobalt, at room temperature, the AB coupling pattern merges into a broad singlet which indicates that the coalescence temperature has already been reached. Unfortunately, due to the high melting point of DMSO, it is not possible to lower the temperature under 25 ˚C. Using 25 ˚C as the coalescence temperature and the chemical shift difference found in the rhodium complex, we find an approximate upper limit to the barrier of activation of 15.4 kcal/mol for the cobalt complex.

The observed behaviour in DMSO is not limited to cobalt. The rhodium and iridium complexes show the expected AB coupling pattern in d_6-DMSO at room temperature. The pattern merges to a singlet peak at around 45˚C for the rhodium complex and 55˚C for the iridium complex (Figure 4.8). The presence of only one quartet at room temperature as well as dependence of the

coalescence temperature on the type of metal are evidence that the phenomenon observed is inversion of stereochemistry and not due to restricted C-N bond rotation. The similar C-N bands in the IR spectra of the complexes, with differences of less than 5cm^{-1}, agree with this conclusion: rotation around bonds of very similar strengths should give very close coalescence temperatures and activation barriers rather than the observed temperature range of at least 40°C.

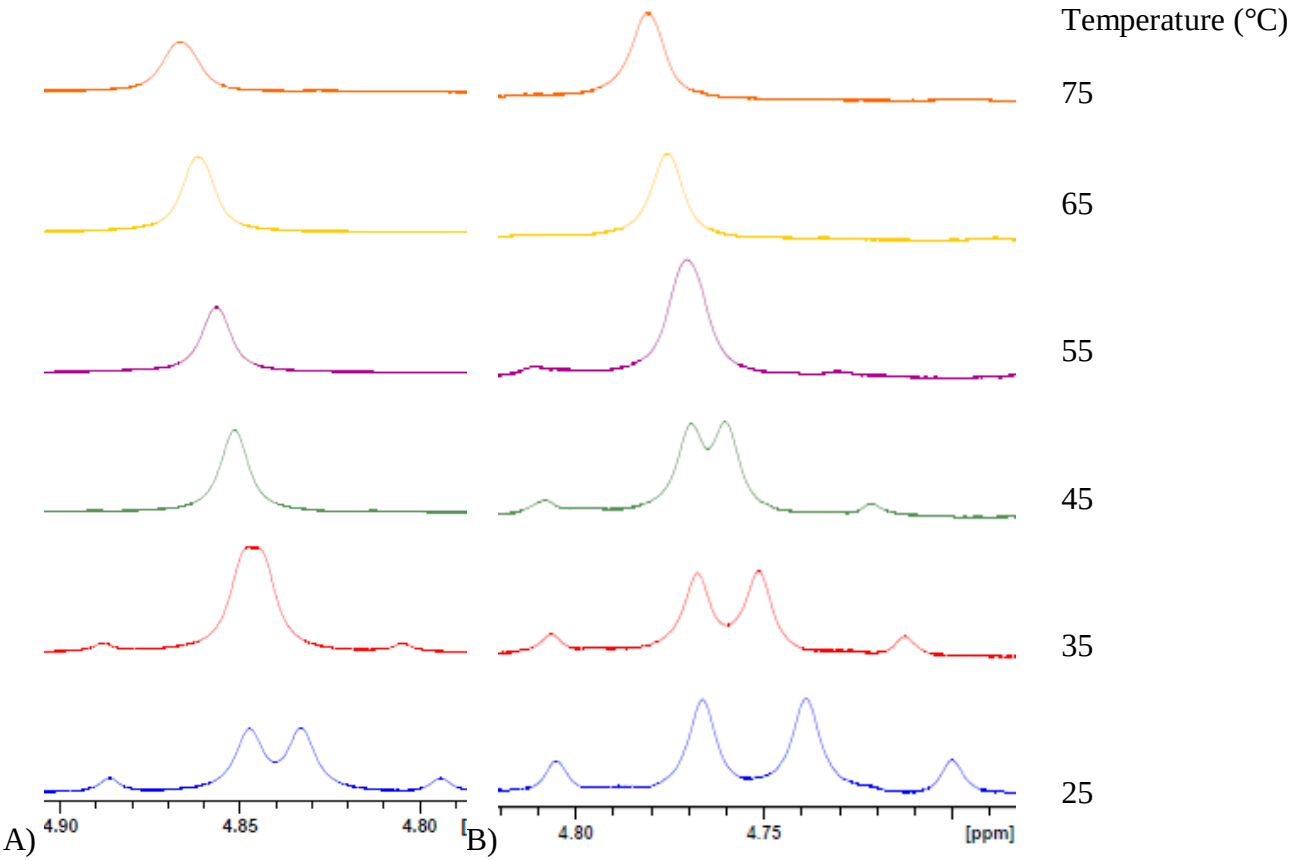

Figure 4.8: ^{1}H-VT NMR of the benzylic proton of A) Rh(Bz$_2$dtc)$_3$ and B) Ir(Bz$_2$dtc)$_3$ at 800 MHz in DMSO-d$_6$

The change in chemical shift of the AB coupling pattern was plotted against temperature: an accurate determination of the coalescence temperature was obtained from the linear dependence, Figure 4.9. We have obtained data using an 800 MHz spectrometer in order to gain better resolution even at temperatures close to the coalescence temperature. These were determined to be 324 K for rhodium and 335 K for iridium. The resulting barriers are respectively 16.4±0.3 kcal/mol and 17.1±0.3 kcal/mol. The activation barrier for the inversion of stereochemistry of the

complexes increases going down the column: this is the expected trend which we have also observed in our study of tris-chelate complexes of substituted tropolones.[14]

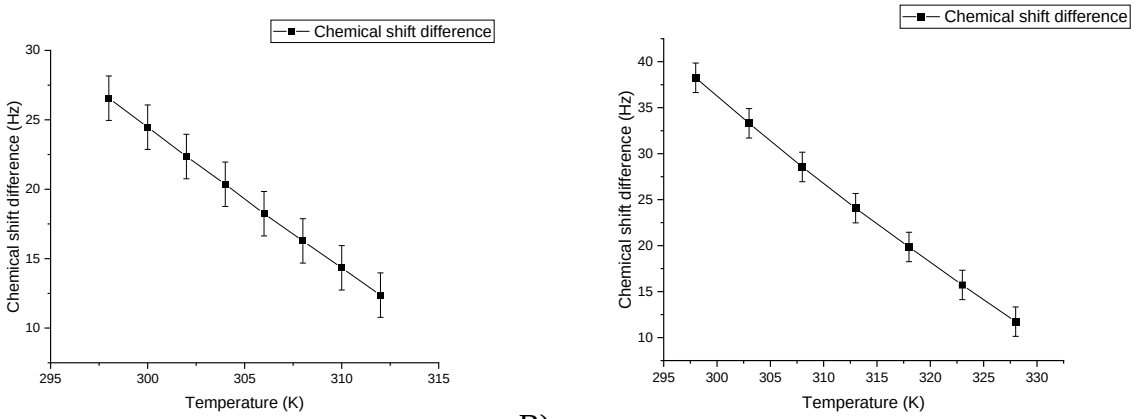

Figure 4.9: Plot of the linear dependence of the difference in chemical shift of the AB pattern vs. temperature of A) Rh(Bz$_2$dtc)$_3$ and B) Ir(Bz$_2$dtc)$_3$

To exclude DMSO solvation reactions as the origin of these differences, the variable temperature behaviour of the diethyl derivative of rhodium was investigated in DMSO and benzene.

In the case of Rh(Et$_2$dtc)$_3$, the diastereotopic nature of the methylene protons results in an ABX$_3$ pattern. At 10 ˚C using an 800 MHz spectrometer in deuterated benzene, the ABX$_3$ patten is well resolved and coupling constants J_{AB}=14.4 Hz and J_{AX}=7.1 Hz can be obtained. In C_6D_6 at 50 ˚C, the pattern merges into a quartet indicating at that temperature the hydrogens are equivalent and coalescence temperature has been reached. Unlike Rh(Bz$_2$dtc)$_3$, the diethyl derivative is fluxional even in non-polar solvents such as C_6D_6. By increasing the temperature in increments of 5 ˚C, a coalescence temperature of 45 ˚C is observed as seen in Figure 4.10. This corresponds to an activation barrier of 16.7±0.3kcal/mol for the inversion of stereochemistry of Rh(Et,Etdtc)$_3$.

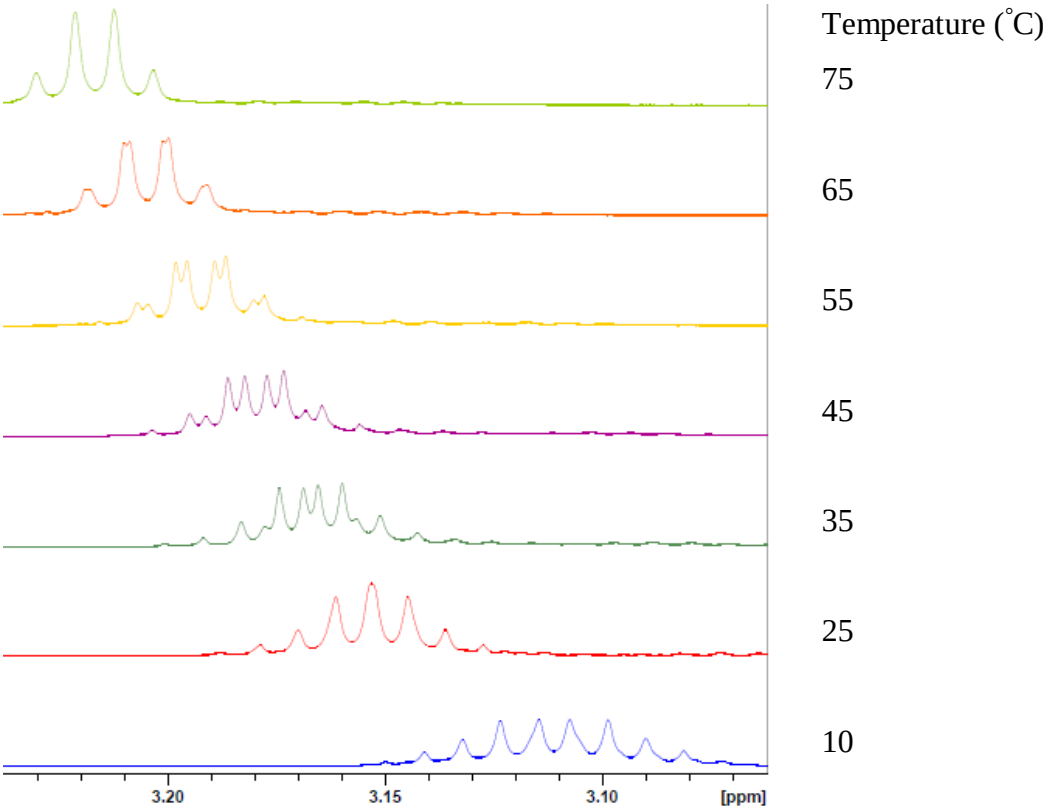

Figure 4.10: Variable temperature ^{1}H-NMR of the methylene protons of $Rh(Et_2dtc)_3$ in C_6D_6 at 800MHz

The dynamic NMR behaviour of $Rh(Et_2dtc)_3$ in DMSO is similar to what is observed in benzene with similar activation barriers (Table 4.5). We can conclude that the rigidity of this complex observed in our previous experiments as well as by Pignolet may be due to the nature of the solvent, but not solvolytic reactions with the solvent. Interactions, such as π-π stacking, of the benzyl groups of $M(Bz_2dtc)_3$ with solvents such as toluene, benzene or nitrobenzene lock the benzyldithiocarbamate complexes into their configurations explaining the absence of dynamic NMR behaviour in these solvents.

	Solvent	Coalescence temperature	Δν (ppm) at 25°C	Activation barrier
$Co(Bz_2dtc)_3$	Toluene	Rigid up to 373 K	0.118	
	DMSO	≤ 298 K	0	< 15.4 kcal/mol
$Rh(Bz_2dtc)_3$	Toluene	Rigid up to 373 K	0.102	
	DMSO	324 K	0.036	16.4±0.3 kcal/mol
$Ir(Bz_2dtc)_3$	Toluene	Rigid up to 373 K	0.0872	
	DMSO	335 K	0.053	17.1±0.3 kcal/mol
$Rh(Et_2dtc)_3$	Benzene	318 K	0.029	16.7±0.3 kcal/mol
	DMSO	323 K	0.032	16.7±0.3 kcal/mol

Table 4.5: Comparison of activation coalescence temperatures and activation barriers of several dithiocarbamate complexes of Co, Rh and Ir in varying solvents obtained at 800MHz

To understand the surprisingly low activation barriers for the complexes, Table 4.5, both ground state destabilization and the electronic structure of the transition states need to be considered. In the ground state the observed distortions can be thought of as an entactic state like destabilization due to the structural distortions.[53] Prior theoretical studies of this type of racemization have dissected the relationships between geometrical distortion, activation barriers and mechanisms of inversion to reveal that tris-chelate complexes distorted towards D_{3h} trigonal prismatic geometry will invert stereochemistry via a trigonal twist mechanism with low activation barriers.[54,55] On the other hand, complexes closer to D_3 symmetry will invert stereochemistry via a bond-breaking mechanism. Several parameters can account for the distortion of the octahedral symmetry: the ligand bite angle α, twist angle φ, pitch angle ψ and compression ratio s/h where s represents the triangle edge distance and h represents the distances between the triangles in the star of David representation of the complexes. The compression ratio is a measure of the compressed or elongated nature of the octahedron. The values for these parameters in ideal octahedral D_3 symmetry are respectively 90°, 60°, 35.3° and 1.22. Higher differences from these ideal values indicate stronger distortion towards D_{3h} symmetry.

The values of the parameters are calculated using equations 1-4 where θ is the polar angle[54]:

$$\cos\left(\frac{\alpha}{2}\right) = \sin(\theta)\cos\left(\frac{\varphi}{2}\right) \quad (1)$$

$$\sin\left(\frac{\alpha}{2}\right) = \frac{\cos(\theta)}{\cos(\psi)} \quad (2)$$

$$s = \sqrt{3}rsin(\theta) \quad (3)$$

$$\cos(\psi) = \frac{h}{d} \quad (4)$$

Geometrical descriptions of the twist, pitch and polar angles are given in Figure S4.1.

These distortion parameters measured for $Co(H_2dtc)_3$, $Rh(Me_2dtc)_3$, $Rh(Bz_2dtc)_3$, and $Rh(Et_2dtc)_3$ along with literature values for $Co(Bz_2dtc)_3$[56] are collected in Table 4.6. Lower values of the twist and pitch angle for the cobalt complex indicate that the distortion is more pronounced for the cobalt complex. Between the rhodium complexes, while the values are slightly higher for the ethyl complex, they do not differ significantly. Overall, the values for the parameters confirm the strong ground state distortion of the complexes. This contributes to the observed low activation barriers of 16.6 kcal/mol and 16.4 kcal/mol. Since VT-NMR analysis of the S_2CNH_2 complexes is impossible due to the hydrogens being equivalent, it cannot be used to calculate the activation barriers of complexes **4** and **5**. By comparing the parameters relating to the geometry distortion with those of the benzyl and ethyl derivatives, an estimation of these barriers can be made. The data collected and presented in Table 4.6 are good evidence of the distorted geometry of complexes **4** and **5**. Very little difference is observed between these complexes and the alkyldithiocarbamate complexes: the identity of the dithiocarbamate does not have a strong effect on the distortion. This confirms the observation made previously that the bond lengths and angles of the different angles are not significantly altered by the nature of the ligand. The parameters calculated for **5** are found to be between those of $Rh(S_2CNEt_2)_3$ and $Rh(S_2CNBz_2)_3$: we can estimate the activation barrier of 5 to be in the range 16.4-16.7 kcal/mol.

	Bite angle α(°)	Twist angle φ(°)	Pitch angle ψ(°)	Compression ratio
Ideal D_3	90	60	35.3	1.22
$Co(S_2CNH_2)_3$	76.46	44	31.8	1.74
$Co(S_2CNBz_2)_3$[55]	76.41	42.8	30.7	1.7
$Rh(S_2CNH_2)_3$	73.7	45.3	33.9	1.5
$Rh(S_2CNMe_2)_3$	73.7	45	33.6	1.5
$Rh(S_2CNEt_2)_3$	73.5	48	35	1.5
$Rh(S_2CNBz_2)_3$	73.8	44.1	32.7	1.48

Table 4.6: Comparison of structural parameters related to distortion of the octahedral geometry of tris-dithiocarbamate complexes

The mechanism of inversion of stereochemistry can either occur via non-dissociative pathways, with the formation of a trigonal prismatic intermediate, or via a dissociative mechanism involving M-S bond scission. The former mechanism is generally characterized by lower values for the activation barriers.[53] The low values found for the complexes are consistent with a non-dissociative mechanism. Two types of non-dissociative mechanisms can occur: the Bailar twist or Ray Dutt mechanism. The Bailar twist is a trigonal twist around the C_3 axis resulting in a trigonal prismatic intermediate. The Ray-Dutt mechanism is a rhombic twist with C_2v intermediate. The type of mechanism can be determined from another parameter, the normalized bite, the ratio of the distance between donor ligands and the metal-ligand bond length. The intramolecular Bailar twist mechanism is preferred when the normalized bite is less than 1.5.[57] Using the average S-S and M-S distance we found a normalized bite of 1.2 for $Co(H_2dtc)_3$, $Rh(H_2dtc)_3$, $Rh(Bz_2dtc)_3$ and $Rh(Et_2dtc)_3$. From this data, it is concluded that the inversion of stereochemistry occurs via a Bailar twist mechanism for all the complexes.

The transition state can also be stabilized by the configuration interaction with higher lying excited states. Indeed, ligand field theory suggests a change in spin state to a quintet state in the inversion of stereochemistry of tris-chelate complexes.[58] Jakubikova demonstrated this computationally for the Fe(II) tris-chelate complex $[Fe(bipy)_3]^{+2}$.[59] Although this complex and those described here are d^6 systems with singlet diamagnetic ground states, for $[Fe(bipy)_3]^{+2}$ the calculated lowest energy ground states is a high spin quintet, and the lowest transition states correspond to quintet configurations. We have used some of these same functionals and methods to examine the distortions and ground states in **4** and **5** and transition states for their racemization. The results using both B3LYP and TPSSh functionals with cc-pvdz and cc-pvtz basis sets are presented in Table 4.7 for both $Co(S_2CNH_2)_3$ and $Rh(S_2CNH_2)_3$: clearly in this system the singlet ground state found experimentally is predicted theoretically. The transition state located for the B3LYP/aug-cc-pvtz is 34.5 kcal/mol above the ground state, Figure S4.2. This is substantially higher that the value found by NMR for the dialkyldithiocarbamates but the ground state distortions have not been well modeled for these gas phase calculations. Significantly the IRC coordinate plot in Figure S4.2 shows substantial Co-S differences in the excited state which then relax to almost equivalent bond lengths. Future efforts will employ other

multiplicities to attempt to model the relative energies of the transition states better. While it is possible that this experimental/theoretical difference is due to amine substitution, the challenge is to rationalize how dialkylamine substituted dithiocarbamates would be that much more fluxional. We have not extended these methods to locate the transition states for racemization, but there may well be low energy intersystem crossing modes for these complexes which allow for changes in multiplicity during racemization. Certainly, the distorted ground state geometries found in the $M(S_2CNR_2)_3$ tris chelates are likely to be along the racemization pathway.

Complex	Method	Basis set	Multiplicity	Energy (Hartrees)	Energy difference (kcal/mol)
$Co(S_2CNH_2)_3$	B3LYP	cc-pvdz	Singlet	-4054.4676	0
			Quintet	-4054.436478	19.53
	TPSSh	cc-pvdz	Singlet	-4054.504475	
		cc-pvdz	Quintet	-4054.460727	27.45
		cc-pvtz	Singlet	-4054.688978	
		cc-pvtz	Quintet	-4054.639972	30.75
$Rh(S_2CNH_2)_3$	TPSSh	cc-pvdz	Singlet	-2781.887467	0
		cc-pvdz	Quintet	-2781.772965	71.85

Table 4.7: Comparison of energies of transition states with different spin states for $Co(S_2CNH_2)_3$ and $Rh(S_2CNH_2)_3$

In the same article by Jakubikova,[59] a modified version of the Bailar twist mechanism is proposed for an iron tris-bipyridine complex. This mechanism involves a C_{3h} intermediate rather than the usual D_{3h} intermediate in the classic mechanism. This particular mechanism has been called the dancing Bailar mechanism. The proposed C_{3h} intermediate had significantly lower energy than the D_{3h} one: this could explain the lower activation barriers we have determined for both the rhodium and iridium complexes compared to the tris-tropolone analogues which do not exhibit this particular distorted geometry.

Recently we have studied the inversion of stereochemistry of another tris-chelate complex of rhodium, $Rh(hino)_3$, where hino is a tropolone derivative, 4-isopropyltropolone or hinokitiol. A

barrier of 18.2 kcal/mol was determined for this complex. A comparison of the activation barriers and structural parameters are presented in Table 4.8. The most noticeable is the significant difference in bite angles being about 8° larger for the tropolone complex. The other parameters are rather similar with a smaller value for the pitch angle of the tropolone complex. Because of the large difference in bite angles, the dithiocarbamate complexes are significantly more distorted: the smaller value of the activation barriers confirms the theory presented by Pignolet suggesting that more distorted complex have lower activation barriers. We have also determined that inversion of stereochemistry of $Rh(hino)_3$ occurs via Bailar twist mechanism, based on similar ground state distortions and values of the activation barriers. Complexes with almost ideal octahedral geometry such as tris-chelate complexes with acetylacetonate derivatives will have much higher barriers and the inversion will involve bond breaking.[49] However, no such examples have been reported for rhodium or iridium.

	$Rh(hino)_3$	$Rh(H_2dtc)_3$	$Rh(Me_2dtc)_3$	$Rh(Et_2dtc)_3$	$Rh(Bz_2dtc)_3$
Bite angle (°)	81.7	73.7	73.7	73.54	73.8
Twist angle (°)	45	45.3	45	48	44.1
Pitch angle (°)	28.7	33.9	33.6	35	32.7
Compression ratio	1.08	1.5	1.5	1.5	1.48
Activation barrier (kcal/mol)	18.2			16.7	16.4

Table 4.8: Comparison of structural parameters related to distortion of the octahedral geometry of tris-dithiocarbamate and tris-tropolonate complexes of rhodium

For the hino system we concluded that the low barriers of inversion of the tris-tropolonate complexes constituted an important limitation in the use of these complexes as candidates to detect parity violation in molecules, where molecules inert towards racemization are preferred. Based on the comparison of the activation barriers, tris-chelate complexes of S_2CNH_2 show the same limitations as the hinokitiol complexes in that regard.

4.5 Conclusion

The d^6 complexes of the S_2CNH_2 ligand synthesized here present similar features to other dithiocarbamate complexes: they are brightly coloured, have good thermal stability and solubility

in organic solvents. The crystal structures of the tris-chelate complexes reveal a strong distortion in the geometry of the MS_6 core. We have determined the rotational barriers for two tris-chelate dithiocarbamate complexes of rhodium and one complex of iridium. To our knowledge this is the first example of such barriers being determined for dithiocarbamate complexes of rhodium and the first example for any tris-chelate complex of iridium. By comparing the structural features of $Rh(S_2CNH_2)_3$ to the other rhodium complexes, we conclude that it must have low activation barriers for inversion of stereochemistry. The unusual geometry of the complexes suggests a modified version of the Bailar twist as the mechanism with a C_{3h} intermediate.

This is important in terms of PVED measurements: complexes with high barriers are required as the complexes must be inert towards racemization. In addition, the low volatility of the complexes as well as difficulty to synthesize the iridium analogue, it appears that these complexes are not ideal candidates for PVED measurements. The example we present in this chapter highlights the difficulty of finding a suitable candidate molecule for such measurements and may explain why experimentally determining PVED in molecules has not been successful yet.

4.6 Experimental

The starting materials $CoCl_2.6H_2O$, $RhCl_3$ and $IrCl_3$ were purchased and used without purification. IR spectra were measured on Bomem MB3000 FTIR spectrometer as KBr pellets, and ^{1}H, ^{13}C NMR and ^{31P}P spectra were measured on a Bruker AVIIIHD 500 spectrometer at 22 °C at 500 MHz for ^{1}H, 131MHz for ^{13}C and 202MHz for ^{31}P. UV-Visible spectra were obtained using an HP 8453 diode array spectrophotometer. TGA-FTIR data was obtained using a Perkin Elmer TGA8000 equipped with a TL8000 gas cell.

4.6.1 Synthetic Procedures

Synthesis of S_2CNH_2 compounds

$NH_4S_2CNH_2$: A flow of NH_3 was passed through a solution of dioxane for 15 min. 2 mL of CS_2 was then added to the solution. After 5 min of stirring, a white precipitate formed and was subsequently filtered and washed with 3x10 mL of dioxane and 50 mL of anhydrous dry diethyl ether. The product was dried further under vacuum for two hours. $NH_4S_2CNH_2$ was obtained in 65% yield (1.03 g). DSC: decomposition T=100 °C ΔH=95.72 J/g IR: KBr(cm^{-1}): 3431m, 3302m, 1631m, 1596vs, 1409vs, 1332s, 842s UV-Vis (H_2O): 342 nm (1.6) ^{1}H-NMR (DMSO-d_6): 7.40(broad, 2H, C-N$\underline{H}_2$) 7.17(broad, 4H, N$\underline{H}_4^+$), ^{13}C- NMR (DMSO-d_6): 218.29

$Co(S_2CNH_2)_3$: $CoCl_2.6H_2O$ (100 mg) and 4 equivalents of $NH_4S_2CNH_2$ (231.6 mg) were dissolved in water and stirred at r.t for 30 min during which a dark green precipitate formed. The precipitate was filtered and washed with 3x10 mL of water. It was then recrystallized from acetone/water giving dark green crystals. Yield: 112 mg (80%) DSC: decomposition T=181.4°C ΔH=265.03 J/g IR: KBr(cm^{-1}): 3354m, 3251m, 1679m, 1596vs, 1390vs, 836s UV-Vis (acetone): 392nm (4.3) 486nm(2.8) 661nm (2.7) ^{1}H-NMR (DMSO-d_6): 9.29(s, 2H, C-N$\underline{H}_2$) ^{13}C- NMR (DMSO-d_6): 210.02 MS(+p ESI-MS): 357.81 $[CoS_6N_3C_3H_6Na]^+$ X-ray diffraction crystals were grown from slow evaporation in acetone.

Substitution of $[Co(en)_3]Cl_3$ with $NH_4S_2CNH_2$

$[Co(en)_3]Cl_3$ (100 mg) and four equivalents of $NH_4S_2CNH_2$ (96 mg) were refluxed in a 1:1 mixture of methanol and water for 1h during which the reaction mixture turned from light orange to dark green. The solvent was removed in vacuo and the dark green solid obtained was washed with 3x10 mL of water and then recrystallized from acetone/water. Yield: 40 mg (41%) IR: KBr(cm^{-1}): 3354m, 3251m, 1679m, 1596vs, 1390vs, 836s UV-Vis (acetone): 486 nm(2.8) 661 nm (2.7)

$Rh(S_2CNH_2)_3$: $RhCl_3.3H_2O$ (100 mg) and 4 equivalents of $NH_4S_2CNH_2$ were dissolved in water and heated at 60 ˚C for 3 hours. During which an orange precipitate formed. The precipitate was washed with 3x10 mL of water and subsequently recrystallized from acetone/water. Yield: 60 mg (42%) DSC: decomposition T=250 ˚C ΔH=101.01 J/g IR: KBr(cm^{-1}): 3347m, 3264m, 1673m, 1589vs, 1402vs, 829s UV-Vis (acetone): 441 nm, (4.2) ^{1}H-NMR (DMSO-d_6): 9.36(s, 2H, C-N<u>H</u>$_2$) ^{13}C- NMR (DMSO-d_6): 213.15 (d,J_{Rh-C}=4.8Hz) MS(-p ESI-MS): 377.78 $[RhS_6N_3C_3H_5]^-$ X-ray diffraction crystals were grown from slow evaporation in acetone.

$[RuH(CO)(MeCN)_2(PPh_3)_2]ClO_4$: $RuHCl(CO)(PPh_3)_3$ (569 mg) was suspended in 15 mL of dichloromethane. Most of the complex dissolved to give a grey-yellow solution. Perchloric acid as 70% $HClO_4$ in water, 50 mg acid in 17 mg solution, 2.5 equiv, was added with 30 mL of acetonitrile. A clear slight yellow solution resulted instantly. After stirring 5 min at R.T.30 mL of a 50/50 ethanol/isopropanol solution was added and the volatile components were removed in vacuo on a rotary evaporator to give a massive white solid suspended in 5 mL of solvent. This was diluted with a further 30 mL isopropanol and concentration continued to a volume of 10 mL. The white crystal mass was filtered and washed with isopropanol, 3x 10 mL, and n-hexane, 2x10 mL, to give 468 mg of white solid after drying. Yield 87%. DSC: T = 147.7 ˚C ΔH = 605.0 J/g(exothermic), IR: KBr (cm^{-1}): 2042.0w, 1959.2 s, 834.8w; Nujol: 2041.8w, 1951.3s, 835.4w, 814.5w. ^{1}H NMR (500 MHz, CD_2Cl_2): -12.93 (t, $^2J_{HP}$=17.7Hz Ru-H, 1), 1.42 (s, 3H), 1.79 (s, 3H), 7.52 (m, PPh_3), 7.61 (m, PPh_3). ^{31}P NMR (202 MHz, CD_2Cl_2): 45.86(s)

Note: Perchlorate salts are explosive and must be handled with precautions.

$RuH(CO)(S_2CNH_2)(PPh_3)_2$: $[RuH(CO)(MeCN)_2(PPh_3)_2]ClO_4$ (51 mg) was dissolved in 10 mL dichloromethane and treated with 4.2 equivalents of $NH_4[S_2CNH_2]$ (28 mg), dissolved in 0.2 ml water and diluted with 10 mL ethanol. On mixing the solution turned an instant lemon yellow solution from which light yellow crystals of product were isolated by concentrating the solution to 5 mL after 15 minutes standing in solution. Filtration of the crystals followed by washing with ethanol, 2x10 mL, and n-hexane, 5 mL, gives 45 mg, 92 % yield. Recrystallization from dichloromethane/ethanol gave long needles of 3a. DSC: T = 209.0 ˚C ΔH = 312.0 J/g(endothermic) followed immediately by an 246 J/g exotherm, IR (cm^{-1}) 3472.8w, 3449.9w, 3319.8s, 1926.5s., 1581.3, 1358.8, 1230.3, 1182.4, 843.4, 832.7, 7 H/D exchange: Sample in CD_2Cl_2/D_2O stirred two hours at RT, recovered by recrystallization following treatment with CD_3OD. ^1H NMR (500 MHz, DMSO-d_6): -11.47 (t, $^2J_{HP}$=20.5 Hz, Ru-H), , 7.38 (m, PPh_3), 7.62 (m, PPh3) 8.06 (brs, 2H, C-N$\underline{H}_2$) $^{13}C\{^1H\}$- NMR (DMSO-d_6): 214.61, 135.96 (t, J_{CP}=4.6Hz), 134.07 (t, J_{CP}=4.6Hz), 129.68, 128.17 (t, J_{CP}=4.2Hz) $^{31}P\{^1H\}$ NMR (202 MHz, DMSO-d_6): 48.83 (s) MS(ESI-MS): 746.0439 $[RuS_2NOP_2C_{38}H_{32}]^+$ Anal. Calcd for $RuC_{38}H_{33}ONP_2S_2$: C, 61.11; H, 4.45; N, 1.88 Found: C, 60.86; H, 4.50; N, 1.90

$RuCl(CO)(S_2CNH_2)(PPh_3)_2$: $RuH(CO)(S_2CNH_2)(PPh_3)_2$ (65 mg) was treated with 1.5 equivalents (12 mg) of N-chlorosucinimide and the mixture was dissolved 30 mL of a 50/50 mixture of dichloromethane/ethanol. Within 15 min the solution took on an orange color and after 30 min the solution was concentrated to 5 ml to give an orange/yellow crystal mass which was isolated by filtration and washing with ethanol (2 x 10 mL) and 5 mL hexane. Yield 62%, 42 mg. DSC: decomposition T>300˚C IR (cm^{-1}): 3431w, 3262w, 3154.1w, 1940.7s, 1588.8w, 1394.0m, 1158.5w, , 853.1w. ^1H NMR (500 MHz, CD_2Cl_2): 6.66(s, 2H) 7.21 (m, PPh_3), 7.35 (m, PPh_3), 7.46 (m, PPh_3), $^{13}C\{1H\}$- NMR (CD_2Cl_2): 134.64 (t, J_{CP}=4.8Hz), 134. 45 (t, J_{CP}=4.5Hz), 129.95, 127.74 (t, J_{CP}=4.8Hz) $^{31}P\{^1H\}$ NMR (202 MHz, CD_2Cl_2): 36.80(s) MS(ESI-MS): 746.0439 $[RuS_2NOP_2C_{38}H_{32}]^+$ due to loss of chloride upon ionization. Absence of a triplet at -11.47 in the ^1H-NMR proves the formation of the desired product. Anal. Calcd for $RuC_{38}H_{32}ONP_2S_2Cl.C_2OH_6$ [confirmed by X-ray diffraction]: C, 58.07; H, 4.63; N, 1.69 Found: C, 57.73; H, 4.11; N, 1.85

Synthesis of other dithiocarbamate complexes

$Rh(Medtc)_3$, $Rh(Etdtc)_3$ and $Rh(Bzdtc)_3$ were prepared according to known literature procedures[60]. Spectroscopic and thermal data are provided.

$Rh(Me_2dtc)_3$: decomposition T>300 ˚C IR: KBr(cm^{-1}): 2916.4m, 1525.3vs, 1383.4vs, 1254.6s, 1138.9s, 1093.6m, 971.3s , d) ^{1}H-NMR ($CDCl_3$): 3.27 (s, 1H, N-C<u>H</u>$_3$), $^{13}C\{^1H\}$- NMR ($CDCl_3$): 38.07, 208.64(d, J_{Rh-C}=4.7Hz) X-ray diffraction crystals were grown from slow evaporation in acetone.

$Rh(Et_2dtc)_3$: decomposition T=263.26˚C ΔH=16.52J/g IR: KBr(cm^{-1}): 2968.1m, 2929.4m, 2858.7w, 2863.4 w, 1525.3vs, 1383.4vs, 1254.6s, 1138.9s, 1093.6m, 971.3s ^{1}H-NMR ($CDCl_3$): 1.27 (t, 3H, N-CH_2-C<u>H</u>$_3$, J_{H-H}=7.2Hz), 3.82 (m, 1H, N-C<u>H</u>$_2$-CH_3) $^{13}C\{^1H\}$- NMR ($CDCl_3$): 12.49, 43.22, 207.69(d, J_{Rh-C}=4.4Hz)

$Rh(Bz_2dtc)_3$: decomposition T=229.02˚C ΔH=28.06J/g IR: KBr(cm^{-1}): 2960.0m, 2919.9w, 2863.4 w, 1585.3vs, 1498.7s, 1422.2s, 1329.6m, 1225.0s , 1180.7w, 1092.1m, 1015.6w, 955.3w, 902.9vw, 798.3m, 733.9m, 677.5m, 576.9m ^{1}H-NMR (C_6D_6): 4.65(d, 2H, N-C<u>H</u>$_2$-Ph, J_{AB}=15.2Hz), 7.12(m, 5H, N-CH_2-<u>Ph</u>) $^{13}C\{^1H\}$- NMR ($CDCl_3$): 50.34, 128.08, 128.52, 128.87, 134.68, 210.97 (d, J_{Rh-C}=4.6Hz) X-ray diffraction crystals were grown from slow evaporation in acetone.

$Ir(Bz_2dtc)_3$: $IrCl_3.3H_2O$ (100mg) and 4 equivalents of NaBzDTC (277mg) were stirred overnight in a 1:1 mixture of MeOH/H_2O. An orange precipitate formed and was washed with 3x10mL of MeOH. The product was recrystallized from 1:1 DCM/MeOH. Yield: 74mg (27%) Decomposition T=229.02˚C ΔH=28.06J/g IR: KBr(cm^{-1}): 3019.7w, 2923.1w, 1590.2s, 1493.6vs, 1422.7m 1351.8m, 1223.0s , 1180.7w, 1081.4s, 753.1m, 695.0vs, ^{1}H-NMR (C_6D_6):, 4.56(d, 2H, N-C<u>H</u>$_2$-Ph, J_{AB}=15.2Hz) 7.06(m, 5H, N-CH_2-<u>Ph</u>) $^{13}C\{^1H\}$- NMR ($CDCl_3$): 49.74, 128.10, 128.53, 128.86, 134.70, 214.00 MS(+p ESI-MS): 1032.12 $[NaIrS_6N_3C_{45}H_{42}]^+$

4.6.2 Crystallographic Methodologies

Crystals are mounted on glass fibers with epoxy resin on Mitogen mounts using Paratone-N from Hampton Research and single-crystal X-ray diffraction experiments are carried out with a BRUKER APEX-II D8 CCD diffractometer by using graphite-monochromated Mo Kα radiation (λ = 0.71073 Å) the SHELX package[61] is used for integration of the intensity reflections, scaling, and absorption correction. Intrinsic phasing methods were used to solve the structures. Non-hydrogen atoms are located by difference Fourier maps and final solution refinements are carried out by full-matrix least-squares methods on F2 for all of the data. The hydrogen atoms are placed in calculated positions and were not refined.

4.6.3 Theoretical calculations

Density functional theory implemented on Gaussian16 with B3LYP functionals were used with cc-pvdz, cc-pvtz, and aug-cc-pvtz basis sets. For calculations of the rhodium complexes effective core potentials based on a fully relativisitic mulitelectron fit of 28 core electrons were used.[62]

4.7 References

1. Quack, M.: How Important is Parity Violation for Molecular and Biomolecular Chirality? *Angew. Chem., Int. Ed.*, **2002**, *41*, 4618−4630
2. Tranter, G. E.: Parity Violating Energy Differences in Chiral Minerals and the Origin of Biological Homochirality, *Nature*, **1985**, *318*, 172-173
3. Wood, C. S; Bennett, S. C; Cho, D.; Masterson, B. P.; Roberts, J. L.; Tanner, C. E.; Wieman, C. E.; Measurement of Parity Nonconservation and an Anapole Moment in Cesium, *Science*, **1997**, *275*, 1759-1763
4. DeMille, D.: Parity Non-Conservation in the $6s^2\ {}^1S_0$->$6s5d\ {}^3D$ Transition in Atomic Ytterbium *Phys. Rev. Lett.*, **1995**, *74*, 4165-4168
5. Macpherson, M. J. D.; Zetie, K. P.; Warrington, R. B.; Stacey, D. N.; Hoare, J. P.: Precise Measurement of Parity Nonconserving Optical Rotation at 876nm in Atomic Bismuth, *Phys. Rev. Lett.*, **1991**, *67*, 2784-2787
6. Meekhof, D. M.; Vetter, P.; Majumder, P. K.; Lamoreaux, S. K.; Fortson, E. N.: High Precision Measurement of Parity Nonconserving Optical Rotation in Atomic Lead, *Phys. Rev. Lett.*, **1993**, *71*, 3442-3445
7. Vetter, P. A.; Meekhof, D. M.; Majumder, P. K.; Lamoreaux, S. K.; Fortson, E. N.: Precise Test of Electroweak Theory from a New Measurement of Parity Nonconservation in Atomic Thallium, *Phys. Rev. Lett.*, **1995**, *74*, 2658-2661
8. Cournol, A.; Manceau, M.; Pierens, M.; Lecordier, L.; Tran, D. B. A.; Santagata, R.; Argence, B.; Goncharov, A.; Lopez, O.; Abgrall, M.; Le Coq, Y.; Le Targat, R.; Álvarez Martinez, R.; Lee, W. K.; Xu, D.; Pottie, P. E.; Hendricks, R. J.; Wall, T. E.; Bieniewska, J. M.; Sauer, B. E.; Tarbutt, M. R.; Amy-Klein, A.; Tokunaga, S. K.; Darquié, B., A New Experiment to Test Parity Symmetry in Cold Chiral Molecules Using Vibrational Spectroscopy, *Quantum Electron.*, **2019**, *49*, 288-292
9. Crassous, J.; Chardonnet, C.; Saue, T.; Schwerdtfeger, P.; Recent Experimental and Theoretical Developments Towards the Observation of Parity Violation (PV) effects in molecules by Spectroscopy, *Org.Biomol. Chem.*, **2005**, *3*, 2218-2224

10. Darquie, B.; Stoeffler, C.; Shelkovnikov, A.; Daussy, C.; Amy-Klein, A.; Chardonnet, C.; Zrig, S.; Guy, L.; Crassous, J.; Soulard, P.; Asselin, P.; Huet, T. R.; Schwerdtfeger, P.; Bast, R.; Saue, T.: Progress Towards the First Observation of Parity Violation in Chiral Molecules by High Resolution Laser Spectroscopy, *Chirality*, **2010**, *22*, 870-884
11. Barra, A. L.; Robert, J. B. : Parity Non-Conservation and NMR Parameters, *Mol. Phys.*, **1996**, *88*, 875-886
12. Lahamer, A. S.; Mahurin, S. M.; Compton, R.N.; House, D.; Laerdahl, J. K.; Lein, M.; Schwerdtfeger, P.: Search for a Parity-Violating Energy Difference Between Enantiomers of a Chiral Complex, *Phys. Rev. Lett*., **2000**, *85*, 4470-4473
13. Medcraft, C.; Wolf, R.; Schnell, M.: High Resolution Spectroscopy of the Chiral Metal Complex [CpRe(CH_3)(CO)(NO)]: A Potential Condidate for Probing Parity Violation, *Angew. Chem. Int. Ed*., **2014**, *53*, 11656-11659
14. Gaydon, Q.; Bohle, D. S.: Separation of Isomers and Mechanism of Inversion of Stereochemistry of Group 9 d^6 Tris-Chelate Complexs of Hinokitiol, *Inorg. Chem*. **2021**, *60*, 13567-13577
15. Hogarth, G.: Transition Metal Dithiocarbamates: 1978-2003. *Prog. Inorg. Chem*. **2005**, *53*, 71-557
16. Coucouvanis, D., The Chemistry of the Dithioacid and 1, 1-Dithiolate Complexes, 1968–1977 *Prog. Inorg. Chem*., **1970**. *11*, 233-469
17. Halls, D. J.: The Properties of Dithiocarbamates, *Mikrochim. Acta* , **1969**, *57*, 62-77
18. Cavell K. J.; Hill J. O.; Magee R. J., Synthesis and Characterization of some Secondary Amine Dithiocarbamate Salts, *J. Inorg. Nucl. Chem.*, **1979**, *41*, 1277-1280
19. Gattow, G.; Hahnkamm, V.: Über Chalkogenocarbonate. XXXII. Untersuchungen über Dithiocarbamidsäure SC(SH)(NH_2). 1. Darstellung und Eigenschaften der Freien Säure, *Z. Anorg. Allg. Chem.*, **1969**, *364*, 161-176
20. Mortag, M.; Möckel, K.: Neuartige Alkylammonium-N-alkyldithiocarbamate und Deren Thermolyze, *Z. Chem*., **1980**, *20*, 101-102
21. Bradley, D. C.; Gitlitz, M. H.: NN-Dialkyldithiocarbamates of Transition-Metals of Groups IV and V. *Chem. Commun. (London)*, **1965,** 289

22. Brown, T. M.; Smith, J. N.: Tetramethylenedithiocarbamates of the Early Transition Metals, *J. Chem. Soc. Dalton. Trans*., **1972**, 1614-1616
23. Rossi, R.; Marchi, A.; Duatti, A.; Magon, L.; Cassellato, U.; Graziani, R. J., Reactivity of Rhenium(I) Pseudo-Allyl Complexes with Heterocumulenes such as RNCS (R = Me or Ph, p-MeC_6H_4) and PhNCO. Part 1. Crystal Structure Determination of Two Isostructural Monothio- and Dithio-carbamate Rhenium(I) Complexes Co-crystallized as $[Re(CO)_2(PPh_3)_2\{S=C(NHPh)–S\}]\cdot[Re(CO)_2(PPh_3)_2\{O–C(NHPh]=S\}]$ *Chem. Soc., Dalton Trans.* **1987**, 2299-2303
24. Critchlow P. B.; Robinson S. D., Complexes of the Platinum Metals. Part VI. Dithiocarbamato-and O-alkyl Dithiocarbonato-Derivatives of Ruthenium, Osmium, and Iridium, *J. Chem. Soc., Dalton Trans*., **1975**, 1367-1372
25. Tan, Y. S.; Yeo, C. I.; Tiekink, E. R. T.; Heard, P. J.: *D*ithiocarbamate Complexes of Platinum Group Metals: Structural Aspects and Applications, *Inorganics* **2021**, *9*, 60-100
26. Williams, M. R. M.; Bertrand, B.; Hughes, D. L.; Waller, Z. A. E.; Schmidt, C.; Ott, I.; O'Connell, M.; Searcey, M.; Bochmann, M.: Cyclometallated Au(iii) Dithiocarbamate Complexes: Synthesis, Anticancer Evaluation and Mechanistic Studies. *Metallomics*, **2018**, *10*, 1655-1666
27. Ajibade. P. A.; Ejelonu, B. C.; Group 12 Dithiocarbamate Complexes: Synthesis, Spectral Studies and Their Use as Precursors for Metal Sulfides Nanoparticles and Nanocomposites, *Spectrochim. Acta Part A*, **2013** *113*, 408-414
28. Sharma, A. K.: Thermal Behaviour of Metal Dithiocarbamates, *Thermochim. Acta*, **1986**, *104*, 339-372
29. Singhal, S.; Garg, A. N.; Chandra, K., Thermal Decomposition of Transition Metal Dithiocarbamates, *J. Therm. Anal. Cal*., **2004**, *78*, 941-952
30. Sengupta, S. K.; Kumar, S.: Thermal Studies on Metal Dithiocarbamato Complexes. A Review, *Thermochim. Acta*, **1984**, *72*, 349-361
31. Ascenzo, G. D.; Wendlandt, W. W.: Iron (III) Diethyldithiocarbamate—A New Volatile Metal Chelate, *J. Inorg. Nucl. Chem*., **1970**, *32*, 2431-2433

32. Holah, D. G.; Murphy, C. N.: On Cobalt(II) N,N-diethyldithiocarbamate, *J. Thermal Anal*., **1971**, *3*, 311-312
33. Teske, C. L., Bensch, W.: On Ammonium-tetrakis(dithiocarbamato)-bismuth(III)-monohydrate and Tris(dithiocarbamato)-bismuth(III), *Z. Anorg. Allg. Chem.*, **2011**, *637*, 406-414; Teske, C. L.; Bensch, W.: On Tris(dithiocarbamato)-Chromium(III), $Cr(S_2CNH_2)_3$, *Z. Anorg. Allg. Chem.*, **2012**, *638*, 2093-2097; Teske, C. L.; On Ammonium-bis(dithiocarbamato)-copper(I)-monohydrate and Mono(dithiocarbamato)-copper(I), *Z. Anorg. Allg. Chem.*, **2013**, *639*, 2767-2773; Teske, C. L.; Bensch, W.: On Mono(dithiocarbamato)-silver(I), AgS_2CNH_2, *Z. Anorg. Allg. Chem.*, **2015**, *641*, 1031-1035; Teske, C. L.; Reinsch, H.; Terraschke, H.; Bensch, W.; Synthesis, Crystal Structure and Selected Properties of Mono(dithiocarbamato)-gold(I), AuS_2CNH_2, *Z. Anorg. Allg. Chem.*, **2017**, *643*, 466-470
34. Raston, C. L.; White, A. H.; Willis, A. C.: Crystal Structure of Tris(dithiocarbamato)cobalt(III), *J. Chem. Soc., Dalton. Trans*., **1975**, 2429-2432
35. Gattow, G.; Hahnkamm, V.; Untersuchungen uber Dithiocarbamidsaure $SC(SH)(NH_2)_3$. Alkalimetalldithiocarbamate $M[SC(S)(NH_2)]$ *Z. Anorg. Allg. Chem*., **1969**, *368*, 127-132
36. Teske, C. L.; Bensch, W.; On Crystal Structure Investigations of α- and β-Ammoniumdithiocarbamate $NH_4CS_2NH_2$ and the Role of Hydrogen Bonding, *Z. Anorg. Allg. Chem.*, **2010**, *636*, 356-362
37. van Gaal, H. L. M.; Diesveld, J. W.; Pijpers, F. W.; van der Linden, J. G. M.: Carbon-13 NMR Spectra of Dithiocarbamates. Chemical Shifts, Carbon-Nitrogen Stretching Vibration Frequencies and π Bonding in the NCS_2 Fragment., *Inorg. Chem*., **1979**, *18*, 3251-3260
38. Nguyen, H. H.; Hoang, N.; Abram, U.: Synthesis and Structures of Two Ruthenium Dibenzoylmethane Triphenylphosphine Mixed Ligand Complexes. *Transition Met. Chem.* **2010**, *35*, 89-93
39. Hiett, N. P.; Lynam, J. M.; Welby, C. E.; Whitwood, A. C.: Ruthenium Carboxylate Complexes as Easily Prepared and Efficient Catalysts for the Synthesis of β-oxopropyl Esters. *J. Organomet. Chem*., **2011**, *696*, 378-387

40. Mishra, D.; Naskar, S.; Drew, M. G. B.; Chattopadhyay, S. Y.: Mononuclear and Binuclear Ruthenium(II) Complexes with 4-(phenyl) Thiosemicarbazone of Benzaldehyde: A Discussion on the Relative Stabilities of the Four-Membered and Five-Membered Chelate Rings Formed by the Ligand, *Polyhedron*, **2005**, *24*, 1861-1868
41. Gaydon Q.; Bohle I. J.; Bohle D. S.: Fluxionality in the Tropolone Hinokitiol Chelate, *Inorg. Chem*. **2021**, *60*, 3305-3313
42. Fernandez E. J.; Lopez-de-Luzuriaga J. M.; Monge M.; Olmos E.; Gimeno M. C.; Laguna A.; Jones P. G.: Dithiocarbamate Ligands as Building-Blocks in the Coordination Chemistry of Gold, *Inorg. Chem.*, **1998**, *37*, 5532-5536
43. Colton, R.; Mackay, M. F.; Tedesco, V.: The Crystal Structure of (N,N-diethyldithiocarbamato)-bis(2-diphenylphosphinoethyl)phenylphosphineplatinum(II) tetraphenylborate, *Inorg. Chim. Acta*, **1993**, *207*, 227-232
44. Xiang, L.; Zhang, Q. F. ; Leung, H. W., Syntheses and Molecular Structures of Ruthenium Complexes with Dithiophosphate Ligands, *J. Coord. Chem.*, **2005**, *58*, 1299-1305
45. Deshpande, S. S.; Gopinathan S.; Gopinathan C., Insertion Reactions of Acroylonitrile with Hydridocarbonylbis(triphenylphosphine)ruthenium(II) Carboxylates, *J. Organomet. Chem.*, **1989**, *378*, 103-107
46. Rosales, M.; Alvarado, B.; Arrieta, F.; De La Cruz, C.; Gonzalez, A.; Molina, K.; Soto O.; Salazar Y.: A General Route for the Synthesis of Hydrido-Carboxylate Complexes of the Type $MH(CO)(\kappa^3\text{-}OCOR)(PPh_3)_2$[M = Ru, Os; R = CH_3,CH_2Cl, C_6H_5, $CH(CH_3)_2$] and Their Use as Precatalysts for Hydrogenation and Hydroformylation Reactions, *Polyhedron*, **2008**, *27*, 530-536
47. Simmons M.; Cumming Premack K.; Guerra E. D.; Bohle M. J.; Rosadiuk H. A.; Bohle D. S.: 2,3,5-Metallotriazoles: Amphoteric Mesoionic Chelates from Nitrosoguanidines, *Inorg. Chem.*, **2021**, *60*, 9621-9630
48. Nakashima, M.; Kida, S.: Photoreaction of Tris(ethylenediamine)cobalt(III) Ion with Bis(2-hydroxyethyl)dithiocarbamate Ion, *Bull. Chem. Soc. Jpn*., **1982**, *55*, 809-812

49. Eaton S. S.; Eaton G. R., Symmetry Groups of Non-rigid Tris-Chelate Complexes, *J. Am. Chem. Soc.*, **1973**, *95*,1825-1829
50. Raston, C. L.; White, A. H.: Crystal Structures of Tris(diethy1dithiocarbamato)-rhodium(III) and -arsenic(III), *J. Chem. Soc., Dalton*, **1975**, 2425-2429
51. Butcher, R. J.; Sinn, E. K.: Crystal and Molecular Structures of Dichloromethane-Solvated Tris-(morpho1inocarbodithioato)-complexes of Chromium(III), Manganese-(III), and Rhodium(III). Comparison of Coordination Spheres, *J. Chem. Soc., Dalton Trans.*, **1975**, 2517-2522
52. Palazzotto, M. C; Duffy, D. J.; Edgar, B. L.; Que, L., Jr.; Pignolet, L.M., Dynamic Stereochemistry of Tris-Chelate Complexes. Tris(dithiocarbamato) Complexes of Iron, Cobalt, and Rhodium, *J. Am. Chem. Soc.*, **1973**, *95*, 4537-4545
53. Vallee, B.L.; Williams R.J.P.: Metalloenzymes: the Entatic Nature of Their Active Sites. *Proc. Natl Acad. Sci. USA*, **1968**, *59*, 498-505
54. Pignolet, L.H.: Dynamics of Intramolecular Metal-Centered Rearrangement Reactions of Tris-Chelate Complexes, *Top. Chr. Chem.*, **1975**, *56*,91-137
55. Rzepa, H. S.; Cass, M. E. In Search of the Bailar and Raŷ−Dutt Twist Mechanisms That Racemize Chiral Trischelates: A Computational Study of ScIII, TiIV, CoIII, ZnII, GaIII, and GeIV Complexes of a Ligand Analogue of Acetylacetonate. *Inorg. Chem*. **2007**, *46*, 8024-8031
56. Healy, P.C.; Connor J. W.; Skelton B. W.; White A. H., Alkyl Substituent Effects in Diamagnetic Dithiocarbamate Cobalt(III) and Nickel(II) Complexes, *Aust. J. Chem.*, **1990**, *43*, 1083-1095
57. Rodger A., Johnson B. F. G., Which Is More Likely: The Ray-Dutt Twist or the Bailar Twist?, *Inorg. Chem.*, **1988**, *27*, 3061-3062
58. VanQuickenborne, L. G.; Pierloot, K. Role of Spin Change in the Stereomobile Reactions of Strong-Field d^6 Transition Metal Complexes., *Inorg. Chem*. **1981**, *20*, 3673−3677.
59. Ashley, D. C.; Jakubikova, E.: Ray-Dutt and Bailar Twists in Fe(II)-Tris(2,2′-bipyridine): Spin States, Sterics, and Fe–N Bond Strengths, *Inorg. Chem.*, **2018**, *57*, 5585−5596.

60. Malatesta, L. : Sui Dithiocarbammati di Rutenio, Rodio, Paladio, *Gazz. Chim. Ital*., **1938**, *68*, 195-198
61. Sheldrick, G. M. SADABS, TWINABS; Siemens Industrial Automation, Inc.: Madison, WI, 1996
62. Peterson, K. A.; Figgen, D.; Dolg, M.; Stoll, H. Effective Core Potentials. *J. Chem. Phys.* **2007**, *126*, 124101

Chapter 5: Organometallic Chemistry of the Difluorodithiophosphate Anion $[S_2PF_2]^-$

5.1 Preface

In our search of volatile tris-chelate complexes of group 9 d^6 transition metals, we have found several reports of complexes of the fluorodithiophosphate ligand S_2PF_2, the first of which were prepared by Tebbe and Muetterties in the 1970s. All the complexes presented were reported to be volatile and purification by sublimation was possible. Of the complexes presented, the tris-chelate $Co(S_2PF_2)_3$ was among them. In addition to volatility, the presence of the heavy atoms sulphur and phosphorus would enhance PVED. Since then, some more complexes have been synthesized but overall, the coordination chemistry of this ligand has been abandoned. It is important to note that a search in the Cambridge Crystallographic Database does not return any results for complexes of $[S_2PF_2]^-$ or the free ligand. The difficulty of obtaining good crystal structures may explain in part why these complexes have not drawn much attention since. Synthesis of $RuXL(CO)(PPh_3)_2$, (X=H, Cl) and $RuL_2(PPh_3)_2$ similar to those presented in Chapters 3 and 4 may facilitate crystallization and allow us to obtain the first examples of crystal structures for these complexes.

In this chapter we present a new synthesis and crystal structure of $[N^nPr_4][S_2PF_2]$ as well as those of three ruthenium complexes. An in-depth analysis of the structural parameters, spectroscopic properties and reactivity towards carbonylation is provided. The work in this chapter has been submitted for publication: Gaydon Q.; Bohle D. S., Organometallic Chemistry of the Difluorodithiophosphate anion, *Eur. J. Inorg. Chem*., under review

5.2 Abstract

An improved synthetic route of $[N^nPr_4][S_2PF_2]$ was devised, and its structure was determined. This unusual dithiophosphate is a good ligand for low valent metal centers and examples of this being hydrolytically stable ruthenium complexes $RuH(CO)(S_2PF_2)(PPh_3)_2$, $RuCl(CO)(S_2PF_2)(PPh_3)_2$ and $Ru(S_2PF_2)_2(PPh_3)_2$.Taken together these results give an insight into the bonding of the S_2PF_2 anion to low oxidation state complexes. A comparison of the structural features and reactivity of the complexes with other known Ru(II) complexes is presented. $Ru(S_2PF_2)_2(PPh_3)_2$ was successfully carbonylated to give a complex with monohapto and dihapto S_2PF_2 ligands, $Ru(CO)(\eta^1\text{-}S_2PF_2)(\eta^2\text{-}S_2PF_2)(PPh_3)_2$ confirming the hemilability of the fluorothiophosphate anion. Isomers of this latter complex have been structurally characterized with *cis* and *trans* PPh_3.

5.3 Introduction

Although the phosphorus sulfides and their anions are a large class of compounds, many with considerable industrial importance, there are three, the dithiophosphates, dithiophosphinates and dithiophosphonates (Figure 5.1), which are widely used as corrosion inhibitors, analytical agents, and ore benefaction agents.[1] Complexes of every metal are known for these ligands, with monodentate, bidentate, or bridging modes being found.[2-11] The relative ease of preparation of the ligands from phosphorus pentasulfide is in part responsible for this extensive chemistry.[11]

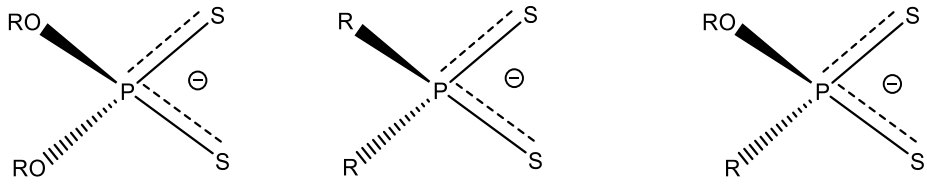

R=alkyl, aryl

Dithiophosphate Dithiophosphinate Dithiophosphonate

Figure 5.1: Dithiophosphate, dithiophosphinate and dithiophosphonate ligands

Unlike the thiophosphates presented in Figure 5.1, halogen-containing thiophosphates of the formula $S_2PX_2^-$ are rare, and those known largely prove to be reactive hydrolysizable salts.[13,14] In contrast, one relatively obscure member of this the family, the $S_2PF_2^-$ anion, has good hydrolytic stability but a limited coordination chemistry: it was first prepared in parallel by four different groups.[15-18] A particularly useful preparation directly from P_4S_{10} and alkali metal fluorides was first described by Roesky, Tebbe, and Muetterties along with several other fluorophosphates and related pseudohalidephosphates.[19] The tractable and useful crystallization of its tetrapropylammonium salt, $[N^nPr_4][S_2PF_2]$ was also reported. Subsequently, coordination of the the F_2PS_2 anion to transition metals by Roesky and Cavell resulted in the synthesis of a handful complexes with various binding modes including monodentate, bidentate and bridging ligands by the oxidative addion of the conjugate acid HS_2PF_2 to base metals.[20-28] Direct coordination of the anion was not utilized. The difluorophosphate anion is spectroscopically rich with the presence of two NMR active nuclei, ^{31}P and ^{19}F, as well as strong fluorine-phosphorus bands in the IR. Taken together the direct spectroscopic characterization of the ground state constitution and stereochemistry as well as their solution dynamics is well determined. Suprisingly a search in the Cambridge Crystallographic Database does not reveal a structure of any transition metal complex or salts of the anion $S_2PF_2^-$. Of interest to us is the observation that many of the complexes, including tris-chelate complexes of cobalt are volatile:[19] such compounds would be good candidates to measure Parity Violation Energy Difference in molecules using gas phase microwave spectroscopy.[29]

Low valent group 8 complexes such as $RuH(\eta^2\text{-}L)(CO)(PPh_3)_2$ were L is a bidentate ligand are attractive complexes when studying new classes of chelates: some advantages include simple synthesis, good solubility, inertness of the coordination sphere, resistance to oxidation, thermal stability, and good spectroscopic handles provided by the H^-, CO and PPh_3 ligands.[30-34] The presence of bulky triphenylphosphine ligands aids in the recrystallization of the complexes as well as crystal growth for X-ray diffraction. Further reactivity, such as substitution of the hydride by chlorine with N-chlorosuccinimide or by hydride cleavage with strong acids can be easily achieved. The five-coordinate $RuCl_2(PPh_3)_3$ has been used as a precursor to a wide range of $RuX_2(PPh_3)_2$ complexes[35] owing to labile chloride and triphenylphosphine ligands.[36-39] Its

dynamic behaviour, as well as that of $OsCl_2(PPh_3)_3$, was elegantly demonstrated by Caulton,[40] both complexes share a labile coordination sphere and access, at least formally, to the 14 electron intermediate $MCl_2(PPh_3)_2$.

Perhaps one important reason why the fluorophosphates have fallen into obscurity is the original syntheses utilized thiophosphoryl fluoride, $S{=}PF_3$, with its attendant difficulties. However, in addition to this issue, they also reported a preparation from P_4S_{10} which also seems to have mired the experimental details. Herein we present: 1) an optimized synthesis of $[N^nPr_4][S_2PF_2]$ from P_4S_{10}; 2) the crystal structure and ground state ab initio calculations for this anion; 3) organometallic chemistry of four Ru(II) complexes, $RuH(CO)(S_2PF_2)(PPh_3)_2$, $RuCl(CO)(S_2PF_2)(PPh_3)_2$, $Ru(S_2PF_2)_2(PPh_3)_2$, and $Ru(CO)(S_2PF_2)_2(PPh_3)_2$ which are readily prepared directly from the anion, and 4) solid state and solution dynamics of these complexes as well as the product of the carbonylation of $Ru(S_2PF_2)_2(PPh_3)_2$, $Ru(CO)(\eta^1\text{-}S_2PF_2)(\eta^2\text{-}S_2PF_2)(PPh_3)_2$.

5.4 Results and Discussion

$$P_4S_{10} + 4NaHF_2 \xrightarrow[NPr_4Br,\ H_2O]{\text{acetonitrile, reflux, 30min}} 4\ [N^nPr_4][S_2PF_2] + 2\ H_2S \qquad 1$$

1

Roesky, Tebbe, and Muetterties proposed two routes to the $S_2PF_2^-$ anion. The first higher yielding of the two involves treating SPF_3 with cesium fluoride. The second route involves treating P_4S_{10} with NaF in acetonitrile, although Meisel *et al.* subsequently obtained $[N^nPr_4]_2[S_5P_2F_2]$ as the major product from the reaction with NaF, as do we.[41] We have found that both the yield and purity for the isolation of the S_2PF_2 anion is improved with the use of sodium hydrogen difluoride, $NaHF_2$ rather than the simple alkali metal fluorides first described.[18] Thus the reaction of P_4S_{10} with 4 equivalents of $NaHF_2$ (equation 1) in acetonitrile followed by precipitation with tetrapropylammonium bromide in water. This is readily purified by a further recrystallization from $MeOH/H_2O$ to afford the salt $[N^nPr_4][S_2PF_2]$ in 60 % yield. We find that

the use of sodium bifluoride rather than fluoride possibly promotes the equilibration of eq. 1 and provides protons to help drive the loss of hydrogen sulfide.

The tetrapropylammonium salt **1** is a hydrolytically stable white crystalline material has a sharp reversible melting point at 164 °C with an enthalpy of fusion of ΔH =18.2 J/g. The distinct ^{31}P and ^{19}F NMR spectra prove particularly useful for its detection.[19] The salt $[N^nPr_4][S_2PF_2]$ crystallizes in the orthorhombic centrosymmetric *P*bca space group where the anion is not disordered. Key experimental crystallographic, spectroscopic, and theoretical values from density functional theory for the salts and model complexes are collected in Table 5.1. The anion adopts a distorted tetrahedral geometry around the phosphorus with a small F-P-F angle of 91.1(3) ° and a larger S-P-S angle of 124.55(13) °. The F-P-S angles vary between 107.90(17) ° and 111.14(19) °. The P-F bond lengths of 1.559(4) Å and 1.586(4) Å are statistically different only at the 2σ level, consistent with one environment being observed in the NMR time scale in solution. The P-S bond lengths of 1.875(2) Å and 1.886(2) Å are quite short and consistent with a multiple bond character. The similar values of the two bonds suggests the electrons are delocalized between the P-S bonds. The structural features of the tetrapropylammonium cation are as expected for tetraalkylammonium salt: the C-N-C angles between 108.3(4)° and 111.4(4)° highlight the tetrahedral geometry of the central nitrogen atoms. C-N bond lengths between 1.510(6) Å and 1.534(6) Å and C-C bond lengths between 1.478(7) Å and 1.510(8) Å are consistent with single bonded C-N and C-C bonds. Slightly larger thermal parameters for C(6) of the cation suggest some minor disorder in the propyl chains.

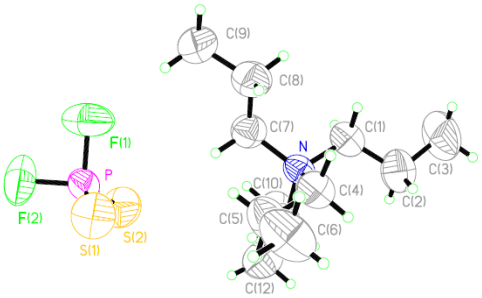

Figure 5.2: ORTEP diagram of $[N^nPr_4][S_2PF_2]$ with 40% thermal ellipsoids

Density functional theory models the bond angles and distances well for those found crystallographically, Table 5.1, and Figure S5.11. However, for the tetramethylammonium salt the phosphorus-fluorine bonds are equidistant and within 0.005 Å for the tetra-n-propylammonium salt. In addition, the frequencies for the alkylammonium salts versus coordination complexes are similar to those exhibited experimentally.

Species	Method	P-F (Å)	P-S (Å)	F-P-F (°)	S-P-S (°)	ν(P-F)	ν(P-S)
$S_2PF_2^-$	DFT	1.61400	1.96365	94.13439	124.5306	787.69 759.75	721.04 531.81
$[NMe_4][S_2PF_2]$	DFT	1.59294	1.98258 1.96228	95.96899	123.07577	830.41 817.74	699.15 530.36
$[N^nPr_4][S_2PF_2]$	XRD	1.559(4) 1.586(4)	1.875(2) 1.886(2)	91.1(3)	124.55(13)	876.7 836.6	707.1 533.3
$[N^nPr_4][S_2PF_2]$	DFT	1.60828 1.59202	1.96238 1.97663	95.66753	123.75809	866.71 827.75	702.41 529.83
$RuH(CO)(S_2PF_2)(PPh_3)_2$	XRD	1.548(3) 1.546(3)	1.951(2) 1.931(2)	95.6(2)	114.11(7)	873.0 836.0	698 520
$Co(S_2PF_2)(CO)_3$	DFT	1.57473 1.57476	1.99837 1.96197	96.57298	112.23612	879.62 863.49	681.14 539.04

Table 5.1: Contrasts of Difluorodithiophosphate theoretical and experimental metric parameters for the salts and coordination complexes. XRD: experimental results from X-ray diffraction, DFT: theoretical results from B3LYP/cc-pvtz. For entries with just one P-F or P-S bond length the pair are equivalent. Experimental IR data was obtained from KBr pellets.

$$[RuH(CO)(MeCN)_2(PPh_3)_2]ClO_4 + NPr_4S_2PF_2 \xrightarrow{\text{DCM, r.t, 15min}} RuH(CO)(S_2PF_2)(PPh_3)_2 \quad 2$$

2

$$RuH(CO)(S_2PF_2)(PPh_3)_2 + \text{N-chlorosuccinimide} \xrightarrow{\text{DCM, r.t, 40min}} RuCl(CO)(S_2PF_2)(PPh_3)_2 \quad 3$$

3

$$RuCl_2(PPh_3)_3 + 2\ NPr_4S_2PF_2 \xrightarrow{\text{DCM, r.t, 20min}} Ru(PPh_3)_2(S_2PF_2)_2 \quad 4$$

4

Several complexes of $S_2PF_2^-$ were synthesized by Cavell, Tebbe, and Roesky. Notably, no group 8 complexes have been reported: we present here four Ru(II) complexes with one and two

coordinating $S_2PF_2^-$ ligands, $RuH(CO)(S_2PF_2)(PPh_3)_2$, **2,** $RuH(CO)(S_2PF_2)(PPh_3)_2$, **3**, and $Ru(S_2PF_2)_2(PPh_3)_2$, **4**, equations 2-4. Complex **2** was synthesized by substitution of the labile acetonitrile ligands of $[RuH(CO)(MeCN)_2(PPh_3)_2]ClO_4$, equation 2, with $[N^nPr_4][S_2PF_2]$ in dichloromethane at room temperature followed by recrystallization from DCM/ethanol. Chlorination of **2** with N-chlorosuccinimide afforded complex **3**, equation 3. The final complex **4** was obtained by substitution of two chlorides and one triphenylphosphine ligand of $RuCl_2(PPh_3)_3$ in dichloromethane, equation 4. The ^{31}P and ^{19}F NMR spectra, discussed in more detail later, along with strong symmetric and asymmetric P-F stretches in the IR spectrum indicate coordination of the ligand and absence of any degradation The presence of the hydride in **2** was confirmed by a triplet of triplets at -12.17 ppm in the ^1H NMR due to coupling to the triphenylphosphines and fluorine atoms, as well as a band at 1989.1 cm^{-1} in the IR.

Different coordination modes of the S_2PF_2 anion are possible: η^1, symmetric η^2 , and asymmetric η^2, Figure 5.3, being plausible. The crystal structure of the three complexes unambiguously results in bidentate coordination of the ligand. Differences in ΔRu-S bond lengths of 0.01 Å in **2**, 0.03 Å in **3** and 0.086 Å in **4** are found. An asymmetric η^2 coordination mode would result in significantly different Ru-S bond lengths: this is especially visible in complexes of dithiocarbamates, another S,S donor ligand, where differences of 0.3 to 0.6 Å were observed.[43] We can conclude that the coordination of S_2PF_2 to Ru(II) is predominantly symmetric η^2 in manner.

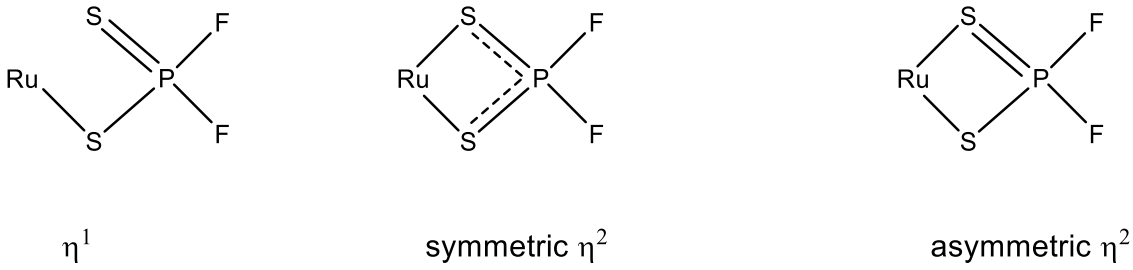

Figure 5.3: Coordination modes of S_2PF_2 to Ru(II)

The crystal structure of **2** reveals the S_2PF_2 ligand is *trans* to the hydride and carbonyl groups, the positions of which were unambiguously determined without CO/H disorder. The final refinement included a hydride hydrogen bound to ruthenium at its calculated position. The *trans*

triphenylphosphines deviate slightly from linearity with a P-Ru-P angle of 166.42(4)°, and a bending towards the space above and below the hydride. The S_2PF_2 ligand is characterized by significant difference of 0.02 Å in the P-S bond lengths as a consequence of the strong *trans* influence of the hydride ligand as well as a significant decrease of 10° of the S-P-S angles along with slightly shorter P-F bonds upon coordination. The Ru-S-P-S chelate ring formed upon coordination is quasi planar with the phosphorus being 0.04 Å above the plane defined by S-Ru-S. The tetrahedral geometry of the phosphorus results in the phosphorus and fluorine atoms being on a plane perpendicular to that of the hydride, carbonyl, and sulfurs.

Upon chlorination of **2**, the geometry of the *trans*-triphenylphosphines changes to *cis*-triphenylphosphines with the chlorine and carbonyl group now adopting a *trans* configuration. A consequence of this is that the fluorines, chlorine and carbonyl are in the same plane which results the fluorine atoms being inequivalent, as is evident in ABX pattern in the phosphorus and fluorine NMR. The shorter P-S bonds in this complex arise from the weaker *trans* influence of the triphenylphosphines compared to the hydride and the carbonyl. No evidence of the *trans*-isomer in solution or the solid state is present. The crystal structure of **4** revealed the formation of the *cis*-triphenylphosphine isomer. While less common than complexes with *trans*-triphenylphosphines, complexes with *cis*-triphenylphosphines have been observed: we have for example observed this with a tropolonate derivative, hinokitiol and it has been reported by others previously. [30,44-46]

2		**3**		**4**		**1**	
Bonds	Å	Bonds	Å	Bonds	Å	Bonds	Å
Ru-S	2.5472(12) 2.5795(12)	Ru-S	2.5186(17) 2.5223(16)	Ru-S	2.449(3) 2.560(3) 2.445(3) 2.531(3)		
P-S	1.9514(16) 1.9309(17)	P-S	1.941(3) 1.946(2)	P-S	1.944(4) 1.921(4) 1.939(4) 1.953(4)	P-S	1.886(2) 1.875(2)
P-F	1.548(3) 1.546(3)	P-F	1.551(6) 1.499(5)	P-F	1.548(7) 1.588(7) 1.548(6) 1.557(6)	P-F	1.559(4) 1.586(4)
Ru-C	1.820(4)	Ru-C	1.843(7)				
Ru-P	2.3623(10) 2.3704(10)	Ru-P	2.3807(15) 2.3629(14)	Ru-P	2.350(3) 2.318(3)		
Angles	°	Angles	°	Angles	°	Angles	°
S-Ru-S	78.91(4)	S-Ru-S	79.79(6)	S-Ru-S	79.88(9) 80.67(9)		
F-P-F	95.6(2)	F-P-F	95.4(4)	F-P-F	95.8(4) 95.2(4)	F-P-F	91.1(3)
F-P-S	112.93(15) 110.48(15) 111.02(16) 111.29(15)	F-P-S	112.3(2) 112.9(3) 112.0(3) 110.6(2)	F-P-S	112.5(3) 111.0(3) 112.5(3) 111.9(3) 112.1(3) 113.2(3) 111.9(3) 111.1(3)	F-P-S	107.90(17) 111.14(19) 109.00(19) 108.01(18)
S-P-S	114.11(7)	S-P-S	112.55(11)	S-P-S	112.22(18) 112.12(17)	S-P-S	124.55(13)
P-Ru-P	166.42(4)	P-Ru-P	101.30(5)	P-Ru-P	99.01(10)		

Table 5.2: Selected bond lengths(Å) and bond angles(°) of $RuH(CO)(S_2PF_2)(PPh_3)_2$, $RuCl(CO)(S_2PF_2)(PPh_3)_2$, $Ru(S_2PF_2)_2(PPh_3)_2$ and $[N^nPr_4][S_2PF_2]$

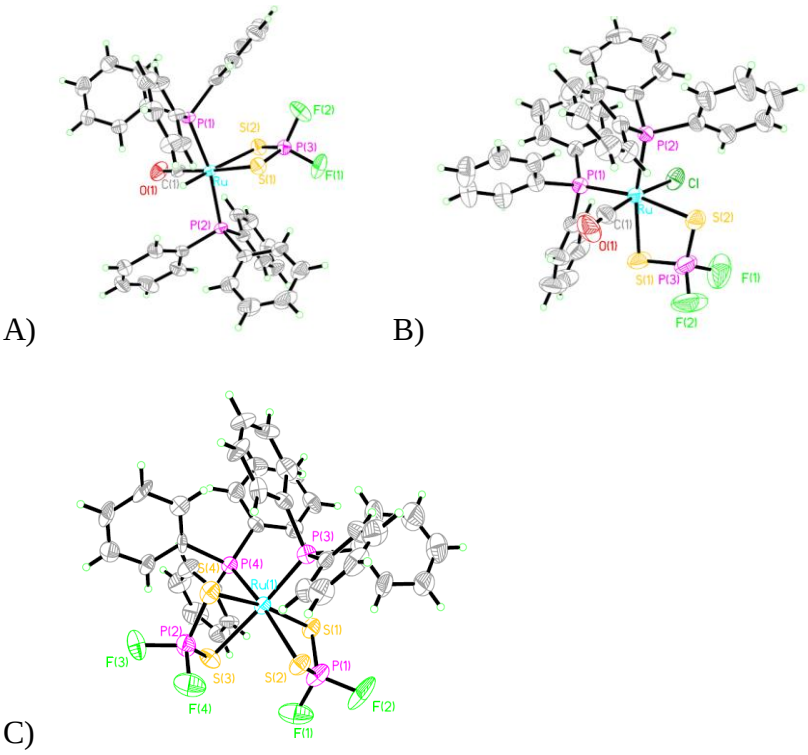

Figure 5.4: ORTEP diagram of A) $RuH(CO)(S_2PF_2)(PPh_3)_2$ (2) and B) $RuCl(CO)(S_2PF_2)(PPh_3)_2$ (3) and C) $Ru(S_2PF_2)_2(PPh_3)_2$ (4) with 40% thermal ellipsoids. Solvates were omitted for clarity.

A comparison with complexes of a different small sulfur-containing ligand, the primary dithiocarbamate analogues $RuH(CO)(S_2CNH_2)(PPh_3)_2$ and $RuCl(CO)(S_2CNH_2)(PPh_3)_2$ reveals several interesting features.[42] Chlorination of the hydrido complexes with N-chlorosuccinimide results in a change in the geometry of the triphenylphosphines from *trans* to *cis* in both cases. Small differences in the IR frequencies are observed. Higher $\Delta(\nu(C=O))$ carbonyl stretching frequencies are found for the S_2PF_2 complexes compared to the pair of S_2CNH_2 complexes: of 11 cm^{-1} for the pair of hydrido complexes and 23 cm^{-1} for the pair of chloro complexes. This can be attributed to less electron density being donated to the metal by the S_2PF_2 ligand resulting in weaker π-backbonding to the carbonyl compared to the S_2CNH_2 complexes. Finally, the strong carbonyl stretching band at 1937.0 cm^{-1} in **2** is at the high end of the range[42] for isostructural $RuH(CO)(chelateanion)(PPh_3)_2$ and also suggests weak σ-donation by the $S_2PF_2^-$ anion, or perhaps a degree of π-backbonding. Structurally, significantly larger ligand bite angles and longer Ru-S bond lengths are observed in the S_2PF_2 complexes. Overall, the comparison between

these two types of ligands suggests poorer donating capabilities of the difluorodithiophosphate ligand compared to the dithiocarbamate.

2		$RuH(CO)(S_2CNH_2)(PPh_3)_2$		**3**		$RuCl(CO)(S_2CNH_2)(PPh_3)_2$	
Bonds	Å	Bonds	Å	Bonds	Å	Bonds	Å
Ru-S	2.5472(12) 2.5795(12)	Ru-S	2.4950(10) 2.5228(10)	Ru-S	2.5186(17) 2.5223(16)	Ru-S	2.4195(15) 2.4390(15)
Ru-C	1.820(4)	Ru-C	1.858(6) 1.872(13)	Ru-C	1.843(7)	Ru-C	1.979(9)*
C-O	1.153(5)	C-O	1.181* 1.160*	C-O	1.123(7)	C-O	0.866*
Ru-P	2.3623(10) 2.3704(10)	Ru-P	2.3673(10) 2.3513(9)	Ru-P	2.3807(15) 2.3629(14)	Ru-P	2.3985(15) 2.3914(15)
Angles	°	Angles	°	Angles	°	Angles	°
S1-Ru-S2	78.91(4)	S1-Ru-S2	69.79(3)	S1-Ru-S2	79.79(6)	S1-Ru-S2	71.82(5)
P1-Ru-P2	166.42(4)	P1-Ru-P2	171.21(3)	P1-Ru-P2	101.30(5)	P1-Ru-P2	106.84(5)
ν(CO)	cm^{-1}	ν(CO)	cm^{-1}	ν(CO)	cm^{-1}	ν(CO)	cm^{-1}
	1937.0		1926.5		1964.0		1940.7

Table 5.3: Comparison of structural features of 2 and 3 with $RuH(CO)(S_2CNH_2)(PPh_3)_2$ and $RuCl(CO)(S_2CNH_2)(PPh_3)_2$. *ESD's are not listed due to the presence of Cl/CO disorder which also accounts for their aberrant Ru-C and C-O bond lengths.

An example of the utility of the ^{31}P and ^{19}F NMR in the characterization of these complexes is the consequences of the relative orientations of the fluorine atoms in the S_2PF_2 ligands with the other ligands in **2** and **3** or relative to each other in **4**. In **2**, the equivalent fluorines result in a simple triplet in the ^{31}P spectrum for the difluorodithiophosphate. Coupling of the fluorines to the S_2PF_2 phosphorus, hydride and triphenylphosphine phosphorus results in a doubled triplet of doublets in the ^{19}F NMR spectrum. On the other hand, the inequivalent fluorines due to *cis-trans* isomerization upon chlorination in **3** results in two inequivalent fluorides with a germinal $^2J_{FF}$ coupling of 96.2 Hz in the ^{19}F NMR spectrum. Finally, the chiral nature of the bis-S_2PF_2

complex would result in diastereotopic fluorine atoms. However, in solution there is only a triplet in the ^{31}P NMR and a complete absence of signal in the ^{19}F NMR in all NMR solvents. This is clearly due to dynamic exchange resulting in equivalent fluorines. The presence of a fluorine signal in **4** was confirmed as broad signals in the solid-state NMR. The NMR data with multiplicities and associated coupling constants is summarized in Table 5.4.

Complex	**2**		**3**		**4**	
Nucleus	^{31}P	^{19}F	^{31}P	^{19}F	^{31}P	^{19}F
Solvent	CD_2Cl_2		CD_2Cl_2		CD_2Cl_2	
Multiplicity	t	dtd	dd	2 ddt	t	N/A
Chemical Shift (ppm)	87.74	3.11	93.19	1.89 -7.43	85.91	
Coupling constants (Hz)	$^1J_{PF}$=1279.4 $^4J_{PF}$=36.1 $^4J_{HF}$=3.0		$^1J_{PF}$=1290.9 $^2J_{FF}$=96.2 $^4J_{PF}$=8.1 $^1J_{PF}$=1303.4 $^2J_{FF}$=97.0 $^4J_{PF}$=8.1		$^1J_{PF}$=1321.9	

Table 5.4: Comparison of ^{31}P and ^{19}F NMR of complexes 2, 3, and 4

A comparison of the $^1J_{PF}$ coupling constants, P-F bond lengths and P-F symmetric and asymmetric stretches in the IR is presented in Table 5.5. Upon coordination, little change in the symmetric and asymmetric P-F stretches are observable. Calculated frequencies in $Co(S_2PF_2)(CO)_3$ (Table 5.1) are in good agreement with those found experimentally.

The most remarkable difference between the free ligand and complexes is seen in the significant increases, 100 to 150 Hz, in the $^1J_{PF}$ coupling constant. The value of the coupling constant is related to the s-character of the P-F σ-bond, this result suggests stronger s-character of the P-F bonds in the complexes than in the S_2PF_2 ligand. In valence bond terms this may be due to different hybridization of the phosphorus(V) center in the anion vs. the complexes. The structural data (Table 5.2) highlights changes in the geometry of the phosphorus upon coordination. Mainly, a remarkable decrease of 12 ° in the S-P-S angles is observed in the complexes from 124.55(13) ° to 112.55(11) °: this is closer to the ideal tetrahedral value of 109.5 ° and may suggest a formally sp^3 hybridized P(V) in the complex and dsp^3 hybridized P(V) in the free ligand. This is consistent with the differences in observed $^1J_{PF}$ values.

.	$^1J_{PF}$ (Hz)	P-F bond lengths (Å)	P-F asymmetric stretch (cm^{-1})	P-F symmetric stretch (cm^{-1})
1	1150.1	1.559(4) 1.586(4)	876.7	836.6
2	1279.4	1.548(3) 1.546(3)	873.0	836.0
3	1290.9 1303.4	1.551(6) 1.499(5)	880.8	849.2
4	1321.9	1.588(7) 1.548(6) 1.557(6) 1.548(6)	873.8	839.0

Table 5.5: Comparison of $^1J_{PF}$, P-F bond lengths and P-F stretches of 1, 2, 3 and 4

$$Ru(S_2PF_2)_2(PPh_3)_2 + CO \xrightarrow[10min]{DCM} Ru(CO)(\eta^1\text{–}S_2PF_2)(\eta^2\text{–}S_2PF_2)(PPh_3)_2 \quad (5)$$

4 **5**

The dynamic nature of **4** was tested further by a carbonylation reaction: the complex was dissolved in dichloromethane and stirred under a stream of CO for 10 min during which time the solution turned from orange to light yellow (eq 5). Crystals were obtained by setting a solution of the product in a 50/50 mixture of DCM/hexanes at -20 °C overnight. We hypothesized that the lability of the complex leads to formation of a 5-coordinate intermediate and addition of CO in the coordination sphere, resulting in a product with a mixture of monodentate and bidentate S_2PF_2 ligands. This was confirmed by both X-ray diffraction and NMR characterization. One single CO stretch in the IR spectrum of the product obtained was observed.

Diffraction grade crystals allowed for the unambiguous determination of the product as having a *trans* triphenylphosphine geometry, and the presence of both mono- and dihapto coordination modes for the difluorodithiophosphate in the solid state structure of *trans*-Ru(CO)(η^1-S_2PF_2)(η^2-S_2PF_2)$(PPh_3)_2$ (Figure 5.5).

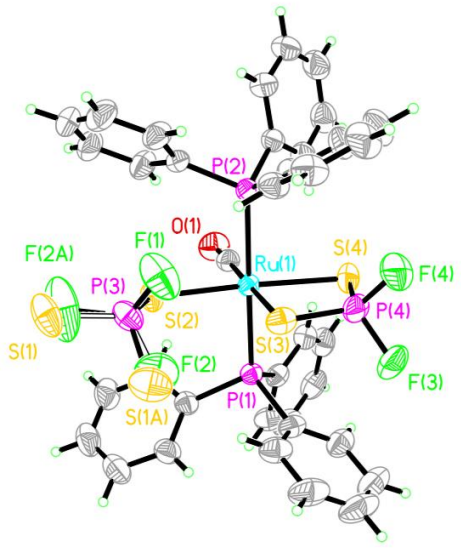

Figure 5.5: ORTEP diagram of trans-Ru(CO)(η^1-S_2PF_2)(η^2-S_2PF_2)(PPh_3)$_2$. For the η^1-difluorodithiophosphate the two disordered positions for F(2) and S(1) are shown. The disordered CH_2Cl_2 solvate was omitted for clarity.

The different coordination modes of the ligand results in some significant differences especially in terms of bond lengths. There is a 70/30 S/F disorder is present in the monohapto ligand. While the differences in the two Ru-S bond lengths in the dihapto ligand can be attributed to *trans* influence of the CO ligand, the Ru-S bond length is significantly shorter than both by 0.6 to 0.11 Å. The differences are not as clear in the P-S distances to the coordinating sulfurs. In the monohapto ligand, the terminal P-S bond is significantly shorter indicating a more double bonded-character for this bond vs. a single bonded or intermediate character for the coordinating P-S bond. In both ligands, the similar P-F bond lengths are consistent with equivalent fluorines.

The presence of equivalent triphenylphosphines and fluorines for both the monohapto ligand and the dihapto ligand would result in two fluorine signals in the ^{19}F-NMR in addition to two triplets and one singlet in the ^{31}P NMR. Surprisingly, the ^{31}P-NMR signal of both the precipitated product as well as the redissolved X-ray diffraction crystals gave two S_2PF_2 triplets and two triphenylphosphine signals, while the ^{19}F-NMR spectra resulted in four doublets of doublets. This can best be explained as being the NMR signature of the *cis*-PPh_3 isomer where all four fluorines are inequivalent and the two triphenylphosphines are *trans* to different ligands.

Concentration of the contents of the NMR tube followed by crystal growth in CH_2Cl_2/hexanes at -20 °C confirmed the formation of the *cis* isomer (Figure 5.6).

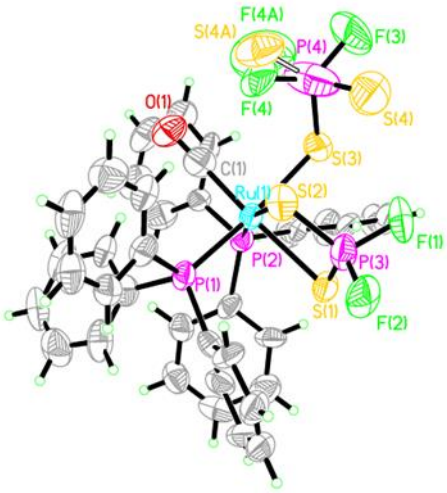

Figure 5.6: ORTEP diagram of *cis*-Ru(CO)(η^1-S_2PF_2)(η^2-S_2PF_2)(PPh_3)$_2$. Note the two disordered positions for F(4) and S(4) for the η^1-S_2PF_2 ligand. The disordered CH_2Cl_2 solvate was omitted for clarity.

Trans isomer				Cis isomer			
η^1-S_2PF_2		η^2-S_2PF_2		η^1-S_2PF_2		η^2-S_2PF_2	
Bonds	Å	Bonds	Å	Bonds	Å	Bonds	Å
Ru-S	2.4231(9)	Ru-S	2.4801(10) 2.5341(10)	Ru-S	2.502(4)	Ru-S	2.518(4) 2.528(4)
P-S (coordinated) (terminal)	1.9631(14) 1.915(6) 1.806(15)	P-S	1.9443(15) 1.9610(15)	P-S (coordinated) (terminal)	1.947(7) 1.843(19) 1.787(16)	P-S	1.953(6) 1.945(6)
P-F	1.559(3) 1.55(3) 1.539(10)	P-F	1.549(3) 1.546(3)	P-F	1.590(2) 1.570(12) 1.726(19)	P-F	1.528(9) 1.554(9)
Angles	°	Angles	°	Angles	°	Angles	°
F-P-F	98.32(4) 114.9(10)	F-P-F	96.05(17)	F-P-F	133.0(2) 88.4(13)	F-P-F	96.83(5)
S-P-S	116.71(10) 119.01(4)	S-P-S	111.00(6)	S-P-S	96.91(7) 134.72(7)	S-P-S	111.72(3)

Table 5.6: Selected bond lengths and angles of monohapto vs. dihapto S_2PF_2 in *trans*-Ru(CO)(η^1-S_2PF_2)(η^2-S_2PF_2)(PPh_3)$_2$. S/F disorder in the monohapto ligand account for large differences in bond lengths and angles

This would suggest *cis-trans* isomerization in solution likely occurs via a dissociative mechanism with the formation of a five-coordinate intermediate followed by a Berry-type pseudo rotation. The structure of the *cis*-isomer in solution was confirmed by diffraction of single crystals obtained by evaporation of contents of the NMR tube and growth in CH_2Cl_2/hexanes at -20˚C. The facile carbonylation of **4** as well as *cis-trans* isomerization in solution of the product confirms the lability of the S_2PF_2 ligand.

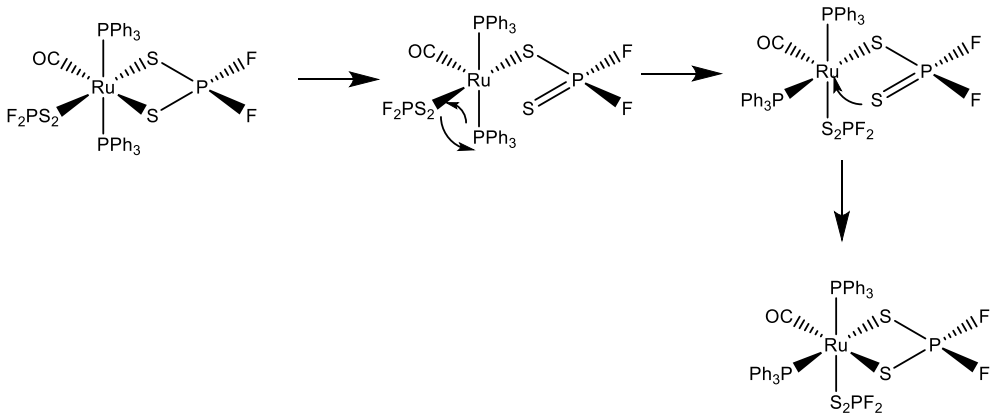

Scheme 5.1: Proposed mechanism for the cis-trans isomerization of 5

5.5 Conclusion

Simple substitution reactions of $[N^nPr_4][S_2PF_2]$ in metal complexes, rather than the here-to-fore employed oxidative addition to a metal with the acid HS_2PF_2, results in Ru(II) complexes which are temperature, air, and water stable. The presence of the difluorodithiophosphate ligand as co-ligands with hydrides, carbonyls, and triphenylphosphines results in readily characterizable complexes by ^1H, ^{31}P and ^{19}F NMR as well as IR spectroscopy. The crystal structure of the ligand as well as the first example of structural determination of complexes of S_2PF_2 provides an insight into the bonding of this useful but understudied ligand. Carbonylation of complex **4** confirmed its dynamic nature and resulted in the formation of a complex with a rare example of a complex containing both monohapto/dihapto thiophosphate ligands. Overall, while Ru(II) complexes of S_2PF_2 can be easily prepared and characterized, the hemilability and poor donor capabilities of the ligand may limit their utility for PVED research. Whether this behavior is also observed in the more inert Os(II) system is of potential interest.

5.6 Experimental

The starting materials P_4S_{10}, $NaHF_2$ and N-chlorosuccinimide were purchased and used without further purification. $RuHCl(CO)(PPh_3)_2$ and $RuCl_2(PPh_3)_3$ were synthesized according to literature procedures.[47] IR spectra were measured on Bomem MB3000 FTIR spectrometer as KBr pellets, and ^1H, $^{31}P\{^1H\}$ and ^{19}F NMR spectra were measured on a Bruker AVIIIHD 500 spectrometer at 22°C at 500.00 MHz for ^1H, 470.59MHz for ^{19}F and 202.46 MHz for ^{31}P.

5.6.1 Syntheses

$[N^nPr_4][S_2PF_2]$ (1): Phosphorus pentasulfide (1.1 g) and 4 equivalents of $NaHF_2$ (0.61 g) were dissolved in acetonitrile (50 mL) and heated to reflux for 30 min. The solvent was removed *in vacuo* and the remaining product was dissolved in water, to give a cloudy off orange solution. This was clarified by filtration through celite before crystallization as a tetraalkylammonium salt. N^nPr_4Br (1.5g) was dissolved in water and added to the solution causing the precipitation of a white product. A second recrystallization from 20 mL of methanol, and heated until dissolution at 40 °C, followed by the slow addition of water, 40mL, to affect crystallization of $[N^nPr_4][S_2PF_2]$ in 60% overall yield. DSC: m.p. T=164°C ΔH=18.2 J/g IR (KBr, cm^{-1}): 2968.0m, 2877.9m, 1474.3vs, 1325.6s, 1100.1s, 971.3vs, 959.1vs, 876.7s, 836.6s, 804.4s, 772.2s, 707.1s, 533.3vs, ^{31}P-NMR (CD_2Cl_2): 116.46 (t, $^1J_{PF}$= 1150.2Hz) ^{19}F-NMR (CD_2Cl_2): -1.71(d, $^1J_{PF}$=1150.2Hz).

$[RuH(CO)(MeCN)_2(PPh_3)_2]ClO_4$: The complex was synthesized according to literature procedures.[42] $RuHCl(CO)(PPh_3)_3$, (569 mg), was suspended in 15 mL dichloromethane. Most of the complex dissolved to give a grey-yellow solution. Perchloric acid as 80% $HClO_4$ in water, 50 mg acid in 17 mg solution, 2.5 equiv, was added with 30 mL of acetonitrile. A clear slight yellow solution resulted instantly. After stirring 5 min at 22 °C. 30 mL of a 50/50 ethanol/isopropanol solution was added and the volatile components removed in vacuo on a rotary evaporator to give a massive white solid suspended in 5 mL or solvent. This was diluted with a further 30 mL isopropanol and concentration continued to a volume of 10 mL. The white crystal mass was

filtered and washed with isopropanol, 3x 10 mL, and n-hexane, 2 x 10 mL, to give 468 mg of white solid after drying. Yield 87%.

$RuH(CO)(S_2PF_2)(PPh_3)_2$ (2): $[RuH(CO)(MeCN)_2(PPh_3)_2]ClO_4$, 152 mg, was dissolved in 10 mL dichloromethane and treated with 86 mg, 1.5 equivalents of $[N^nPr_4][S_2PF_2]$, dissolved in 10 mL dichloromethane. On mixing the solution turned an instant lemon yellow solution from which light yellow crystals of product were isolated by concentrating the solution to 5 mL after 15 minutes standing in solution. Filtration of the crystals followed by washing with ethanol, 2x10 mL, and n-hexane, 5 mL, gave 129 mg, 91 % yield. Recrystallization from dichloromethane/ethanol gave long needles. DSC: T=142.3˚C ΔH=12.1 J/g; 216.7 ˚C, 29.4 J/g (irreversible decomposition.) IR (KBr, cm^{-1}): 1989.1w,(ν(Ru-H); 1937.0s, (ν(CO)); 873.0s, (ν_{asym} (PF_2)); 836.1s, (ν_{sym} (PF_2)); 808.2s 698. br, (ν_{asym} (PS_2)); 520 br, (ν_{sym} (PS_2)). ^{1}H NMR (500 MHz, CD_2Cl_2) ppm: δ -12.17 (tt, 1, Ru-H, $^2J_{P\text{-}H}$ = 20.3, $^4J_{H\text{-}F}$ = 3.4 Hz), 7.33 (m, 24, PPh_3), 7.59 (m, 6, PPh_3). ^{31}P NMR (202.46 MHz, CD_2Cl_2) ppm: δ = 43.4 (s(br), 2, PPh_3), 87.74(t, 1, $^1J_{P\text{-}F}$ = 1279.4 Hz, S_2PF_2). ^{19}F NMR (470.59 MHz, CD_2Cl_2) ppm: δ = 3.11 (dtd, 2,$^1J_{P\text{-}F}$ = 1279.4, $^4J_{P\text{-}F}$ = 36.1, $^4J_{H\text{-}F}$ = 3.0 Hz, S_2PF_2). Elemental analysis calcd for $C_{37}H_{31}F_2OS_2P_3Ru.CH_2Cl_2$ (confirmed by x-ray diffraction) (787.77 g mol^{-1}) % C, 52.30; H, 3.81. Found % C 52.10 H: 3.88

$RuCl(CO)(S_2PF_2)(PPh_3)_2$ (3): $[RuH(CO)(S_2PF_2)(PPh_3)_2]$, 52 mg, was treated with 11 mg N-chlorosucinimide, 1.25 equivalents, and the mixture was dissolved in 30 mL of dichloromethane. Within 20 min the solution took on a deep yellow color and after 20 min the solution was diluted with 20 mL ethanol and then concentrated to 5 ml to give an orange/yellow crystal mass which was isolated by filtration and washing with ethanol (2 x 10 mL) and 5 mL hexane. Yield 37%, 20 mg. Crystals grown from dichloromethane/isopropanol. DSC: T=242.09˚C ΔH=8.7 J/g IR (KBr, cm^{-1}): 1988.9w, 1964.0s, (ν(CO)); 880.8s, (ν_{asym} (PF_2)); 849.2w, (ν_{sym} (PF_2)); 698. ^{1}H NMR (500 MHz, CD_2Cl_2) ppm: δ 7.43 (m, 24, PPh_3), 7.51 (m, 6, PPh_3). ^{31}P NMR (202.46 MHz, $CDCl_3$) ppm: δ = 37.04 (t, 2, $^4J_{P\text{-}F}$ = 8.1, PPh_3), 93.19(dd, 1, $^1J_{P\text{-}F}$ = 1303.4, 1290.9 Hz, S_2PF_2). ^{19}F NMR (470.59 MHz, $CDCl_3$) ppm: δ = 1.89 (ddt, 1,$^1J_{P\text{-}F}$ = 1290.0, $^4J_{P\text{-}F}$ = 8.1 $^2J_{F\text{-}F}$ = 96.2 Hz, S_2PF_2) –7.43 (ddt, 1,$^1J_{P\text{-}F}$ = 1303.4, $^4J_{P\text{-}F}$ = 8.1, $^2J_{F\text{-}F}$ = 97.0 Hz, S_2PF_2) Elemental analysis calcd. for $C_{37}H_{30}F_2OS_2P_3RuCl$. (822.21 g mol^{-1}) % C, 54.05; H, 3.68. Found % C 53.83 H: 3.81

$Ru(S_2PF_2)_2(PPh_3)_2$ (4): $[RuCl_2(PPh_3)_3]$, 122 mg, was treated with 102 mg of $[N^nPr_4][S_2PF_2]$, 2.5 equivalents, in 40 mL of dichloromethane at room temperature. Within 20 min the solution went from a brown-red to a bright orange. After diluting the solution to 50 mL with ethanol and concentrating to ~ 10 ml the deep orange crystal mass was isolated by filtration and washing with ethanol (2x10mL) and 5 mL hexane. Yield 88%, 102 mg. Crystals grown from dichloromethane/ethanol. DSC: T=175.8°C ΔH=8.5 J/g; 207.6°C, (irreversible decomposition with endothermic onset and exothermic tail.) IR (KBr, cm^{-1}): 873.8s, 839.8m, 741.5m, 698.9s, 519.5s, $F_2PS_2^-$ bands. ^1H NMR (500 MHz, CD_2Cl_2) ppm: δ 7.43 (m, 4, PPh_3), 7.35 (m, 4, PPh_3), 7.27 (m, 12, PPh_3), 7.21 (m, 10, PPh_3). ^{31}P NMR (202.46 MHz, CD_2Cl_2) ppm: 85.91 (t, 2, $^1J_{PF}$=1321.9Hz, S_2PF_2) 43.80 (s, 2, PPh_3) ^{19}F NMR (470.59 MHz, CD_2Cl_2): absence of signal due to dynamic behaviour, ^{19}F NMR (470.59 MHz, SS-NMR) ppm: -9.4ppm (br s), -19.83 (br t) Elemental analysis calcd for $C_{36}H_{30}F_4S_4P_4Ru.C_2H_5OH$ (Confirmed by X-ray diffraction) (891.85 g mol^{-1}) % C, 48.98; H, 3.24. Found % C 49.00 H: 3.34

Carbonylation of $Ru(S_2PF_2)_2(PPh_3)_2$, 4, to give 5 as an isomeric mixture with *cis* with and *trans* PPh_3.

$Ru(S_2PF_2)_2(PPh_3)_2$ (100 mg) was dissolved in 20 mL of DCM and treated with a stream of CO gas for 10 min during which the solution turned from orange to pale yellow. The solvent was evaporated to ca. 5 mL and 20 mL of hexanes was added to the solution. The mixture was reduced to 5 mL *in vacuo* resulting in the precipitation of a yellow solid. The precipitate was filtered and washed with hexanes (10 mL) and ethanol (10 mL). Yield: 61 mg (59%) X-ray diffraction grade crystals were obtained by dissolution in 5 mL of 50/50 DCM/hexanes and stored over several days at -20°C. DSC: thermally stable up to 300° IR (KBr, cm^{-1}): 1963.5vs (ν(CO)), 894.7s, 746.6s, 682.2s, 514.7s ^1H NMR (500 MHz, CD_2Cl_2) ppm: δ 7.75 (m, 2, PPh_3), 7.59 (m, 6, PPh_3), 7.50 (m, 12, PPh_3), 7.38 (m, 10, PPh_3) ^{31}P NMR (202.46Hz, CD_2Cl_2) ppm: 93.34 (t, 1, $^1J_{PF}$=1295.0Hz, S_2PF_2) 90.25 (t, 1, $^1J_{PF}$=1313.5Hz, S_2PF_2) 49.08 (s, 2, PPh_3) ^{19}F NMR (470.59 MHz, CD_2Cl_2): 4.54 (dd, 1, $^1J_{PF}$=1293.6.5Hz , $^2J_{FF}$=93.4Hz) 2.67 (ddd, 1, $^1J_{PF}$=1313.0Hz , $^2J_{FF}$=96.4Hz, $^4J_{PF}$=5.8Hz), -7.12 (dd, 1, $^1J_{PF}$=1313.7Hz , $^2J_{FF}$=95.0Hz) -11.22 (dd, 1, $^1J_{PF}$=1295.6Hz , $^2J_{FF}$=93.4Hz). Elemental analysis calcd for $C_{36}H_{30}F_4S_4P_4Ru$: (919.78 g mol^{-1}) % C, 48.31; H, 3.29. Found % C 48.44 H, 3.37.

5.6.2 Theoretical calculations

Density functional theory implemented on Gaussian16 with B3LYP functionals were used with cc-pvdz, cc-pvtz, and aug-cc-pvtz basis sets. Metric and spectroscopic data presented correspond to local minima with all positive vibrational frequencies.

5.6.3 Crystallographic Methodologies

Crystals are mounted on glass fibers with epoxy resin on Mitegen mounts using Paratone-N from Hampton Research and single-crystal X-ray diffraction experiments are carried out with a BRUKER APEX-II D8 CCD diffractometer by using graphite-monochromated Mo Kα radiation (λ = 0.71073 Å) the SHELX package[48] is used for integration of the intensity reflections, scaling, and absorption correction. Intrinsic phasing methods were used to solve the structures. Non-hydrogen atoms are located by difference Fourier maps and final solution refinements are carried out by full-matrix least-squares methods on F2 for all of the data. The hydrogen atoms are placed in calculated positions and were not refined. Disordered solvates were found in complexes **2, 4** and *cis* and *trans* isomers of **5**: CH_2Cl_2 in **2** and **5** and ethanol for **4**. The solvates were refined anisotropically.

5.7 References

1. Corbridge, D. E. C.: Phosphorus: An Outline of Its Chemistry, Biochemistry,and Technology; 4th ed.; Elsevier: Amsterdam, **1990**.
2. Wasson J. R.; Woltermann G. M.; Stoklosa H. J.: Transition Metal Dithio- and Diselenophosphate Complexes. *Inorg. Chem.*, **1973**, 65-129.
3. Sánchez G. ; Garcia J. ; Meseguer D. J. ; Serrano J. L.; Perez J.; Molins E. ; G. Lopez G.: Organometallic Nickel(II) Complexes with Dithiophosphate, Dithiophosphonate and Monothiophosphonate Ligands, *Inorg. Chim. Acta*, **2004**, *357*, 677-683.
4. Fackler Jr J. P.; Thompson L. D.; Lin I. J. B.; Stephenson T. A.; Gould R. O.; Alison J. M. C.;Fraser A. J. F.: Phosphine Adducts to Palladium(II) and Platinum(II) 1,1-Dithiolates. Single Crystal X-Ray Structures of Bis(diethyldithiocarbamato)(triphenylphosphine)platinum(II), Bis(diphenylphosphinodithioato)(triphenylphosphine)palladium(II), Bis(O,O-diethyl dithiophosphato)(triphenylphosphine)platinum(II), and (diphenylphosphinodithioatobis(triethylphosphine)palladium(II) diphenylphosphinodithioate. Solution Phosphorus-31 NMR Studies of the Dithiophosphate Complexes, *Inorg Chem*, **1982**, *21*, 2397-2403.
5. Haiduc I.; Goh L. Y.: Reactions of Bis(thiophosphoryl)disulfanes and Bis(thiophosphinyl)disulfanes with Metal Species: an Alternative, Convenient Route to Metal Complex and Organometallic Dithiophosphates and Dithiophosphinates *Coord. Chem. Rev.*, **2002**, *224*, 151-170
6. McCleverty J. A.; Kowalski R. S. Z.; Bailey N. A.; Mulvaney R.; O'Cleirigh D. A.: Aspects of the Inorganic Chemistry of Rubber Vulcanisation. Part 4. Dialkyl- and Diaryl-Dithiophosphate and -Dithiophosphinate Complexes of Zinc: Phosphorus-31 Nuclear Magnetic Resonance Spectral Studies and Structures of $[NMe_4][Zn\{S_2P(OC_6H_4Me\text{-}p)_2\}_3]$ and $[NEt_4][Zn(S_2PPh_2)_3]$ *J. Chem. Soc., Dalton Trans.*, **1983**, *4*, 627-634.

7. Barrado G.; Miguel D.; Riera V.; Garcia-Granda S.:, η^3-Allyl Molybdenum Dithiophosphate and Dithiophosphinate Complexes with Uni- and Bidentate Nitrogen Donor Ligands. X-Ray Structure of $[Mo_2(\eta^3\text{-}C_3H_5)_2(CO)_4\{S_2P(OEt)_2\}_2(\mu\text{-}NH_2NH_2)]$*J. Organomet Chem*, **1995**, *489*, 129-135.
8. van Zyl W. E.; Lopez de Luzuriaga J. M.; Fackler Jr J. P.; Staples R. J.: Dithiophosphinates of Gold(I); Oxidative Addition of Cl_2 to a Neutral, Dinuclear Gold(I) Dithiophosphinate Complex, and X-Ray Crystal Structures of $[AuS_2P(C_2H_5)_2]_2$, $[AuS_2PPh_2]_2$, $Au_2(CH_2)_2PMe_2(S_2PPh_2)$, and $Au_2Cl_2[(CH_2)_2PMe_2][S_2PPh_2]$*Can. J. Chem.*, **2001**, *79*, 896-903.
9. van Zyl W. E.; Staples R. J.; Fackler Jr J. P.: Dinuclear Gold(I) Dithiophosphonate Complexes: Formation, Structure and Reactivity *Inorg. Chem. Commun.*, **1998**, *1*, 51-54.
10. Haiduc I.; Sowerby D. B.; Lu S. F.: Stereochemical Aspects of Phosphor-1,1-dithiolato Metal Complexes (Dithiophosphates, Dithiophosphinates): Coordination Patterns, Molecular Structures and Supramolecular Associations—I *Polyhedron*, **1995**, *14*, 3389-3472.
11. Haiduc I.; David L.; Cozar O.; Micu-Semeniuc R.; Mezei G.; Armenean M.: Spectroscopic and Magnetic Studies of Some Copper(II) and Chromium(III) Complexes with Dithiophosphonates as Ligands *J. Mol. Struct.*, **1999**, *482*, 153-157.
12. Mastin T. W.; Norman G. R.; Weilmuenster E. A.; Chemistry of the Aliphatic Esters of Thiophosphoric Acids. I *J. Am. Chem. Soc.*, **1945**, *67*, 1662-1664.
13. Roesky, H. W.: Darstellung und untersuchung von dichlorothiophosphaten und chlororfluorothiophosphaten. *Chem Ber.*, **1967**, *100*, 1447-1450
14. Roesky, H. W.: Darstellung und Untersuchung von Difluorothiophosphaten., *Chem Ber.*, **1967**, *100*, 950-953
15. Lustig, M.; Ruff, J. K.: Studies Involving Some Nonmetal Oxy and Thiofluoride Salts., *Inorg. Chem.*, **1967**, *6*, 2115-2117
16. Roesky, H. W.; Tebbe, F. N.; Muetterties, E. L.: New Phosphorus-Sulfur Chemistry., *J. Am. Chem. Soc.*, **1967**, *89*, 1272-1274

17. Mitchell, R. W.; Lustig, M.; Hartman, F. A.; Ruff, J. K.; Merritt, J. A.: Synthesis and Properties of Difluorodithiophosphoric Acids., *J. Am. Chem. Soc*., **1968**, *90*, 6329-633
18. Charlton, T. L.; Cavell, R. G.: The Synthesis and Properites of Difluorodithiophosphoric Acid., *Inorg. Chem*., **1969**, *8*, 281-285.
19. Roesky H. W.; Tebbe F. N.; Muetterties E. L.: Thiophosphate Chemistry.1 The Anion Set $X_2PS_2^-$, $(XPS_2)_2S_2^-$, and $(XPS_2)_2S_2^{2-}$ *Inorg. Chem.*, **1970**, *9*, 831-836.
20. Tebbe F. N.; Muetterties E. L.; Metal Complexes of the Difluorodithiophosphate Ligand *Inorg. Chem.*, **1970**, *9*, 629-637.
21. Cavell R. G.; Byers W.; E. D. Day: Metal Complexes of Substituted Dithiophosphinic Acids. I. Complexes of Trivalent Chromium *Inorg. Chem.*, **1971**, *10*, 2710-2715.
22. Cavell R. G.; Day E. D.; Byers W.; Watkins P. M.: Metal Complexes of Substituted Dithiophosphinic Acids. V. Complexes of Manganese, Iron, and Cobalt *Inorg. Chem.*, **1972**, *11*, 1759-1772.
23. Cavell R. G.; Byers W.; Day E. D.; Watkins P. M.: Metal Complexes of Substituted Dithiophosphinic Acids. IV. Complexes of Divalent Nickel, Palladium, and Platinum *Inorg. Chem.*, **1972**, *11*, 1598-1606.
24. Cavell R. G.; Day E. D.; Byers W.; Watkins P. M.: Metal Complexes of Substituted Dithiophosphinic Acids. III. Vanadyl Complexes *Inorg. Chem.*, **1972**, *11*, 1591-1597
25. Cavell R. G. : Sanger A. R.: Metal Complexes of Substituted Dithiophosphinic Acids. VI. Reactions of Difluorodithiophosphinic Acid with Chlorides and Oxychlorides of Chromium, Molybdenum *Inorg. Chem.*, **1972**, *11*, 2011-2016.
26. Cavell R. G.; Sanger A. R.: Metal Complexes of Substituted Dithiophosphinic Acids. VII. Reactions of $TiCl_4$, $VC1_4$, $NbCl_4$, $NbCl_6$, and $TaCl_5$ with Difluorodithiophosphinic Acid, *Inorg. Chem.*, **1972**, *11*, 2016-2019.
27. Hartman F. A.; Lustig M.: Preparation and Reactions of Tetracarbonyl-μ-bis(difluorodithiophosphato)-dirhodium(I)*Inorg. Chem.*, **1968**, *7*, 2669-2670.
28. Islam M. Q.; Hill W. E.; Webb T. R.; Quadruply Bonded Dimolybdenum Complexes of $PF_2S_2^-$. Comparison with Complexes of PR_2S_{2p-} (R= Et, Me) *J. Fluor. Chem.*, **1990**, *48*, 429-440

29. Medcraft C.; Wolf R.; Schnell M.: High-Resolution Spectroscopy of the Chiral Metal Complex [CpRe(CH_3)(CO)(NO)]: A Potential Candidate for Probing Parity Violation *Angew. Chem. Int. Ed.*, **2014**, *53*, 11656-11659
30. Gaydon Q.; Bohle I. J.; Bohle D. S. : Fluxionality in the Tropolone Hinokitiol Chelate *Inorg. Chem.* **2021**, *60*, 3305-3313
31. Xiang L. ; Zhang Q. F. ; Leung H. W.: Syntheses and Molecular Structures of Ruthenium Complexes with Dithiophosphate Ligands. *J. Coord. Chem.*, **2005**, *58*, 1299-1305
32. Deshpande S. S.; Gopinathan S.; Gopinathan C.: Insertion Reactions of Acrylonitrile with Hydridocarbonylbis(triphenylphosphine)ruthenium(II) Carboxylates *J. Organomet. Chem.*, **1989**, *378*, 103-107
33. Rosales M.; Alvarado B.; Arrieta. F.; De La Cruz C.; Gonzalez A.; Molina K.; Soto O.; Salazar Y.: A General Route for the Synthesis of Hydrido-Carboxylate Complexes of the Type MH(CO)(κ^3-OCOR)(PPh_3)$_2$ [M = Ru, Os; R = CH_3, CH_2Cl, C_6H_5, $CH(CH_3)_2$] and Their Use as Precatalysts for Hydrogenation and Hydroformylation Reactions *Polyhedron*, **2008**, *27*, 530-536
34. Simmons M.; Cumming Premack K.; Guerra E. D.; Bohle M. J.; Rosadiuk K. A.; Bohle D. S.: 2,3,5-Metallotriazoles: Amphoteric Mesoionic Chelates from Nitrosoguanidines *Inorg. Chem.*, **2021**, 60, 9621-9630
35. Menon M.; Pramanik A.; Bag N.; Chakravorty A.: Geometrical Preference of Ruthenium Oxidation States: Metal Redox and Isomerisation of [Ru(S_2CNEt_2)$_2$(PPh_3)$_2$]$^{0,+}$ *J. Chem. Soc., Dalton Trans.*, **1995**, 1543-1547.
36. Thornback J. R.; Wilkinson G.: Schiff-Base Complexes of Ruthenium(II) *J. Chem. Soc., Dalton Trans.*, **1978**, 110-115.
37. Bhattacharya S.; Pierpont C. G.: Structure and Bonding in Bis(quinone) Complexes of Ruthenium. Synthesis and Characterization of the Ru(PPh_3)$_2$(SQ)$_2$ (SQ = 3,5-tert-butylsemiquinone, tetrachloro-1,2-semiquinone) Series *Inorg. Chem.*, **1991**, *30*, 1511-1516.
38. Ülküseven B.; Bal-Demirci T.; Akklurt M.; Pinar Yalcin S.; Buyukgungor O.: Chelate Structures of 5-(H/Br)-2-hydroxybenzaldehyde-4-allyl-thiosemicarbazones (H_2L):

Synthesis and Structural Characterizations of [Ni(L)(PPh_3)] and [Ru(HL)$_2$(PPh_3)$_2$] *Polyhedron*, **2008**, *27*, 3646-3652.

39. Seddon, E. A.; Seddon, K. R.: *The Chemistry of Ruthenium*; Elsevier: Amsterdam, **1984**
40. Hoffman P. R.; Caulton K. G.; Solution Structure and Dynamics of Five-Coordinate d^6 Complexes *J. Am. Chem. Soc.*, **1975**, *97*, 4221-4228.
41. Meisel M.: On the Nucleophilic Degradation of Phosphorus Chalcogenides with Adamantane-Like Structure by Fluorides. *Phosphorus Sulfur Silicon Relat Elem*, **1990**, *51*, 137-140.
42. Fernandez E. J.; Lopez-de-Luzuriaga J. M.; Monge M.; Olmos E.; Gimeno M. C.; Laguna A.; Jones P. G.: Dithiocarbamate Ligands as Building-Blocks in the Coordination Chemistry of Gold *Inorg. Chem.*, **1998**, *37*, 5532-5536
43. Gaydon, Q.; Bohle, D. S.: Coordination Chemistry of the Parent Dithiocarbamate $H_2NCS_2^-$: Organometallic Chemistry and Trischelates of Group 9 Metals, *Inorg. Chem.*, **2022**, *61*, 4660-4772
44. Nguyen H. H.; Hoang N.; Abram U.: Synthesis and Structures of Two Ruthenium Dibenzoylmethane Triphenylphosphine Mixed Ligand Complexes *Transition Met. Chem.* **2010**, *35*, 89-93
45. Hiett N. P.; Lynam J. M.; Welby C. E.; Whitwood A. C.: Ruthenium Carboxylate Complexes as Easily Prepared and Efficient Catalysts for the Synthesis of β-oxopropyl Esters *J. Organomet. Chem.* **2011**, *696*, 378-387
46. Mishra D.; Naskar S.; Drew M. G. B.; Chattopadhyay S. Y.: Mononuclear and Binuclear Ruthenium (II) Complexes with 4-(phenyl) Thiosemicarbazone of Benzaldehyde: A Discussion on the Relative Stabilities of the Four-membered and Five-Membered Chelate Rings Formed by the Ligand. *Polyhedron*, **2005**, *24*, 1861-1868
47. Collins T. J.; Grundy K. R.; Roper W. R.: The Tris(triphenylphosphine)osmium Zerovalent Complexes Os(CO)$_2$(PPh_3)$_3$, .Os(CO)(CNR)(PPh_3)$_3$, Os(CO)(CS)(PPh_3)$_3$, Os(CS)(CNR)(PPh_3)$_3$ and derived compounds *J. Organomet. Chem.*, **1982**, *231*, 161−172
48. Sheldrick G. M.;, SADABS, TWINABS; Siemens Industrial Automation, Inc.: Madison, WI, **1996**

Chapter 6: Diversity in the Coordination Chemistry of the $[S_5P_2F_2]^{2-}$ Anion to Late Transition Metals

6.1 Preface

In chapter 5, the synthesis of several ruthenium complexes of the $[S_2PF_2]^-$ anion were presented. In the original paper by Tebbe and Roesky describing the synthesis of the ligand, mention of a different fluorodithiophosphate, difluoropentathiodiphosphate, $[N^nPr_4]_2[S_5P_2F_2]$ was made, consisting of two S_2PF units linked by a bridging sulphur atom. Unlike the aforementioned $[S_2PF_2]^-$, no attempts at coordination to transition metals of $[S_5P_2F_2]^{2-}$ have been made Furthermore, the ligand itself was only mentioned once since its original description by Meisel. The presence of the terminal sulphur atoms as well as the same spectroscopic handles present with the $[S_2PF_2]^-$ ligand would make this a good ligand and it is therefore surprising that no attempts at coordination chemistry have been made.

In this chapter we present the crystal structure of the ligand as well as the syntheses of various transition metal complexes of zinc, cadmium, and copper with $[N^nPr_4]_2[S_5P_2F_2]$ that are presented here. The result is a variety of complexes with different ligands and different coordination modes. Crystal structures as well as spectroscopic characterization are provided. Overall, the resulting complexes may have interesting applications in bioinorganic chemistry as protein mimics or in the capping of cadmium sulfide semiconductors.

The work presented in this chapter has been submitted as a communications manuscript: Gaydon Q.; Bohle D. S.: The sulfur rich fluorothiophosphate anions $[S_5P_2F_2]^{2-}$ and $[S_3PF]^{2-}$: cluster and chelation control of P-S heterolysis , *Chem. Eur. J.*, under review

6.2 Abstract

The sulfur rich diphosphate dianion $[S_5P_2F_2]^{2-}$ from fluoride addition to P_4S_{10} has a somewhat checkered history but proves to be the main product of the reaction in acetonitrile. Its optimized synthesis, and structural characterization, as the tetrapropylammonium salt, $[N^nPr_4]_2[S_5P_2F_2]$ allows for the first coordination chemistry for this dianion. Reaction of $S_5P_2F_2$ with d^{10} metals zinc, cadmium, and d^9 copper resulted in a surprisingly diverse array of binding modes and structural motifs. In addition to the simple bis-chelate coordination of $S_5P_2F_2$ with zinc, cleavage of the P-S bond resulted in complexes with the unusual S_3PF fluorothiophosphate. This was observed in two cluster complexes: a trinuclear cadmium complex with mixed $S_5P_2F_2/S_3PF$ ligands, $[Cd_3(S_5P_2F_2)_3(S_3PF)_2]^{4-}$ as well as an octanuclear copper cluster, $[Cu_8(S_3PF)_6]^{4-}$ form at room temperature. These new metal/sulfur/ligand clusters are of relevant to understanding multimetal binding to metallothionines, and to the condensed cadmium chalcogenide semiconductors CdS and CdSe.

6.3 Introduction

Sulfur-containing clusters and nanomaterials of late transition metal chalcogenides are of considerable technological and biological interest. For example, the cadmium sulfide and selenides are important semiconductors;[1,2] their use in nanoparticles is now well advanced. These and related clusters also have considerable interest as models/analogs for the metallothioniens, the multimetal cysteine rich (~30% of residues) metal scavenging protein for zinc, cadmium, mercury, and copper, among many metals. Structural mimics of these proteins with dithiolate ligands include several motifs, such as ZnS_4, Cd_3S_9, Cd_4S_{10}, Hg_4S_6 or Cu_8S_{12} with dithiolate ligands.[3,4] Metallothioneins have important biological roles including heavy metal detoxification or copper homeostasis. It is an important task to have a good mimic of these proteins and therefore easy access to different structural motifs with sulfur donor ligands is required. A limitation of currently known thiolate and sulfide clusters are the long reaction times under high temperature reflux in an inert atmosphere of the ligands.[5,6]

Among sulfur-donor ligands, the fluorothiophosphate are a rare subset of the much wider thiophosphate family. In studying the coordination chemistry of thiophosphates, fluorothiophosphate the advantage of both possessing two NMR-active nuclei, ^{31}P and ^{19}F greatly facilitates their spectroscopic characterization and minimizes charge buildup due to F/S substitution.[7] Several groups described the synthesis of the first fluorothiophosphate anion, S_2PF_2,[8-10] the most thorough by Muetterties, Tebbe, and Roesky, both as the tetrapropylammonium salt and the acid HS_2PF_2.[11] The synthesis of volatile complexes of this ligand were attempted first by Roesky and Muetterties and then Cavell in the 1970s.[12-20] Since this class of ligands has been neglected: only now have we been able to obtain to the first crystal structures of complexes of S_2PF_2 in several Ru(II) complexes.[21] In the same paper describing the synthesis of $[N^nPr_4][S_2PF_2]$, mention was made of a different fluorothiophosphate: $[N^nPr_4]_2[S_5P_2F_2]$, reported again later on be Meisel.[22] Interestingly, while this ligand should also be amenable to coordination chemistry, no such attempts have ever been reported: consequently no structures with $S_5P_2F_2$ are present in the Cambridge Crystallographic Database.

In the present work we present a system in which, starting from one simple fluorothiophosphate anion, $S_5P_2F_2^{2-}$, we obtain coordination complexes with multiple coordination modes, to d^{10} transition metals, zinc, cadmium, and copper. In addition to the crystal structures of the complexes, the structure of the tetrapropylammonium salt of the ligand is contrasted.

6.4 Results and Discussion

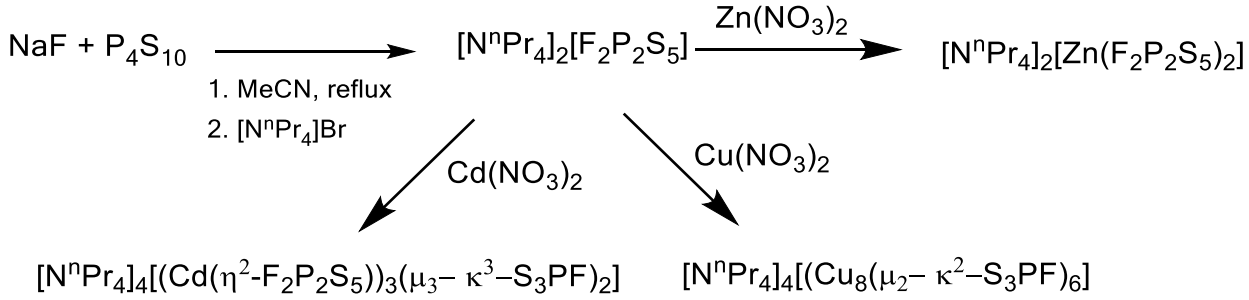

$[N^nPr_4]_2[S_5P_2F_2]$ is easily obtained by reaction of P_4S_{10} with 6 equivalents of NaF or KF, followed by precipitation in water with N^nPr_4Br. The metathesis of tetrapropylammonium is

essential as it allows for easy recrystallization from MeOH/H_2O affording colorless needles. X-ray diffraction crystals were grown in MeOH/H_2O and the crystal structure confirms the identity of the desired product as only one of the conformers, A, in which the $S_5P_2F_2^-$ anion adopts a staggered arrangement with the two fluorine atoms on opposite sides.

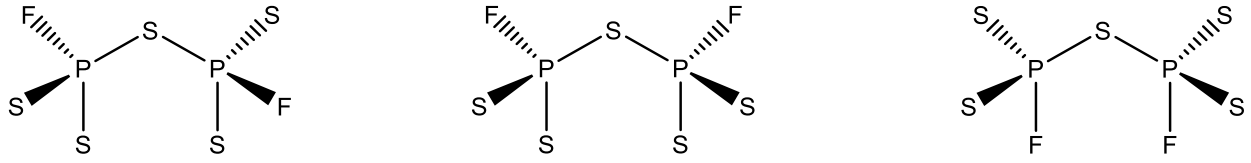

Conformer A Conformer B Conformer C

Figure 6.1: Possible conformers of the $S_5P_2F_2^{2-}$ anion

^{31}P and ^{19}F NMR confirm the formation of only one conformer: major doublet signals are mirrored in the ^{31}P and ^{19}F spectra with δ at 113.74 ppm (^{31}P) and 7.33 pm (^{19}F) respectively. Surrounding each branch of the doublet are doublets of doublets which arise from non-first order effects in an AA'XX' pattern with the associated coupling constants $^1J_{PF}$=1157.8Hz, $^3J_{PF}$=23.8Hz, $^2J_{PP}$=4.4Hz and $^4J_{FF}$=3.5Hz.[23] Upon heating to 100 °C, no change in the NMR patterns were observed confirming the assignment as due to non-first order effects.

Tetrahedral geometries are present around each phosphorus atom which are connected by a bridging sulfur atom with a P-S-P angle of 111.87(5) °. This is in good agreement with bridging sulfurs in other reported thiodiphosphates including $P_2S_7^{4-}$[24-26] or the cyanide adduct of P_2S_5, $[(NCPS)_2S]^{2-}$ (Table S6.2).[27]

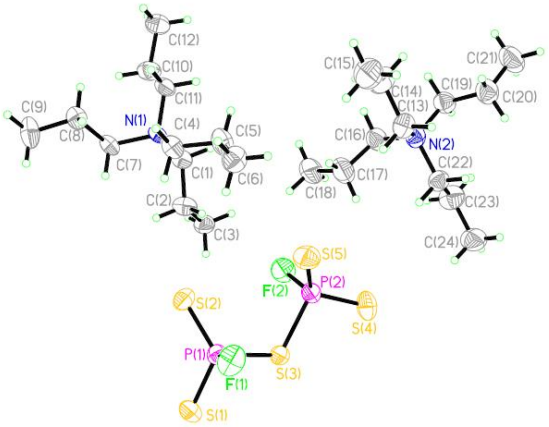

Figure 6.2: ORTEP diagrams of $[N^nPr_4]_2[S_5P_2F_2]$ with 40% ellipsoids

Addition of 2 equivalents of $[N^nPr_4]_2[S_5P_2F_2]$ in a methanolic solution of $Zn(NO_3)_2$ resulted in the immediate formation of a white precipitate. In CD_2Cl_2, nearly identical ^{31}P and ^{19}F NMR patterns as those of $[N^nPr_4]_2[S_5P_2F_2]$ were observed with small changes in chemical shifts and coupling constants, Figure S6.4-S6.5. X-ray diffraction confirmed this and revealed the formation of a simple bis-chelate complex, $[N^nPr_4]_2[Zn(S_5P_2F_2)_2]$. The absence of disorder in the structure, R_1 = 4.53% and S_{goof} =0.988 suggests the presence of only one conformer of $[S_5P_2F_2]^{2-}$, **A** coordinated to zinc. This results in a chiral compound which also crystallizes in the noncentrosymmetric monoclinic space group, $P2_1$ although the limited high angle reflections does not allow for unambiguous determination of the absolute configuration. The zinc adopts a tetrahedral geometry with chelate angles of 114.09(8) ° and 112.99(9) ° and Zn-S bond lengths ranging from 2.3243(19) Å to 2.341(2) Å.

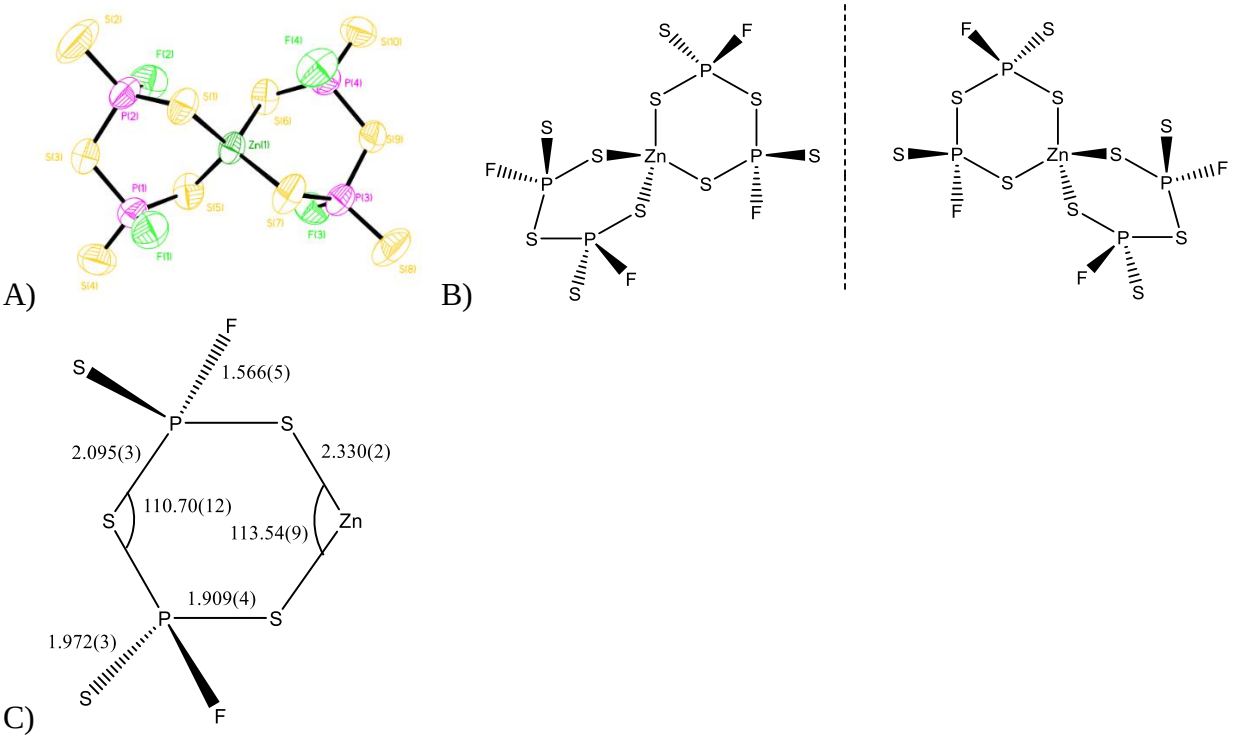

Figure 6.3: A) The anion of $[N^nPr_4]_2[Zn(S_5P_2F_2)_2]$ with 40% ellipsoids. B) possible enantiomers of crystallized isomer of $[Zn(S_5P_2F_2)_2]^{2-}$ and C) selected average bond lengths and angles. Tetrapropylammonium cations were omitted for clarity.

The reaction of two equivalents of $[N^nPr_4]_2[S_5P_2F_2]$ with methanolic cadmium nitrate hexahydrate also results in the immediate precipitation of a white product, characterized by a shoulder in the UV-Vis with an onset at 290 nm. Moreover, X-ray diffraction of the crystals obtained revealed the formation of a trinuclear cadmium cluster with mixed $[S_5P_2F_2]^{2-}$ and $[S_3PF]^{2-}$ ligands: coordination of 3 $[S_5P_2F_2]^{2-}$ and 2 $[S_3PF]^{2-}$ ligands results in the formation of $[N^nPr_4]_4[Cd_3(S_5P_2F_2)_3(S_3PF)_2]$. Elemental analysis and FTIR, with bands assigned to both $[S_5P_2F_2]^{2-}$ and $[S_3PF]^{2-}$ (Table S6.4), confirms the structure in the solid state. In solution at room temperature, the typical pattern for the $S_5P_2F_2$ ligand is observed but no signal was observed for the S_3PF ligands, usually located downfield by 10-20ppm in the ^{31}P NMR. At -15 ˚C, the presence of a broad doublet at 141 ppm clearly demonstrates the presence of S_3PF and the absence of signal at room temperature as being due to dynamic behaviour: this isn't unexpected as we have previously noted remarkable dynamic behaviour of the related fluorothiophosphate S_2PF_2 in Ru(II) complexes.[22]

One bidentate $[S_5P_2F_2]^{2-}$ ligand is coordinated to each tetrahedral cadmium center while two tripodal $[S_3PF]^{2-}$ ligands connect the metal centers forming tetrahedral geometries around the three cadmium centers. Each sulfur on the $[S_3PF]^{2-}$ ligands is coordinated to one cadmium resulting in the observed coordination sphere and the formation of a central cage structure. The central structure can be best described as cryptand-like with 3 branches consisting of P-S-Cd-S-P atoms with an estimated volume of 52 $Å^3$ using a sphere encompassing the cavity. The three cadmium centers are almost equidistant: the Cd-Cd separations are 4.399 Å, 4.426 Å and 4.438 Å. The fluorine and phosphorus atoms on each capping S_3PF ligand are aligned: viewed down this F-P-P-F axis, the three $Cd(S_5P_2F_2)$ sections are related by a C_3 symmetry axis (Figure 6.4.B). In this centrosymmetric space group, *P-1*, both C_3 helicities are present.

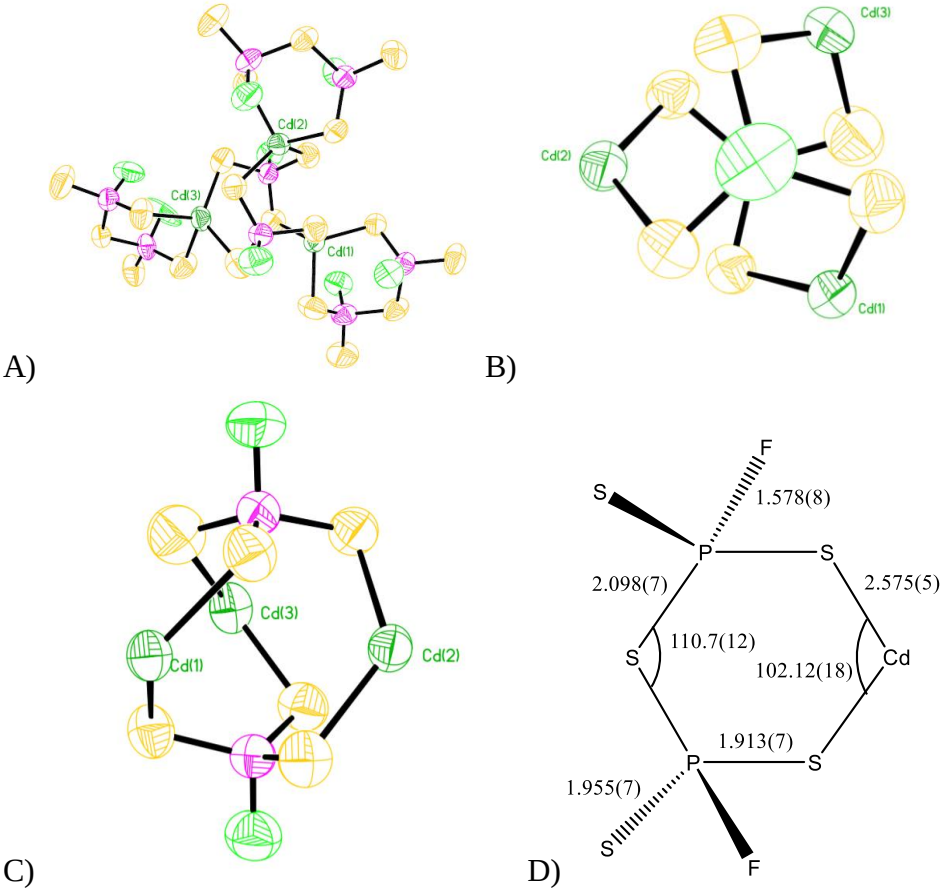

Figure 6.4: ORTEP diagram of A) The anion of $[N^nPr_4]_4[Cd_3(S_5P_2F_2)_3(S_3PF)_2]$, B) the $Cd_3(S_3PF)_2$ cage viewed down the F-P-P-F axis, C) the $Cd_3(S_3PF)_2$ cage-like core and D) Selected bond lengths and angles in $Cd(S_5P_2F_2)$. Disordered tetrapropylammonium salts are omitted for clarity.

While longer M-S bond lengths and smaller chelate angles are present in the cadmium structure compared to the zinc complex, resulting in a slightly larger chelate ring size, the structural features of the ligand remain almost identical between the two complexes and very similar to those in the free ligand (Table S6.3). There is little indication of the fate of the formal FPS_2 elimination fragment in these precipitates and efforts are underway to characterize the solution phases of these reaction mixtures.

The reaction of the copper (II) salt $Cu(NO_3)_2{\cdot}2.5H_2O$ with 2.5 equivalents of $[N^nPr_4]_2[S_5P_2F_2]$ resulted in an instant change of the colour of the solution from blue to colorless indicating reduction of Cu(II) to Cu(I). X-ray diffraction confirmed the identity of the product as the anionic Cu_8S_{12} type cluster $[N^nPr_4]_4[Cu_8(S_3PF)_6]$ with a methanol solvate. The synthesis of the cluster presented here is rather unusual: Cu_8S_{12} clusters have been studied previously and usually involve reactions with Cu(I) species rather than Cu(II) as described here.[28,29]

The geometry of the cluster consists of a Cu_8S_{12} core arranged into an icosahedron with 6 faces consisting of 4 copper atoms and 4 sulfur atoms (Figure 6.5B). The 8 copper atoms form an almost perfect cubic geometry. Each copper atom is coordinated to three sulfurs in a trigonal planar geometry. Four stereoisomers are possible relative to the orientation of each fluorine on opposite faces of the cube as cis or trans: trans/trans/trans (ttt), trans/trans/cis (ttc), trans/cis/cis (tcc) and cis/cis/cis (ccc), Figure S6.11. The structure obtained is that of the ttt isomer. No disorder in the structure suggests the presence of only one isomer which crystallized in the solid state. In solution, the presence of two doublets in a 1:3 ratio indicates the presence of two isomers. Broadened multiplets in the ^{31}P and the ^{19}F NMR may be due a combination of $^{63/65}Cu$, ^{31}P or ^{19}F coupling. Elemental analysis rules out the presence of substantive paramagnetic impurities as the cause of broadening in the NMR.

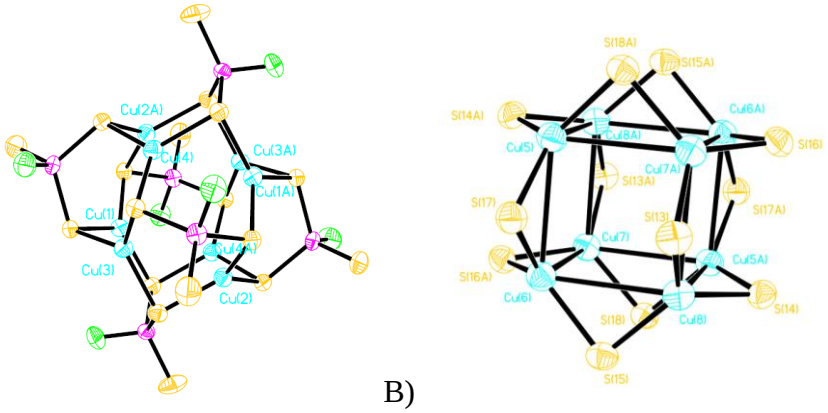

A) B)

Figure 6.5: ORTEP diagram of A) $[N^nPr_4]_4[Cu_8(S_3PF)_6]$ and B) the Cu_8S_{12} core highlighting the cubic structure with 40% ellipsoids. Tetrapropylammonium salts were ommited for clarity.

As shown in Figure S6.10 the Cu_8 cube has a volume of 30.79 $Å^3$, similar to other reported cubic cores in Cu_8S_{12} clusters.[30,31] Certainly this volume is sufficient to encapsulate an ion, as found in Cu_8 cationic clusters which encapsulate hydride or fluoride. The structure of the $Cu_8(S_3PF)_6$ tetra anion has no indication of ion encapsulation but an intriguing possibility is that, due to charge, cations may bind there.

The facile abstraction of fluorotrithiophosphate in the copper and cadmium complexes suggested Lewis acid heterolysis of the P-S-P framework. This would generate the observed coordinated dianion and what is formally fluorodithiometaphosphate, $F\text{-}P(=S)_2$ as either a reactive intermediated or substrate. Monitoring these reactions with in situ NMR indicates that a range of P-F containing products suggesting the presence of reactive intermediates. Efforts are underway to trap these reactive intermediates, with one goal being the development of catalytic and or stereospecific thiophosphorylation reagents.

6.5 Conclusion

In conclusion, the first exploration of the coordination chemistry of the now easily accessible fluorothiophosphate anion $[S_5P_2F_2]^{2-}$ to zinc, cadmium and copper gives easy access to a variety of new complexes with tractable solubility. Diverse structural motifs including ZnS_4, Cd_3S_{12} and Cu_8S_{12} reminiscent of metallothionein dithiolate clusters allow for new models of metallothionein and potentially allow for the capping of CdS semiconducting nanoparticles.

6.6 Experimental

6.6.1 Synthetic Procedures

Synthetic Procedures

The starting materials P_4S_{10}, KF, $Zn(NO_3)_2.6H_2O$, , $Cd(NO_3)_2,6H_2O$ and $Cu(NO_3)_2.2.5H_2O$ were purchased and used without further purification. IR spectra were measured on Bomem MB3000 FTIR spectrometer as KBr pellets, and ^{1}H, $^{31}P\{^{1}H\}$ and ^{19}F NMR spectra were measured on a Bruker AVIIIHD 500 spectrometer at 22 °C at 500 MHz for ^{1}H, and 202 MHz for ^{31}P and 470 MHz for ^{19}F.

Synthesis of the ligand

$[N^nPr_4]_2[S_5P_2F_2]$: Phosphorus pentasulfide (1.1 g) and 6 equivalents of MF (M=Na (0.625 g), K (1.72 g)) were dissolved in acetonitrile (50 mL) and heated at reflux for 30 min. The solvent was removed under vacuo and the remaining product was dissolved in water. N^nPr_4Br (1.5 g) was dissolved in water and added to the solution of $MS_2P_5F_2$ causing the precipitation of a white product. Recrystallization of the product occurred as follows: the crude product was dissolved in 20 mL of methanol and heated at 40 ˚C until dissolution was complete. 40 mL of water was added to the solution causing precipitation of pure $[N^nPr_4]_2[S_5P_2F_2]$. Yield: 2.75 g (93%) DSC: broad exotherm at 205 ˚C IR: 2968.0m, 2877.9m, 1473.8vs, 1325.6s, 1100.1s, 971.3vs, 770.3s, 707.1s, 589.4w, 533.3vs, ^{31}P-NMR (CD_2Cl_2): 115.01 (AA'XX' pattern, $^{1}J_{PF}$=1157.8Hz, , $^{3}J_{PF}$=23.8Hz, $^{2}J_{PP}$=4.3Hz), ^{19}F-NMR (CD_2Cl_2): 6.24 (d, $^{1}J_{PF}$=1157.8Hz, $^{3}J_{PF}$=23.8Hz, $^{4}J_{FF}$=3.5Hz) 7.33 (ddd, $^{1}J_{PF}$=1147.7Hz, $^{2}J_{PP}$=23.8Hz, $^{3}J_{PF}$=3.5Hz) Anal. Calcd for $N_2C_{24}H_{56}F_2P_2S_5$: C, 45.54; H, 8.92; N, 4.43 Found: C, 45.45; H, 8.66; N, 4.33 X-ray diffraction crystals grown from $MeOH/H_2O$

Synthesis of complexes

$[N^nPr_4]_2[S_5P_2F_2]$ was freshly recrystallized before the synthesis of each complex.

$[N^nPr_4]_2[Zn(S_5P_2F_2)_2]$: Zinc nitrate hexahydrate (100mg) and 2.5 equivalents of $[N^nPr_4]_2[S_5P_2F_2]$ (531mg) were dissolved in methanol. Upon stirring at room temperature, a

white precipitate formed. It was filtered and washed with 3x10mL of water and 3x10mL of methanol. The product was recrystallized from 1:1 DCM/ethanol. Yield: 167mg (40%) DSC: sharp exotherm at 120˚C followed by a broad exotherm at 275˚C IR: 2968.0m, 2877.9m, 1467.2s, 1383.4m, 1325.6w, 1267.7w, 1164.5w, 1035.7m, 971.3s, 789.7s, 695.3m, 622.0w, 532.9s ^{31}P-NMR (CD_2Cl_2): 112.06 (AA'XX' pattern, $^1J_{PF}$=1194.3Hz $^3J_{PF}$=27.4Hz, $^2J_{PP}$=8.3Hz) ^{19}F-NMR (CD_2Cl_2): 1.26 (d, $^1J_{PF}$=1194.3Hz) Anal. Calcd for $N_2C_{24}H_{56}ZnF_4P_4S_{10}$: C, 30.07; H, 5.89; N, 2.92 Found: C, 30.23; H, 5.80; N, 2.87 X-ray diffraction crystals were grown from DCM/ethanol.

$[N^nPr_4]_4[Cd_3(S_3PF)_2(S_5P_2F_2)_3]$: Cadmium nitrate hexahydrate (100mg) and 2.5 equivalents of $[N^nPr_4]_2[S_5P_2F_2]$ (513mg) were dissolved in methanol. Upon stirring at room temperature, a white precipitate formed. It was filtered and washed with 3x10mL of water and 3x10mL of methanol. The product was recrystallized from 1:1 DCM/ethanol. DSC: broad exotherm at 258˚C IR: 2968.0s, 2877.9m, 1467.2s, 1383.4w, 1319.0w, 1267.7vw, 1164.5vw, 964.8s, 789.1s, 756.1m, 698.1s, 697.1s, 627.6m, 597.2s, 562.0m, 532.6s ^{31}P-NMR (acetone-d_6): AA'XX' pattern: 112.90 $^1J_{PF}$=1157.8Hz, , $^3J_{PF}$=28.9Hz, $^2J_{PP}$=5.5Hz ^{19}F-NMR (acetone-d_6 AA'XX' pattern: $^1J_{PF}$=1187.3Hz, , $^3J_{PF}$=23.8Hz, $^2J_{PP}$=6.1Hz Anal. Calcd for $N_4C_{48}H_{112}Cd_3F_8P_8S_{21}$: C, 26.74; H, 5.24; N, 2.60 Found: C, 26.79; H, 5.15; N, 2.62. X-ray diffraction crystals grown from DCM/EtOH at -20˚C.

$[N^nPr_4]_4[Cu_8(S_3PF)_6]$: Copper nitrate hemipentahydrate (100mg) and 2.5 equivalents of $[N^nPr_4]_2[S_5P_2F_2]$ (680mg) were dissolved in methanol. A white precipitate formed instantly. It was filtered and washed with 3x10mL of water and 3x10mL of methanol. The product was recrystallized from 1:1 DCM/ethanol. Yield: 508mg (55%) DSC: sharp exotherm at 231.77˚C followed by broad exotherm at 272˚C IR: 2968.0m, 2877.9m, 1473.8vs, 1325.6s, 1100.1s, 971.3vs, 755.7s, 698.3s, 594.8w, 552.7s, ^{31}P-NMR (CD_2Cl_2): isomer A: 125.27 (broad d, 1, $^1J_{PF}$=1174.1Hz) 123.61 (broad d, 3, $^1J_{PF}$=1177.0Hz) ^{19}F-NMR (CD_2Cl_2): 4.22 (broad d, J_{PF}=1178.7Hz) X-ray diffraction crystals grown from DCM/ethanol. Anal. Calcd for $N_4C_{48}H_{112}Cu_8F_6P_6S_{18}$: C, 27.90; H, 5.46; N, 2.51 Found: C, 27.73; H, 5.28; N, 2.59

6.6.2 Crystallographic Methodologies

Crystals are mounted on glass fibers with epoxy resin or Mitogen mounts using Paratone-N from Hampton Research and single-crystal X-ray diffraction experiments are carried out with a BRUKER APEX-II D8 CCD diffractometer by using graphite-monochromated Mo Kα radiation ($\lambda = 0.71073$ Å) the SHELX package[32] is used for integration of the intensity reflections, scaling, and absorption correction. Intrinsic phasing methods were used to solve the structures. Non-hydrogen atoms are located by difference Fourier maps and final solution refinements are carried out by full-matrix least-squares methods on F2 for all of the data. The hydrogen atoms are placed in calculated positions and were not refined.

6.7 References

1. Joswig, J. O.; Springborg, M.; Seifert, G.: Structural and Electronic Properties of Cadmium Sulfide Clusters, *J. Phys. Chem. B* 2000, 104, 12, 2617–2622
2. Zhang, Q. C.; Bu X. H.; Zhang, J.; Wu, T.; Feng, P. Y.: Chiral Semiconductor Frameworks from Cadmium Sulfide Clusters, *J. Am. Chem. Soc.* **2007**, *129*, 27, 8412–8413
3. Henkel, G.; Krebs, B.: Metallothioneins: Zinc, Cadmium, Mercury, and Copper Thiolates and Selenolates Mimicking Protein Active Site Features – Structural Aspects and Biological Implications, *Chem.Rev.*, **2004**,*104*, 801−824
4. Stillman, M. J.: Meallothioneins, *Coord. Chem. Rev.*, **1995**, *144*, 461-511
5. Otto, J.; Jolk, J.; Villand, T.; Wonnemann, R.; Krebs, B.: Metal(II) Complexes with Monodentate S and N Ligands as Structural Models for Zinc-Sulfur DNA-Binding Proteins, *Inorg. Chim. Acta*, **1999**, *285*, 262-268
6. Tang, K. L.; Jin, X. L.; Li A. Q.; Li, S. J.; Li, Z. F.; Tang, Y. Q.: Studies of Trinuclear Cadmium Cluster Complexes. Syntheses and Crystal Structures of $[NMe_4][Cd_3(SC_6H_2Pr^i2,4,6)_7]C_5H_{12}$ and $[Cd_3(SC_6H_2Pr^i_3\text{-}2,4,6)_6(HSC_6H_2Pr^i_3\text{-}2,4,6)].CH_3OH.7H_2O$, *J. Coord. Chem.*, **1994**, *31*, 305-320
7. Schmedt auf der Günne, J. ; Eckert, H.: High-Resolution Double Quantum ^{31}P NMR: a New Approach to Structural Studies of Thiophosphates., *Chem. Eur. J.*, **1998**, *4*, 1762-1767
8. Lustig, M.; Ruff, J. K.: Nonmetal Oxy-and Thiofluoride Salts *Inorg. Chem.*, **1967**, *6*, 2115-2117.
9. Roesky, H. W.; Tebbe, F. N.; Muetterties, E. L.: New Phosphorus-Sulfur Chemistry *J. Am. Chem. Soc.* **1967**, *89*, 1272-1274.
10. Mitchell, R. W.; Lustig, M.; Hartman, F. A.; Ruff, J. K.; Merritt, J. A.: Synthesis and Properties of Difluorodithiophosphoric Acids, HPS_2F_2 and DPS_2F_2, *J. Am. Chem. Soc.* **1968**, *90*, 6329-6332.

11. Roesky, H. W.; Tebbe, F. N.; Muetterties, E. L.: Thiophosphate Chemistry. Anion set $X_2PS_2^-$, $(XPS_2)_2S^{2-}$ and $(XPS_2)_2S_2^{2-}$, *Inorg, Chem.*, **1970**, *9*, 831-830
12. Tebbe, F. N.; Muetterties, E. L.: Metal Complexes of the Difluorodithiophosphate Ligand, *Inorg. Chem.*, **1970**, *9*, 629-637
13. Cavell R. G.; Byers W.; Day, E. D.: Metal Complexes of Substituted Dithiophosphinic Acids. I. Complexes of Trivalent Chromium *Inorg. Chem.*, **1971**, *10*, 2710-2715.
14. Cavell R. G.; Day E. D.; Byers W.; Watkins P. M.: Metal Complexes of Substituted Dithiophosphinic Acids. V. Complexes of Manganese, Iron, and Cobalt *Inorg. Chem.*, **1972**, *11*, 1759-1772.
15. Cavell R. G.; Byers W.; Day E. D.; Watkins P. M.: Metal Complexes of Substituted Dithiophosphinic Acids. IV. Complexes of Divalent Nickel, Palladium, and Platinum *Inorg. Chem.*, **1972**, *11*, 1598-1606.
16. Cavell R. G.; Day E. D.; Byers W.; Watkins P. M.: Metal Complexes of Substituted Dithiophosphinic Acids. III. Vanadyl Complexes *Inorg. Chem.*, **1972**, *11*, 1591-1597
17. Cavell R. G. : Sanger A. R.: Metal Complexes of Substituted Dithiophosphinic Acids. VI. Reactions of Difluorodithiophosphinic Acid with Chlorides and Oxychlorides of Chromium, Molybdenum *Inorg. Chem.*, **1972**, *11*, 2011-2016.
18. Cavell R. G.; Sanger A. R.: Metal Complexes of Substituted Dithiophosphinic Acids. VII. Reactions of $TiCl_4$, $VC1_4$, $NbCl_4$, $NbCl_6$, and $TaCl_5$ with Difluorodithiophosphinic Acid, *Inorg. Chem.*, **1972**, *11*, 2016-2019.
19. Hartman F. A.; Lustig M.: Preparation and Reactions of Tetracarbonyl-μ-bis(difluorodithiophosphato)-dirhodium(I)*Inorg. Chem.*, **1968**, *7*, 2669-2670.
20. Islam M. Q.; Hill W. E.; Webb T. R.; Quadruply Bonded Dimolybdenum complexes of $PF_2S_2^-$. Comparison with complexes of PR_2S_{2p-} (R= Et, Me) *J. Fluor. Chem.*, **1990**, *48*, 429-440
21. Gaydon, Q.; Bohle, D. S.: Organometallic Chemistry of the Dithiophosphate anion, *in review*

22. Meisel M.: On the Nucleophilic Degradation of Phosphorus Chalcogenides with Adamantane-Like Structure by Fluorides. *Phosphorus Sulfur Silicon Relat Elem*, **1990**, *51*, 137-140.
23. Bain, D. A.; Bornais, J.; Brownstein, S.: Analysis of Generalized Two-Dimensional Homonuclear NMR Spectra, *Can. J. Chem*., **1981**, *59*, 723-730
24. Jandali, M. Z.; Eulengerber, G. ; Hahn, H.: Preparation and Crystal Structure of Mercury(II) Thiodiphosphate ($Hg_2P_2S_7$)., *Z. Anorg. Allg. Chem*., **1978**, *445*, 184-192
25. Babo, J.-M.; Jouffret, L. ; Lin, J. ; Villa, E. M. ; Albrecht-Schmidt, T. E.: Synthesis, Structure and Spectroscopy of Two Ternary Uranium(IV) Thiophosphates: UP_2S_9 and UP_2S_7 Containing $P_2S_9^{2-}$ and $P_2S_7^{2-}$ Ligands., *Inorg. Chem*., **2013**, *52*, 7747-7751
26. Gutzmann, A.; Naether, C.; Bensch, W.: $Cs_3Hf_2(P_2S_7)_2(PS_4)$. *Acta. Crystallogr., Sect. E*, **2004**, *60*, 42-44
27. Roesky, H. W.; Noltemeyer, M.; Sheldrick, G. M.: Preparation and Crystal Structures of $[Ph_4As^+][PS_2(N_3)^{2-}]$ and $[(n\text{-}C_3H_7)_4N^+]_2$ $[(NCPS_2)_2S^{2-}]$, *Z. Naturforsch*., **1986**, *41b*, 803-807
28. McCandlish, L. E.; Bissell, E. C.; Coucovanis, D.; Fackler, J,. P.; Know, K: A New Metal Cluster System Containing a Cube of Metal Atons, *J. Am. Chem. Soc*., **1968**, *90*, 7357-7358
29. Hollander, F. J.; Coucovannis, D.: Metallocubanes. Crystal and Molecular Structure of Tetrakis(tetraphenylphosphonium)hexakis(dithiosquarato)octacuprate(I) and Tetrakis(tetrbutylammoniumhexakis(1,1-dicarboethoxyethylene-2,2-dithiolato)octabuprate(I) Clusters with a Common Cu_8S_{12} Core, *J. Am. Chem. Soc*., **1977**, *99*, 6268-6280
30. Liu, C. W.; Sarkar B. ; Huang, Y. J. ; Liao, P. K. ; Wang, J. C.; Saillard, J. Y.; Kahlal, S.: Octanuclear Copper(I) Clusters Inscribed in a Se_{12} Icosahedron: Anion-Induced Modulation of the Core Size and Symmetry, *J. Am. Chem. Soc.*, **2009**, *131*, 11222-11233
31. Fenske, D. Rothenberger, A.; Fallaz, M. S.: Synthesen und Kristallstrukturen von Cu- und Ag-Komplexen mit Dithiophosphinat-und Trithiophosphonat-Liganden, *Z. Anorg. Allg. Chem.*, **2004**, *630*, 943-947

32. Sheldrick, G. M., SADABS, TWINABS; Siemens Industrial Automation, Inc.: Madison, WI, 1996

Chapter 7: P-S Bond Heterolysis in the Coordination of the $[S_5P_2F_2]^{2-}$ Anion to d^8 Square Planar Complexes

7.1 Preface

In chapter 6, coordination of the bidentate fluorodithiophosphate ligand $[S_5P_2F_2]^{2-}$ to group 11 and 12 metals, zinc, cadmium and copper resulted in complexes with different motifs including simple bis-chelate complexes to more unusual complexes including a cage like trinuclear cadmium complex with capping $[S_3PF]^{2-}$ ligands and $[S_5P_2F_2]^{2-}$ ligand pointing outwards, as a well as a cubic Cu_8S_{12} icosahedron with $[S_3PF]^{2-}$ ligands bridging the copper centers. This new fluorothiophosphate, trithiofluorophosphate, must be a result of heterolysis of the P-S bond in $[S_5P_2F_2]^{2-}$.

While the diversity in coordination of the ligand leads to exciting new complexes, a more systematic approach towards the coordination of trithiofluorophosphate is required in order to gain a better understanding the chemistry of the $[S_5P_2F_2]^{2-}/[S_3PF]^{2-}$ system. In this chapter we attempt to gain a better control over the coordination of this unusual ligand by synthesizing square planar d^8 group 10 complexes of nickel, palladium and platinum including a detailed spectroscopic characterization of the complexes. In addition, we extend the coordination chemistry to d^6 metals with the synthesis of a binuclear Ru(II) complexes. Simple reactivity of the complexes towards alkylation and hydrolysis is also presented.

The work presented in this chapter is a draft of a manuscript to be submitted: Gaydon, Q.; Bohle, D. S.: Fluorotrithiophosphate abstraction from the difluoropentathiodiphosphate dianion: d^8 and d^6 complexes of $[\eta^2\text{-}S_3PF]^{2-}$, *in preparation.*

7.2 Abstract

Coordinative heterolysis of the fluorothiophosphate anion $[S_5P_2F_2]^{2-}$ by formal elimination of $[S_2PF]$ by the group 10 divalent metals nickel, palladium, and platinum results in diphosphate cleavage and coordination of $[S_3PF]^{2-}$. Several complexes with the novel fluorotrithiophosphate were characterized structurally and spectroscopically with X-ray diffraction, IR, ^{31}P, and ^{19}F NMR. In addition to mononuclear η^2 chelate complexes, bridging complexes with η^2- μ_2-S_3PF configurations result in binuclear nickel and ruthenium adducts. Facile methylation with methyl triflate of the uncoordinated sulfur atom leads to a complex with the methylthiofluorodithiophosphate ligand in a cationic complex which hydrolyses with loss of fluoride to give complexed $[S_2P(O)SMe]^{2-}$. Alternatively hydrolysis can also lead to a binuclear $Ni_2(dppe)_2(S_3PF)(S_2POF)$ complex. Divalent ruthenium aryl complexes form fluorotrithiophosphate complexes rapidly at room temperature to give bridged dimers with complete chloride substitution.

7.3 Introduction

Thiophosphates, of the general formula $[P_xS_y]^{n-}$ are a class of compounds with roots in alchemy but with considerable modern technological relevance. Several different coordination motifs have been reported for these thiophosphates, their esters and salts. The most common monomer is the tetrahedral $[PS_4]^{3-}$ anion (Figure 7.1A) and dimeric thiophosphates and pyrophosphate analogs such as $[P_2S_6]^{2-}$, $[P_2S_6]^{4-}$,$[P_2S_7]^{4-}$ or $[P_2S_9]^{4-}$ are relatively common as well (Figure 7.1B-7.1E). [1,2] The presence of terminal sulfur atoms in these structures suggest the possibility of forming bidentate ligands in transition metal complexes.[3] Complexes with $[PS_4]^{3-}$,[4] $[P_2S_6]^{2-}$, $[P_2S_6]^{2-}$,[5-7] $[P_2S_7]^{4-}$,[7-11] and $[P_2S_9]^{4-}$ [11] ligands or mixtures thereof [12-16] have been reported. The complexes are synthesized using two techniques: either by solid state reaction in vacuum sealed tubes[17,18] or by flux growth.[19,20] The variety of different coordination patterns with different metals leads to formation of chains, layers, or 3D networks. Similar complexes of selenophosphates are known, albeit not as common.[21-26] Thiophosphates and selenophosphates

have been used in a variety of applications, including non-linear optics[27-29], electrolytes in batteries[30-32] or by making use of their complex magnetic properties.[33,34]

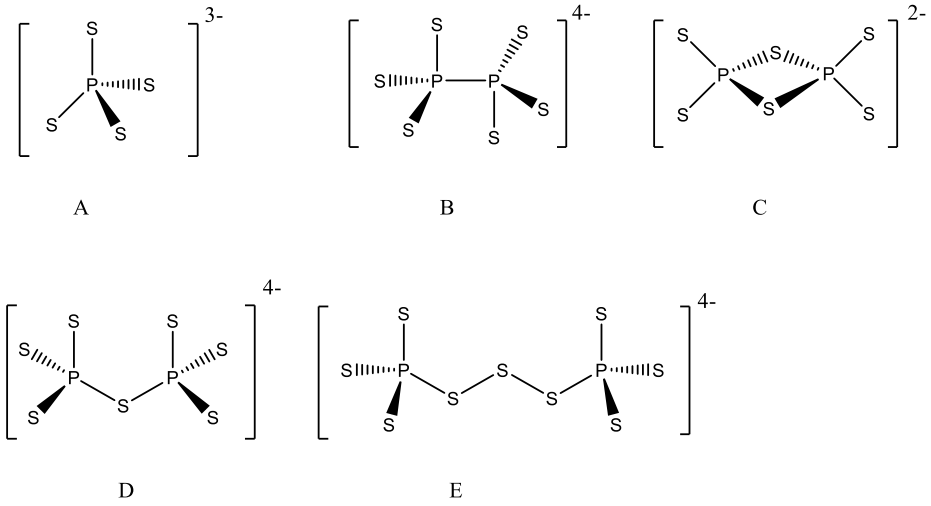

Figure 7.1: Structures of common thiophosphate motifs

Fluorodithiophosphates are a poorly studied class of thiophosphates with an additional fluorine atom bound to the phosphorus. Very little is known about fluorothiophosphates: several groups have described the synthesis of the $[S_2PF_2]^-$ anion as the acid or as the tetrapropylammonium salt.[35-41] Complexes of $[S_2PF_2]^-$ were then prepared using the acid HS_2PF_2 by Roesky as well as Cavell,[42-50] many of which have been reported as being volatile. Recently we have determined the first crystal structures of the tetrapropylammonium salt as well as complexes containing the S_2PF_2 anion with four new complexes of Ru(II). In the original article by Roesky,[42] the mixture of two different fluorothiophosphates, $[S_5P_2F_2]^{2-}$ and the more insoluble $[S_6P_2F_2]^{2-}$, were prepared by reaction in methoxyethanol under inert atmosphere. Meisel later proposed that the synthesis of $[S_2PF_2]^-$, $[S_5P_2F_2]^{2-}$ and $[S_6P_2F_2]^{2-}$ can be controlled by varying the equivalents of MF added in acetonitrile.[51] Since we have studied the coordination of $S_5P_2F_2^{2-}$ to the late transition metals zinc, cadmium, and copper and have observed either coordination of $[S_5P_2F_2]^{2-}$, $[S_3PF]^{2-}$ as a product of P-S heterolysis, or a mixture of both. Coordination of ligands to metals are often accompanied by geometrical distortions in at the metal center and in the ligand to accommodate for the new coordinated geometry. In very rare cases, this results in bond cleavage within the ligand. This has been reported in the S-S bond cleavage in the coordination of bis[2-

(1H-benzimidazol-2-yl)phenyl]disulfide to nickel(II) which was not observed in its coordination to zinc, cadmium, or copper.[52] In order to gain a better understanding of the coordination chemistry of this new fluorotrithiophosphate, a more systematic approach towards the type of coordination is required.

We present here a system in which s coordination of the $[S_5P_2F_2]^{2-}$ anion to group 8 metals results consistently in P-S bond cleavage in the ligand and coordination of $[S_3PF]^{2-}$. Much like $[S_5P_2F_2]^{2}$, the coordination chemistry of $[S_3PF]^{2-}$ has not been reported. Herein, we report the first examples of this class, their structures, reactions, and spectroscopic characterization of complexes with the fluorotrithiophosphate ligand.

7.4 Results and discussion

The tetrapropylammonium salt of $[S_5P_2F_2]^{2-}$ is readily synthesized by the reaction of P_4S_{10} with 6 equivalents of NaF or KF. Recrystallization with N^nPr_4Br and $MeOH/H_2O$ results in an anhydrous pure stable salt. In our studies of the coordination chemistry of the anion to zinc, a simple tetrahedral bis-chelate complex of $[S_5P_2F_2]^{2-}$ was obtained by immediate precipitation using $Zn(NO_3)_2$ and $[N^nPr_4]_2[S_5P_2F_2]$.

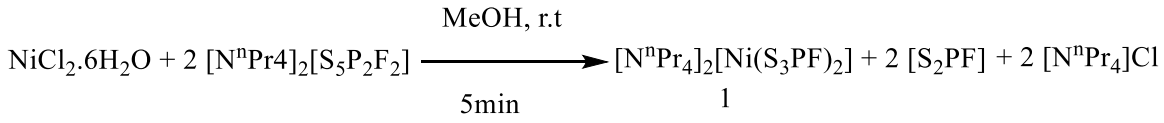

1

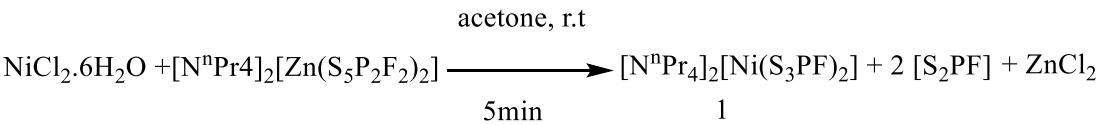

2

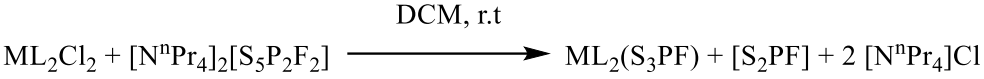

3

2a: M=Ni, L=dppe
2b: M=Ni, L=dpph
3: M=Pd, L=PPh_3
4a: M=Pt, L=PPh_3
4b: M=Pt, L=PPh_2Me

The chemistry of the ligand with square planar d^8 complexes of nickel, palladium and platinum is remarkably different from that of zinc. The reaction of $NiCl_2.6H_2O$ and $[N^nPr_4]_2[S_5P_2F_2]$ in methanol, equation 1, resulted in the immediate precipitation of a purple product, characterized by d-d transitions at 520 and 667 nm observed in the UV-Vis spectrum. The ^{31}P NMR spectra of the complex shows a doublet of doublet of doublets from second order effects with identical $^4J_{PP}$ and $^5J_{PF}$ coupling constants, shifted downfield by 20 ppm compared to the AA'XX' pattern observed in the zinc complex and free ligand. A broad doublet in the ^{19}F-NMR at 17 ppm is present with $^1J_{PF}$=1170.45Hz. The large differences in chemical shift between the zinc complex and this product, as well as the absence of AA'XX' pattern suggests a different coordination environment around the nickel center.

This was confirmed by X-ray diffraction: the crystal structure of the complex revealed coordination of two $[S_3PF]^{2-}$ ligands to the nickel center rather than the expected $S_5P_2F_2$, resulting in the formation of $[N^nPr_4]_2[Ni(S_3PF)_2]$, **1**. This can only be a consequence of cleavage of the P-S bond in $[S_5P_2F_2]^{2-}$ and coordination of the resulting $[S_3PF]^{2-}$ fragment. Stochiometrically the cleavage of $[S_5P_2F_2]^{2-}$ would result in the formation of $[S_3PF]^{2-}$ and $[S_2PF]$ fragments. While coordination of the latter isn't observed, following the reaction by NMR results

in the appearance of a signal corresponding to $[N^nPr_4]_2[Ni(S_3PF)_2]$ as well as a doublet shifted upfield by 40 ppm in a 1:1 integration with the singal from the complex. Additionally, ESI-MS of the reaction reaction mixture results in a fragment at 94 m/z with the isotopic pattern corresponding to PS_2^+. This fragment isn't present in either the ESI-MS spectra of the starting material or $[N^nPr_4]_2[Ni(S_3PF)_2]$. These two pieces of evidence point towards the formation of $[S_2PF]$ in the reaction mixture. Attempts at forming the known pyridine betaine $py.S_2PF$[53] by addition of pyridine to the reaction mixture were unsuccesful.

The nickel atom was located on an inversion center and disorder is present in the positions of the fluorine and terminal sulfur atoms. The complex adopts a square planar geometry with S-Ni-S angle of 87.78° very close to the ideal value of 90° as well as Ni-S bonds of 2.2212(8) Å and 2.2263(8) Å. The phosphorus is located 0.0827 Å beneath the plane defined by the nickel and sulfur atoms: the four membered ring formed upon coordination is therefore very close to planarity. The geometry of the phosphorus is tetrahedral: the angle between the coordinated sulfurs and the phosphorus was 99.83° while the angles between the fluorine, phopshorus and terminal sulfur were 104.6(7) ° and 108.4(9)°.

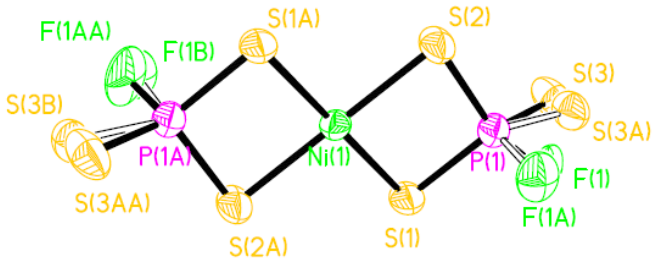

Figure 7.2: ORTEP diagram of $[N^nPr_4]_2[Ni(S_3PF)_2]$ with 40% ellipsoids. Tetrapropylammonium cations were ommited for clarity.

In an attempt to obtain $[N^nPr_4]_2[Ni(S_5P_2F_2)_2]$, the transmetallation reaction of $[N^nPr_4]_2[Zn(S_5P_2F_2)_2]$ with $NiCl_2.6H_2O$ was investigated, equation 2. The immediate colour change to deep purple indicates the immediate formation of a Ni(II) complex. Surprisingly, **1** was formed once again.

The observations were extended to several square planar d^8 complexes of nickel, palladium and platinum complexes: Ni(dppe)(S_3PF) **2a**, Ni(dpph)(S_3PF) **2b**, Pd(PPh_3)$_2$(S_3PF) **3**,

$Pt(PPh_3)_2(S_3PF)$ **4a**, and $Pt(PPh_2Me)_2(S_3PF)$ **4b**, were synthesized by reaction of $[N^nPr_4]_2[S_5P_2F_2]$ with corresponding $LMCl_2$ precursors of nickel, palladium and platinum salts and were structurally characterized, equation 3. A full comparison of bond lengths and angles for the complexes reported is given in Table S7.3, with key data contrasted in Table 7.1. One common trend among these complexes are the small bite angles of the $[S_3PF]^{2-}$ ligand ranging from 80˚ to 90˚. In comparison to the coordination of the fluorothiophosphate anion to late transition metals which results in either $S_5P_2F_2$ (zinc), S_3PF (copper) or even a mixture of the two ligands (cadmium), the group 8 meteals consistently coordinate $[S_3PF]^{2-}$.

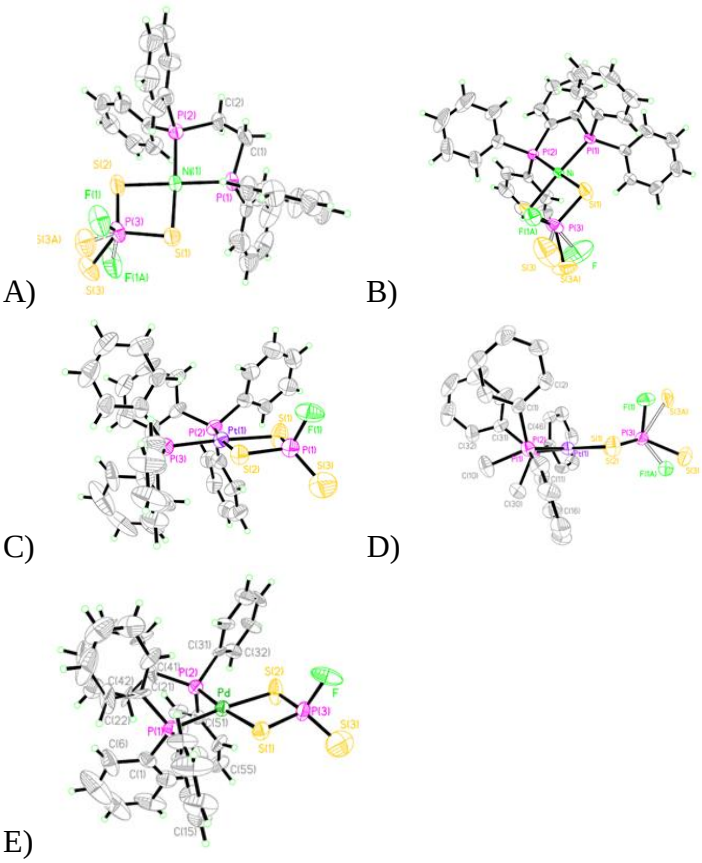

Figure 7.3: ORTEP diagrams of A) Ni(dppe)(S_3PF), 2a, B) Ni(dpph)(S_3PF), 2b, C) Pd(PPh_3)$_2$(S_3PF), 3, D) Pt(PPh_3)$_2$(S_3PF), 4a, and E) Pt(PPh_2Me)$_2$(S_3PF), 4b, with 40% ellipsoids. Only one of the two independent molecules of Pt(PPh_2Me)$_2$(S_3PF) is shown and only the non-hydrogen atoms for D.

1		2b		3		4b	
Bonds	Å	Bonds	Å	Bonds	Å	Bonds	Å
Ni-S	2.2212(8) 2.2263(8)	Ni-S	2.207(2) 2.212(2)	Pd-S	2.346(3) 2.347(4)	Pt-S	2.359(4) 2.359(4)
P-S (coordinated)	2.0107(11) 2.0192(11)	P-S (coordinated)	2.010(3) 2.015(3)	P-S (coordinated)	2.028(5) 2.006(5)	P-S (coordinated)	2.016(6) 2.038(5)
P-S (terminal)	1.918(8) 1.976(14)	P-S (terminal)	1.812(7) 1.846(5)	P-S (terminal)	1.858(6)	P-S (terminal)	1.878(8) 1.641(10)
P-F	1.665(17) 1.470(3)	P-F	1.676(7) 1.789(15)	P-F	1.696(8)	P-F	
Angles	°	Angles	°	Angles	°	Angles	°
S-P-S	99.83(5)	S-P-S	98.94(11)	S-P-S	100.2(2)	S-P-S	100.3(2)
F-P-S	108.4(9) 104.6(7)	F-P-S	106.5(3) 96.9(8)	F-P-S	102.7(4)	F-P-S	104.2(5)
S-Ni-S	87.78(3)	S-Ni-S	87.60(8)	S-Pd-S	82.48(12)	S-Pt-S	82.56(14)

Table 7.1: Selected bond lengths and angles of 1, 2b, 3 and 4a

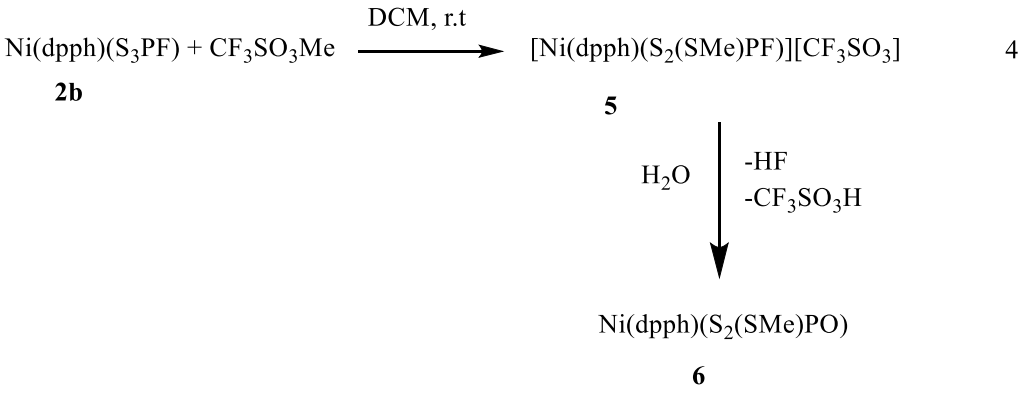

The nucleophilic nature of the terminal sulfur in the ligand leaves it susceptible to methylation in the presence of strong methylating agents such as methyl triflate. Ni(dpph)(S_3PF) was succesfully methylated under these conditions resulting in the formation of a cationic nickel species with a triflate counteranion, **5**, equation 4. Sulfur methylation gives an η^2-S_2P(SMe)F with a doublet at 2.52 ppm in the ^{1}H-NMR with associated $^3J_{HP}$= 19.7Hz coupling constant. The complex was successfully characterized by spectroscopic methods as well as elemental analysis, however poor diffraction grade crystals resulted in a structure with a high R_1 value. As a side reaction, hydrolysis of the P-F bond results in formation of the neutral complex **6**, characterized by a doublet at 2.22 ppm in the ^{1}H NMR. The very close bond lengths between P-O and P-F may

result in ambiguity in the crystal structure. However, the absence of a counter anion, absence of any ^{19}F NMR signal and presence of a strong P-O stretching band at 1261.2 cm^{-1} in the IR confirms the proper assignment of the structure.

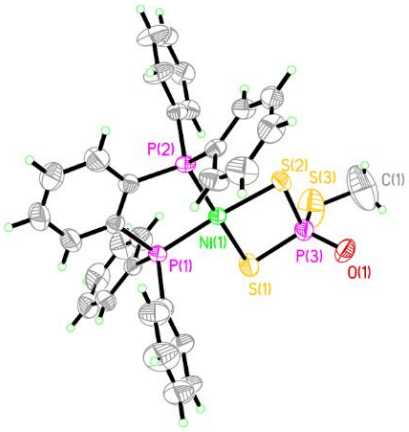

Figure 7.4: ORTEP diagrams of Ni(dpph)(S_2(SMe)PO), with 40% ellipsoids

The propensity of the ligand to hydrolyze was observed further in the reaction of $NiCl_2$(dppe) with $[N^nPr_4]_2[Zn(S_5P_2F_2)_2]$. Under wet conditions, the formation of an orange precipitate is observed. Two sets of dppe resonances are observed in the ^{31}P-NMR as well as two sets of doublets of triplets, one at 131 ppm and one at 54 ppm in a 1:2:2:1 ratio with the larger integrations corresponding to the dppe resonances. The DSC of the newly formed complex exhibited similar behaviour to that of **2a** but at different temperatures. Along with different solubility than **2a** in acetone, this suggests the formation of a different complex. A clear P-O band at 1222.46 cm^{-1} is present in the IR spectrum along with the P-S and P-F bands typically observed for the S_3PF ligand. We have proposed the binuclear nickel complex $Ni_2(dppe)_2(S_3PF)(S_2POF)$, **7**, as a possible product: the bridging S_3PF and S_2POF would account for the spectroscopic observations. The presence of the S_2POF ligand is the likely result of hydrolysis in the presence of water. This product was confirmed by ESI-MS with the presence of the molecular ion at 1189m/z and elemental analysis. Attempts at obtaining diffraction grade crystals in various solvent combinations resulted in the formation of droplet shaped crystals unsuitable for X-ray diffraction studies.

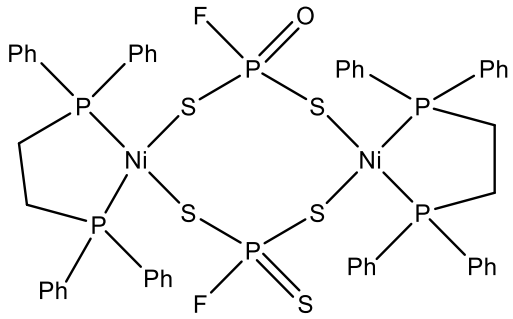

Figure 7.5: Proposed structure of $Ni_2(dppe)_2(S_3PF)(S_2POF)$

$$[(cymene)RuCl_2]_2 + 2\ [N^nPr_4]_2[S_5P_2F_2] \xrightarrow[\text{r.t, overnight}]{\text{DCM}} [(cymene)Ru(S_3PF)_2]_2 + 4\ N^nPr_4Cl + 2\ "[S_2PF]" \quad 5$$

8

In order to gain more insight into the coordination chemistry of the $S_5P_2F_2/S_3PF$ system, we extended our knowledge to a d^6 Ru(II) complex by investigating the reaction of $[(cymene)RuCl_2]_2$ with $[N^nPr_4]_2[S_5P_2F_2]$, equation 5. $[(cymene)RuCl_2]_2$ is a well-known complex with extensive organometallic chemistry. Substitution of the two chlorides resulted in the formation of a binuclear ruthenium species with two bridging S_3PF ligands: $[(cymene)Ru(S_3PF)]_2$, **8**. The presence of cis and trans isomers in solution was confirmed by ^{31}P and ^{19}F NMR while in the solid state, the X-ray diffraction crystals grown only revealed the presence of the trans isomer. Trans-$[(cymene)Ru(S_3PF]_2$ crystallized in the triclinic P-1 space group with the molecule located on the inversion center: The coordination sphere around each ruthenium center consists of η^6-cymene, two bridging sulfur atoms and one sulfur due to bidentate coordination of one of the bridging ligands. The Ru-S-Ru-S ring is planar with one bridging ligand above the plane and one below the plane in a chair like conformation with two of the P-S bonds being almost parallel to the plane. This results in two trapezoidal Ru-S-P-S above and below the Ru-S-Ru-S plane. The geometry around the ruthenium atoms is tetrahedral with rather small angles: S-Ru-S angles of 83.02(4)° and 81.27(4)° are observed.

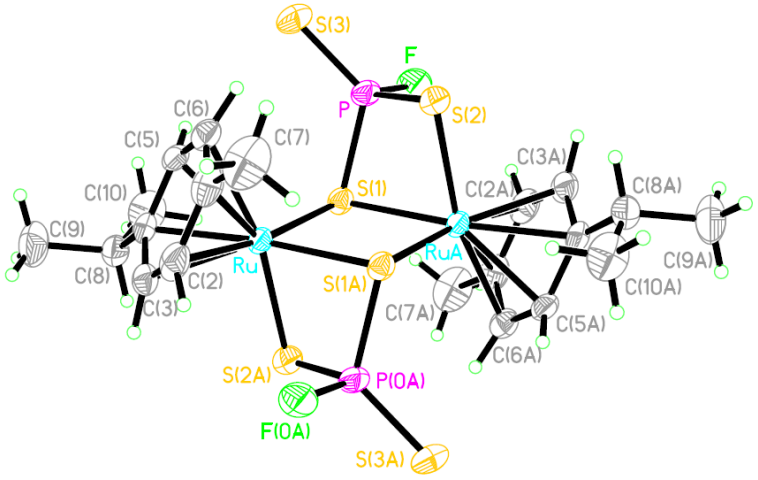

Figure 7.6: ORTEP diagram of [(cymene)Ru(S_3PF)]$_2$

[(cymene)Ru(S_3PF)]$_2$	
Bonds	Å
Ru-S1 (bridging)	2.4336(13) 2.4159(15)
Ru-S2	2.4305(15)
Ru-C (average)	2.211(4)
P-F	1.592(3)
P-S (bridging)	2.0953(18)
P-S (terminal)	1.9286(13)
P-S	2.0110(18)
Angles	°
S-Ru-S	81.27(4) 83.02(4)
S-P-S	99.57(7)
F-P-S	106.51(12)

Table 7.2: Selected bond lengths and angles of [(cymene)Ru(S_3PF)]$_2$

One striking feature of the complexes are their characteristic ^{31}P and ^{19}F NMR spectra (Table 7.3). Two important observations can be made. The first observation is the difference in chemical shift between the different ligands in the ^{31}P NMR: the presence of oxygen in the

S_2POF and $S_2(SMe)PO$ ligands results in the shift being significantly upfield: a chemical shift of 54 ppm was observed in **7** and 63 ppm in **6**. The $S_5P_2F_2$ ligand, both in the free ligand and the zinc complex give shifts at around 110 ppm while the S_3PF ligand is shifted downfield the most of the three ligands: it is found at around 130 ppm. A similar trend is observed in the ^{19}F-NMR: the shifts in the S_2POF complexes are in the negative region from -2.81 to -10.11 ppm while the S_3PF complex have shifts much more downfield at 11-18 ppm. Similar values of the $^1J_{PF}$ coupling constants between the salt and the complexes are found with the largest value of 1266.5 Hz found in **5**. This suggests similar s character of the P-F bond in the $S_5P_2F_2$, S_3PF and S_2POF ligands, but slightly more s-character in $S_2(SMe)PF$. The related fluorothiophosphate S_2PF_2 showed a remarkable increase in $^1J_{PF}$ of 100-150 Hz upon coordination of the ligand to Ru(II). This behaviour does not translate to the same extent here.

The second observation comes from possible isomerism in the complexes formed. The NMR data and crystal structure of the zinc complex suggested the formation of only one isomer. Similar behaviour can be observed for the nickel complex $[N^nPr_4]_2[Ni(S_3PF)_2]$ where the relative positions of the fluorines to the Ni-SPS plane could result in two different isomers. In the ^{31}P NMR spectrum of **1**, a doublet of doublet of doublets arises from non first order effects. In the ^{19}F NMR only one broad doublet is present, suggesting the formation of only one isomer. The crystal structures of both complexes do not show any S/F disorder which confirms this observation, with only the trans-isomer being present. The only example of cis-trans isomerism was observed with the formation of cis and trans **8** in a 4:1 trans/cis ratio in solution. While no significant change in chemical shift between the isomers was present in the ^{31}P-NMR, a large difference in chemical shift of 50 ppm was observed in the ^{19}F NMR.

Complex	^{31}P multiplicity	δ (^{31}P)	^{19}F multiplicity	δ(^{19}F)	$^{1}J_{PF}$
$[N^nPr_4]_2[S_5P_2F_2]$	AA'XX"	113.74	AA'XX'	7.33	1157.6
$[N^nPr_4]_2[Zn(S_5P_2F_2)_2]$	AA'XX'	112.06	AA'XX'	1.26	1194.3
1	ddd	133.88	d	17.82	1170.4
2a	dt	128.61	d	14.46	1171.8
2b	dt	128.27	d	14.63	1173.3
5	dt	125.67	dt	-5.45	1266.5
7	dt dt	128.60 57.45	d d	14.40 -2.81	1171.8 1171.7
3	dt s	 134.87 43.33	d	8.80	1168.8
4a	dt s	126.97 16.98	d	7.72	1171.2
4b	dt s	130.00 32.03	d	9.56	1171.9
trans-**8**	d	139.46	d	-4.37	1167.3
cis-**8**	d	140.18	d	44.56	1137.8

Table 7.3: Comparison of ^{31}P and ^{19}F NMR chemical shifts of the ligands and $^{1}J_{PF}$ coupling constants of the different complexes

A comparison to other complexes can be made for the S_3PF ligand. A library of complexes with the monodentate PO_3F ligand, was described by Weil *et al.*[55] The geometry of the PO_3F anion is tetrahedral with mean P-O bond lengths of 1.506(13) Å, P-F bond lengths of 1.578(20) Å, O-P-O angles of 113.7(1.7) ° and O-P-F angles of 104.8(1.7)° for all the complexes presented. Overall, the various PO_3F complexes have similar ligand geometries to the S_3PF complexes presented here even with a monodentate coordination mode, except for the cymene ruthenium complexes with much smaller S-P-S angles, likely due to the bridging nature of the ligand. The nickel complex of PO_3F resulted in an octahedral environment with two monodentate ligands and four water molecules. The authors reported the synthesis of $(NH_4)_2Zn(PO_3F)_2(H_2O)_{0.2}$: interestingly we have not been able to isolate a zinc complex of the S_3PF anion.

7.5 Conclusion

In conclusion, we have delved into the unexplored coordination chemistry of the S_3PF^{2-} anion and discovered a rich and complex new class of ligands: simple coordination with several

different metals resulted in the formation of complexes with the S_3PF ligand. This is a unique case in which coordination of a ligand results in bond cleavage. Unlike the late transitions metal counterparts zinc, cadmium and copper, control over the coordination mode of the ligand with group 8 metals is much simpler as coordination of $S_5P_2F_2$ is not observed. In addition to simple bis-chelates, binuclear complexes of nickel and ruthenium have been synthesized and structurally characterized. Overall, the complexes formed are easy to synthesize, stable under atmospheric conditions and have excellent spectroscopic handles with the presence of phosphorus and fluorine. This adds several new members to the already rich family of thiophosphate ligands and the lesser known fluorothiophosphates.

7.6 Experimental

The starting material $NiCl_2.6H_2O$, was purchased and used without further purification. $Ni(dppe)Cl_2$, $Ni(dpph)Cl_2$, cis-$Pd(PPh_3)_2Cl_2$, cis-$Pt(PPh_3)_2Cl_2$, cis-$Pt(PPh_2Me)_2Cl_2$ and $[(cymene)RuCl_2]_2$ were prepared according to literature procedures.[56-58] IR spectra were measured on Bomem MB3000 FTIR spectrometer as KBr pellets, and ^1H, $^{31}P\{^1H\}$ and ^{19}F NMR spectra were measured on a Bruker AVIIIHD 500 spectrometer at 22 ℃ at 500 MHz for ^1H, 202 MHz for ^{31}P and 470 MHz for ^{19}F. UV−visible spectra were obtained using an HP 8453 diode array spectrophotometer.

$[N^nPr_4]_2[S_5P_2F_2]$ was synthesized according to a previous synthesis and freshly recrystallized before the synthesis of each complex.

$[N^nPr_4]_2[Ni(S_3PF)_2]$ (1): Nickel chloride hexahydrate (100 mg) and 2.5 equivalents of $[N^nPr_4]_2[S_5P_2F_2]$ (666 mg) were dissolved in methanol. Upon stirring at room temperature, a purple precipitate formed instantly. It was filtered and washed with 3x10 mL of water and 3x10 mL of methanol. The product was recrystallized from 1:1 DCM/ethanol. Yield: 380mg (89%) DSC: sharp exotherm at 231.70 ˚C (ΔH=15.85 J/g) followed by broad exotherm at 267.1˚C (ΔH=96.81 J/g) IR: 745.9s, 674.9vs, 591.1s, ^{31}P-NMR (DMSO-d_6): 133.88 (ddd, $^1J_{PF}$=1170.4Hz, $^4J_{PP}$=$^5J_{PF}$=13.3Hz), ^{19}F-NMR (DMSO-d_6): 17.5(d, $^1J_{PF}$=1170.4Hz) UV-Vis (acetone): 520nm (2.7), 667nm(2.7) Anal. Calcd for $N_2C_{24}H_{56}NiF_2P_2S_6$: C, 39.83; H, 7.80; N, 3.87 Found: C, 40.21; H, 7.69; N, 3.81 X-ray diffraction crystals grown from DCM/EtOH.

Ni(dppe)(S_3PF) (2a): $NiCl_2$(dppe), (170 mg), was dissolved in 50 mL dichloromethane and 1.2 equivalents of $[N^nPr_4]_2[S_5P_2F_2]$, (244 mg), was added and the resulting orange solution stirred at r.t. for 20 min. The yellow orange solution was diluted with 20 mL ethanol and concentrated to 10 mL to give a bright orange solid which was filtered and washed with 10 mL each of ethanol, water, ethanol, and hexanes. Yield: 161 mg (83%) DSC: sharp exotherm at 233.1˚C (ΔH=38.62 J/g) IR: 860.2m, 816.8s, 765.3s, 745.9s, 681.5vs, 572.0m, 527.0vs ^{31}P-NMR (DMSO-d_6): 128.60 (dt, $^1J_{PF}$ =1171.8Hz, $^3J_{PP}$ =15.5Hz) 64.80 (d, $^3J_{PP}$=15.5Hz) ^{19}F-NMR (DMSO-d_6): 14.45 (d, $^1J_{PF}$

=1171.8Hz) Anal. Calcd. for $NiS_3P_3FC_{26}H_{24}$: C, 51.76; H, 4.01; Found: C, 51.36; H, 3.93; X-ray diffraction crystals grown from DCM/EtOH.

Ni(dpph)(S_3PF) (2b): $NiCl_2$(dpph), (140 mg), was dissolved in 50 mL dichloromethane and 1.2 equivalents of $[N^nPr_4]_2[S_5P_2F_2]$, (201 mg), was added and the resulting orange solution stirred at r.t. for 20 min. The yellow orange solution was diluted with 20 mL ethanol and concentrated to 10 mL to give a bright orange solid which was filtered and washed with 10 mL each of ethanol, water, ethanol, and hexanes. Yield: 160 mg, (77%). DSC: thermally stable up to 300 °C IR: 780.4w, 687.5brs, 497.5m, 455.2w ^{1}H NMR (500 MHz, CD_2Cl_2) ppm: 7.65(m, 2) 7.59(m,10), 7.51(m,4), 7.41(m, 8, dpph). ^{31}P NMR (202.46 MHz, CD_2Cl_2) ppm: 62.48 (dd, 2, $^4J_{PF}$ = 16.1Hz, $^3J_{PP}$ = 2.1 Hz, PPh_3), 128.55(dt, 1, $^1J_{PF}$ = 1186.4, $^3J_{PF}$= 15.9 Hz, S_3PF). ^{19}F NMR (470.59 MHz, $CDCl_3$) ppm: 11.04(d,1, $^1J_{PF}$ = 1186.4,S_3PF). Anal. Calcd for $NiS_3P_3FC_{26}H_{24}$: C, 55.32; H, 3.71; Found: C, 55.36; H, 3.61; X-ray diffraction crystals grown from DCM/ethanol.

Pd(PPh_3)$_2$(S_3PF) (3): $PdCl_2(PPh_3)_2$, (169 mg), was dissolved in 50 mL dichloromethane. Most of the complex dissolved to give a pale yellow solution. 1.2 equivalents of $[N^nPr_4]_2[S_5P_2F_2]$, (180 mg), were added and the resulting solutions stirred at r.t. for 15 min. The yellow orange solution was diluted with 20 mL ethanol, and concentrated to 10 mL to give a yellow solid which was filtered and washed with 10 mL each of ethanol, water, ethanol, and hexanes. Yield: 141 mg (76%). DSC: sharp exotherm at 227.9°C (ΔH=21.17 J/g) immediately followed by broad exotherm at 249.0 °C (ΔH=45.61 J/g) IR: 780w, 760.1m, 691.7s, 573.2w ^{1}H NMR (500 MHz, CD_2Cl_2) ppm: 7.42 7.33 (m, 30, PPh_3). ^{31}P NMR (202.46 MHz, CD_2Cl_2) ppm: 32.03 (d, 2, $^3J_{PF}$ = 4.0 Hz, PPh_3), 113.6(dt, 1, $^1J_{PF}$ = 1163.6, $^3J_{PF}$ = 3.9 Hz, S_3PF) ^{19}F-NMR (CD_2Cl_2) 8.80 (d, $^1J_{PF}$ =1163.6Hz) Anal. Calcd for $PdS_3P_3FC_{36}H_{30}$: C, 54.38; H, 4.06; Found: C, 54.08; H, 3.88. X-ray diffraction crystals grown from DCM/ethanol.

Pt(PPh_2Me)$_2$(S_3PF) (4a): $PtCl_2(PMePh_2)_2$, (26 mg) was dissolved in 20 mL dichloromethane and treated with 1.5 equivalents (38 mg), of $[N^nPr_4]_2[S_5P_2F_2]$. The mixture was stirred overnight at room temperature, then diluted with 20 mL ethanol, and concentrated to 5 mL. After cooling at -23 °C overnight copious white crystals formed. The resulting white solid was isolated by filtration and successive washes with ethanol, water, ethanol, and hexanes to give white crystals

of $Pt(PPh_2Me)_2(S_3PF)$. Yield: 26mg 88% DSC: broad exotherm at 204.40°C (ΔH=19.64 J/g) followed by broad exotherm at 280.9°C (ΔH=10.92 J/g) IR: 883.6s, 743.6s, 692.47s. ^{1}H NMR (500 MHz, CD_2Cl_2) ppm: 7.42 - 7.50 (m, 20, PPh_2), 1.88(d, $^2J_{HP}$ = 9.5Hz, $^3J_{HPt}$ = 26.8Hz, 4, PCH_3). ^{31}P NMR (202.46 MHz, CD_2Cl_2) ppm: 32.03 (d, 2, $^3J_{PF}$ = 4.0 Hz, PPh_3), 130.00 (dt, 1, $^1J_{PF}$ = 1171.9, $^3J_{PF}$ = 8.1 Hz, , $^3J_{PPt}$ = 269.2Hz S_3PF) ^{19}F NMR (470.59 MHz, CD_2Cl_2) ppm: 9.56(dt, $^1J_{PF}$ = 1171.9 Hz, $^4J_{PF}$ = 7.7 Hz, S_3PF) Anal. Calcd for $PtS_3P_3FC_{26}H_{26}$: C, 42.10; H, 3.53; Found: C, 42.36; H, 3,93; X-ray diffraction crystals grown from DCM/ethanol.

$Pt(PPh_3)_2(S_3PF)$ (4b): $PtCl_2(PPh_3)_2$, (258 mg), was dissolved in 50 mL dichloromethane with moderate warming. 1.2 equivalents of $[N^nPr_4]_2[S_5P_2F_2]$, (248 mg), were added and the resulting solution stirred at r.t. overnight. The clear faint yellow solution was diluted with 20 mL ethanol and concentrated to 10 mL to give a colorless solid which was filtered and washed with 10 mL each of ethanol, water, ethanol, and hexanes. Yield: 243 mg (85%) DSC: sharp exotherm at 298.42°C (ΔH=19.66 J/g) IR: 879.8mw, 699.5s ^{1}H NMR (500 MHz, CD_2Cl_2) ppm: 7.42 7.33 (m, 30, PPh_3). ^{31}P NMR (202.46 MHz, CD_2Cl_2) ppm: 16.98 (d, 2, $^3J_{PF}$ = 3.1 Hz, $^1J_{PPt}$ = 336.2 Hz, PPh_3), 127.69(dt, 1, $^1J_{PF}$ = 1171.2, $^3J_{PP}$ = 8.1 Hz, $^2J_{PPt}$ = 273.3Hz, S_3PF). ^{19}F NMR (470.59 MHz, CD_2Cl_2) ppm: 7.72(dt, $^1J_{PF}$ = 1175.6 Hz, $^4J_{PF}$ = 7.7 Hz, S_3PF). Anal. Calcd for $PtS_3P_3FC_{36}H_{30}$: C, 49.94; H, 3.49; Found: C, 49.73; H, 3.38; X-ray diffraction crystals were grown from DCM/ethanol.

$[Ni(S_2PF(SMe))(dpph)]CF_3SO_3$ (5): $Ni(S_3PF)(dpph)$ (50 mg) was dissolved in 50 mL dichloromethane and treated with 1.1 equivalent of CF_3SO_3Me (0.013g, 8.4 μL). The resulting solution was stirred for 10 min at r.t., and n-hexane, 30 mL, was added and the solution concentrated to give an orange crystal mass. An additional 30 mL n-hexane was added and the resulting suspension concentrated to ca. 5 mL. Filtration and 3 washes with n-hexane gave an orange product, Yield: 57mg, 92%. Analytical sample obtained from dichloromethane/benzene. DSC: 216.7 °C, (ΔH=29.4 J/g) (irreversible decomposition.) IR (KBr, cm^{-1}): 1271.7s, 1139.0m, 1030.8s, 837.5br, 743.4w, 637.1brs, 497.5m, 455.2w. ^{1}H NMR (500 MHz, CD_2Cl_2) ppm: δ = 2.52(d, $^3J_{HP}$=19.7Hz, 3), 7.85(m, 2) 7.67(m,6), 7.57(m,16, dpph). ^{31}P NMR (202.46 MHz, CD_2Cl_2) ppm: 64.83(dd, 2, $^4J_{PF}$ = 9.2Hz, $^3J_{PP}$ = 10.5 Hz, PPh_2), 125.67(dt, 1, $^1J_{P-F}$ = 1266.5, $^3J_{PP}$=

10.7 Hz, $S_2P(SMe)F$). ^{19}F NMR (470.59 MHz, CD_2Cl_2) ppm: -5.45(dt,1, $^1J_{P\text{-}F}$ = 1266.9, $^4J_{PF}$ = 7.8Hz,) -78.87(s,3). Anal. Calcd for $NiS_4P_3F_4C_{32}H_{27}O_3$: C, 47.13; H, 3.34; Found: C, 46.76; H, ; 3.67

$Ni_2(dppe)_2(S_3PF)(S_2POF)$ (7): $Ni(dppe)Cl_2$ (170mg) and 0.5 equivalents of $[N^nPr_4]_2[Zn(S_5P_2F_2)_2]$ (50mg) were dissolved in acetone and stirred at room temperature during which an orange precipitate formed. The precipitate was filtered and washed 3x10mL of methanol and 3x10mL of water. The product was precipitated from DCM/methanol. Yield: 170mg (65%) DSC: sharp exotherm at 231.77°C (ΔH=72.23 J/g) followed by broad exotherm at 272.9°C (ΔH=27.98 J/g) IR:3051.8w, 2922.9w, 1705.5w, 1570.4w, 1480.0s, 1435.0vs, 1306.2m, 1222.4vs, 1190.2s, 990.7s, 861.9m, 810.3s, 765,2vs, 694.3vs, 597.7s, 527.0vs, 475.4s ^{31}P-NMR (DMSO-d_6): ^{31}P-NMR (DMSO-d_6): 128.60 (dt, 1, $^1J_{PF}$ =1171.8Hz, $^3J_{PP}$=15.5Hz) 65.19 (dd, 2, $^3J_{PP}$=18.3Hz, $^4J_{PF}$=4.2Hz), 64.80 (dd, 2, $^3J_{PP}$=15.5Hz, $^4J_{PF}$=2.0Hz), 57.45 (dt, 1, $^1J_{PF}$ =1171.7Hz, $^3J_{PP}$=18.3Hz) ^{19}F-NMR (DMSO-d_6): 14.40 (d, 1, $^1J_{PF}$ =1172.1Hz) -3.94 (d, 1, $^1J_{PF}$ =1171.8Hz) Anal. Calcd for $Ni_2S_5P_6F_2OC_{52}H_{48}$: C, 52.46; H, 4.06; Found: C, 52.21; H, 4.06;

$[(cymene)Ru(S_3PF)]_2$ (8): $[Ru(\eta^6\text{-cymene})(\eta^2\text{-}\mu_2\text{-}Cl_2)]_2$ (53 mg, 0.086mmol), is dissolved in 50 mL dichloromethane. 1.02 equivalents of $[N^nPr_4]_2[S_5P_2F_2]$, (118 mg, 0.186mmol), is added and the resulting solutions stirred at r.t. overnight. A bright orange crystalline solid forms under a brown solution. The solid is filtered and washed with 10 mL dichloromethane to give 61 mg, 92%, of orange crystals as a mixture of 4:1 trans:cis isomers. This can be further recrystallized from dichloromethane/hexane or purified by column chromatography from silica with 1:1 acetone/dichloromethane. DSC: broad exotherm at 228.41°C (ΔH=9.06 J/g) (irreversible decomposition) IR (KBr, cm^{-1}): Strong cymene bands at: 1435.5, 1094.3, 744.1, 688.0. Trithiofluorophosphate bands at: 821.8m, 715.3s, 481.8w. DSC: T= 228.4°C ΔH= 27.4 J/g (irreversible decomposition.) Anal. Calcd for $C_{20}H_{28}F_2P_2Ru_2S_6$: C, 31.49; H, 3.70; Found: C, 30.83; H, 3.81

Major isomer with trans fluorines: ^1H NMR (500 MHz, CD_2Cl_2) ppm: Broad singlets at 6.51, 6.33, 5.57, 4.72(1 proton each), 2.19 (brs, 3), 2.65 (brs,1), 1.21 (br d,6). ^{31}P NMR (202.46 MHz, CD_2Cl_2) ppm: 139.46 (d, 2, $^1J_{PF}$ = 1135.5 Hz), ^{19}F NMR (470.59 MHz, CD_2Cl_2) ppm: –4.38 (d, $^1J_{P\text{-}F}$ = 1167.3 Hz).

Minor isomer with cis fluorines:

^{1}H NMR (500 MHz, CD_2Cl_2) ppm: δ = 6.69, 6.24, 5.85, 5.01(broad d, 1 proton each, with a coupling of 6 Hz), 2.13(s, 3), 2.73(sept, $^{3}J_{HH}$=6.8Hz, 1), 1.22(d, $^{3}J_{HH}$=6.8Hz, 6). ^{31}P NMR (202.46 MHz, CD_2Cl_2) ppm: δ =140.18(d, 2, $^{1}J_{PF}$ = 1137.8 Hz), ^{19}F NMR (470.59 MHz, CD_2Cl_2) ppm: δ = 44.56 (d, $^{1}J_{P\text{-}F}$)= 1137.8 Hz

7.6.1 Crystallographic Methodologies

Crystals are mounted on glass fibers with epoxy resin or Mitogen mounts using Paratone-N from Hampton Research and single-crystal X-ray diffraction experiments are carried out with a BRUKER APEX-II D8 CCD diffractometer by using graphite-monochromated Mo Kα radiation (λ = 0.71073 Å) the SHELX package[59] is used for integration of the intensity reflections, scaling, and absorption correction. Intrinsic phasing methods were used to solve the structures. Non-hydrogen atoms are located by difference Fourier maps and final solution refinements are carried out by full-matrix least-squares methods on F2 for all of the data. The hydrogen atoms are placed in calculated positions and were not refined.

7.7 References

1. Yang, Y.; Song, M.; Wu, X. W.; Wu, K.: A Review of the Structural Diversity of $[PxSy]^{n-}$ Motifs and Their Potential Application Prospects in Metal Thiophosphates, *J. Phys. D: Appl. Phys*., **2021**, *54*, 463002
2. Roedl, T.; Weihrich, R.; Wack, J.; Senker, J.; Pfitzner, A.: Rational Syntheses and Structural Characterization of Sulfur-Rich Phosphorus Polysulfides: α-P_2S_7 and β-P_2S_7. *Angew. Chem., Int. Ed.* **2011**, *50*, 10996-11000
3. Samal, R.; Sanyal, G.; Chakraborty, B.; Rout, C. S.: Two-Dimensional Transition Metal Phosphorous Trichalcogenides (MPX_3): a Review on Emerging Trends, Current State and Future Perspectives. *J. Mater. Chem. A* **2021**, *9*, 2560-2591.
4. Alahmari, F.; Davaasuren, B.; Khanderi, J. ; Rothenberger, A.: Synthesis and Characteization of the Rubidium Thiophosphate $Rb_6(PS_5)(P_2S_{10})$ and the Rubidium Silver Tiophosphates Rb_2AgPS_4, $RbAg_5(PS_4)_4$., *Z. Anorg. Allg. Chem.*, **2016**, *642*, 361-367
5. Dong, Y; Lee, K.; Yun, H. ; Hur, N.-H.: Synthesis, Structure and Magnetic Properties of One-Dimensional Thiophosphate, $A_2NiP_2S_6$ (A=Rb, Cs). *J. Korean, Chem. Soc*., **2001**, *45*, 242-246
6. Goh, E.-Y.; Kim, E.-J.; Kim, S.-J.: Modification on Quaternary Rare Earth Thiophosphates: $NaYbP_2S_6$, $NaSmP_2S_6$ and $KSmP_2S_7$, *J. Solid, State. Chem.*, **2001**, *160*, 195-204
7. Jandali, M. Z.; Eulenberger, G. ; Hahn, H.: Synthesis and Crystal Structure of Titanium Thiohypophosphate (TiP_2S_6), *Z. Anorg. Allg. Chem*., **1980**, *470*, 39-44
8. Hanko, J. A.; Sayettat, J.; Jobic, S.; Brec, R.; Kanatzidis, M. G.: $A_2CuP_3S_9$ (A=K, Rb), $Cs_2Cu_2P_2S_6$, and $K_3CuP_2S_7$: New Phases from the Dissolution of Copper in Molten Polyhiophosphate Fluxes, *Chem. Mater*., **1998**, *10*, 3040-3049
9. Lott, D. R.; Fincher, T.; LeBret, G. C.; Cleary, D. A.; Breneman, G. L.: Synthesis and Crystal Structure of ZrP_2S_6 and ZrP_2S_7, *J. Solid. State. Chem.*, **1999**, *143*, 239-245
10. Jandali, M. Z.; Eulengerber, G. ; Hahn, H.: Preparation and Crystal Structure of Mercury(II) Thiodiphosphate ($Hg_2P_2S_7$)., *Z. Anorg. Allg. Chem*., **1978**, *445*, 184-192

11. Babo, J.-M.; Jouffret, L. ; Lin, J. ; Villa, E. M. ; Albrecht-Schmidt, T. E.: Synthesis, Structure and Spectroscopy of Two Ternary Uranium(IV) Thiophosphates: UP_2S_9 and UP_2S_7 Containing $P_2S_9^{2-}$ and $P_2S_7^{2-}$ Ligands., *Inorg. Chem.*, **2013**, *52*, 7747-7751
12. Gutzmann, A.; Naether, C.; Bensch, W.: $Cs_3Hf_2(P_2S_7)_2(PS_4)$. *Acta. Crystallogr., Sect. E*, **2004**, *60*, 42-44
13. Gutzmann, A.; Naether, C.; Bensch, W.: Synthesis, Crystal Structure and Optical Properties of $A_3Zr_2P_5S_{18}$ (A=Rb, Cs): the First Quaternary Zirconium Thiophosphates., *Solid State Sci*., **2004**, *6*, 205-211
14. Gutzmann, A.l Bensch, W.: Synthesis and Crystal Structure of the New Quaternary Niobium Thiophosphate $Rb_2Nb_2P_2S_{11}$, *Solid State Sci*., **2002**, *4*, 835-840
15. Jandali, M. Z.; Eulenberger, G. ; Hahn, H.: Preparation and Crystal Structure of the Titanium(IV) Thiophosphate(V) $Ti_4P_8S_{29}$., *Z. Anorg. Allg. Chem*., **1985**, *530*, 144-154
16. Wu, Y.; Bensch, W.: $Rb_3Ti_3(P_4S_{13})(PS_4)_3$ and $Cs_2Ti_2(P_2S_8)(PS_4)_2$: Two Polar Titanium Thiophosphates with Complex One-Dimensional Tunnels., *Inorg. Chem*., **2007**, *46*, 6170-6177
17. Kuhn, A.; Eger, R.; Nuss, J.; Lotsch, B. V.: Synthesis and Structural Characterization of the Alkali Thiophosphates $Na_2P_2S_6$, $Na_4P_2S_6$, $K_4P_2S_6$ and $Rb_4P_2S_6$, *Z. Anorg. Allg. Chem*., **2014**, *640*, 689-692
18. Suto, K.; Bonnick, P.; Nagai, E.; Niitani, K.; Arthur, T. S.; Muldoon, J.: Microwave-Aided Synthesis of Lithium Thiophosphate Solid Electrolyte, *J. Mater. Chem. A*., **2018**, *6*, 21261-21265
19. McCarthy, T. J.; Kanatzidis, M. G.: Synthesis in Molten Alkali Metal Polythiophosphate Fluxes, The New Quaternary Bismuth and Antimony Thiophosphates $ABiP_2S_7$ (A=K, Rb), $A_3M(PS_4)_2$ (A=K, Rb, Cs; M= Sb, Bi), $Cs_3Bi_2(PS_4)_3$, and $Na_{0.16}Bi_{1.28}P_2S_6$, *J. Alloys. Comp*., **1996**, *236*, 70-85
20. Chica, D. G.; Iver, M.; Cheng, M., Ryan, K. M.; Krantz, P.; Laing, C. ; dos Reis, R.; Chandrasekhar, V.; Dravid, V. P.; Kanatzidis, M. G.; P_2S_5 Reactive Flux Method for the Rapid Synthesis of Mono- and Bimetallic 2D Thiophosphates $P_{2-x}M'_xP_2S_6$, *Inorg. Chem*., **2021**, *60*, 3502-3513

21. Haynes, A. S.; Lee, K.; Kanatzidis, M. G. : One-Dimensional Zinc Selenophosphates : $A_2ZnP_2Se_6$ (A= K, Rb, Cs)., *Z. Anorg. Allg. Chem*., **2016**, *642*, 1120-1125
22. Chondroudis, K.; Kanatzidis, M. G. : $[M_4(Se_2)_2(PSe_4)_4]^{8-}$: a Novel, Tetranuclear, Cluster Anion with a Stellane-Like Core., *Chem. Commun. (Cambridge)*, **1997**, 401-402
23. Chondroudis, K.; Kanatzidis, M. G. : Group 10 and group 12 One-Dimensional Selenodiphosphates: $A_2MP_2Se_6$ (A= K, Rb, Cs; M= Pd, Zn, Cd, Hg)., *J. Solid. State. Chem*., **1998**, *138*, 321-328
24. Ma, H. W.; Guo, G. C.; Chem, W. T. ; Deng, L. ; Zhhou, G. W. ; Dong, Z. C. ; Huang, J. S. : Synthesis and Structure of Ag_3PSe_4, *Jiegou Huaxue*, **2003**, *22*, 161-164
25. Ma, H. W.; Guo, G. C.; Zhou, G. W.; Wang, M. S.; Lin, S. H.; Dong, Z. C.; Huang, J. S.: Synthesis and Re-Refinement of Cu_3PSe_4., *Jiegou Huaxue*, **2002**, *21*, 288-291
26. Friedrich, D.l Schlosser, M.; Naether, C.; Pfitzner, A.: In Situ X-ray Diffraction Study of the Thermal Decomposition of Selenogallates $Cs_2[Ga_2(Se_2)_{2-x}Se_{2+x}]$ (x=0,1,2)., *Inorg. Chem*., **2018**, *57*, 5292-5298
27. Gutzmann, A.; Bensch, W.: Synthesis, Crystal Structure and Optical Properties of the New Layered Quaternary Tantalum Thiophosphate $Rb_4Ta_4P_4S_{24}$ Based on the Interconnection of Ta_2S_{11} Units by PS_4 Tetrahedra, *Solid. State. Sci*., **2003**, *5*, 1271-1276
28. Feng, J.; Hu, C. L.; Li, B. ; Mao, J. G.: $LiGa_2PS_6$ and $LiCd_3PS_6$: Molecular Designs of Two New Mid-Infrared Nonlinear Optical Materials, *Chem. Mater*., **2018**, *30*, 3910-3908
29. Li, M. Y.; Ma, Z.; Li, B.; Wu, X. T.; Lin, H.; Zhu, Q. L.: $HgCuPS_4$: an Exceptional Infrared Nonlinear Optical Material with Defect Diamond-Like Structure, *Chem. Mater*., **2020**, *32*, 4331-4339
30. Auvergniot, J.; Cassel, A.; Ledeuil, J.-B.; Viallet, V.; Seznec, V.; Dedryvere, R.: Interface Stability of Argyrodite Li_6PS_5Cl toward $LiCoO_2$, $LiNi_{1/3}Co_{1/3}Mn_{1/3}O_2$, and $LiMn_2O_4$ in Bulk All-Solid-State Batteris., *Chem. Mater*., **2017**, *29*, 3883-3890
31. Bron, P.; Johansson, S.; Zick, K.; Schmedt Auf Der Grunne, J.; Dehnen, S.; Roling, B.: $Li_{10}SnP_2S_{12}$: an Affordable Lithium Superionic Conductor, *J. Am. Chem. Soc*., **2013**, *135*, 15694-15697

32. Dietrich, C.; Weber, D. A.; Culver, S.; Senshyn, A.; Sedlmaier, S. J.; Indris, S.; Janck, J.; Zeier, W. G.: Synthesis, Structural Characterization, and Lithium Ion Conductivity of the Lithium Thiophosphate $Li_2P_2S_6$, *Inorg. Chem.*, **2017**, *56*, 6681-6687
33. Rao, R. R.; Raychaudhuri, A. K.: Magnetic Studies of a Mixed Antiferromagnetic System $Fe_{1-x}Ni_xPS_3$, *J. Phys. Chem. Solids.*, **1992**, *53*, 577-583
34. Maisonneuve, V.; Cajipe, V. B.; Simon, A.; Von Der Muhll, R. ; Ravez, J.: Ferrielectric Ordering in Lamellar $CuInP_2S_6$, *Phys. Rev. B.: Condens. Matter*, **1997**, *56*, 10860-10868
35. Roesky, H. W.: Darstellung und Untersuchung von Dichlorothiophosphated und Chlororfluorothiophosphated. *Chem Ber*., **1967**, *100*, 1447-1450
36. Roesky, H. W.: Darstellung und Unersuchung von Difluorothiophosphaten., *Chem Ber*., **1967**, *100*, 950-953
37. Lustig, M.; Ruff, J. K.: Studies Involving Some Nonmetal Oxy and Thiofluoride Salts., *Inorg. Chem*., **1967**, *6*, 2115-2117
38. Roesky, H. W.; Tebbe, F. N.; Muetterties, E. L.: New Phosphorus-Sulfur Chemistry., *J. Am. Chem. Soc*., **1967**, *89*, 1272-1274
39. Mitchell, R. W.; Lustig, M.; Hartman, F. A.; Ruff, J. K.; Merritt, J. A.: Synthesis and Properties of Difluorodithiophosphoric acids., *J. Am. Chem. Soc*., **1968**, *90*, 6329-633
40. Charlton, T. L.; Cavell, R. G.: The Synthesis and Properites of Difluorodithiophorphoric Acid., *Inorg. Chem*., **1969**, *8*, 281-285.
41. Roesky H. W.; Tebbe F. N.; Muetterties E. L.: Thiophosphate Chemistry.1 The Anion Set $X_2PS_2^-$, $(XPS_2)_2S_2^-$, and $(XPS_2)_2S_2^{2-}$ *Inorg. Chem.*, **1970**, *9*, 831-836.
42. Tebbe F. N.; Muetterties E. L.; Metal Complexes of the Difluorodithiophosphate Ligand *Inorg. Chem.*, **1970**, *9*, 629-637.
43. Cavell R. G.; Byers W.; E. D. Day: Metal Complexes of Substituted Dithiophosphinic Acids. I. Complexes of Trivalent Chromium *Inorg. Chem.*, **1971**, *10*, 2710-2715.
44. Cavell R. G.; Day E. D.; Byers W.; Watkins P. M.: Metal Complexes of Substituted Dithiophosphinic Acids. V. Complexes of Manganese, Iron, and Cobalt *Inorg. Chem.*, **1972**, *11*, 1759-1772.

45. Cavell R. G.; Byers W.; Day E. D.; Watkins P. M.: Metal Complexes of Substituted Dithiophosphinic Acids. IV. Complexes of Divalent Nickel, Palladium, and Platinum, *Inorg. Chem.*, **1972**, *11*, 1598-1606.
46. Cavell R. G.; Day E. D.; Byers W.; Watkins P. M.: Metal Complexes of Substituted Dithiophosphinic Acids. III. Vanadyl Complexes *Inorg. Chem.*, **1972**, *11*, 1591-1597
47. Cavell R. G. : Sanger A. R.: Metal Complexes of Substituted Dithiophosphinic Acids. VI. Reactions of Difluorodithiophosphinic Acid with Chlorides and Oxychlorides of Chromium, Molybdenum *Inorg. Chem.*, **1972**, *11*, 2011-2016.
48. Cavell R. G.; Sanger A. R.: Metal Complexes of Substituted Dithiophosphinic Acids. VII. Reactions of $TiCl_4$, $VC1_4$, $NbCl_4$, $NbCl_6$, and $TaCl_5$ with Difluorodithiophosphinic Acid, *Inorg. Chem.*, **1972**, *11*, 2016-2019.
49. Hartman F. A.; Lustig M.: Preparation and Reactions of Tetracarbonyl-μ-bis(difluorodithiophosphato)-dirhodium(I)*Inorg. Chem.*, **1968**, *7*, 2669-2670.
50. Islam M. Q.; Hill W. E.; Webb T. R.; Quadruply Bonded Dimolybdenum Complexes of $PF_2S_2^-$. Comparison with Complexes of PR_2S_{2p-} (R= Et, Me) *J. Fluor. Chem.*, **1990**, *48*, 429-440
51. Neels, J.; Grimmer, A.-R.; Meisel, M.: Salze von Halogenophosphorsäuren. XV. Sulfan-α, ω-diyl-bis (fluorodithiophosphate), Reaktionsprodukte des Fluoridabbaus Schwefelreicher Phosphorsulfide., *Z. Anorg. Allg. Chem.*, **1987**, *547*, 83-90
52. Esparza-Ruiz, A.; Gonzalez-Gomez, G.; Mijangos, E.; Pena-Hueso, A.; Lopez-Sandoval, H.; Flores-Parra, A.; Contreras, R.; Barba-Behrens, N.: Coordination Chemistry of a Bis(benzimidazole) Disulfide: Eleven Membered Chelate Ring in Cobalt(II), Zinc(II) and Cadmium(II) Halide Compounds; Oxidative Disulfide Cleavage when Coordinated to Nickel(II), *Dalton Trans.*, 2010, *39*, 6302–6309
53. Fluck, E.; Retuert, P. J.; Binder, H.: Dithiophosphorsaurebetaine, *Z. Anorg. Allg. Chem.*, **1973**, *397*, 225-230
54. Solari, E.; Gauthier, S. ; Scopelliti, R. ; Severin, K. ; Multifaceted Chemistry of $[(cymene)RuCl_2]_2$ and PCy_3, *Organometallics*, **2009**, *28*, 4519-4526

55. Weil, M.: Monofluorophosphates-New Examples and a Survey of the PO_3F^{2-} Anion, *Chemistry*, **2021**, *3*, 45-73
56. Van Haecke, G. R.; Horrocks Jr., W. D. W.: Ditertiary Phosphine Complexes of Nickel. Spectral, Magnetic, and Proton Resonance Studies. A Planar-Tetrahedral Equilibrium, Inorg. Chem., 1966, 5, 1968-1974
57. Jenkins, J. M.; Shaw, B. L.: Nuclear Magnetic Resonance Studies on Metal Complexes. Part 1. Dimethylphenylphosphine Complexes of Platinum (II) and Palladium(II), J. *Chem. Soc. A.*, **1966**, 770-775
58. Bennett, M. .A.; Huang,T.-N.; Matheson,T.W.; Smith,A. K., 16. (η6-Hexamethylbenzene)Ruthenium Complexes, *Inorg.Synth.*, **1982**, *21*, 74-78
59. Sheldrick, G. M., SADABS, TWINABS; Siemens Industrial Automation, Inc.: Madison, WI, 1996

Chapter 8: Conclusions, Contributions to Original Knowledge and Future Perspectives

In this thesis, we have investigated several transition metal complexes and their potential use as candidates to experimentally measure PVED in molecules. The conclusion from chapter 1 was that despite years of research, using many different techniques on a variety of chiral molecules, PVED has not been detected in molecules so far. From this observation, it was essential to determine criteria for which a molecule should respect in order to be a viable candidate for such measurements. It was concluded that neutral tris-chelate complexes of cobalt, rhodium and iridium fit most of the criteria as they contain heavy elements, were believed to be stereochemically rigid, and have been described as being obtainable in the gas phase. We have focused our attention on three classes of ligands: tropolonates, dithiocarbamates and fluorothiophosphates, each of which presented unique challenges.

In chapters 2 and 4 we have synthesized new tris-chelate complexes of two different ligands: a tropolone derivative, hinokitiol, and the lesser-known parent dithiocarbamate S_2CNH_2. Interestingly, in both cases variable temperature NMR revealed the complexes to be very stereochemically labile with low barriers of activation even for the heavier elements of the triad. This was an unexpected result as it had been previously accepted that such complexes are stereochemically rigid, as was reported for example by Muetterties in his analysis of tris-chelate complexes of α-isopropyltropolone[1] or by Pignolet with complexes of dibenzyldithiocarbamates.[2] Since complexes inert towards racemization are required for PVED measurements, future work regarding PVED and dynamic behaviour of tris-chelate complexes will have to take this observation into consideration.

Both these cases have also revealed the importance to have a good understanding of the mechanisms of inversion of stereochemistry of tris-chelate complexes. The analysis of the crystal structure of tris-chelate complexes with the S_2CNH_2 ligand revealed an unusually distorted structure never reported previously. Whether or not this distortion has an impact on the value of the rotational barrier remains to be determined and will require considerable theoretical analysis.

Experimentally, it will be important to find other cases in which this distortion is observed: perhaps tris-chelate complexes with other sulfur donor atoms such as other dithiocarbamates or different ligands inlcuding dithiolates or dithiophosphates such as those presented in chapter 5. It is finally worth noting that $Co(hino)_3$ showed lability towards substitution with ethylenediamine: this may be extended to different ligands such as acetylacetonate and could be used a new synthetic route towards the synthesis of Co(III) tris-chelate complexes. This may also be extended to rhodium and iridium.

In chapter 3 we observed that this stereochemical lability is not limited to tris-chelate complexes as it was observed that Os(II) complexes of hinokitiol presented similar dynamic behaviour of their tris-chelate counterparts. While this is important in understanding dynamic behaviour of metal complexes with tropolonate derivatives it may also have an impact on the biochemistry of hinokitiol especially with regards to it being a potential iron chelator. This may be extended further to substituted catechols and their Ru(II) and Os(II) derivatives.

In chapters 5-7, our search of potentially volatile tris-chelate complexes has led us to investigate the coordination chemistry of two fluorothiophosphate ligands, the first being the S_2PF_2 anion. The first crystal structures of such complexes are reported in Ru(II) complexes and their carbonylation. This class of ligands is still uncharted: obtaining crystal structures is a first step in increasing our knowledge of the bonding properties of this ligand. The synthesis and characterization of new complexes will be important but having a good understanding of the reactivity of such complexes is equally as useful. The synthesis of rhodium and iridium tris-chelate complexes with this ligand should also be obtained and rotational barriers calculated using the same methods as with the tropolonate and dithiocarbamate complexes.

Our study of the S_2PF_2 ligand was complemented by that of the $S_5P_2F_2$ ligand. This resulted in the formation of many different complexes with either $S_5P_2F_2$, S_3PF or S_2POF ligands: simple bis-chelates of zinc and nickel as well as more complex binuclear ruthenium and nickel species and finally cage-like clusters with cadmium and copper were successfully synthesized and characterized. This is a new area in coordination chemistry, and much research will be needed to have a better understanding of this system. Coordination to earlier transition metals as well as

gaining a better understanding of the mechanisms leading to cleavage of the P-S bond in $S_5P_2F_2$ will be necessary. As anions, the cadmium and copper clusters may be used to trap cations such as lithium within their cavities. Modulation of the size of the copper cluster may be achieved by alkylation of the terminal sulfurs. One exciting perspective is the potential use of these complexes as phosphorylating agents due to the release of S_2PF upon coordination.

It is clear from the examples presented in this thesis that finding a good candidate molecule for PVED measurements is a difficult task. Due to their low rotational barriers, tris-chelate complexes of tropolonate derivatives and dithiocarbamates would not fit the criteria. Our early studies on fluorothiophosphate ligands point towards some dynamic behaviour being present which may translate to similarly low isomerization barriers in their tris-chelate complexes. While finding such a molecule is essential, finding a suitable technique precise enough to determine very small energy differences due to PVED is equally essential. Rotational spectroscopy can be used for the volatile complexes. NMR may be a viable option: cobalt, rhodium and iridium all have NMR active nuclei, albeit with very low gyromagnetic ratios. Finally, the different types of complexes are characterized by distinct features in their vibrational spectra: changes in these bands between the different enantiomers may also be observed.

Among non tris-chelate complexes, suitable candidate complexes worth investigating include tetranuclear gold complexes with the four gold atoms in plane and bridging thiolate ligands such as those described previously by Piovesana *et al.*[3] The presence of four gold centers would increase PVED experimentally. Additionally, chiral Schiff base macrocyles with uranium may be a good possibility. Coordination of such ligands to lanthanides is well established, but no such attempts have been made with actinides.[4,5] Uranium being the non man-made element with the largest atomic number, complexes of it are also good choices for PVED measurements. Chiral cluster complexes containing the actinides uranium or thorium as well as other heavy elements such as bismuth may be considered.

Concluding Remarks

Understanding the origin of biological homochirality is a fascinating topic and essential in our knowledge of how life on Earth developed to where it stands today. The search for Parity Violation in molecules as its source has spawned a wide area of research where synthesis, spectroscopy and theoretical calculations meet. While Parity Violation is only one plausible explanation, unambiguously determining its existence in molecules is an essential task in understanding biological homochirality.

References

1. Eaton S. S., Hutchison J. R., Holm R. H., Muetterties E. L., Intramolecular Rearrangement Reactions of Tris-Chelate Complexes. III. Analysis of the Rearrangements of Tris(a:-isopropenyl- and -isopropyltropolonato) aluminum (III) and -cobalt(III). Examples of Stereochemically Nonrigid Aluminum (III) and Cobalt (III) Complexes, *J. Am. Chem. Soc.*, **1972**, *94*, 6411-6426
2. Palazzotto, M. C; Duffy, D. J.; Edgar, B. L.; Que, L., Jr.; Pignolet, L.M., Dynamic Stereochemistry of Tris-Chelate Complexes..Tris(dithiocarbamato) Complexes of Iron, Cobalt, and Rhodium, *J. Am. Chem. Soc.*, **1973**, *95*, 4537-4545
3. Piovesana, O.; Zanazzi, P. F.; Gold(I)-Gold(I) interactions. Tetrameric Gold(I) Thioacetate, *Angew. Chem. Int. Ed. Engl*., **1980**, 19, 561-562
4. Gerus, A.; Ślepokura, K.; Lisowski, J.: Anion and Solvent Induced Chirality Inversion in Macrocyclic Lanthanide Complexes, *Inorg. Chem*. **2013**, *52*, 12450−12460
5. Gregolinski, J.; Slepokura, K.; Lisowski, J.: Lanthanide Complexes of the Chiral Hexaaza Macrocycle and Its meso-Type Isomer: Solvent-Controlled Helicity Inversion, *Inorg. Chem*., **2007**, 46, 7923-7934

APPENDIX

APPENDIX A: Supplementary Data for Chapter 2

Figure S2.1: ^{1}H NMR of Co(hino)$_3$ (mixture of isomers) in MeOD at 500 MHz and 25 ^{0}C

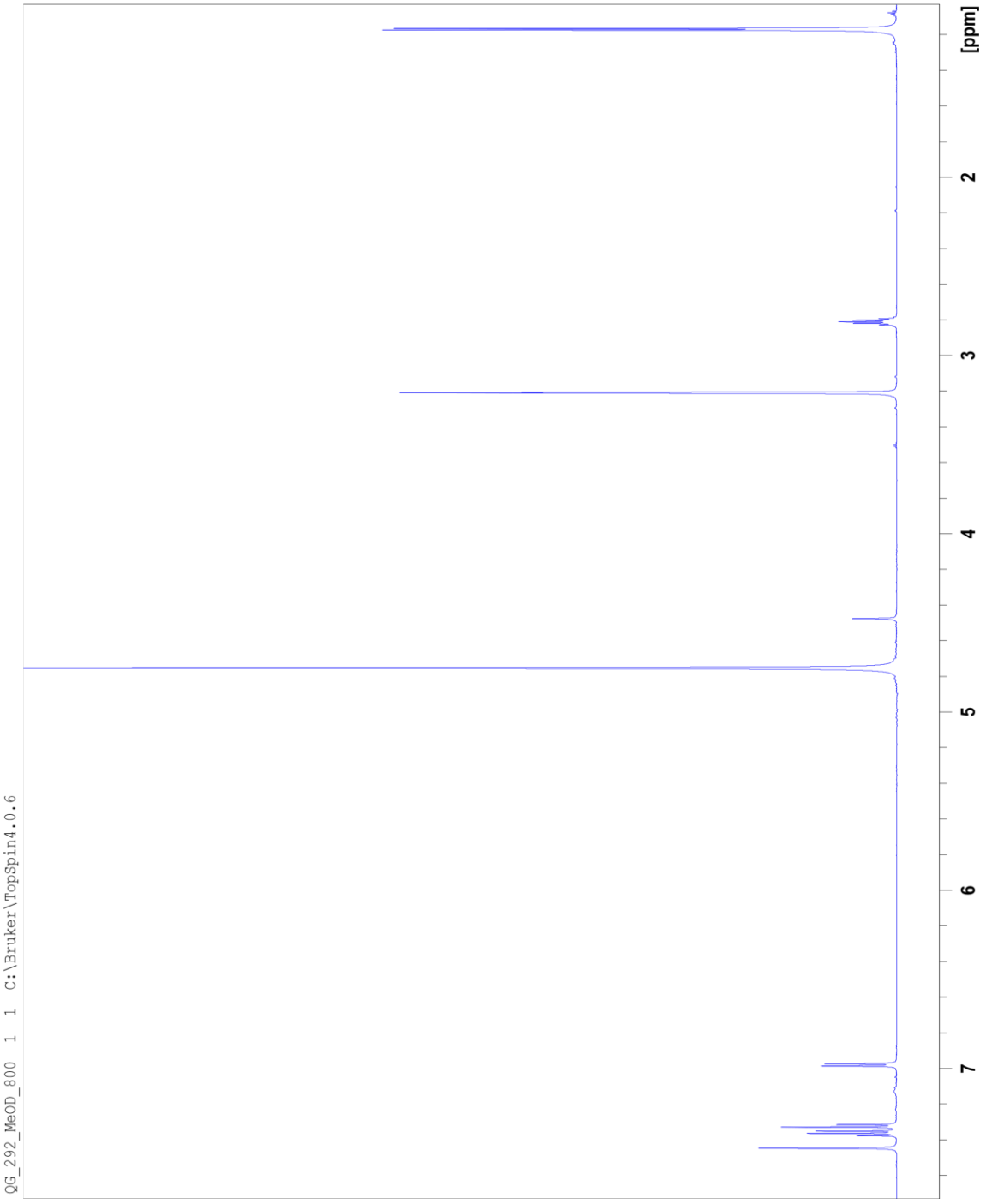

Figure S2.2: ^{1}H NMR of the aromatic region of Co(hino)$_3$ (mixture of isomers) in MeOD at 500 MHz and 25 ^{0}C. Representative sample for all tris chelates.

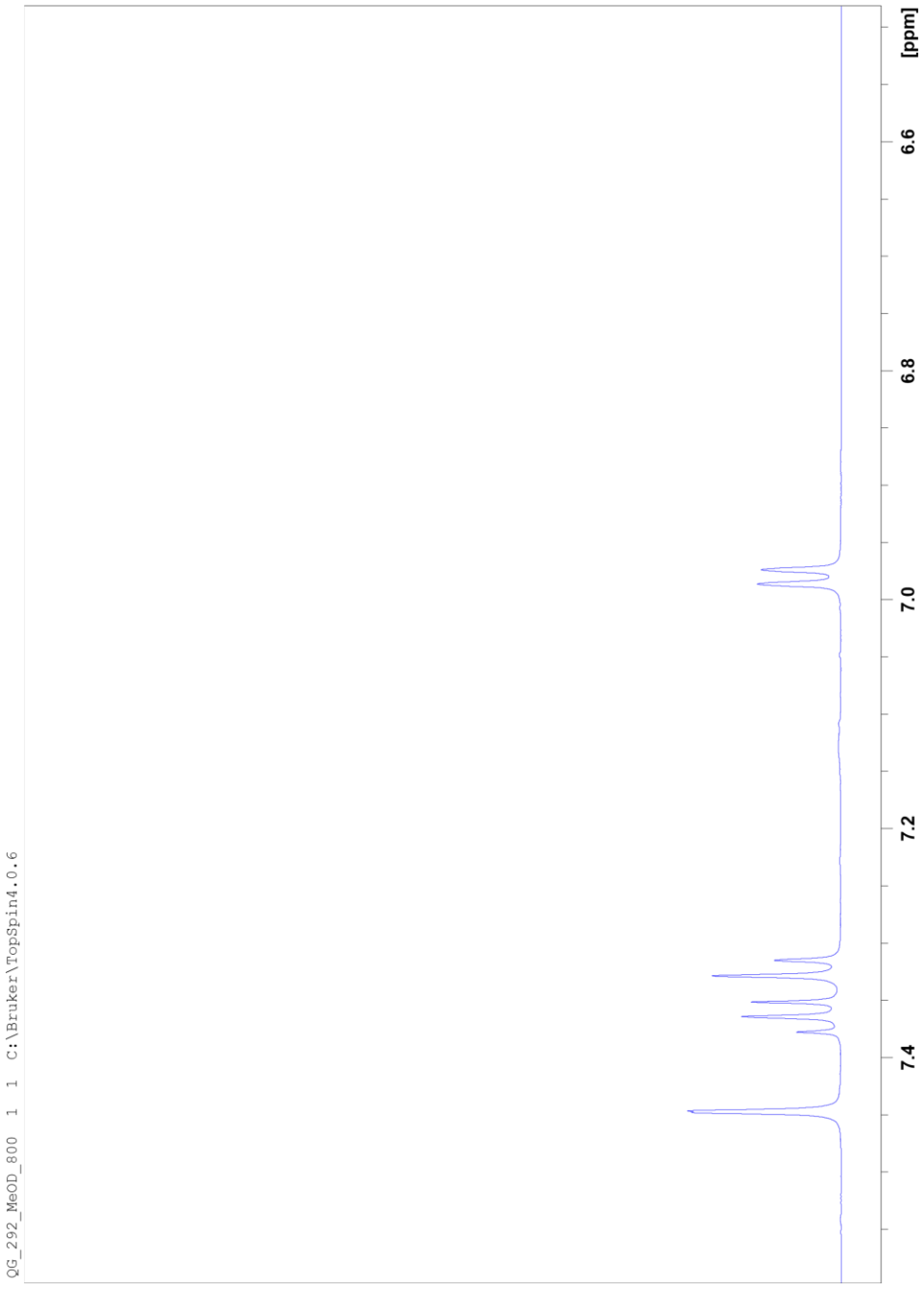

Figure S2.3: ^{1}H NMR of the isopropyl region of Co(hino)$_3$ (mixture of isomers) in MeOD at 500 MHz and 25 ^{0}C. Representative sample for all tris chelates.

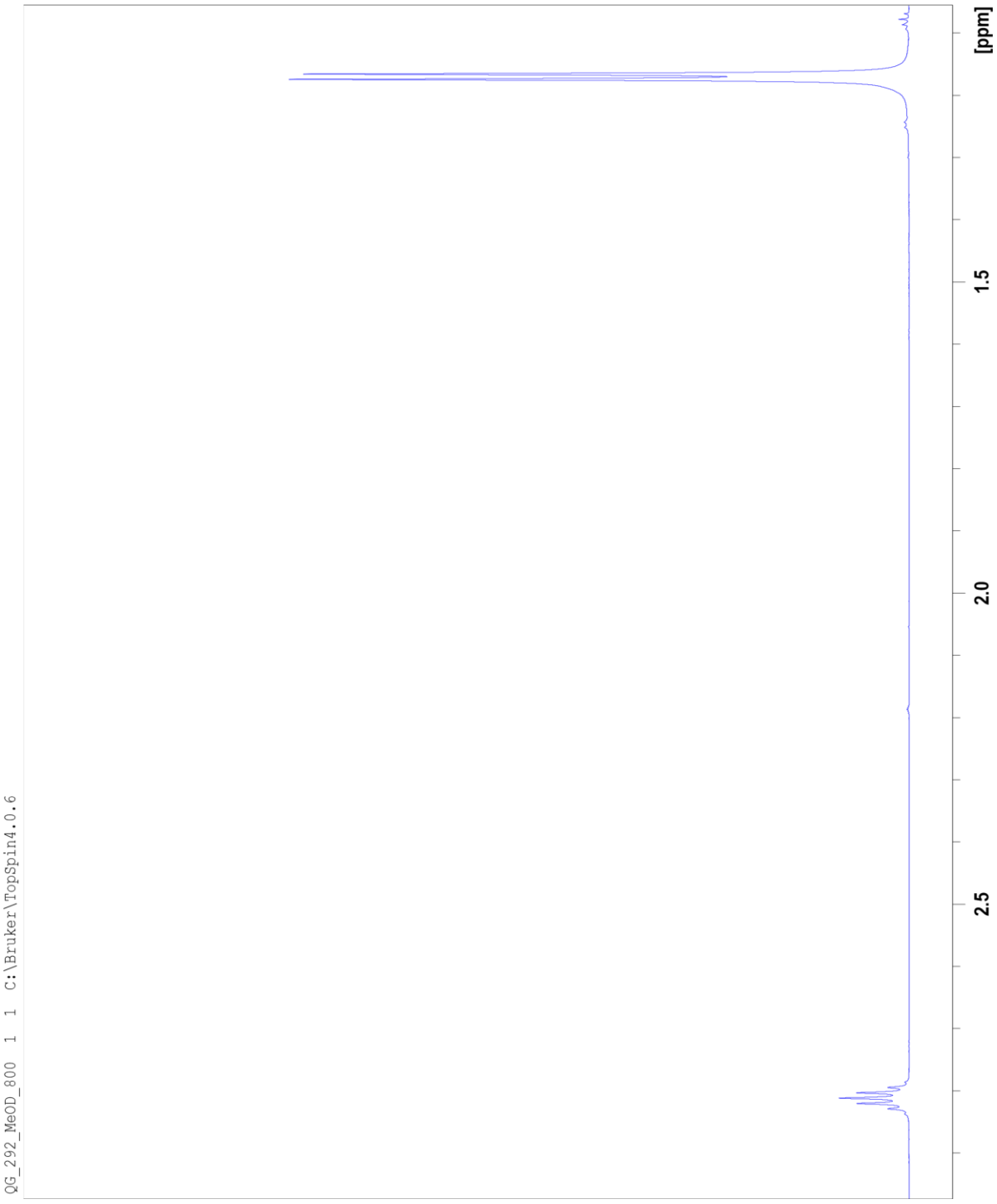

Figure S2.4: ^{13}C-NMR of Co(hino)$_3$ in MeOD at 500 MHz and 25 ^{0}C

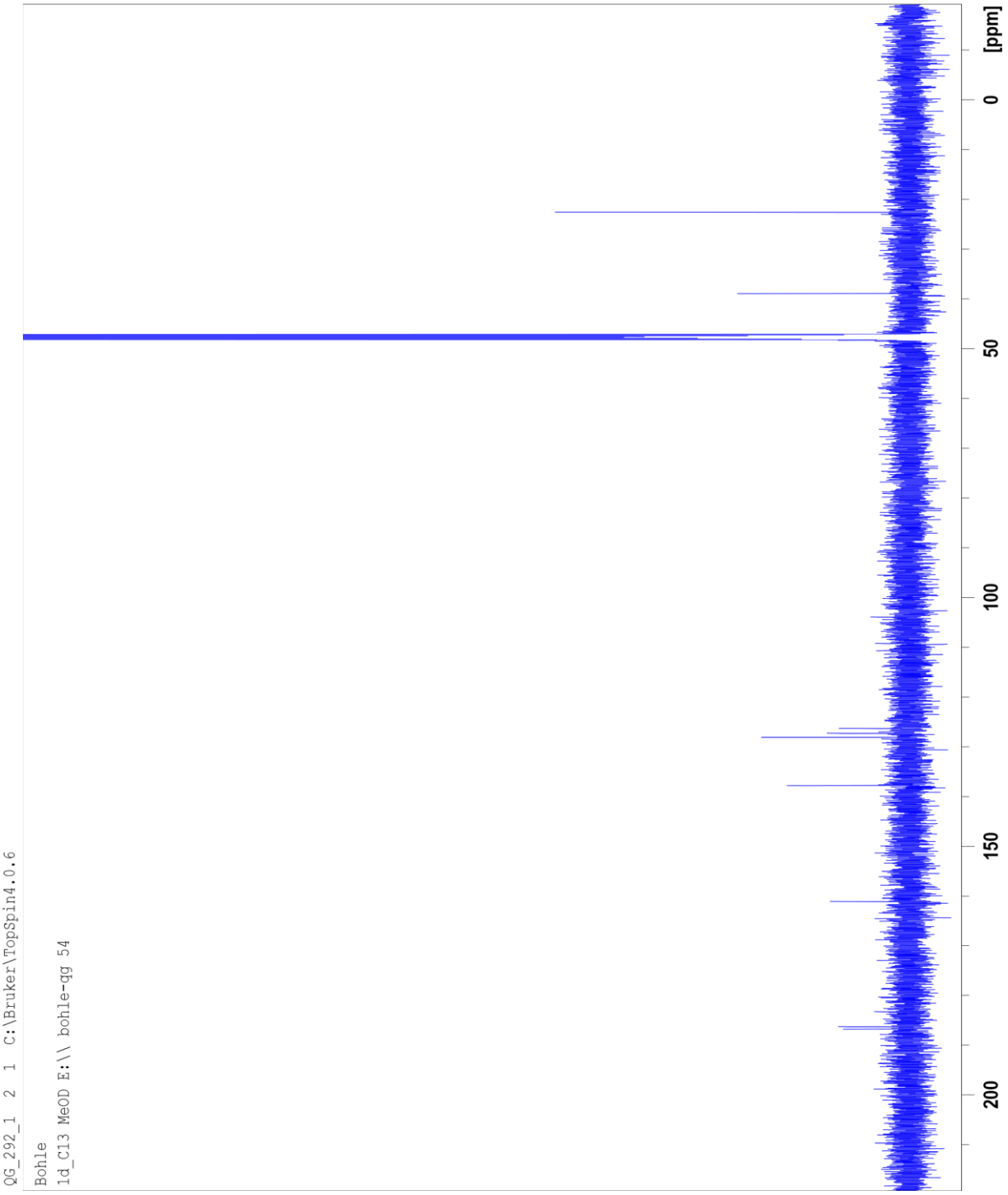

Figure S2.5: HSQC of Co(hino)$_3$ in MeOD at 500 MHz and 25 ^{0}C

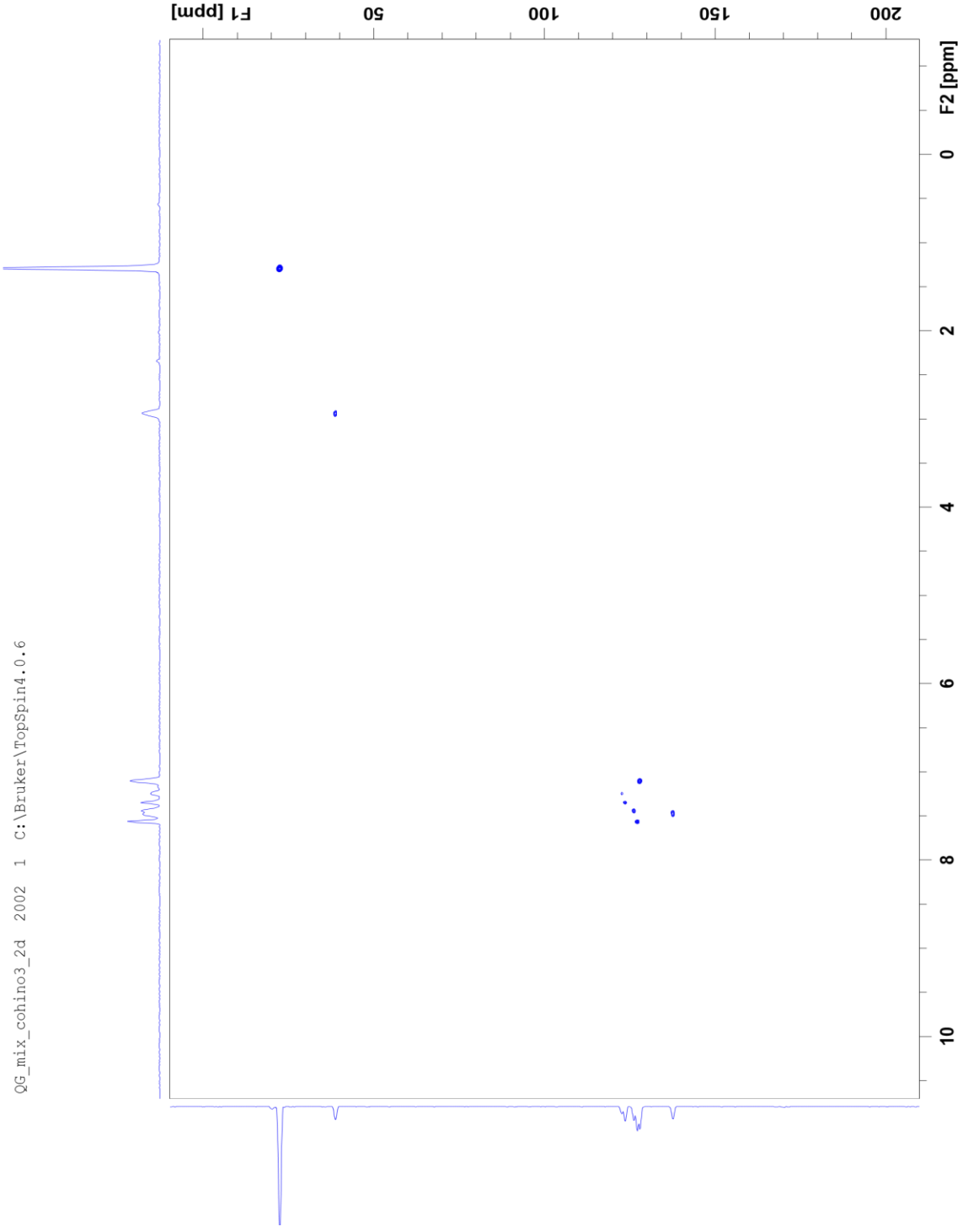

Figure S2.6: HMBC of Co(hino)$_3$ in MeOD at 500 MHz and 25 ^{0}C

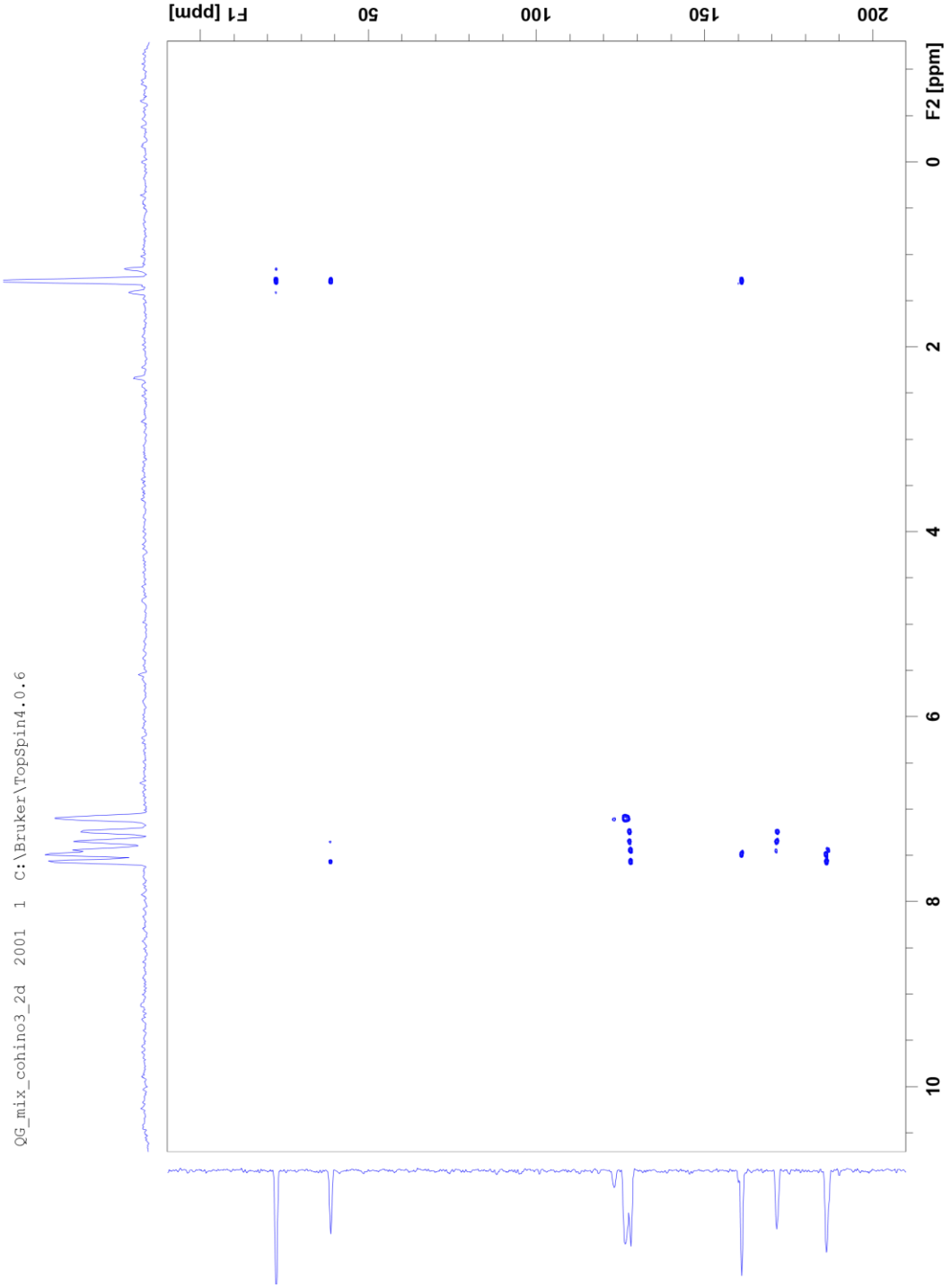

Figure S2.7: COSY of $Co(hino)_3$ in MeOD at 500 MHz and 25 ^0C

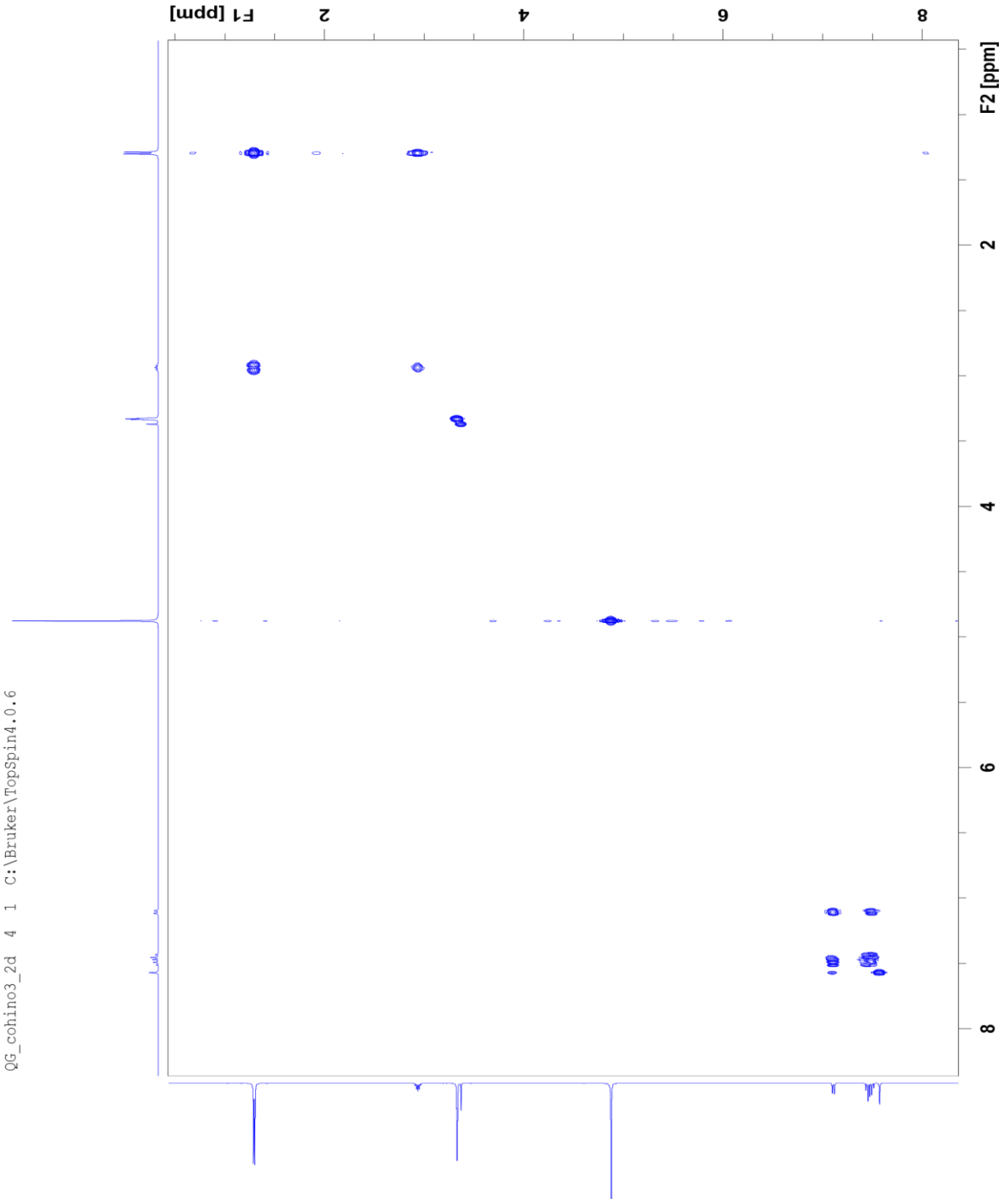

Figure S2.8: NOESY of Co(hino)$_3$ in MeOD at 500 MHz and 25 ^{0}C

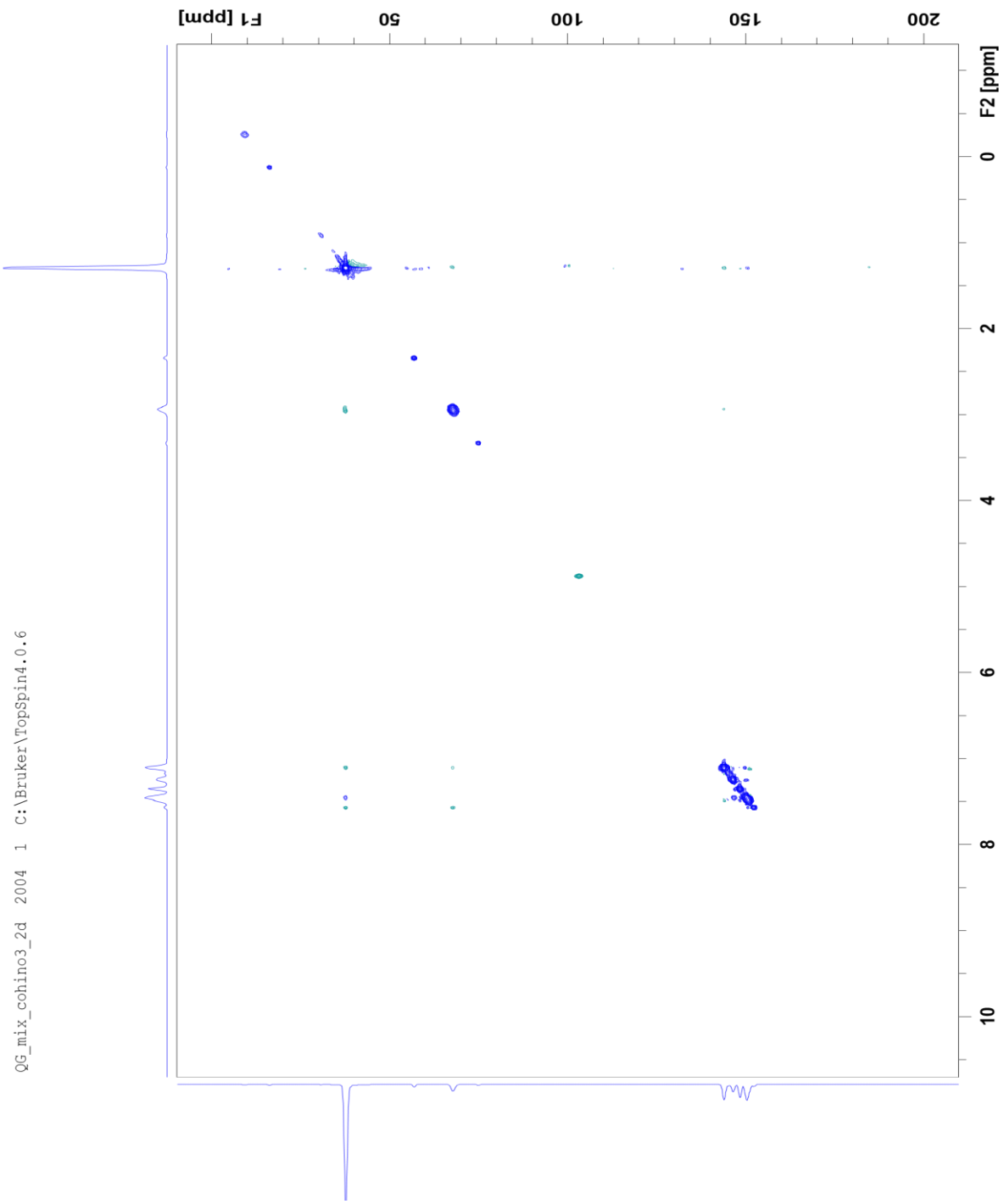

Figure S2.9: ^{1}H NMR of Rh(hino)$_3$ (mixture of isomers) in MeOD at 500 MHz and 25 ^{0}C

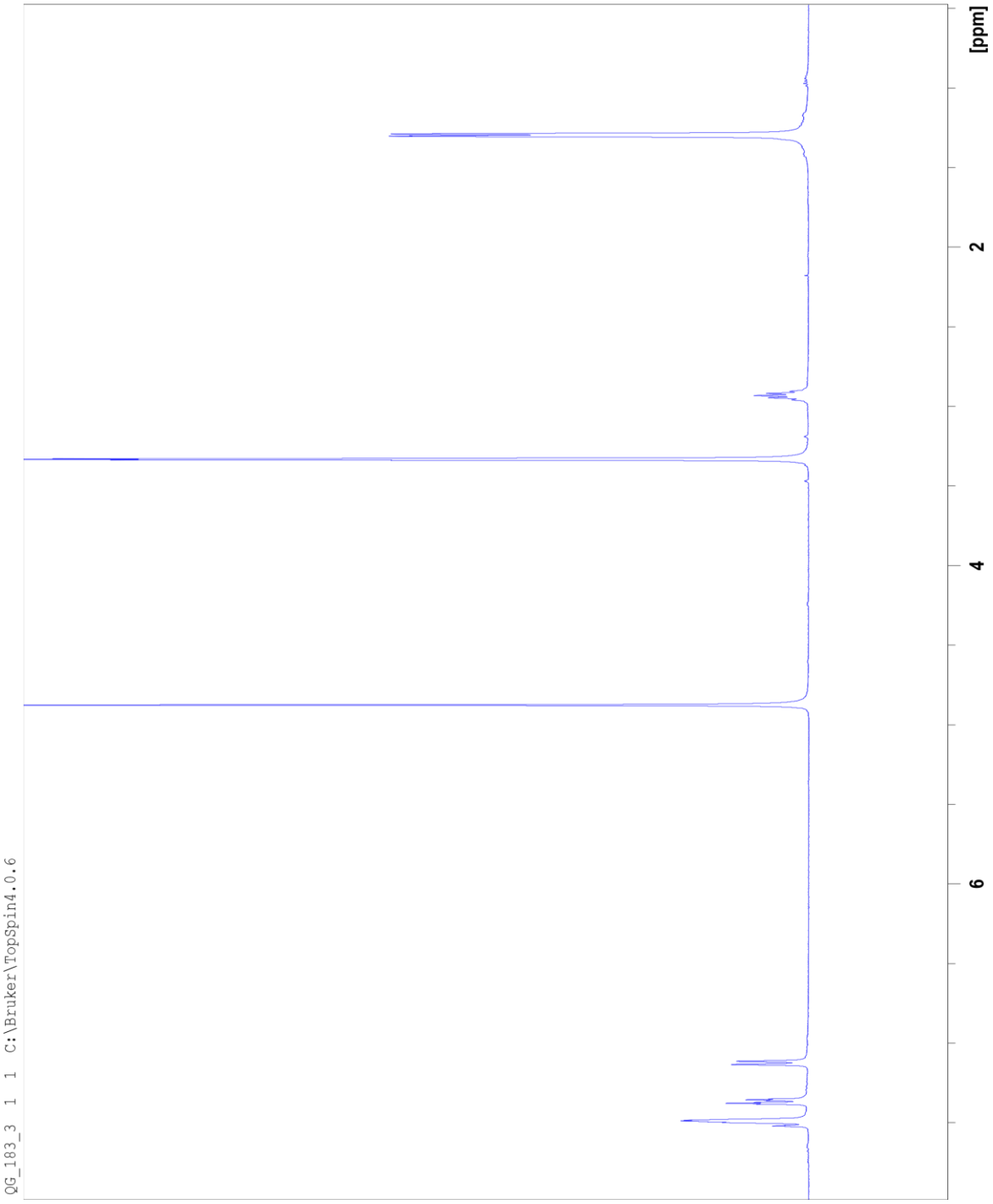

Figure S2.10: ^{13}C NMR of $Rh(hino)_3$ in MeOD at 500 MHz and 25 ^{0}C

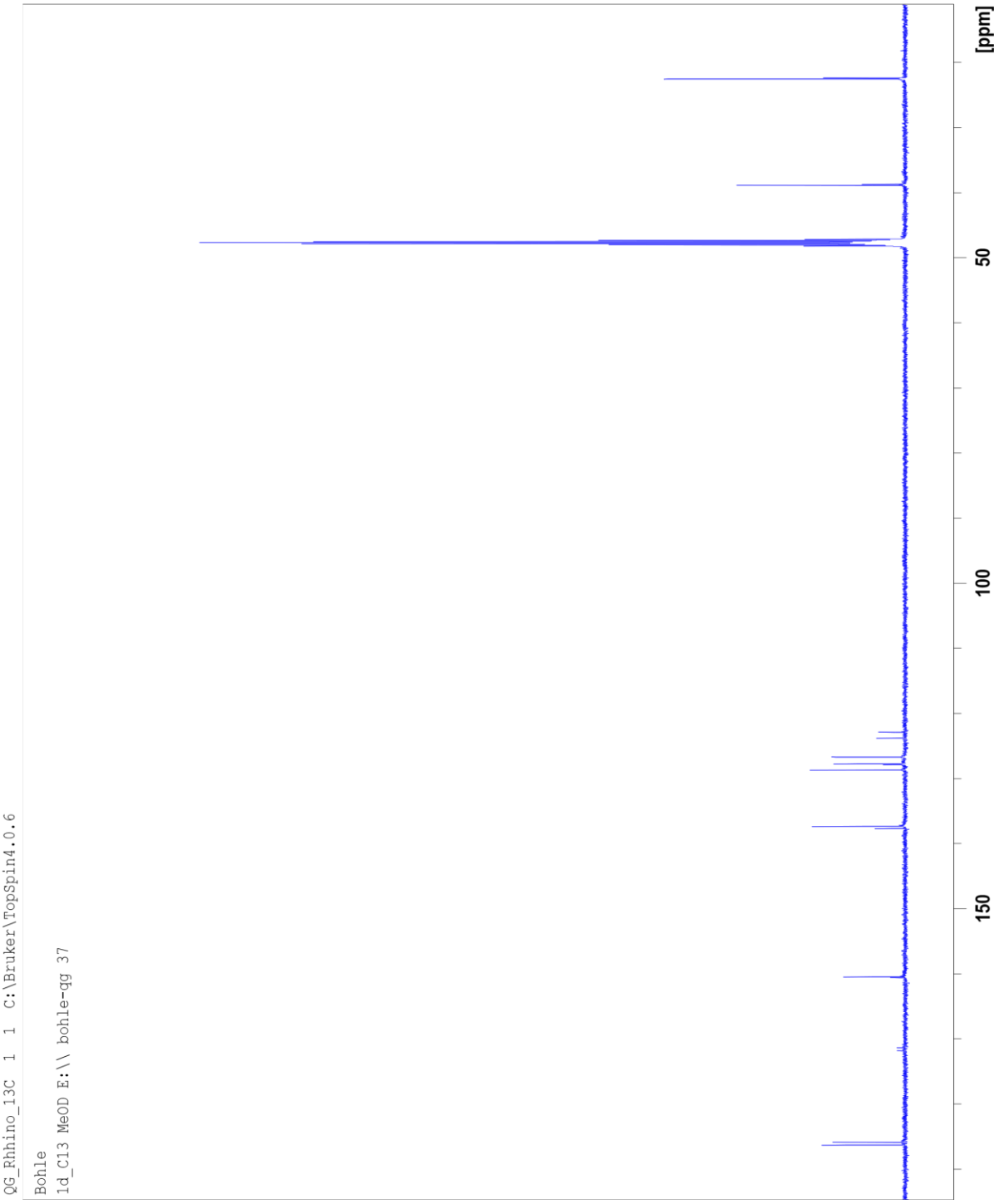

Figure S2.11: ^{1}H NMR for Ir(hino)$_3$ (mixture of isomers) in MeOD at 500 MHz and 25 ^{0}C

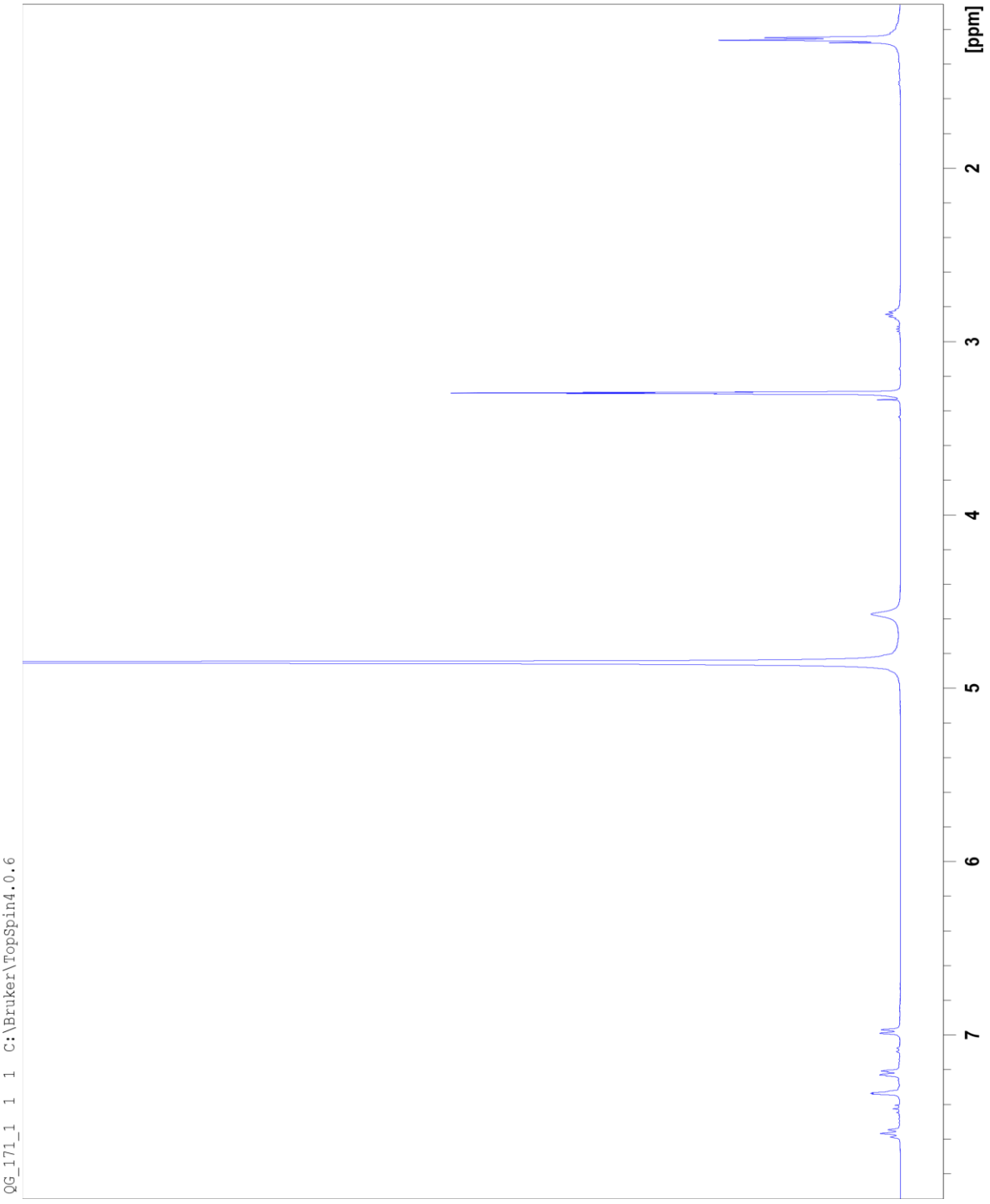

Figure S2.12: ^{13}C NMR of $Ir(hino)_3$ in MeOD at 500 MHz and 25 ^{0}C

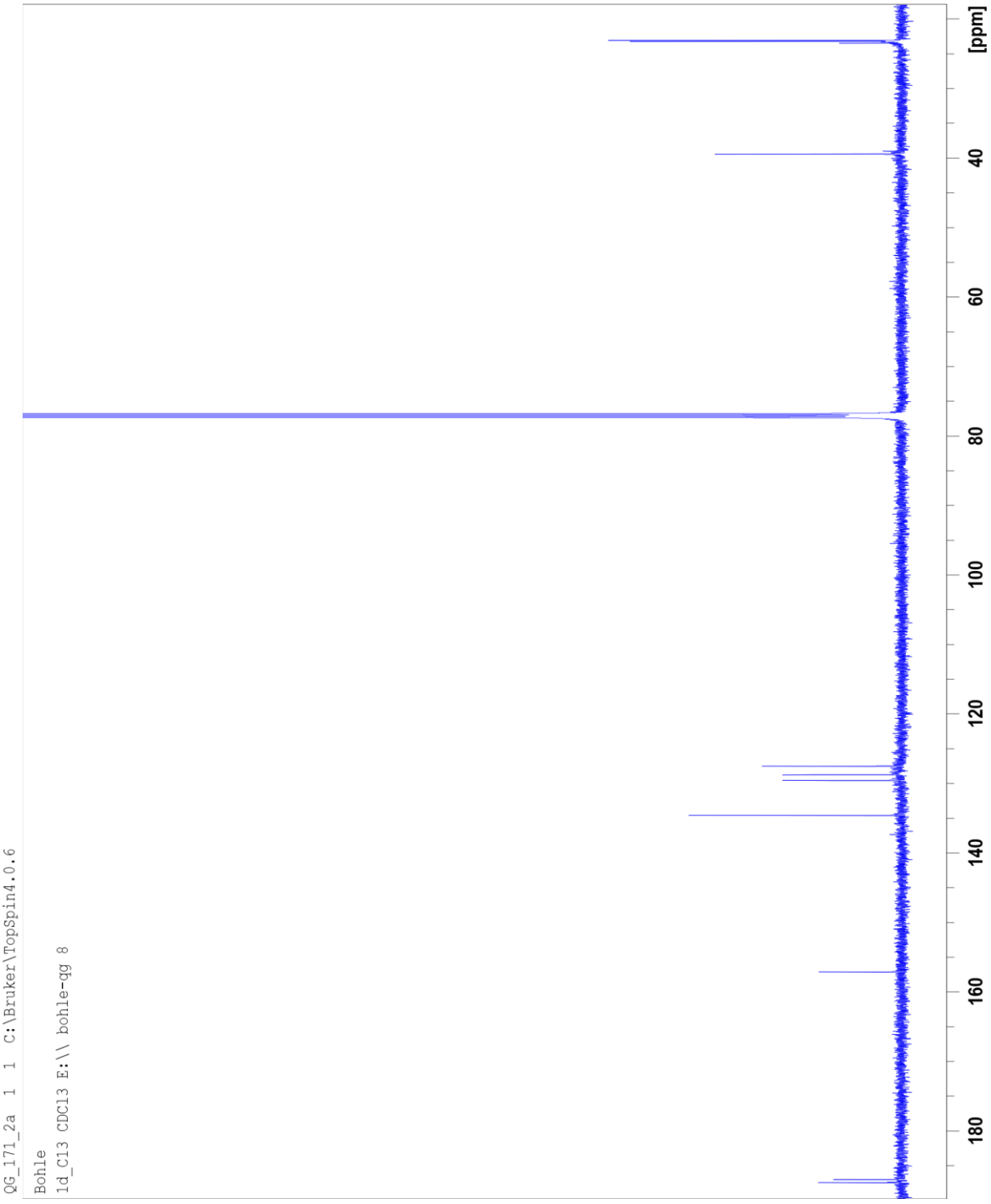

Figure S2.13: ^{1}H NMR for Co(en)(hino)$_2$Cl in MeOD at 500 MHz and 25 ^{0}C

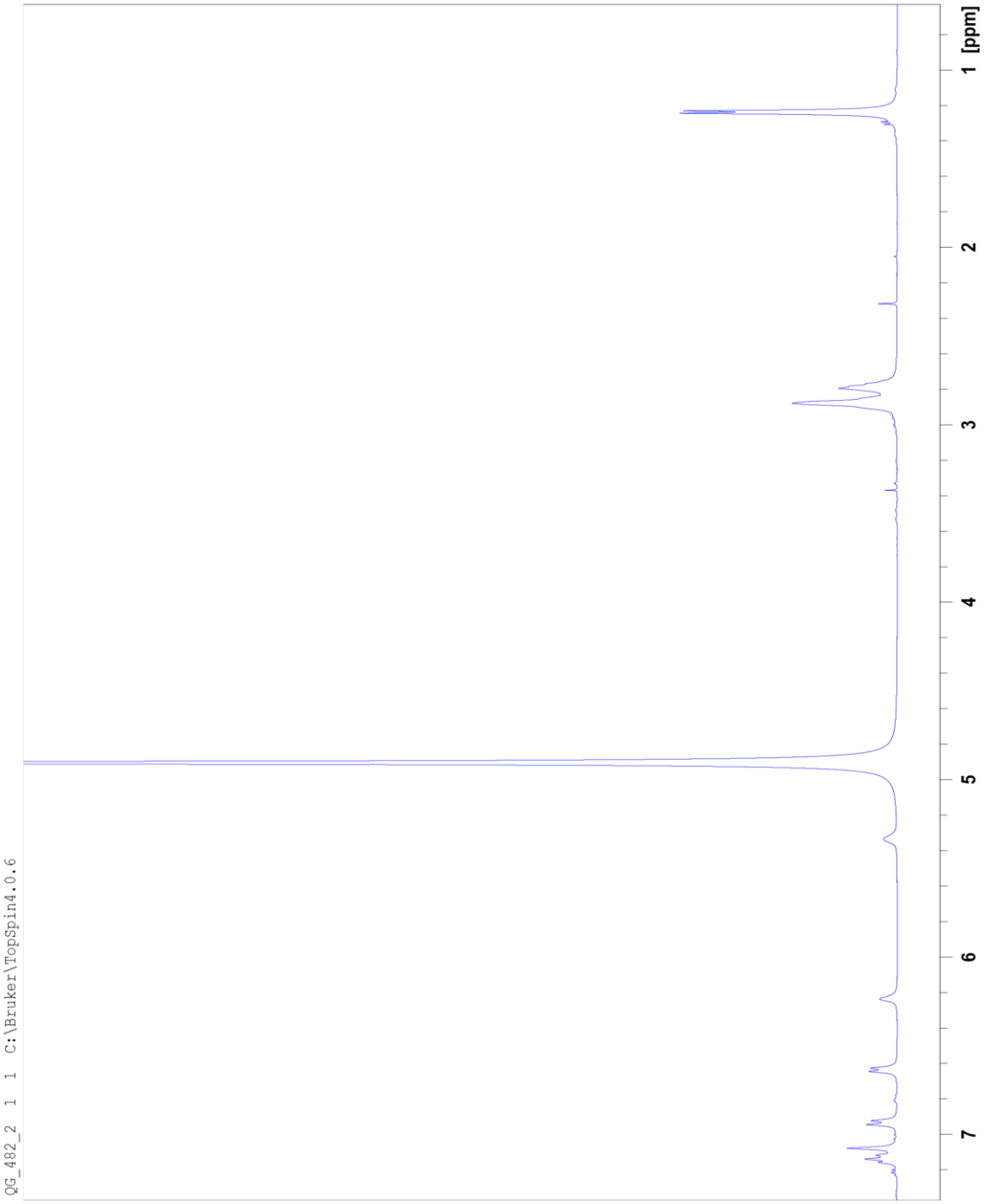

Figure S2.14: ^{13}C NMR of $Co(en)(hino)_2Cl$ in MeOD at 500 MHz and 25 ^0C

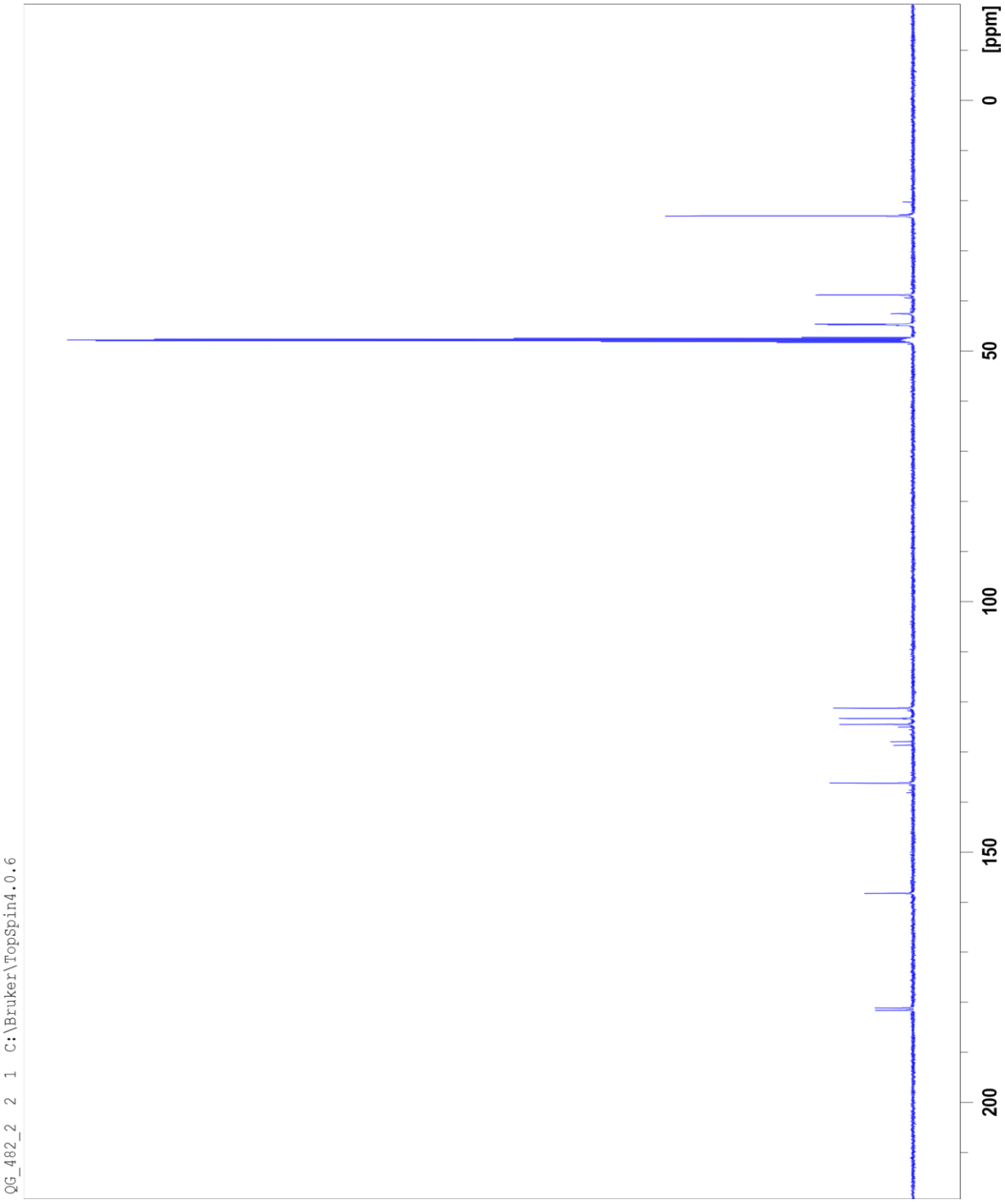

Figure S2.15: ^{1}H NMR of the aromatic region of Co(en)(hino)$_2$Cl in MeOD at 500 MHz and 25 ^{0}C

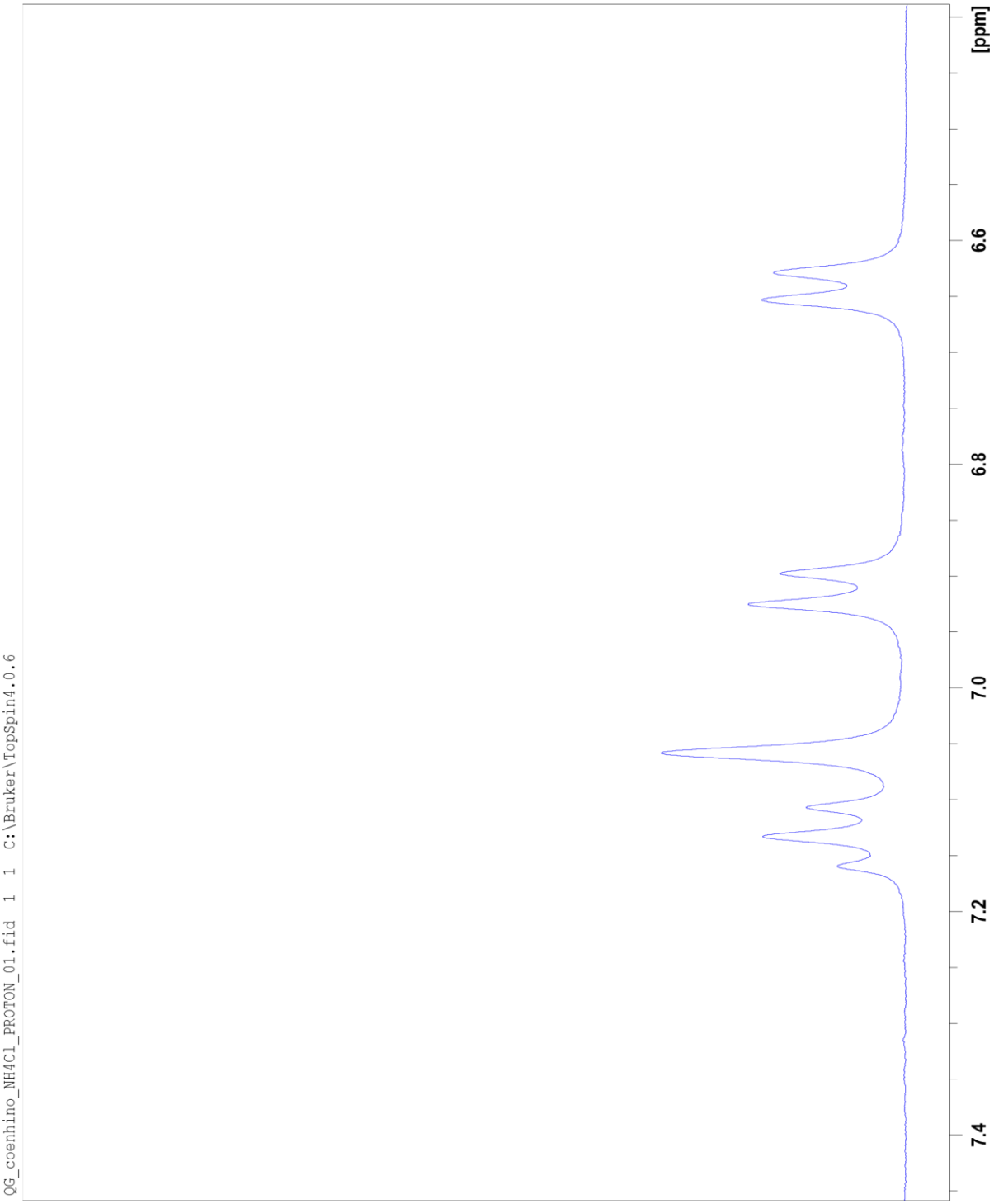

Figure S2.16: ^{1}H NMR of the isopropyl methyl signal of Co(en)(hino)$_2$Cl in MeOD at 500 MHz and 25 ^{0}C

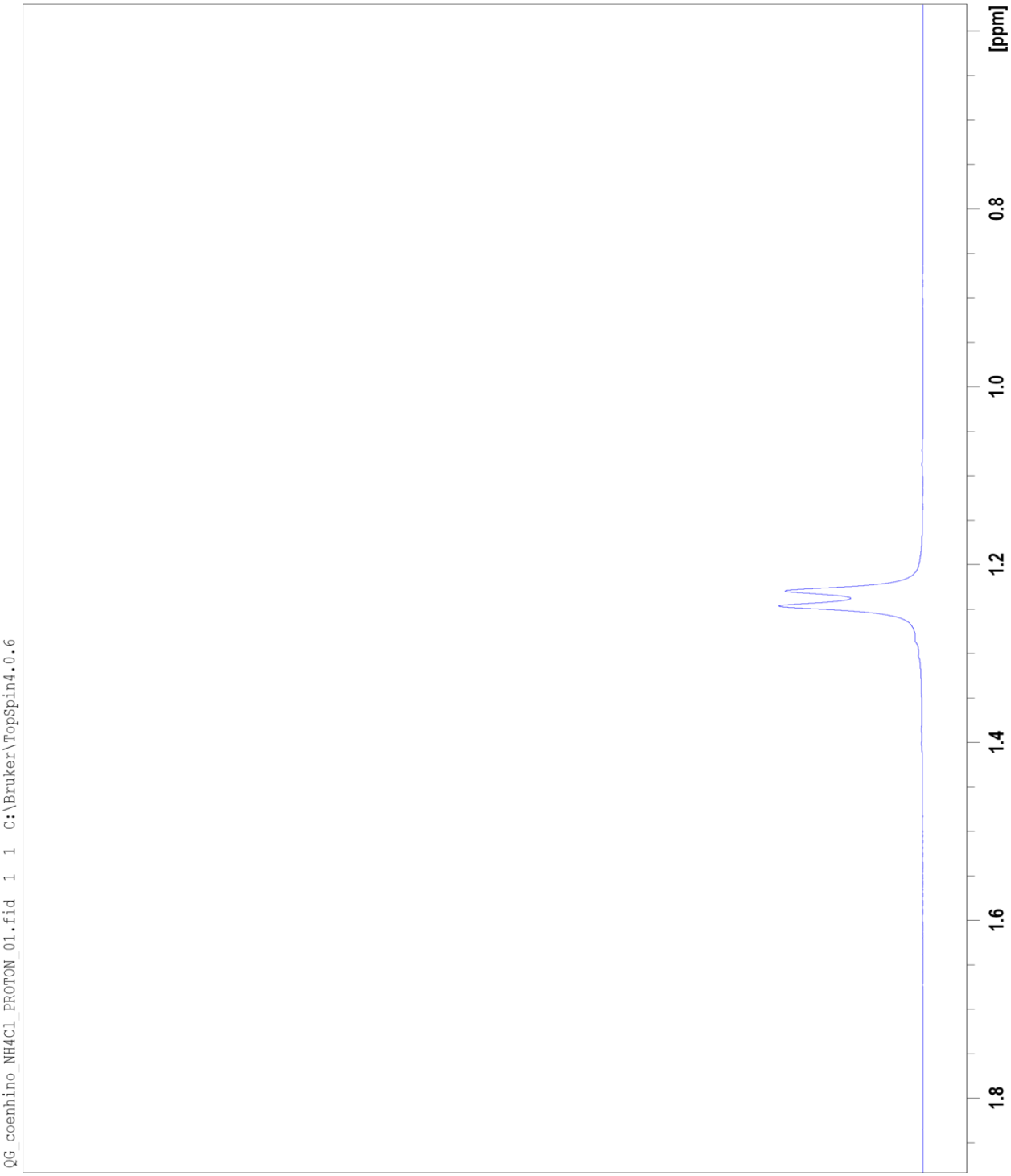

Figure S2.17: ^{1}H NMR of the ethylenediamine region of Co(en)(hino)$_2$Cl in MeOD at 500 MHz and 25 ^{0}C

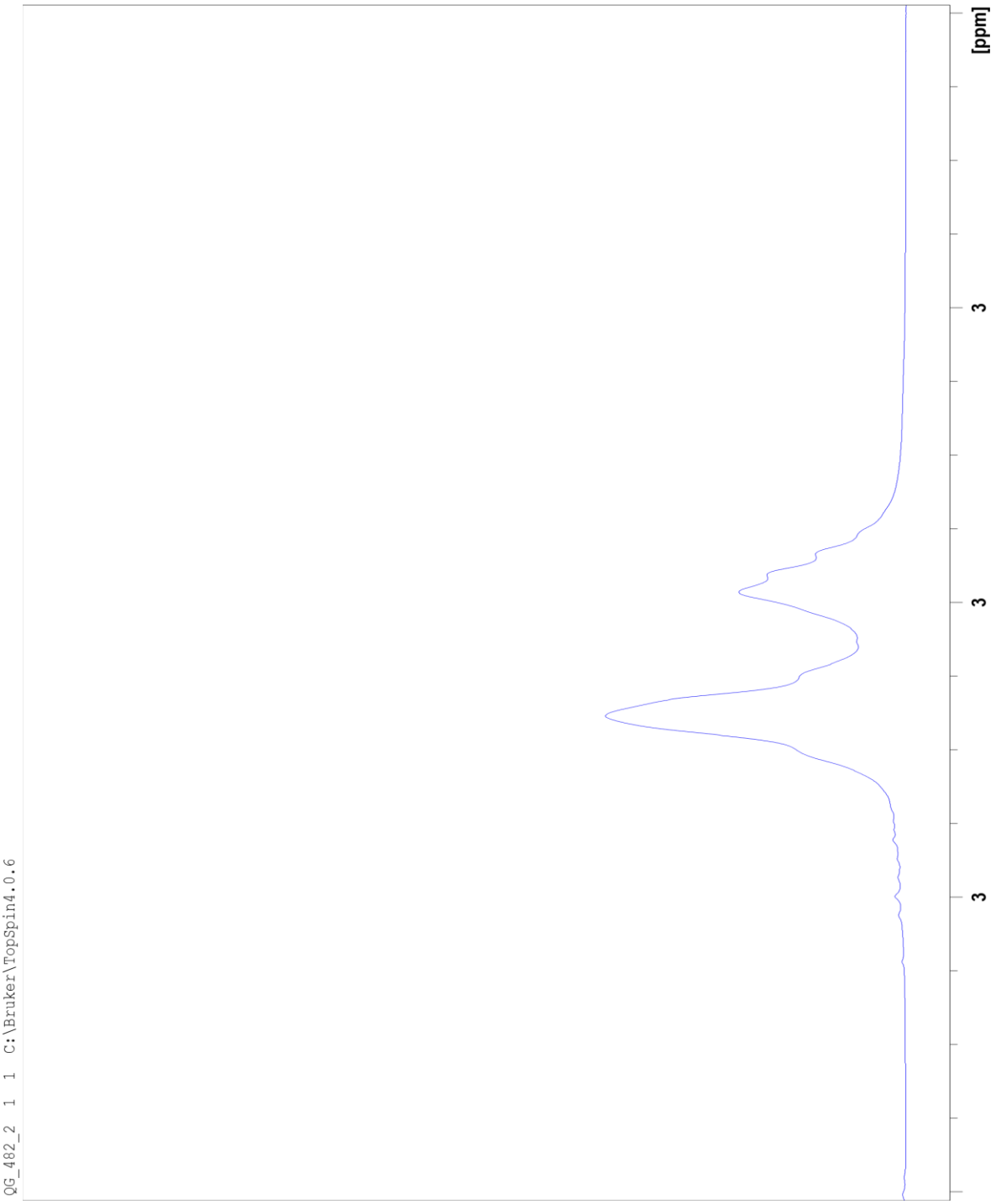

Table S2.1: Vibrational motions of M(hino)$_3$

Frequency	Vibrational mode	MOCCO ring motion
1551	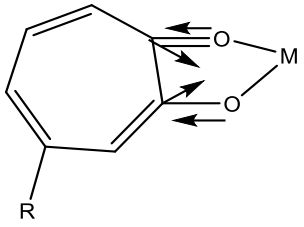	Symmetric Breathing
1511	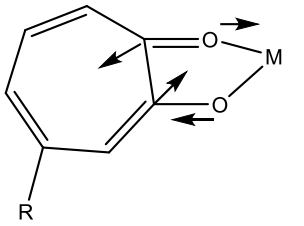	Asymmetric breathing
1453	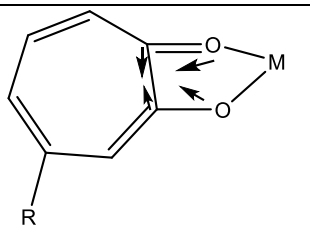	O-M-O scissoring symmetric C-C stretching
1400	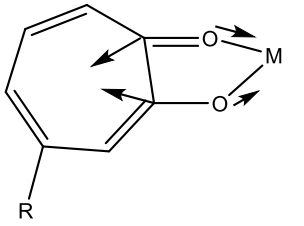	O-M-O symmetric stretching C-C scissoring
1289	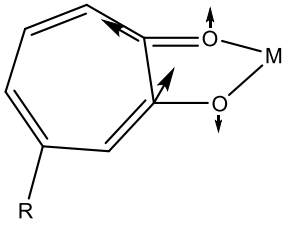	O-M-O scissoring Asymmetric C-C stretching

Table S2.2: X-ray diffraction data

	Rh(hino)$_3$
Empirical Formula	$C_{30}H_{33}O_6Rh$
Formula Weight	592.47
Crystal System	Hexagonal
Space Group	P6(3)
a(Å)	14.464(3)
b(Å)	14.464(3)
c(Å)	8.0198(15)
α(°)	90
β(°)	9095
γ(°)	120
Volume(Å^3)	1453.0(6)
Density(g/cm^3)	2.031
Z	3
T(K)	571(2)
Reflections collected	19927
Independent reflections	3651
Rint	0.0528
Goodness-of-fit	0.695
R1	0.0355
wR2	0.0919
CCSD Number	2087119

Figure 2.18: Time dependent UV-Vis measurements at different concentrations of ethylenediamine

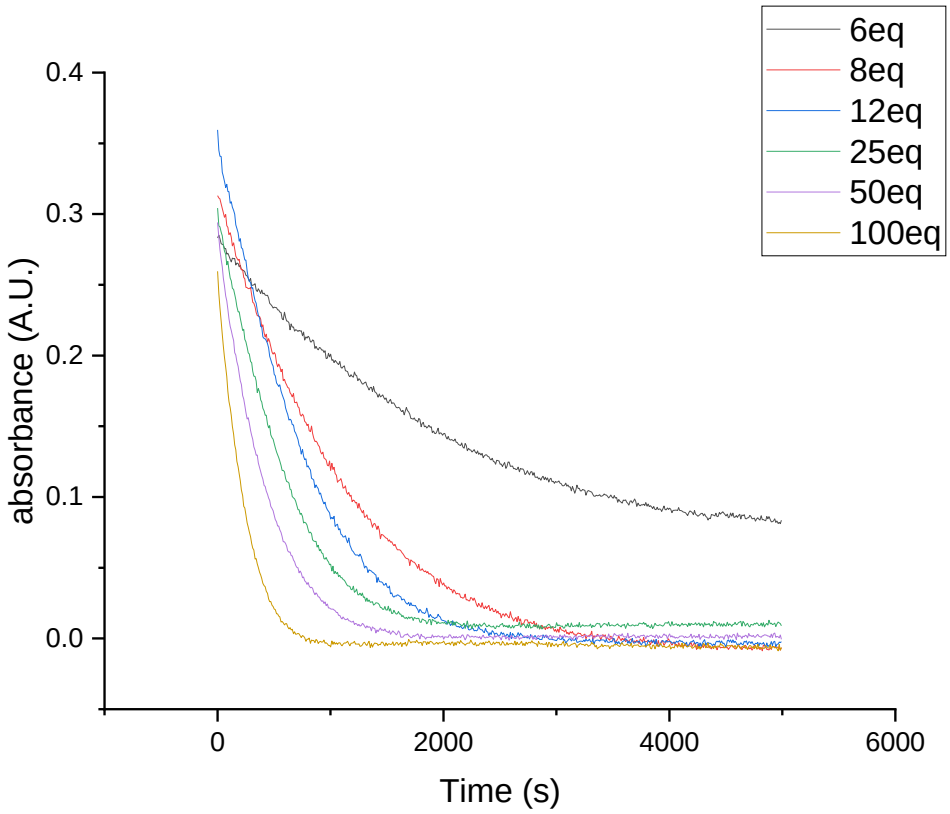

Table 2.3: DFT calculations of the vibrational frequencies of the isomers of $Co(hino)_3$

	fac Isomer		Mer Isomer	
Band	Frequency	IR Intensity	Frequency	IR Intensity
1	13.83	0.4813	12.79	0.4064
2	14.12	0.4881	16.07	0.6778
3	20.28	0.951	20.62	0.8375
4	29.97	0.0312	26.68	0.4129
5	30.37	0.0345	30.88	0.1092
6	30.59	0.0593	32.68	0.2923
7	35.57	0.3364	37.19	0.2318
8	35.85	0.3092	39.75	0.7284
9	39.3	1.1364	46.99	0.3407
10	111.12	0.0954	100.52	0.0018
11	111.25	0.0966	111.08	0.0801
12	115.54	0.0077	119.48	0.0748
13	126.14	0.166	121.93	0.0983
14	137.7	0.1581	126.85	0.0116
15	137.7	0.1582	134.34	0.1376
16	155.95	0.3945	148.29	0.5747
17	156.12	0.3934	159.11	0.5384
18	160.29	0.4497	176.76	0.0554
19	189.1	0.4486	181.72	0.4008
20	189.23	0.2023	189.81	0.5323
21	189.31	0.2332	194.1	0.0622
22	223.97	0.2073	223.27	0.4006
23	224.59	0.4683	224.23	0.6088
24	224.71	0.5363	227.4	0.0527
25	231.14	0.4927	228.11	0.1114
26	231.31	0.5007	231.79	0.3595
27	231.94	0.2167	239.28	0.8557
28	244.51	0.0552	245.05	0.0356
29	249.88	0.8073	247.58	0.2318
30	250.33	0.8062	250.22	0.6361
31	254.74	0.5034	256.7	0.6796
32	272.06	0.212	268.37	0.088
33	272.18	0.2065	273.08	0.1629
34	282.48	0.0011	283.26	0.1111
35	296.75	0.3232	295.3	0.256

36	296.91	0.3207	306.23	0.444
37	314.1	0.2442	312.71	0.4127
38	314.23	0.2396	315.6	0.0796
39	316.33	0.1664	321.42	0.4031
40	377.21	3.0361	375.55	10.1769
41	381.87	25.809	379.2	22.1724
42	381.89	25.6738	383.85	20.1567
43	405.71	1.195	405.28	0.1824
44	405.85	1.1396	405.84	0.7665
45	406.08	0.2455	406.82	0.6236
46	408.87	0.0087	411.86	5.9408
47	414.57	9.9649	413.75	5.0158
48	414.63	9.8791	424.05	12.5075
49	437.27	0.5049	438.07	1.1787
50	454.12	30.7165	456.29	41.006
51	454.15	30.8174	457.85	26.7929
52	507.93	21.3847	501.95	1.8017
53	508.05	21.4186	508.28	21.7192
54	512.27	1.127	510.96	6.8981
55	519.16	2.6009	519.3	3.5533
56	519.55	7.0098	519.54	6.7154
57	519.57	6.9863	524.57	5.599
58	590.71	138.4768	586.71	92.1619
59	590.75	138.3165	590.26	127.5871
60	605.28	0.6153	602.49	20.2263
61	638.4	16.9663	620.73	54.0208
62	638.44	16.9022	638.81	25.7471
63	640.43	1.3163	639.69	7.0086
64	682.86	54.6472	680.66	21.1008
65	682.91	55.0167	688.64	42.4477
66	689.79	10.1952	690.03	14.3992
67	689.97	9.5931	690.18	4.353
68	690.14	9.6647	690.33	9.8743
69	694.56	10.4547	698.06	40.9203
70	755.59	9.4781	755.07	5.7544
71	755.6	9.4487	756.05	13.084
72	756.4	15.5358	761.69	17.3338
73	769.48	7.883	768.71	7.4417
74	769.52	7.8057	769.57	7.3873
75	769.87	7.341	769.83	8.1385

76	794.49	9.5631	794.59	7.1315
77	794.7	2.2757	794.75	2.0984
78	794.74	2.256	799.02	1.6368
79	824.11	25.0227	822.36	23.8228
80	824.28	25.4495	824.3	25.6735
81	824.36	24.1034	824.38	24.2648
82	888.33	9.0786	886.04	3.3431
83	888.37	9.1836	888.24	8.9636
84	888.58	0.1099	888.41	3.0199
85	915.39	2.1771	914.43	0.6543
86	915.44	2.2891	915.56	2.2575
87	915.79	1.929	915.83	2.0306
88	930.25	4.3532	930.48	4.6634
89	930.45	4.9605	930.74	5.1936
90	930.52	5.2427	932.63	12.331
91	939.77	7.2765	938.49	1.8711
92	939.86	8.3884	939.99	8.0648
93	940.06	7.9244	940.32	7.4185
94	965.05	0.0095	965.1	0.0092
95	965.14	0.009	965.23	0.012
96	965.38	0.0105	965.83	0.4598
97	987.68	85.4091	978.51	76.2384
98	987.71	85.3466	987.67	86.1309
99	989.31	2.1229	988.8	23.3847
100	1018.19	0.7087	1016.31	0.7082
101	1018.2	0.8516	1018.2	0.7821
102	1018.28	0.7848	1018.26	0.7578
103	1035.69	47.8508	1035.63	47.7937
104	1035.74	47.6258	1036.11	29.5524
105	1036.43	18.6819	1060.28	20.7711
106	1117.09	0.5572	1100.76	8.3034
107	1117.22	0.5645	1117.13	0.5555
108	1117.25	0.555	1117.32	0.5795
109	1124	9.3243	1117.34	0.5509
110	1124.08	7.432	1124.08	9.1026
111	1124.3	4.1699	1124.21	4.9048
112	1157.32	11.2192	1157.36	11.1299
113	1157.43	10.9944	1157.56	10.2197
114	1157.58	10.6425	1170.76	1.3124
115	1207.44	4.2011	1207.2	4.3599

116	1207.56	3.7845	1207.51	3.4193
117	1207.68	3.5213	1207.63	3.2307
118	1273.64	35.4375	1272.95	51.1503
119	1274.1	32.3952	1274.1	17.5
120	1274.24	32.668	1274.48	38.2102
121	1298.31	10.9261	1298.3	10.1001
122	1298.41	11.0658	1298.48	7.4433
123	1298.74	12.9677	1298.79	20.4434
124	1340.75	30.3353	1330.15	31.2392
125	1340.93	45.8456	1340.83	45.6526
126	1341	66.1807	1341.1	45.418
127	1349.8	1.8427	1348.74	1.13
128	1349.93	1.9214	1349.74	1.8946
129	1349.96	1.7536	1350.06	1.8131
130	1385.33	15.0035	1385.83	33.7453
131	1388.15	51.1247	1388.14	54.6673
132	1388.21	50.7284	1392.96	119.0291
133	1403.11	7.1911	1402.98	7.0699
134	1403.13	7.0946	1403.54	8.1767
135	1403.38	7.7897	1403.75	2.6746
136	1404.63	735.1278	1404.14	714.0868
137	1404.66	734.0862	1405.72	647.9561
138	1414.49	1.0342	1414.72	0.8518
139	1424.38	0.0702	1423.28	17.8371
140	1424.44	0.083	1424.29	0.173
141	1424.49	0.0759	1424.59	0.2737
142	1456.01	138.64	1455.06	216.8275
143	1456.22	254.5772	1456.25	198.2684
144	1456.32	256.6183	1457.56	155.8378
145	1464.93	987.9147	1463.64	1116.32
146	1465	979.83	1465.29	957.3342
147	1480.68	30.2684	1480.74	18.605
148	1487.06	214.2455	1487.14	221.8605
149	1487.14	213.8923	1488.71	201.3228
150	1489.74	0.0379	1489.77	0.0271
151	1489.75	0.095	1489.89	0.0289
152	1489.79	0.0354	1489.92	0.6031
153	1492.38	2.7232	1492.38	2.7777
154	1492.5	2.6322	1492.68	2.5396
155	1492.6	2.637	1492.69	3.1312

156	1495.21	10.5265	1495.22	4.9782
157	1504.63	8.4147	1504.66	9.2471
158	1504.77	7.8054	1504.94	11.838
159	1504.91	15.1574	1506.27	19.2329
160	1510.99	30.5608	1510.95	4.912
161	1511.14	30.2763	1511.05	27.5839
162	1511.73	11.961	1511.53	17.9802
163	1544.65	449.8301	1544.3	425.4246
164	1544.7	448.9692	1544.68	457.0729
165	1551.53	1.3565	1551.31	1.4153
166	1620.87	190.625	1618.72	102.1156
167	1620.95	190.1592	1620.94	194.5477
168	1622.5	15.1521	1622.29	31.7653
169	1630.34	406.3664	1630.36	389.7562
170	1630.36	404.576	1631.01	482.1293
171	1637.55	19.4156	1638.43	12.6296
172	3025.79	22.733	3025.9	22.4166
173	3025.82	22.4716	3025.93	22.7166
174	3025.86	22.5649	3026.44	23.0016
175	3029.25	49.3553	3029.34	44.2105
176	3029.27	49.5784	3029.42	33.0595
177	3029.35	9.8261	3029.77	22.8796
178	3036.93	6.4252	3030.48	14.1325
179	3037.06	6.3915	3036.86	6.3874
180	3037.1	6.2112	3037.31	6.1522
181	3084.67	0.1511	3084.79	0.1854
182	3084.73	0.1626	3084.82	0.2162
183	3084.77	0.2159	3086.49	1.0924
184	3090.88	51.8664	3090.92	55.9604
185	3090.88	50.7943	3090.97	107.6825
186	3090.98	118.4493	3091.31	61.364
187	3094.48	16.452	3094.37	16.4741
188	3094.53	16.582	3094.56	16.6821
189	3094.57	16.8233	3094.62	16.4836
190	3097.14	32.0456	3097.23	30.9603
191	3097.19	33.8688	3097.3	28.7677
192	3097.21	23.5487	3097.75	35.905
193	3137.62	9.0213	3137.09	6.5515
194	3137.68	9.2448	3137.59	8.8913
195	3137.74	10.0395	3137.68	9.5448

196	3152.68	5.3073	3152.52	5.3551
197	3152.78	5.4364	3152.68	5.3631
198	3152.91	5.4989	3159.01	21.6018
199	3165.76	13.7024	3159.86	4.5188
200	3165.83	11.1396	3165.83	12.2069
201	3166.01	10.3796	3165.95	11.0807
202	3172.08	12.3158	3170.43	8.5978
203	3172.14	12.0201	3172.16	12.1688
204	3172.32	12.1457	3172.26	12.0795

APPENDIX B: Supplementary Data for Chapter 3

Table S3.1: Key Crystallographic data

	1	**2**	**3b**	**3c**	**4b**
Empirical Formula	$C_{46}H_{41}Cl_2O_2P_2Ru$	$C_{56}H52O_4P_2Ru$	$C_{48}H_{41}O_4P_2Os$	$C_{53}H_{53}O_3P_2Os$	$C_{47}H_{41}O_3P_2ClOs$
Formula Weight	859.70	951.98	933.95	933.95	904.09
Crystal System	Monoclinic	Monoclinic	Monoclinic	Monoclinic	Monoclinic
Space Group	$P2_1/c$	$P2_1/c$	$P2_1/n$	$P2_1/c$	$P2_1/c$
a(Å)	12.866(6)	9.783(3)	16.310(5)	12.3394(6)	23.4006(8)
b(Å)	30.028(15)	19.782(6)	11.028(3)	13.6836(6)	12.1601(4)
c(Å)	11.341(6)	24.106(7)	24.922(7)	27.5582(12)	29.2744(11)
α(°)	90	90	90	90	90
β(°)	110.748(6)	96.350(4)	109.083(4)	95.882(2)	104.143(2)
γ(°)	90	90	90	90	90
Volume($Å^3$)	4097.0(4)	4637.0(2)	4236.0(2)	4628.6(4)	8077.6(5)
Density(g/cm^3)	1.394	1.364	1.464	1.421	1.548
Z	4	4	4	4	8
T(K)	571(2)	571(2)	571(2)	571(2)	571(2)
Reflections collected	32609	51874	25985	66605	125182
Independent reflections	5526	9922	4213	11288	15976
Rint	0.0574	0.0397	0.0791	0.0978	0.1736
Goodness-of-fit	1.156	1.090	1.084	0.802	1.077
R1	0.0381	0.0431	0.0347	0.0598	0.0560
wR2	0.0918	0.1090	0.1169	0.1342	0.1410
CCSD Number	1982226	1982227	1982225	2049542	2049541

Table S3.2: Selected bond lengths (Å) and bond angles (°) around the metal centers

	1	**2**	**3b**	**3c**	**4b**
M-O1	2.033(3)	2.084(2)	2.142(6)	2.177(5)	2.102(4)
					2.091(4)
M-O2	2.048(3)	2.112(2)	2.190(6)	2.106(5)	2.112(4)
					2.121(4)
M-O11		2.075(2)			
M-O12		2.106(2)			
M-P1	2.4172(17)	2.2894(10)	2.348(2)	2.3315(18)	2.3757(12)
					2.3732(13)
M-P2	2.3906(17)	2.2883(10)	2.342(2)	2.3258(18)	2.3851(13)
					2.3776(13)
O1-M-O2	76.93(13)	77.20(8)	73.2(2)	73.77(18)	76.15(15)
					76.29(15)
O11-M-O12		77.47(8)			
P1-M-P2	177.90(4)	97.79(3)	177.75(8)	176.77(6)	177.59(5)
					177.34(5)

Table S3.3: UV-Vis data[a] of $Ru(hino)_2(PPh_3)_2$, $RuH(hino)(CO)(PPh_3)_2$, $RuCl_2(hino)(PPh_3)_2$, $OsH(CO)(hino)(PPh_3)_2$

Complex	λ(nm)	log(ε)
1	244 301 378 647	4.6 4.3 3.9 2.3
2	331 384 490	4.6 4.3 4.1
3a	335 430	4.3 4.1
3b	333 430	3.8 4.1
3c	431	2.8
4a	447	2.8
4b	453	3.3

a. □ given in $M^{-1}cm^{-1}$ and are measured in dichloromethane at room temperature.

Table S3.4: IR data of the new complexes.[a]

	1	**2**	**3a**	**3b**	**3c**	**4a**	**4b**
Hinokitiol bands	2961.7w 1583.2m 1563.1m 1499.4m 1480.1m 951.9w 803.8w	2955.12w 1576.7m 1493.1m 951.9w 797.5m	2961.7w, 1586.0m 1563.8m 1493.6m 1480.8m 958.53w 798.2m	2961.7w, 1588.0m, 1499.9m 1473.8m 964.8w 810.3m	2961.6w 1588.0m 1499.9m 1473.8m 964.8w 810.3m	2959.1w 1587.5m 1495.6m 1481.2m 957.6w 803.0m	2955.3w 1588.4m 1499.9m 1480.6m 959.1wm 798.2m
Other bands	3058.2w 1428.7m 1364.5w 1229.0w 1183.9w 1093.6m 745.9m	3058.1w 1422.2m 1357.8w 1229.0w 1183.9w 1093.6m 739.3m	3058.2w 1931.3vs 1912.2m 1429.2s 1358.3m 1235.5w 1183.9w 1094.2m 746.6s	3051.9w, 2098.8m 1886.3vs, 1429.2s, 1358.2m 1235.5w 1183.9w 1087.9m 746.6s	3051.9 2098.9w 1886.3s 1429.3s 1358.2m 1235.5w 1183.9w 1087.9w 746.6s	3056.5w 1934.1s 1433.9s 1357.7m 1238.1w 1186.0w 1092.8m 745.2s	3051.9w 1911.9s 1435.6s 1351.8m 1236.1w 1178.0w 1094.2m 740.1s

a. Values given in cm^{-1} and measured in KBr pellets.

Figure S3.1: X-band EPR spectrum of $RuCl_2(hino)(PPh_3)_3$ measured at 4.2K

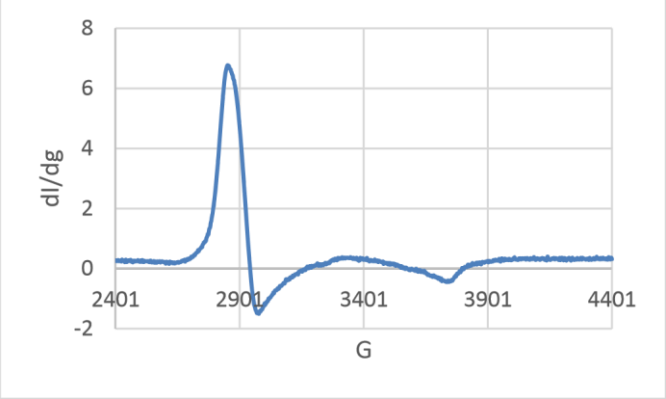

Figure S3.2: ^{1}H NMR for $Ru(hino)_2(PPh_3)_2$

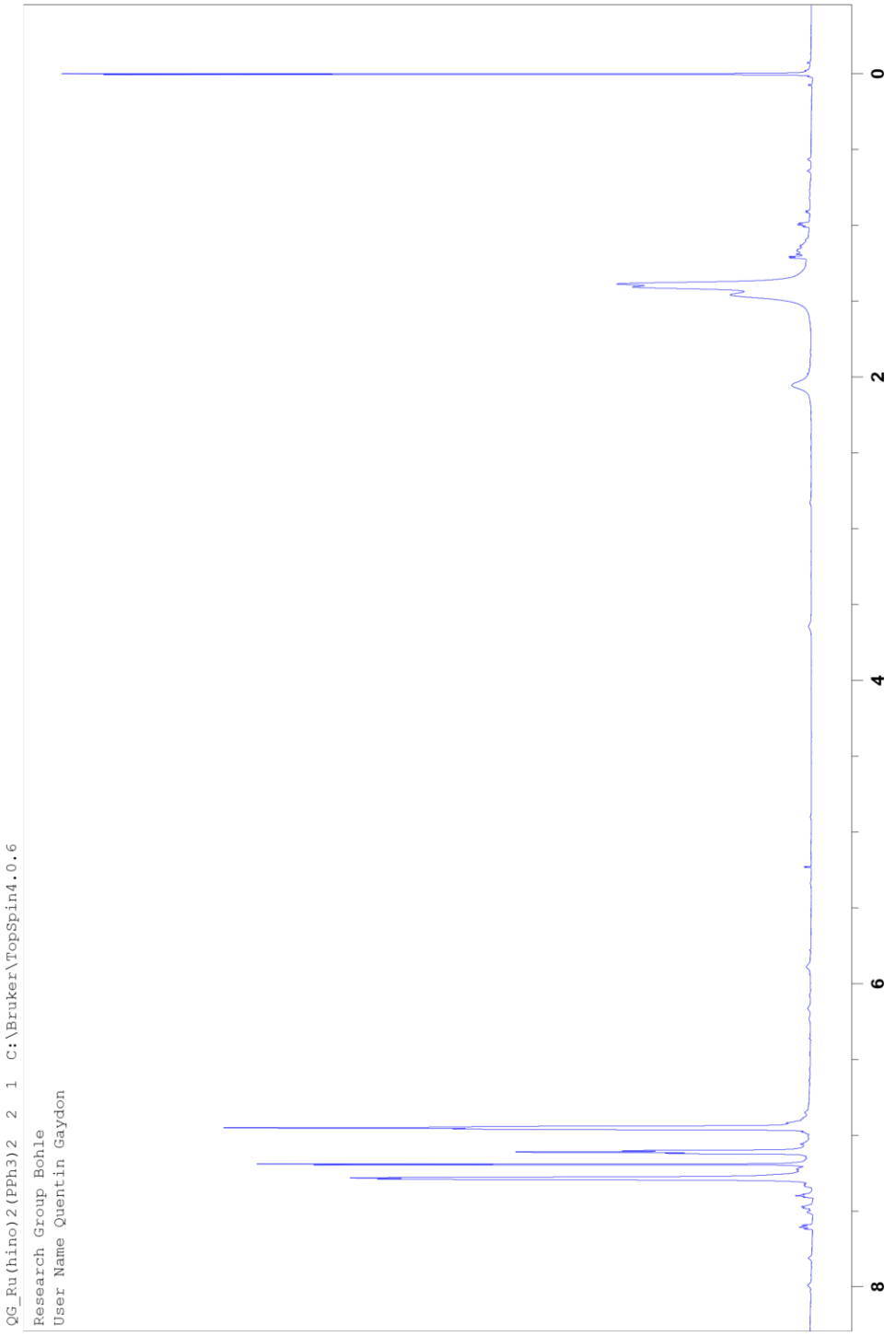

Figure S3.3: ^{1}H NMR for $RuH(CO)(hino)(PPh_3)_2$ 3a

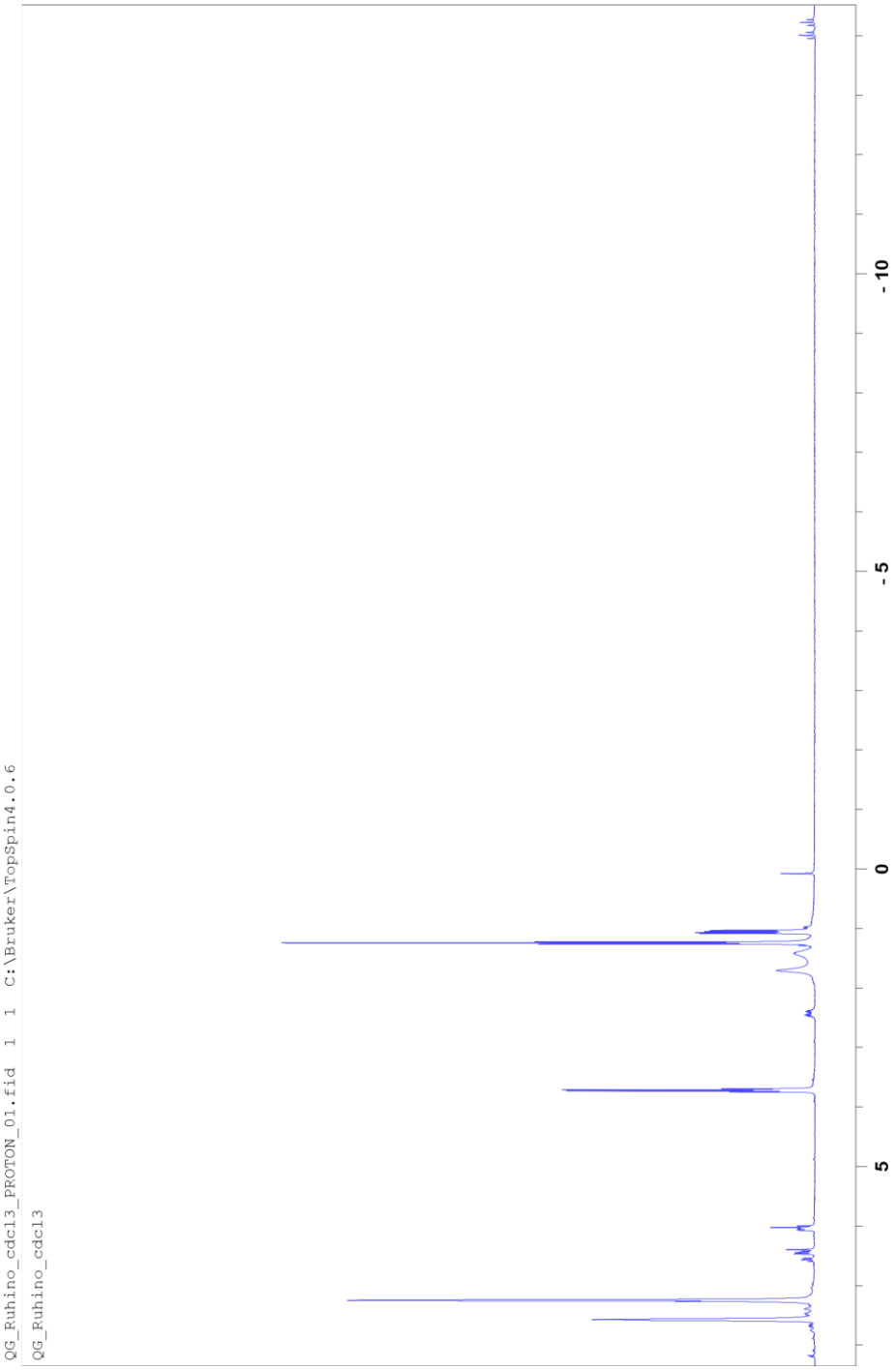

Figure S3.4: ^{1}H NMR for hinokitiol aromatic region fo $OsH(CO)(hino)(PPh_3)_2$ 3b

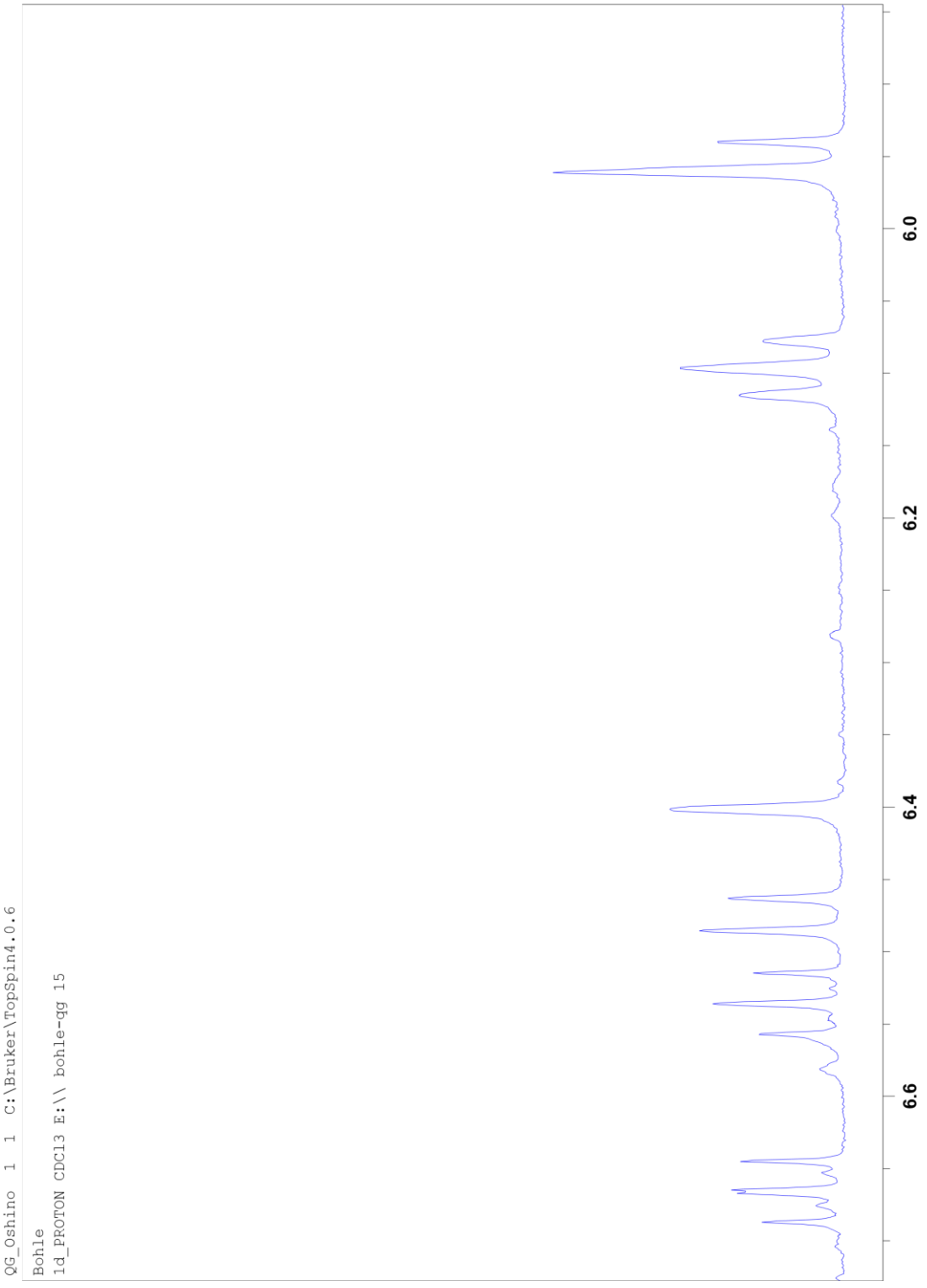

Figure S3.5: ^{1}H NMR for hydride region of OsH(CO)(hino)(PPh_3)$_2$ 3b

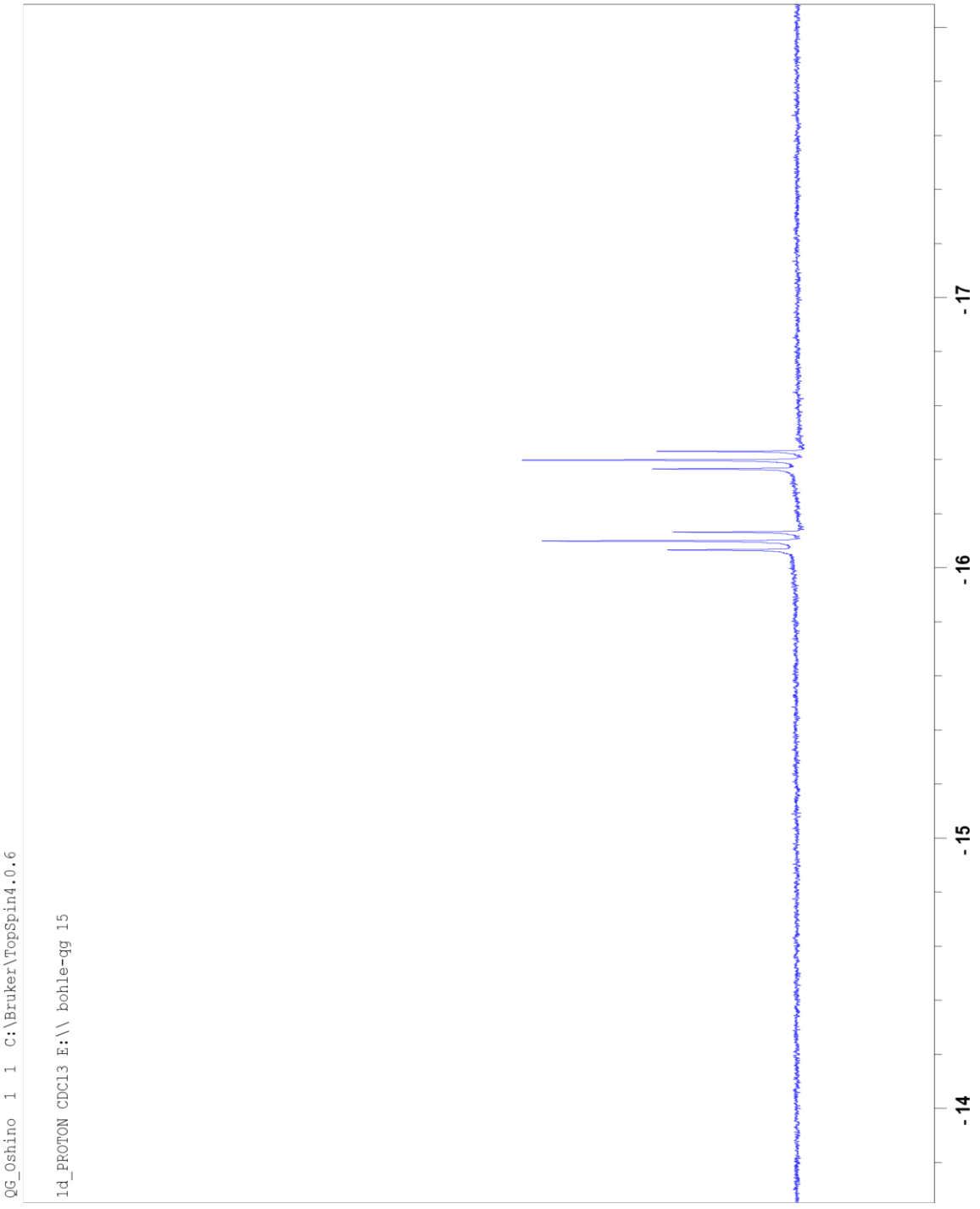

Figure S3.6: Full ^{1}H NMR for OsH(CO)(hino)(PPh_3)$_2$ 3b

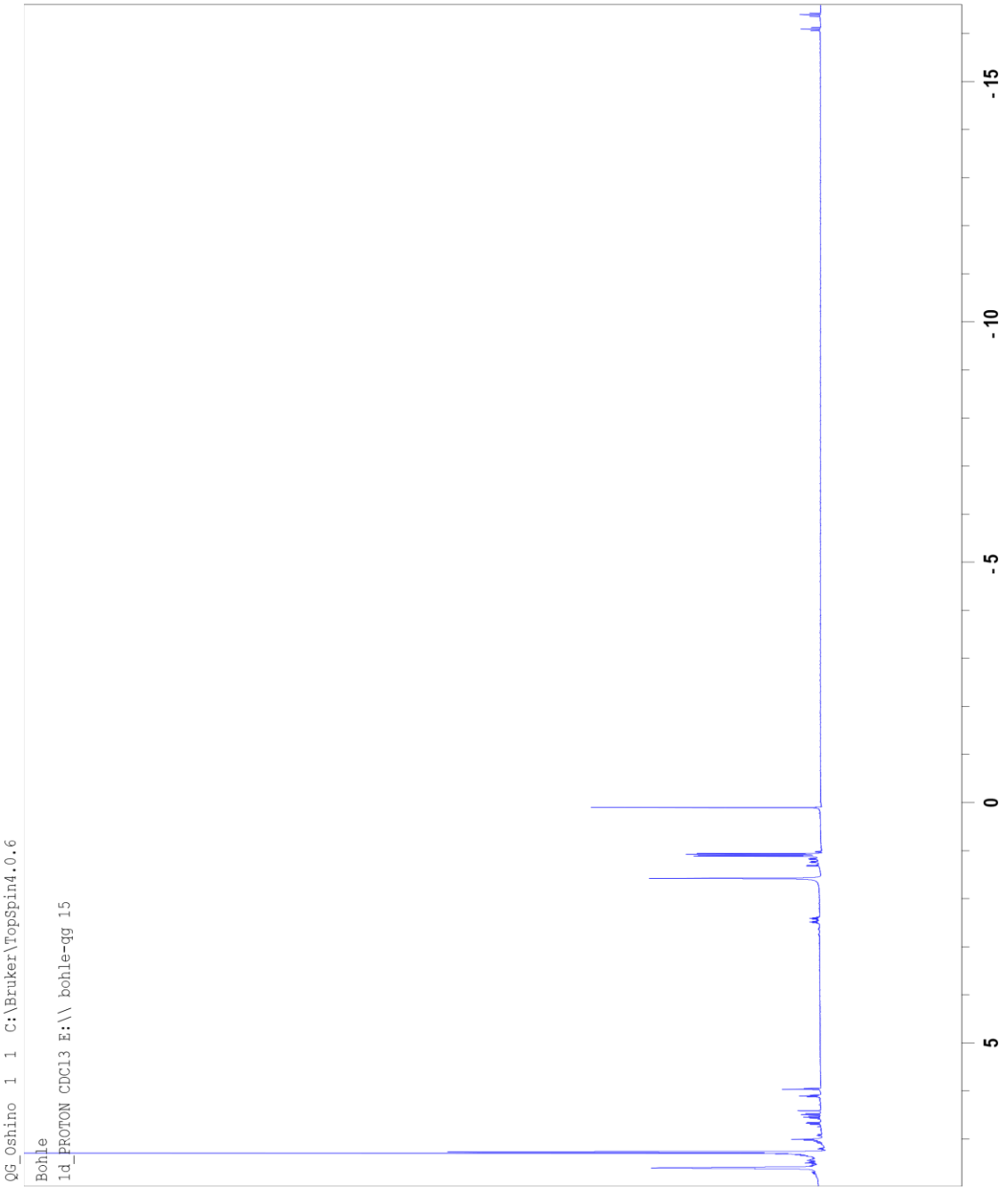

Figure S3.7: Full ^{1}H NMR for OsH(CO)(hino)(P(p-tolyl)$_3$)$_2$ 3c

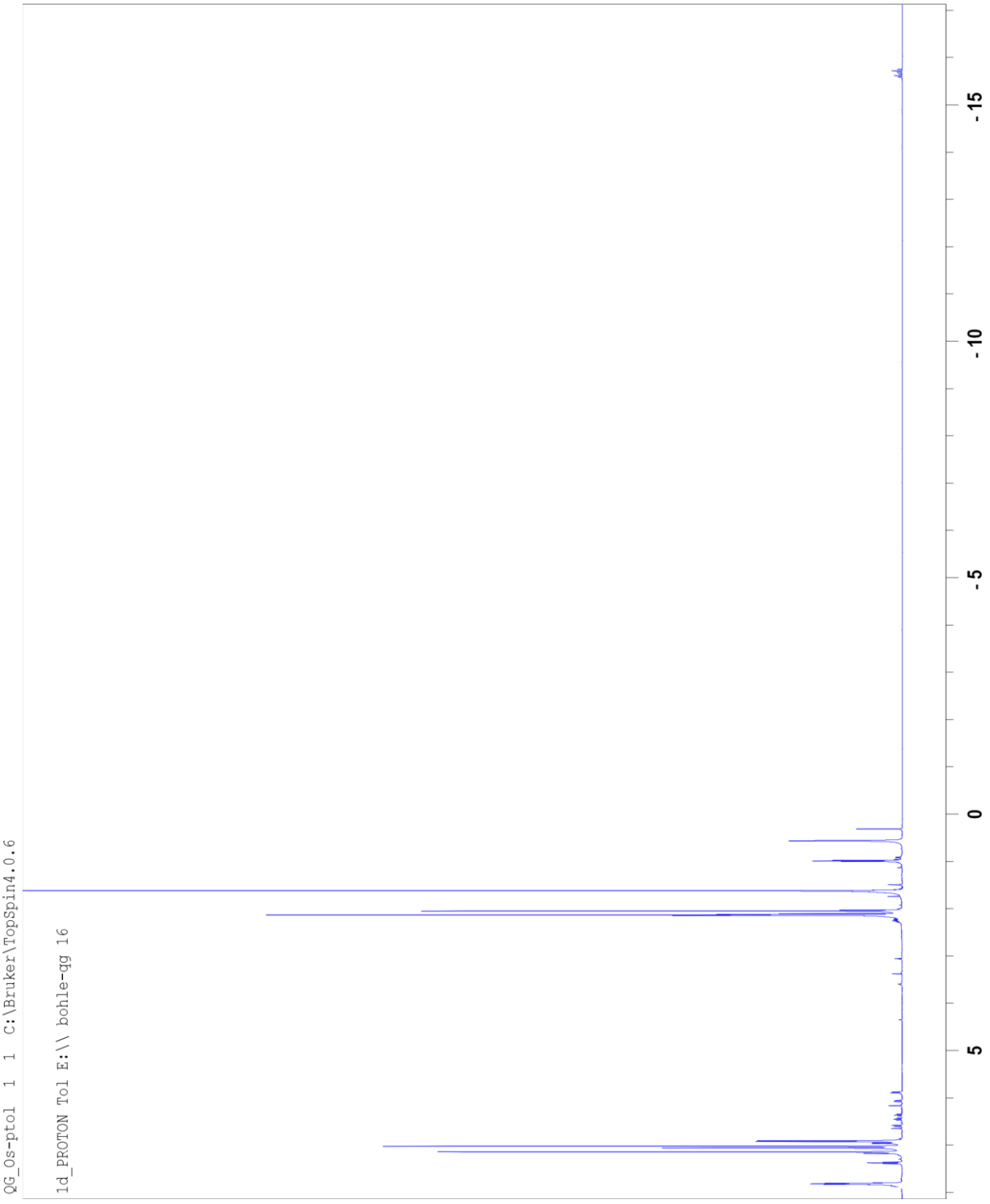

Figure S3.8: Expansion of ^{1}H NMR for $OsH(CO)(hino)(P(p\text{-}tolyl)_3)_2$ 4a

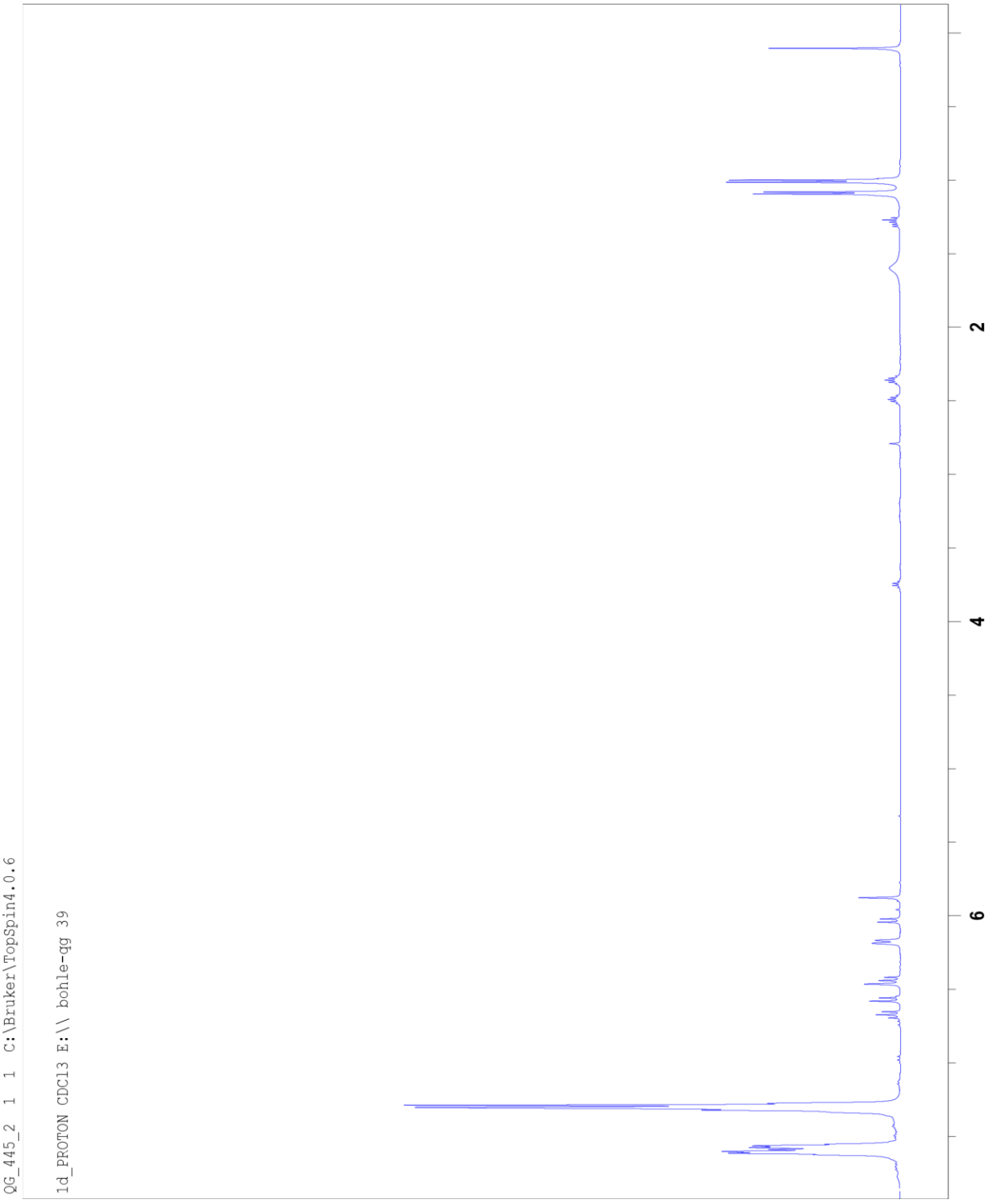

Figure S3.9: Full ^{1}H NMR for OsCl(CO)(hino)(PPh$_3$)$_2$ 4b

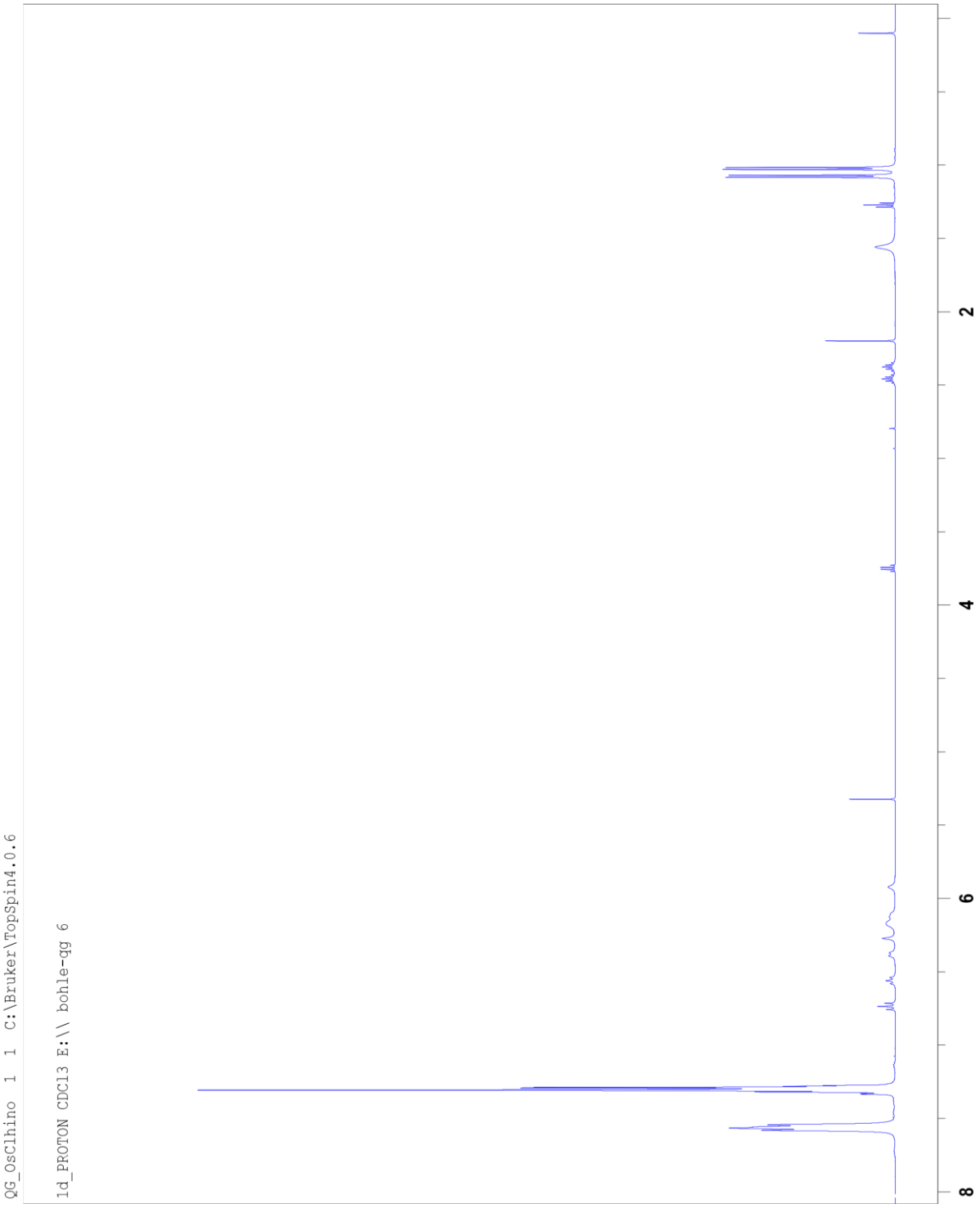

APPENDIX C: Supplementary Data for Chapter 4

Table S4.1: Experimental IR frequencies using KBr pellets at 25^0C and calculated IR frequencies using DFT calculations with B3LYP-6-31++G(d,p) basis sets in a vacuum of $NH_4S_2CNH_2$

Experimental Frequencies	Calculated Frequencies
842cm^{-1}	843cm^{-1}
1332 cm^{-1}	1325 cm^{-1}
1409 cm^{-1}	1483 cm^{-1}
1596 cm^{-1}	1548 cm^{-1}
1631 cm^{-1}	1617 cm^{-1}
3302 cm^{-1}	3502 cm^{-1}
3431 cm^{-1}	3571 cm^{-1}

Table S4.2: Comparison of experimentally determined IR frequencies (cm^{-1}) of $RuH(CO)(S_2CNH_2(PPh_3)_2$ and $RuCl(CO)(S_2CNH_2(PPh_3)_2$

$RuH(CO)(S_2CNH_2(PPh_3)_2$	$RuCl(CO)(S_2CNH_2(PPh_3)_2$
843.4w	853.1w
1182.4w	1158.5w
1358.8m	1394.0m
1581.3s	1588.8m
1926.5s	1940.7s
3319.8w	3154.1w
3449.9w	3262.0w
3472.8w	3431.0w

Table S4.3: Comparison of experimentally determined IR frequencies of $NH_4S_2CNH_2$, $Co(S_2CNH_2)_3$ and $Rh(S_2CNH_2)_3$

$NH_4S_2CNH_2$	$Co(S_2CNH_2)_3$	$Rh(S_2CNH_2)_3$
842cm^{-1}	836cm^{-1}	829cm^{-1}
1332 cm^{-1}	N/A	N/A
1409 cm^{-1}	1390 cm^{-1}	1402 cm^{-1}
1596 cm^{-1}	1596 cm^{-1}	1589 cm^{-1}
1631 cm^{-1}	1679 cm^{-1}	1673 cm^{-1}
3302 cm^{-1}	3251 cm^{-1}	3264 cm^{-1}
3431 cm^{-1}	3354 cm^{-1}	3347 cm^{-1}

Table S4.4: Assignment of vibrational motions to IR frequencies of $Co(S_2CNH_2)_3$ using DFT calculations with B3LYP aug-cc-pVTZ basis sets in a vacuum

Experimental Frequencies	Calculated Frequencies	Vibrational motion
836cm^{-1}	854 cm^{-1}	N-H rocking + C-S rocking
1390 cm^{-1}	1377 cm^{-1}	C-S symmetrical stretching+ C-N stretching
1596 cm^{-1}	1629 cm^{-1}	N-H bending + C-N stretching
3251 cm^{-1}	3568 cm^{-1}	N-H symmetrical stretching
3354 cm^{-1}	3695 cm^{-1}	N-H asymmetrical stretching

Table S4.5: UV-Vis data[a] of the tris-chelate complexes

Complex	λ(nm	Log(ε)
$Co(S_2CNH_2)_3$	392	4.3
	486	2.8
	661	2.7
$Rh(S_2CNH_2)_3$	446	4.3

a. ε given in $M^{-1}.cm^{-1}$ measured in acetone at room temperature

Table S4.6: Attempted syntheses of $Ir(S_2CNH_2)_3$ with IR frequencies in the 2200-2000cm^{-1} range of the obtained products

Reaction Solvent	Starting material	Observed frequencies a 2200-2000cm^{-1} range
1:1 EtOH/H_2O	$IrCl_3$	2101
MeOH	$IrCl_3$	2105
THF	$IrCl_3$	2053
EtOAc	$IrCl_3$	2105
1:1 EtOH/H_2O	K_2IrCl_6	2075
1:1MeOH/H_2O	K_2IrCl_6	2106

Figure S4.1: A) TGA data of the decomposition of $Co(S_2CNH_2)_3$ from 30^0C to 700^0C B) IR spectrum of the decomposition products at 180^0C and C) expanded view of the IR spectrum in the 2500cm^{-1}-1000cm^{-1} region

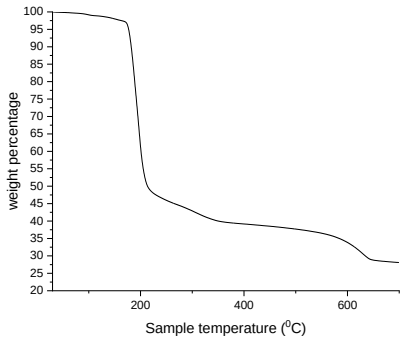

A)

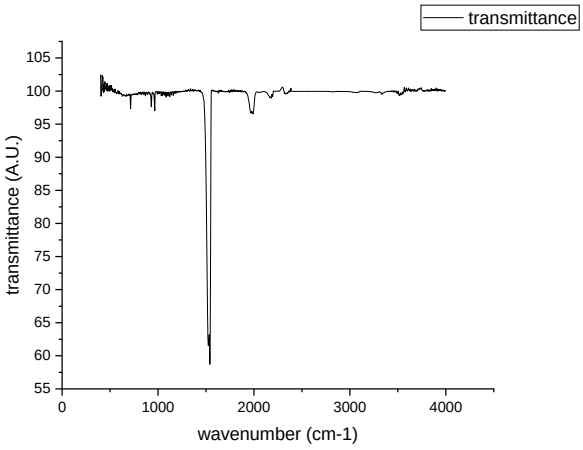

B)

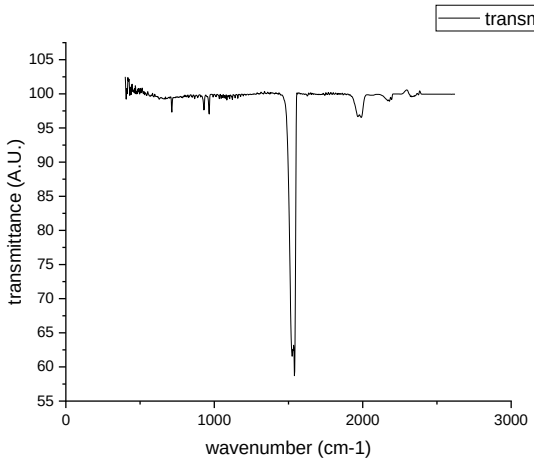

C)

Table S4.7: X-ray diffraction data of Ru(II) complexes

	2	**3**
Empirical Formula	$C_{39}H_{32}NO_{1.5}P_2RuS_2$	$C_{44}H_{42}NO_3P_2RuS_2$
Formula Weight	765.78	873.36
Crystal System	Triclinic	Triclinic
Space Group	P-1	P-1
a	9.1016(5)	10.1363(5)
b	15.3488(9)	13.2225(7)
c	15.3776(9)	15.6437(9)
α	118.5640(10)	96.710(4)
β	92.9500(10)	92.181(4)
γ	94.5280(10)	91.832(4)
V	1871.08(19)	2079.41(19)
Density	1.359	1.395
Z	2	2
T(K)	571(2)	571(2)
Reflections Collected	22075	14357
Independent reflections	8628	6943
R_{int}	0.0216	0.0389
Goodness of fit	1.158	1.059
R_1	0.0455	0.0542
wR_2	0.1397	0.1464
CCSD number	2113837	2113834

Table S4.8: X-ray diffraction data of tris-chelate complexes

	4	**5**	**$Rh(S_2CNMe_2)_3$**	**$Rh(S_2CNBz_2)_3$**
Empirical Formula	$C_3H_6CoN_3S_6$	$C_3H_8N_3ORhS_6$	$C_{11}H_{21}N_3ORhS_6$	$C_{45}H_{42}N_3RhS_6$
Formula Weight	335.40	397.39	506.58	920.08
Crystal System	Monoclinic	Monoclinic	Monoclinic	Triclinic
Space Group	$P2_1/c$	$P2_1/c$	$P2_1/n$	P-1
a	7.104(5)	7.1495(8)	13.286(11)	9.913(4)
b	10.058(7)	14.8551(16)	9.575(8)	12.851(6)
c	16.301(11)	11.4510(12)	16.963(14)	16.771(7)
α	90	90	90	92.063(5)
β	101.007(7)	97.034(7)	108.626(9)	97.092(5)
γ	90	90	90	102.265(5)
V	1143.3(13)	1207.0	2045.0(3)	2067.5(15)
Density	1.948	2.187	1.645	1.478
Z	4	4	4	2
T(K)	571(2)	571(2)	571(2)	571(2)
Reflections Collected	12923	24866	12677	11891
Independent reflections	2762	2840	2198	4078
R_{int}	0.0296	0.1162	0.0636	0.0364
Goodness of fit	0.897	0.997	0.999	0.923
R_1	0.0254	0.0414	0.0367	0.0329
wR_2	0.0640	0.0676	0.0927	0.0967
CCSD number	2113833	2113835	2113832	2113836

Table S4.9: Selected bond lengths(Å) and bond angles(°) of $Rh(S_2CNH_2)_3$ and $Co(S_2CNH_2)_3$

Bonds	Value	Angles	Value	Bonds	Value	Angles	Value
Rh-S	2.3605(15)	S-Rh-S (bite angle)	73.71(5)	Co-S	2.2750(12)	S-Co-S (bite angle)	76.61(4)
	2.3365(15)		73.89(5)		2.2837(11)		76.45(4)
	2.3387(16)		73.59(5)		2.2563(13)		76.33(4)
	2.3490(15)				2.2937(11)		
	2.3606(14)				2.2673(12)		
	2.3546(15)				2.2799(12)		
C-S	1.705(6)	S-C-S	112.0(3)	C-S	1.693(2)	S-C-S	111.37(14)
	1.693(6)		112.7(3)		1.698(3)		111.72(14)
	1.679(6)		112.7(3)		1.713(3)		111.58(14)
	1.706(6)				1.711(2)		
	1.692(6)				1.691(3)		
	1.700(5)				1.714(3)		
C-N	1.312(7)	S-Rh-S (trans sulfurs)	166.84(5)	C-N	1.319(3)	S-Co-S (trans sulfurs)	166.85(3)
	1.304(7)		166.895)		1.318(3)		167.64(3)
	1.303(7)		168.12(5)		1.320(3)		167.54(3)

Table S4.10: Selected bond lengths(Å) and bond angles(°) of $Rh(S_2CNH_2)_3$, $Rh(S_2CNMe_2)_3$, $Rh(S_2CNEt_2)_3$ and $Rh(S_2CNBz_2)_3$

	$Rh(S_2CNH_2)_3$	$Rh(S_2CNMe_2)_3$	$Rh(S_2CNEt_2)_3$	$Rh(S_2CNBz_2)_3$
Reference	This work	This work	46	This work
Space Group	$P2_1/c$	$P2_1/n$	$P2_1/a$	P-1
Rh-S	2.3605(15)	2.352(3)	2.364(7)	2.3385(15)
	2.3365(15)	2.345(3)	2.360(7)	2.3477(15)
	2.3387(16)	2.353(3)	2.379(7)	2.3636(14)
	2.3490(15)	2.353(3)	2.360(6)	2.3416(14)
	2.3606(14)	2.361(3)	2.369(7)	2.3619(15)
	2.3546(15)	2.347(3)	2.355(7)	2.3759(15)
C-S	1.705(6)	1.719(13)	1.69(2)	1.702(5)
	1.693(6)	1.726(12)	1.74(2)	1.706(5)
	1.679(6)	1.693(12)	1.73(2)	1.709(5)
	1.706(6)	1.711(13)	1.71(2)	1.710(5)
	1.692(6)	1.673(12)	1.73(2)	1.698(5)
	1.700(5)	1.734(12)	1.70(2)	1.698(5)
C-N	1.312(7)	1.311(14)	1.36(2)	1.324(6)
	1.304(7)	1.343(14)	1.32(3)	1.324(6)
	1.303(7)	1.304(13)	1.37(3)	1.334(6)
S-Rh-S bite angle	73.71(5)	73.84(12)	73.6(2)	73.94(5)
	73.89(5)	73.80(12)	73.6(2)	73.91(5)
	73.59(5)	73.55(11)	73.4(2)	73.53(5)
S-Rh-S trans angles	166.84(5)	166.06(12)	165.7(2)	167.14(5)
	166.89(6)	166.59(12)	168.3(2)	164.66(5)
	168.12(6)	168.05(12)	164.8(2)	166.51(5)
S-C-S	112.0(3)	110.0(7)	113(1)	111.7(3)
	112.7(3)	112.2(8)	110(1)	112.1(3)
	112.7(3)	109.8(8)	111(1)	112.0(3)
C-N-C	N/A	118.0(11)	119(1)	116.5(4)
		117.7(12)	121(2)	117.1(4)
		119.0(11)	120(2)	116.8(4)

Figure S4.2: Representation of the twist angle, polar angle and pitch angle.

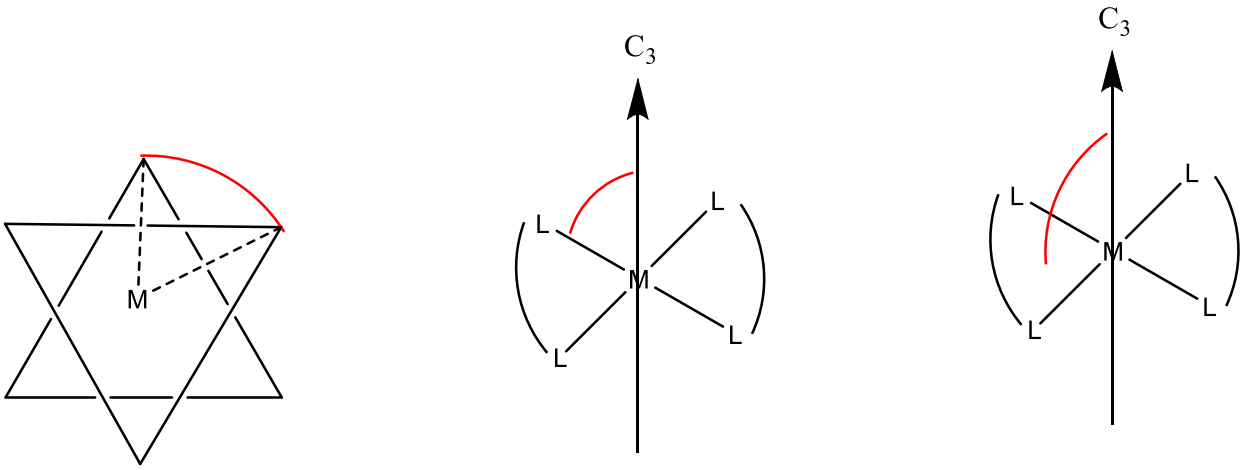

twist angle polar angle pitch angle

The twist angle is the projection of the bite angle onto the plane perpendicular to the C3 axis. The polar angle is the angle between the M-L bonds and the C3 axis. The pitch angle is the angle formed by the plane of the chelate ring and the C3 axis.

Figure S4.3: B3LYP/aug-cc-pvdz Singlet Transition and Ground States and One direction of the racemization pathway from the TS, above left, to the GS, right.

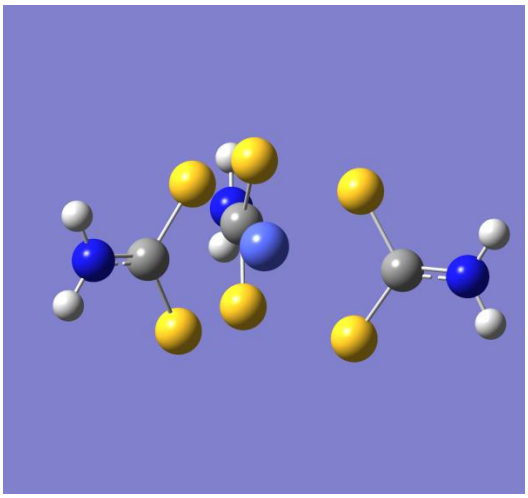

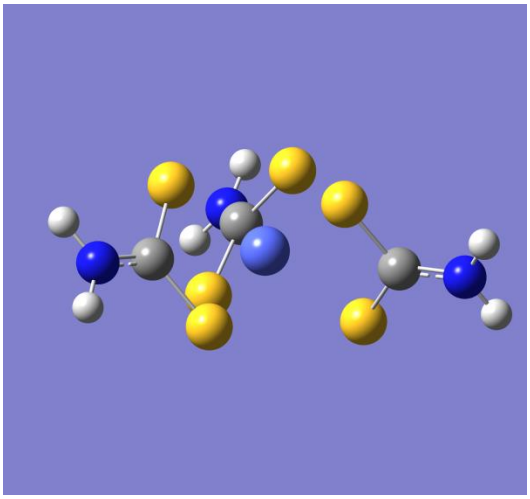

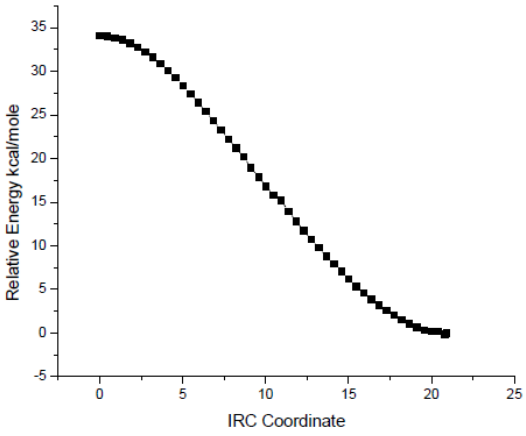

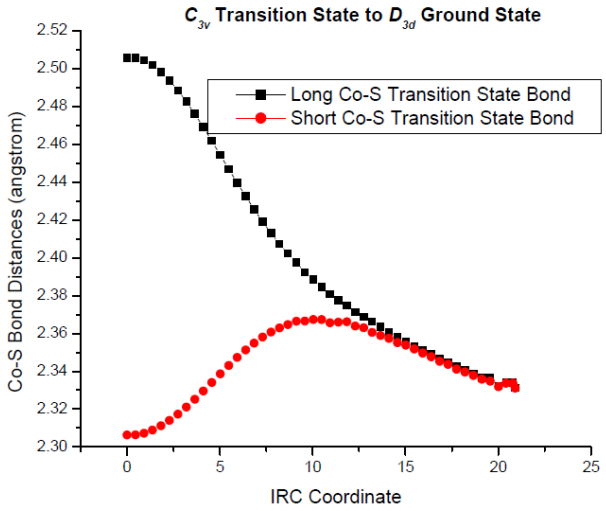

Figure S4.4: ^{1}H NMR spectrum $Co(S_2CNH_2)_3$

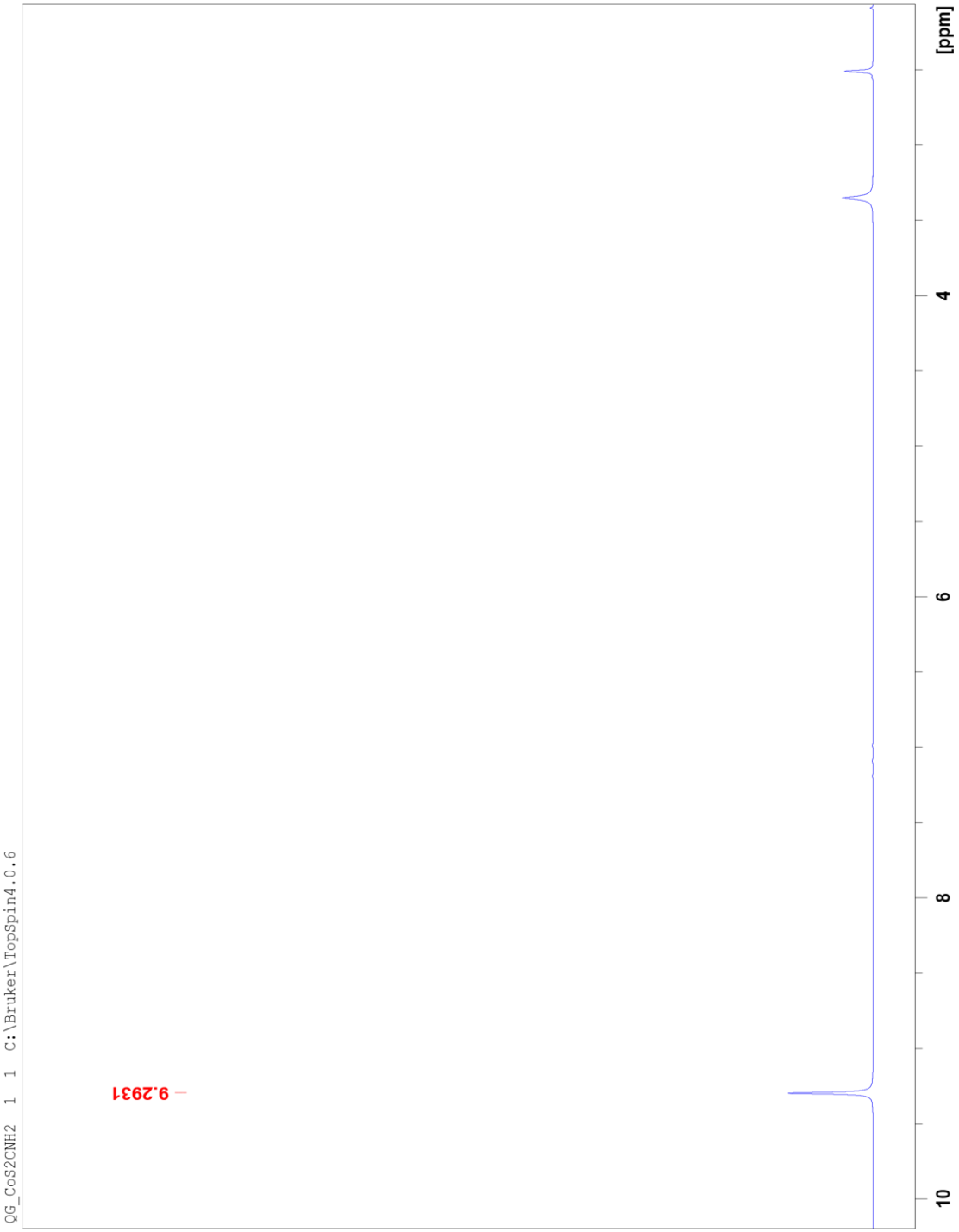

Figure S4.5: ^{13}C NMR spectrum of $Co(S_2CNH_2)_3$

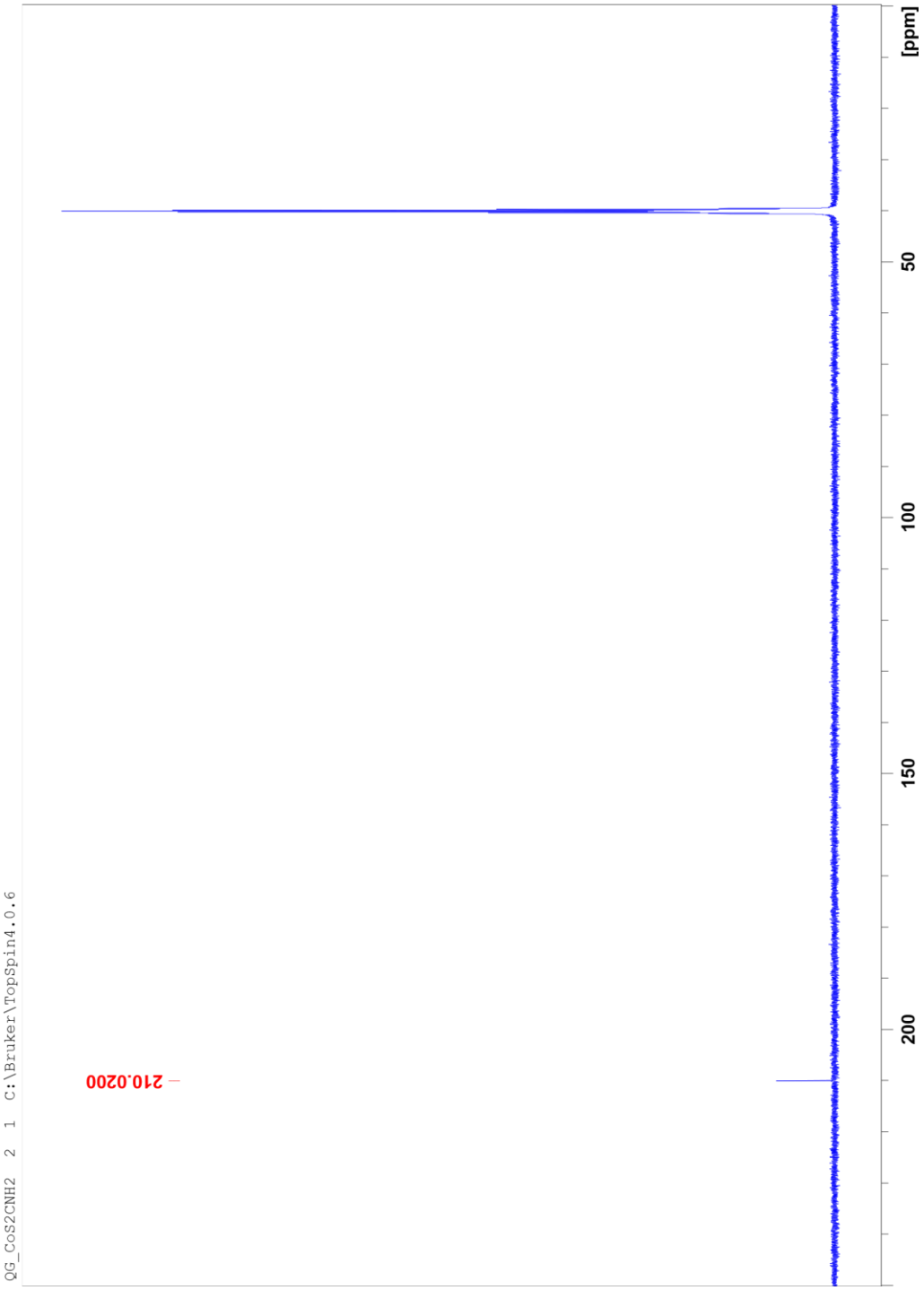

Figure S4.6: ^{1}H NMR spectrum of $Rh(S_2CNH_2)_3$

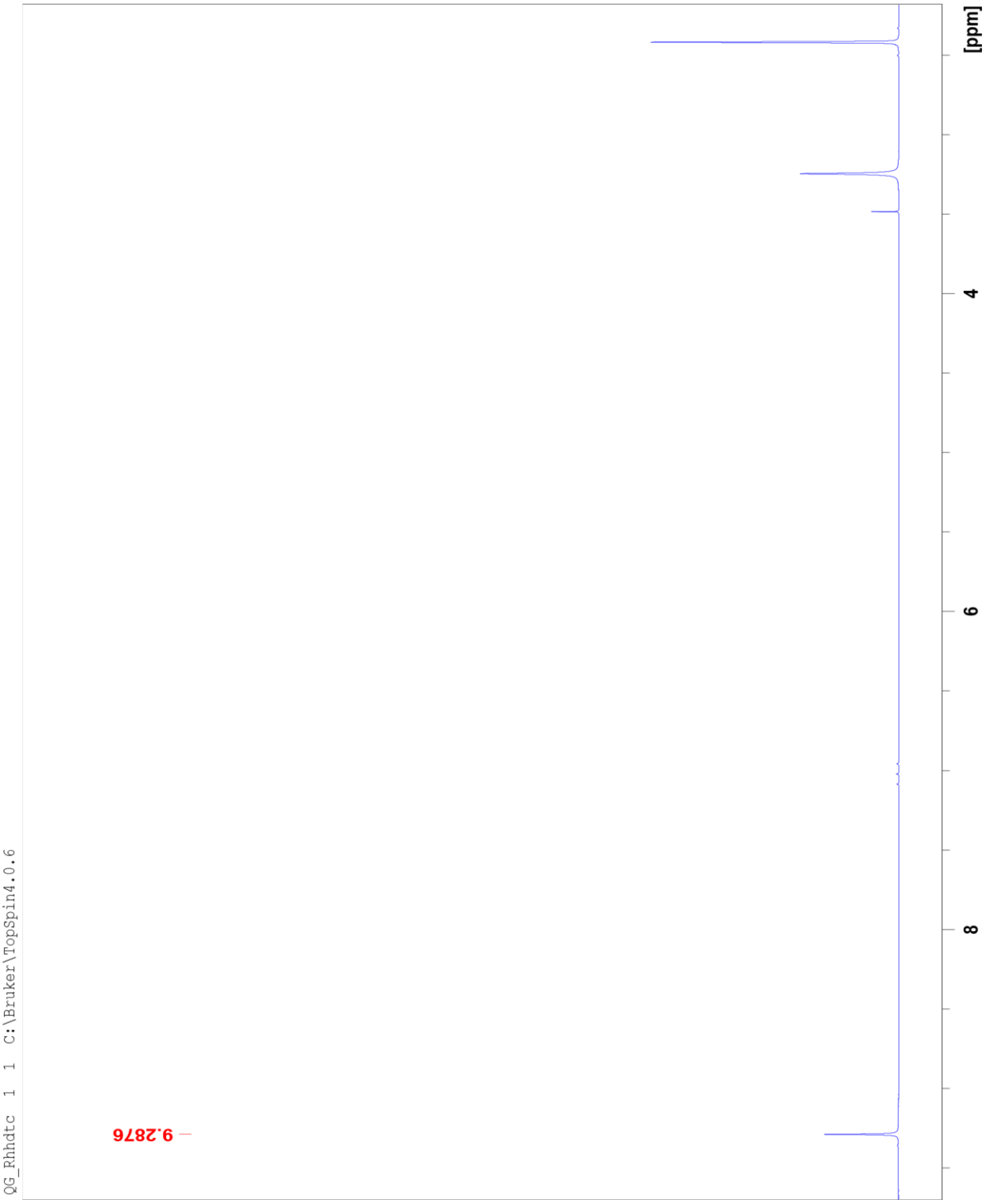

Figure S4.7: ^{13}C NMR spectrum of $Rh(S_2CNH_2)_3$

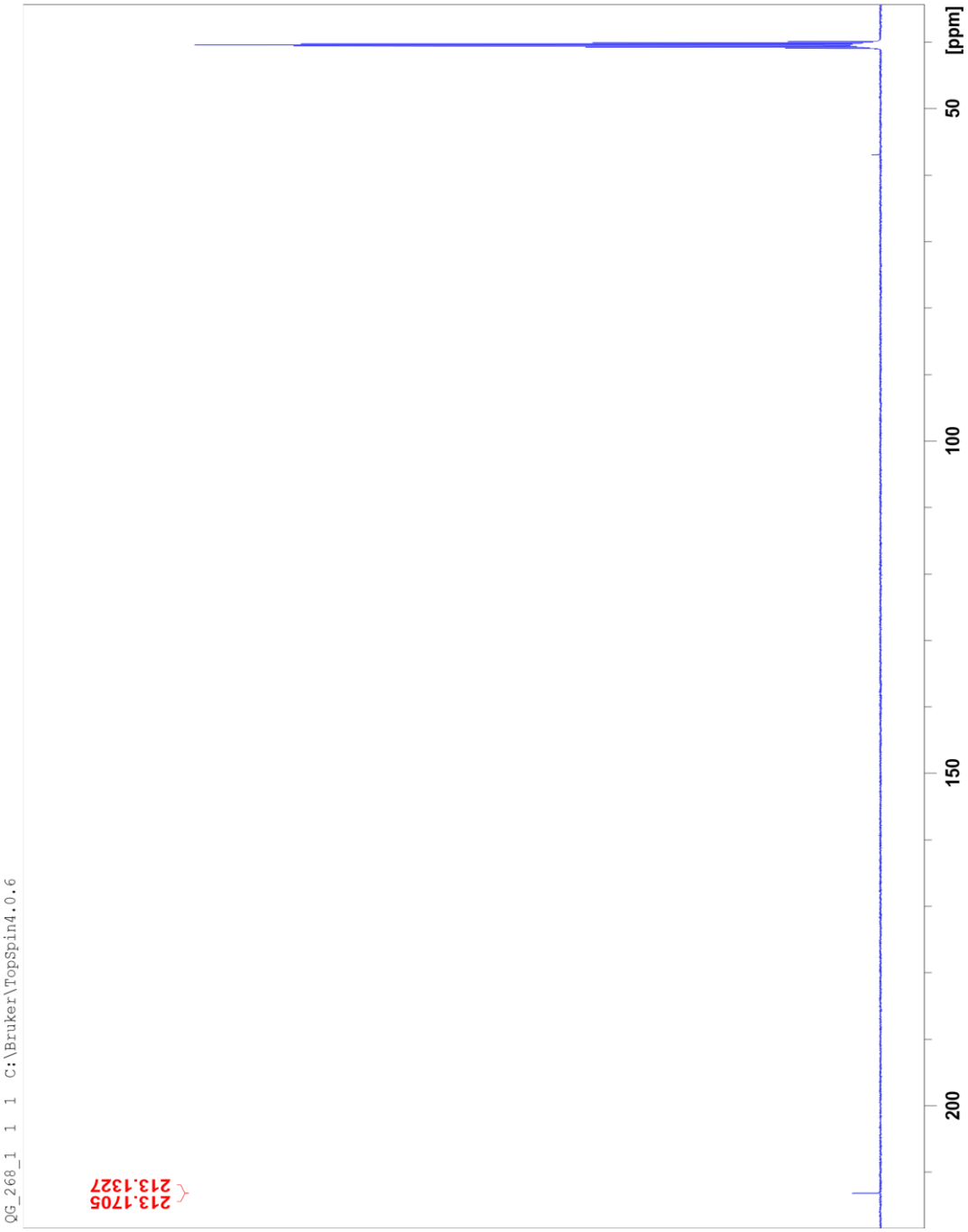

Figure S4.8: Full ^{1}H NMR spectrum of $RuH(CO)(S_2CNH_2)(PPh_3)_2$

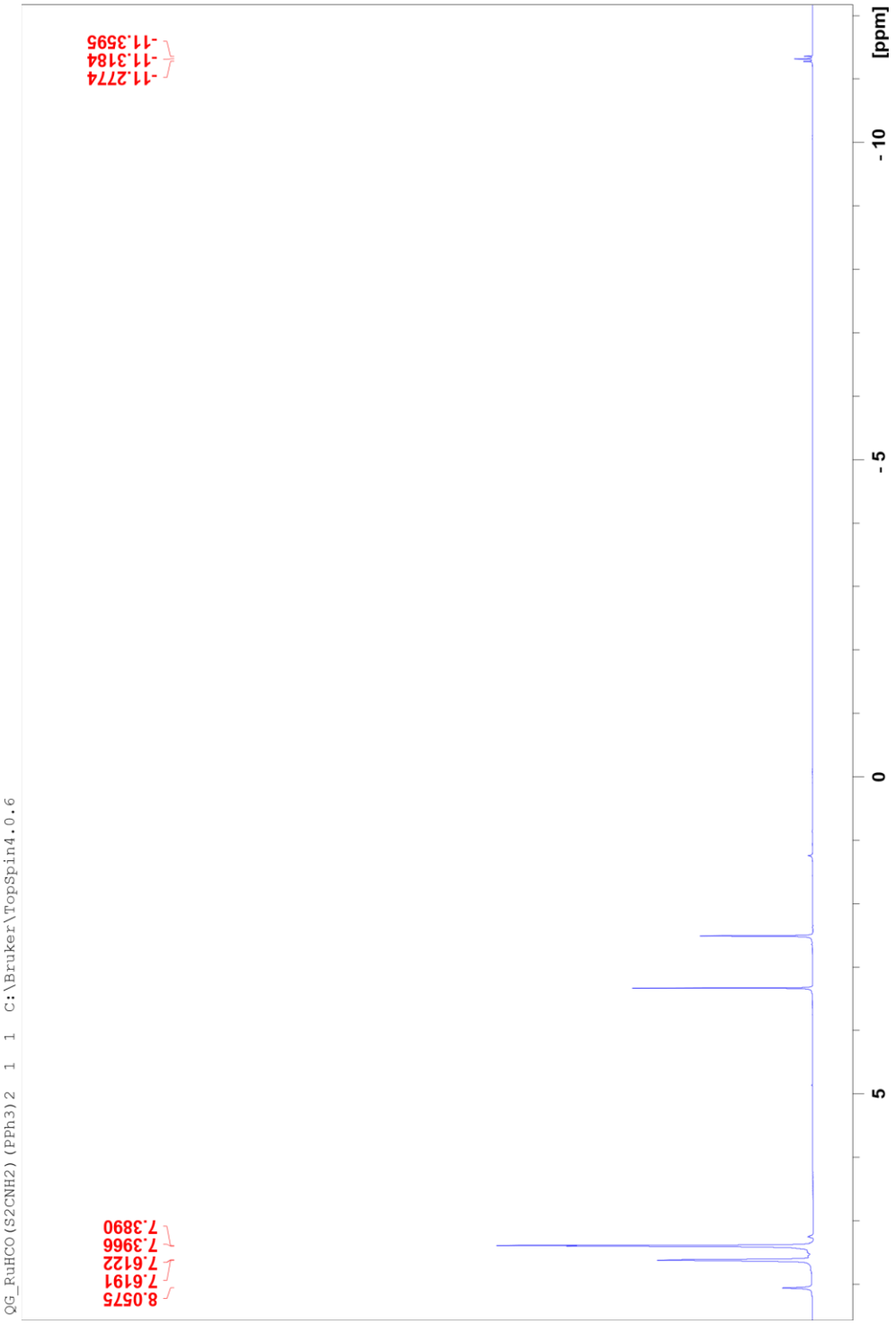

Figure S4.9: Hydride region in the ^{1}H NMR spectrum of $RuH(CO)(S_2CNH_2)(PPh_3)_2$

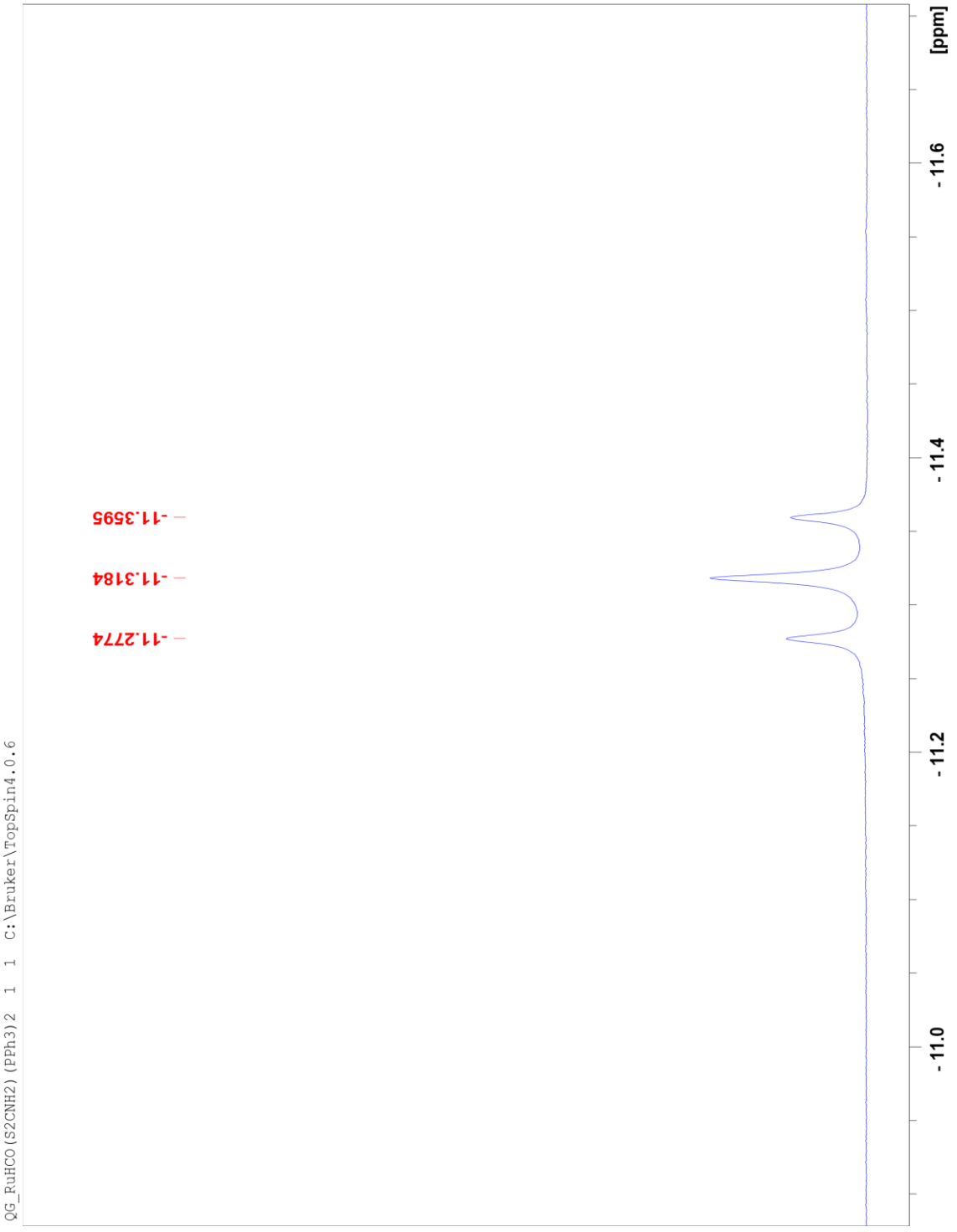

Figure S4.10: ^{13}C NMR spectrum of $RuH(CO)(S_2CNH_2)(PPh_3)_2$

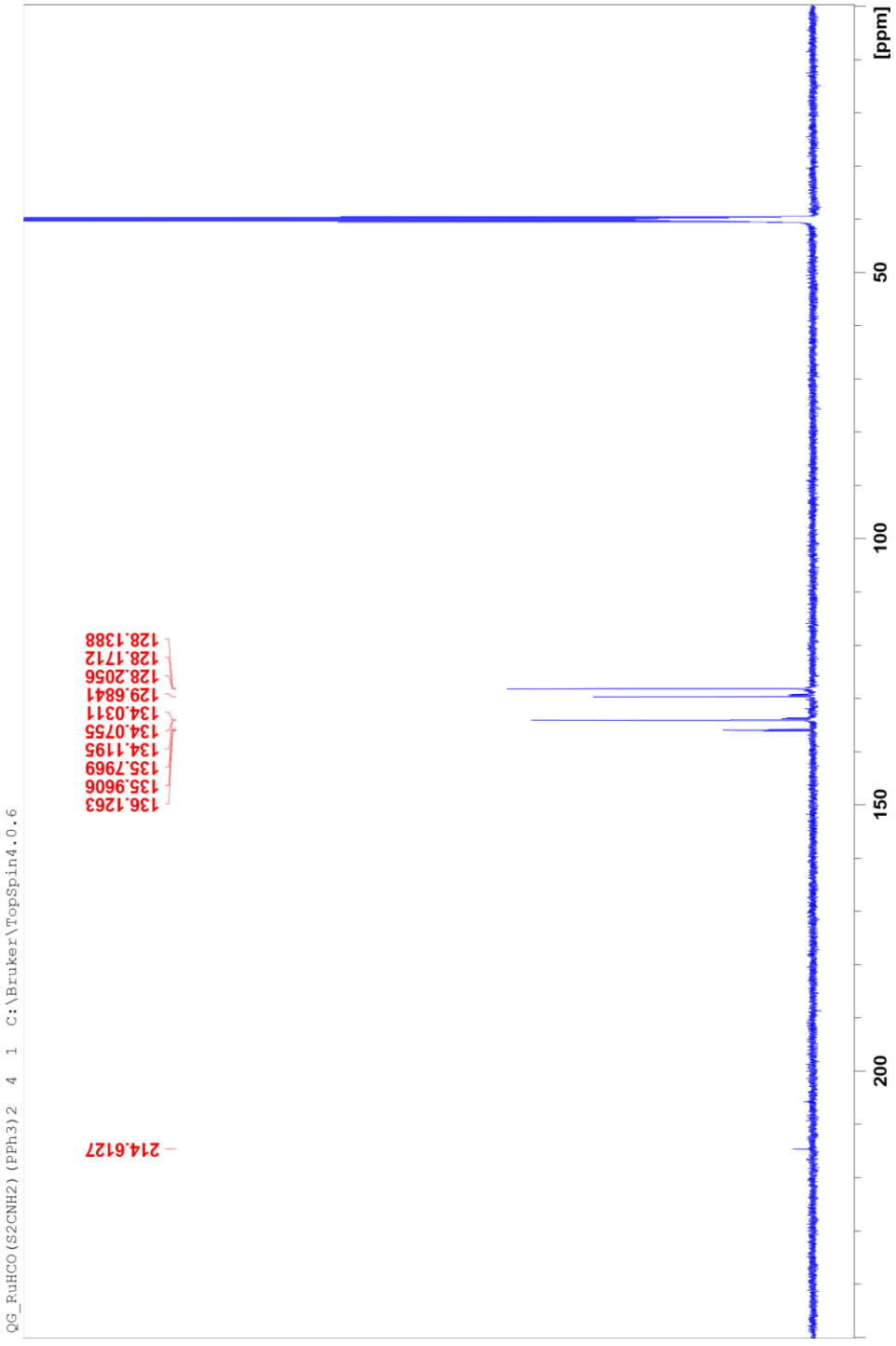

Figure S4.11: ^{31}P NMR of $RuH(CO)(S_2CNH_2)(PPh_3)_2$

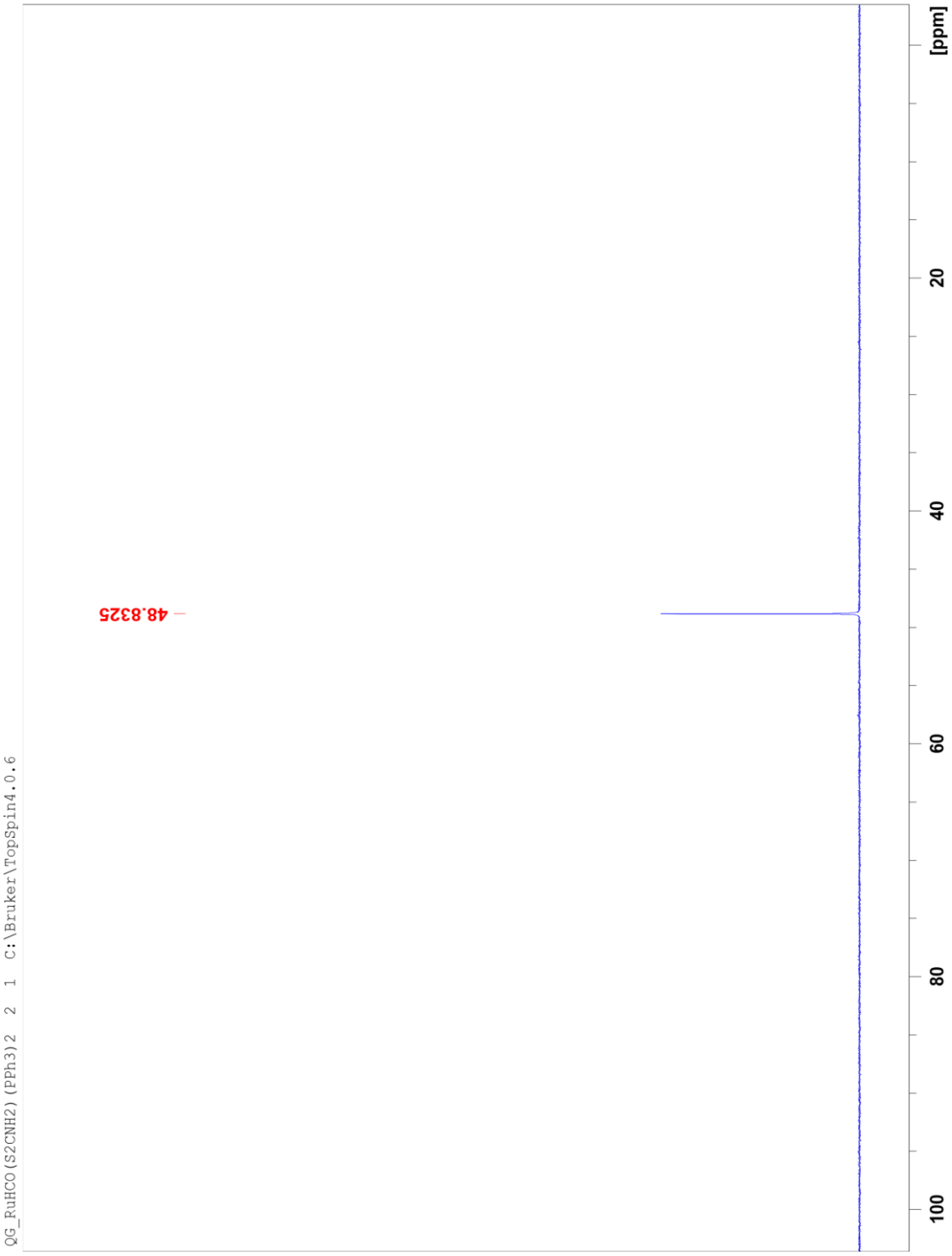

Figure S4.12: ^{1}H NMR spectrum of $RuCl(CO)(S_2CNH_2)(PPh_3)_2$

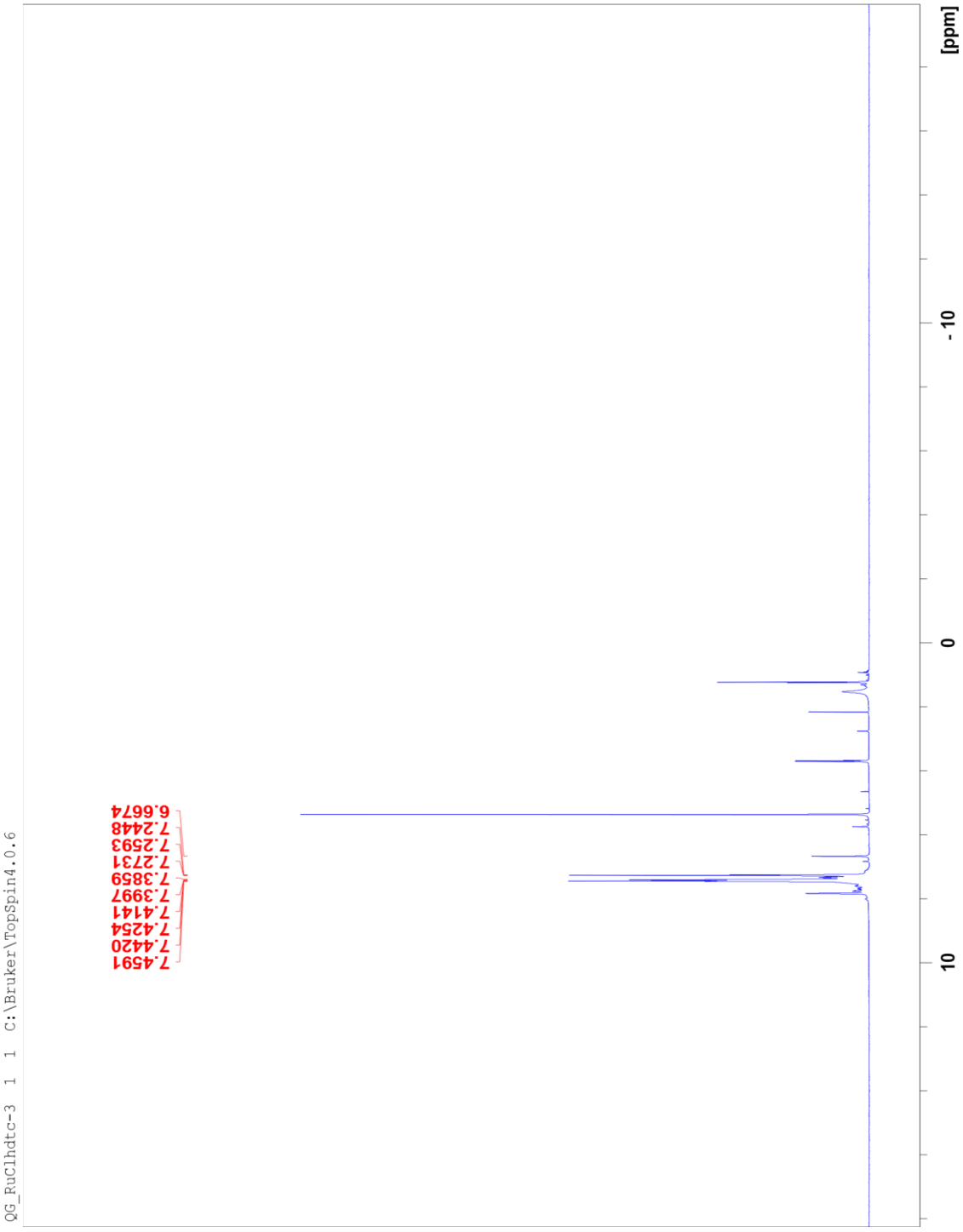

Figure S4.13: ^{13}C NMR spectrum of $RuCl(CO)(S_2CNH_2)(PPh_3)_2$

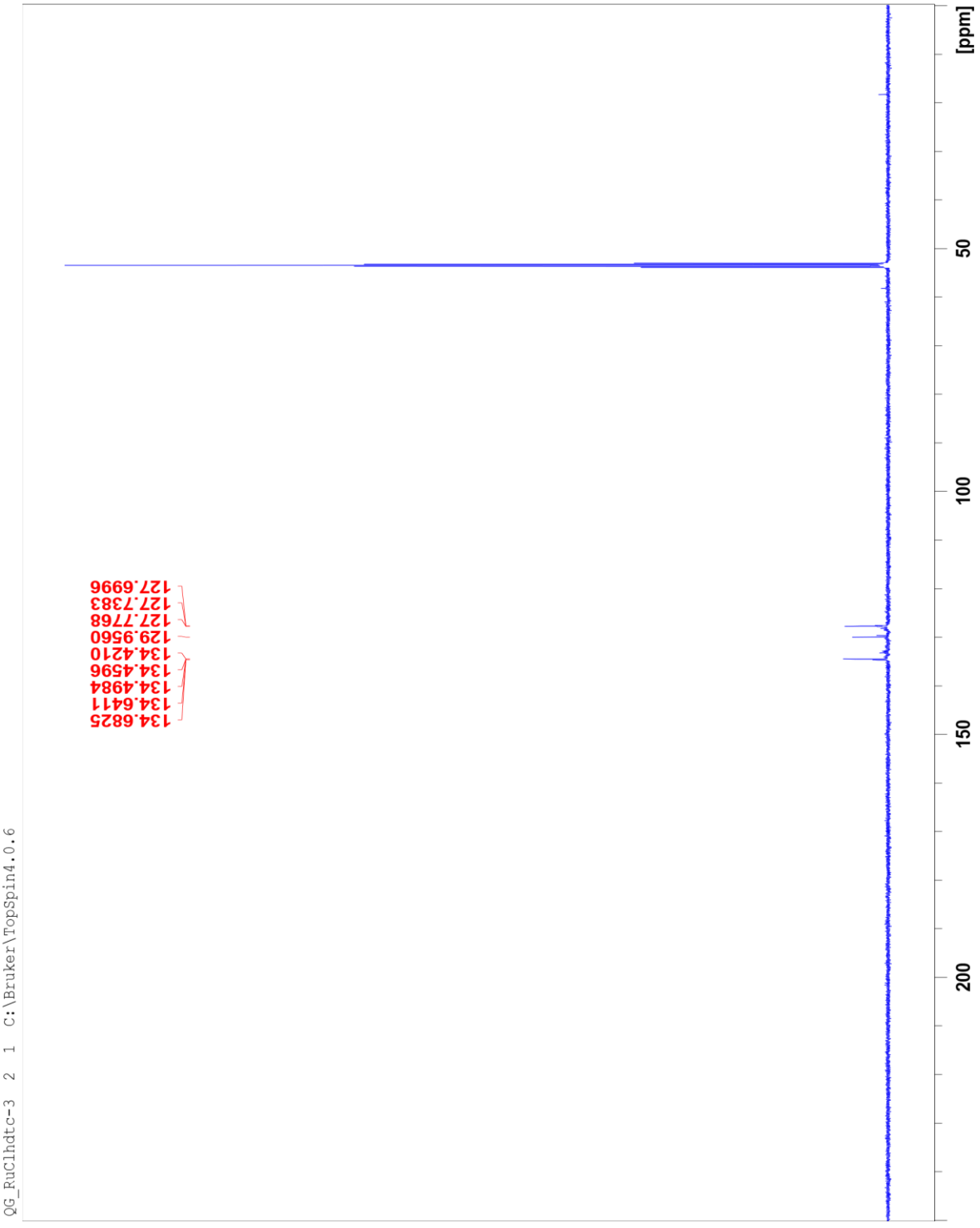

Figure S4.14: ^{31}P NMR spectrum of $RuCl(CO)(S_2CNH_2)(PPh_3)_2$

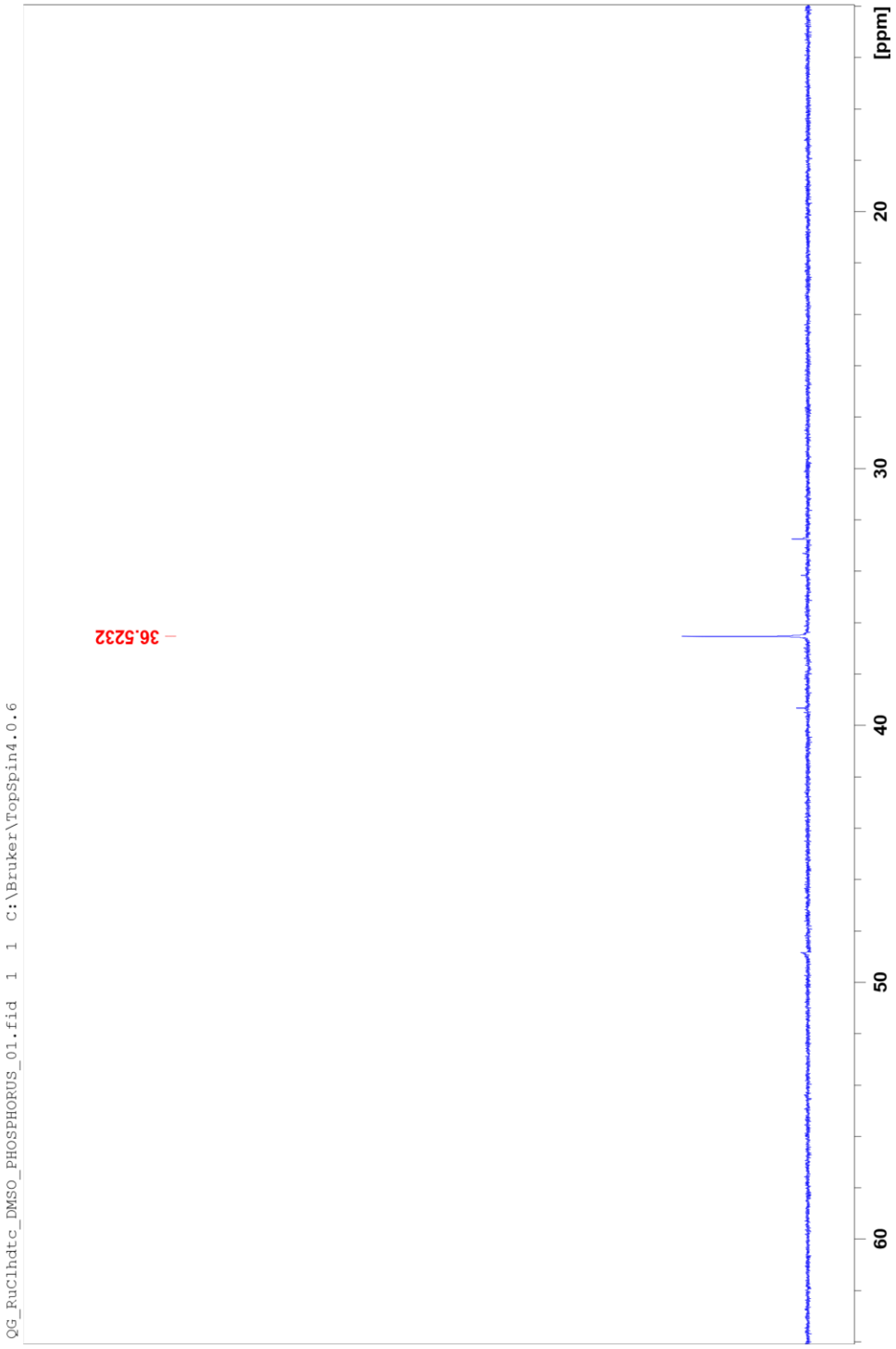

APPENDIX D: Supplementary Data for Chapter 5

Table S5.1: Crystallographic information of 1, 2, 3 and 4

	1	**2**	**3**	**4**
Empirical Formula	$C_{12}H_{28}NF_2PS_2$	$C_{37.50}H_{31}Cl_{0.50}F_2OP_3RuS_2$	$C_{37}H_{30}ClF_2OP_3RuS_2$	$C_{38}H_{30}F_4OP_4RuS_4$
Formula Weight	319.44	811.45	822.16	931.81
Crystal System	Orthorhombic	Triclinic	Monoclinic	Monoclinic
Space Group	Pbca	P-1	$P2_1/c$	C2/c
a(Å)	14.9466(6)	11.127(3)	17.325(3)	39.987(6)
b(Å)	14.6702(6)	12.345(3)	10.1385(16)	9.8867(6)
c(Å)	16.8033(7)	13.689(3)	20.967(3)	21.910(3)
α(°)	90	88.239(3)	90	90
β(°)	90	81.183(3)	104.443(2)	116.810(2)
γ(°)	90	76.965(3)	90	90
Volume($Å^3$)	3684.5(3)	1810.2(8)	3566.5(10)	7731.0(2)
Density(g/cm^3)	1.151	1.489	1.531	1.601
Z	8	2	4	8
T(K)	571(2)	571(2)	571(2)	571(2)
Reflections collected	6320	21156	28836	20320
Independent reflections	1522	8507	5314	3207
Rint	0.0253	0.0428	0.0606	0.1707
Goodness-of-fit	1..140	0.899	0.926	0.989
R1	0.0685	0.0475	0.0381	0.0504
wR2	0.1621	0.1410	0.0994	0.1147
CCSD Number	2154866	2154868	2154867	2154869

Table S5.2: Crystallographic information of cis and trans isomers of 5

	5 (trans isomer)	**5 (cis isomer)**
Empirical Formula	$C_{39}H_{30}Cl_2F_4OP_4RuS_4$	$C_{38}H_{30}Cl_2F_4OP_4RuS_4$
Formula Weight	1014.72	1002.71
Crystal System	Triclinic	Monoclinic
Space Group	P-1	$P2_1/n$
a(Å)	12.271(3)	13.279(5)
b(Å)	13.058(3)	20.031(7)
c(Å)	15.012(4)	15.762(6)
α(º)	80.397(3)	90
β(º)	82.335(3)	91.664(5)
γ(º)	63.243(2)	9093
Volume($Å^3$)	2113.1(9)	4191.0(3)
Density(g/cm^3)	1.595	1.589
Z	2	4
T(K)	571(2)	572(2)
Reflections collected	24779	18725
Independent reflections	9884	2838
Rint	0.0268	0.0863
Goodness-of-fit	1.054	1.045
R1	0.0455	0.0705
wR2	0.1326	0.1855
CCSD Number	2154871	2154870

Figure S5.1: ^{31}P-NMR spectrum of 1

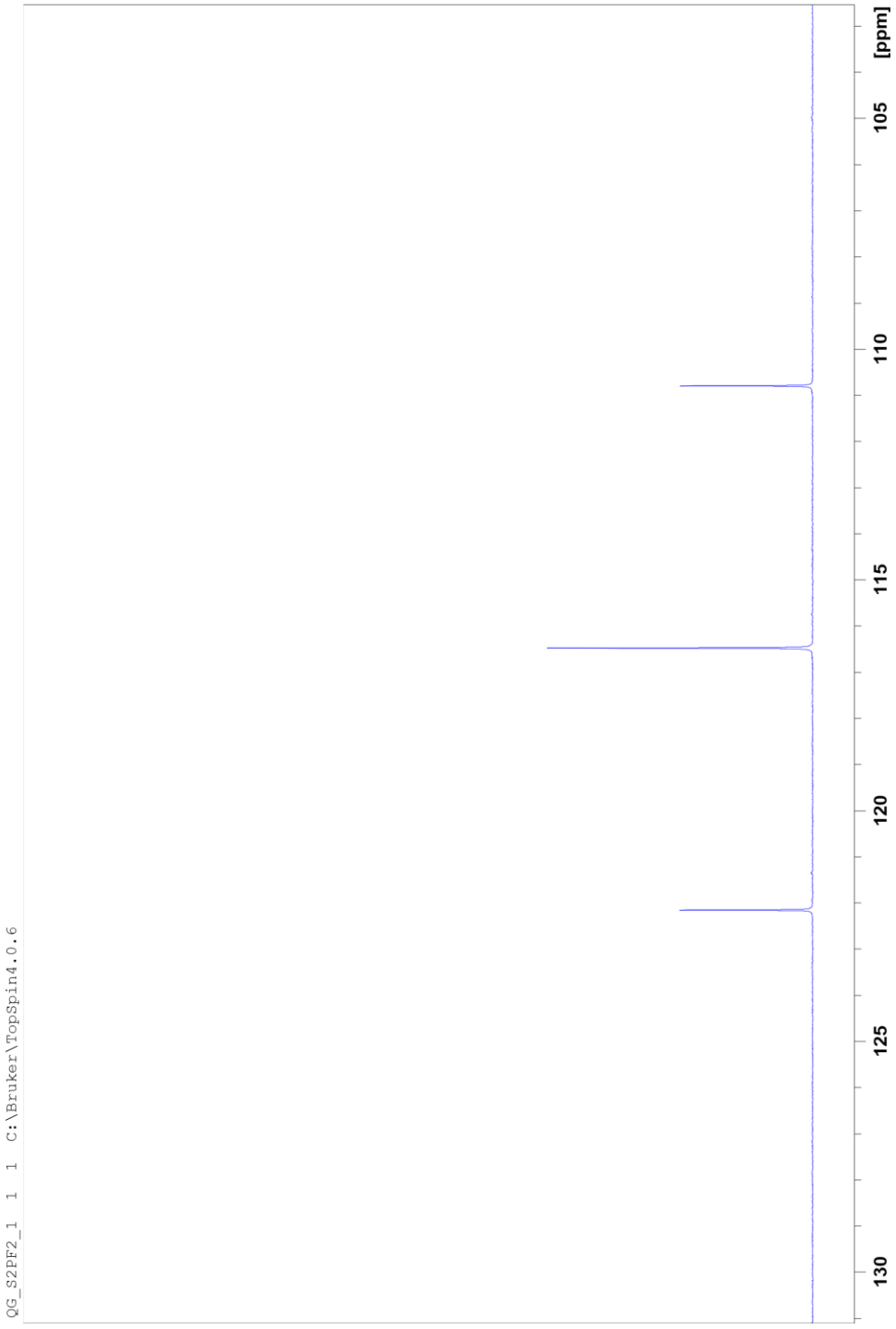

Figure S5.2: ^{19}F-NMR spectrum of 1

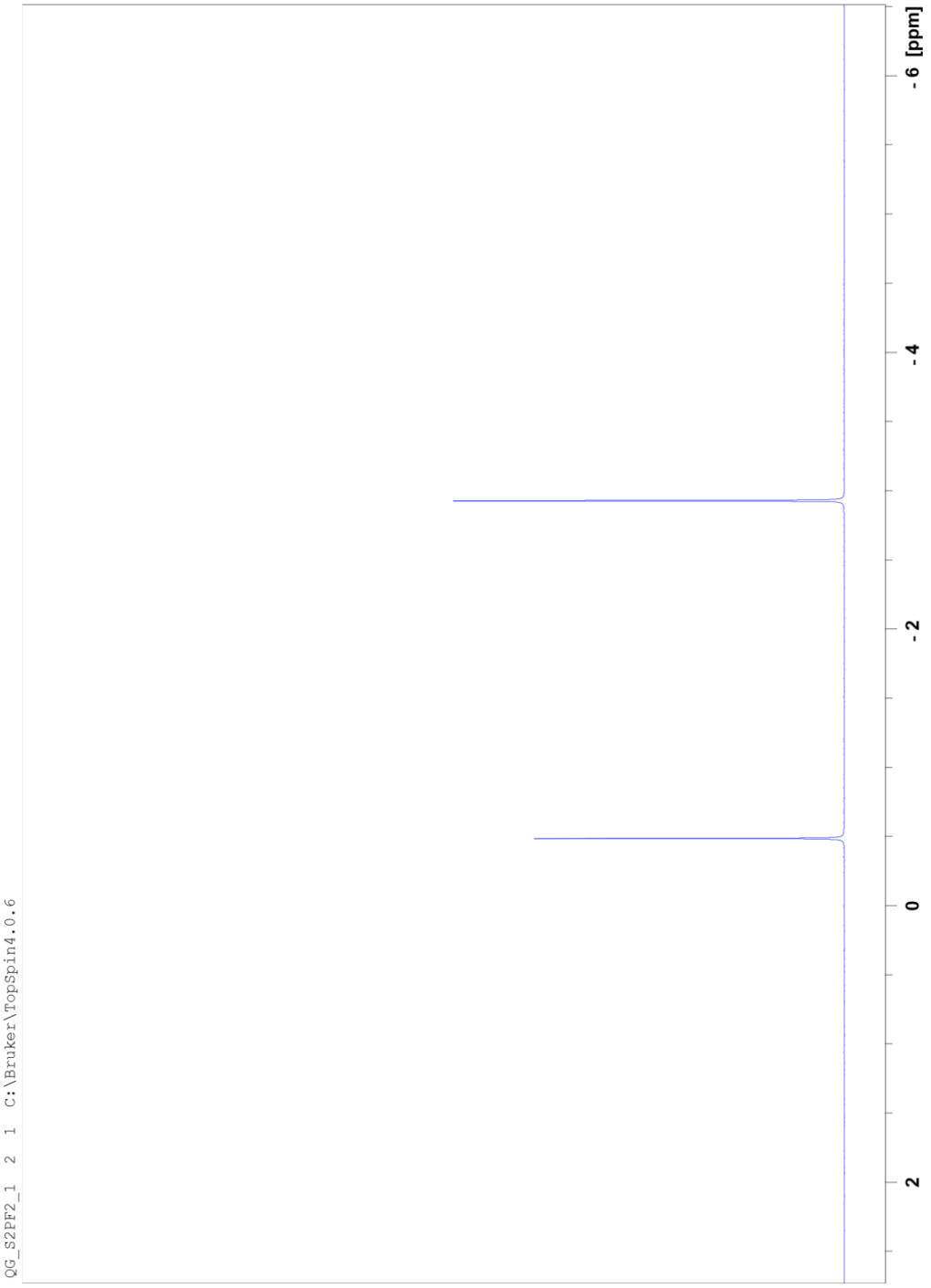

Figure S5.3: Hydride region of the 1H NMR spectrum of 2

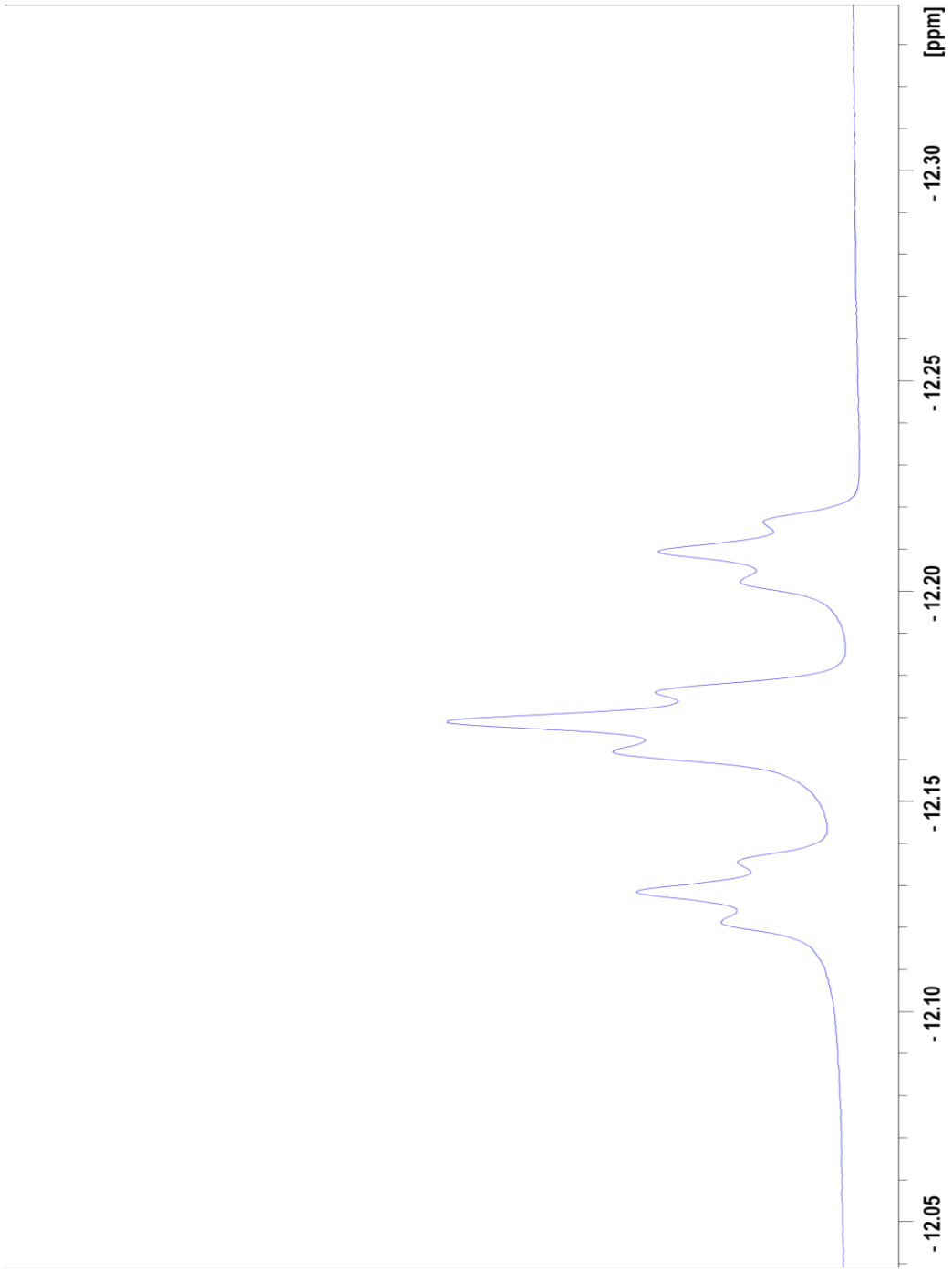

Figure S5.4: ^{31}P NMR spectrum of 2

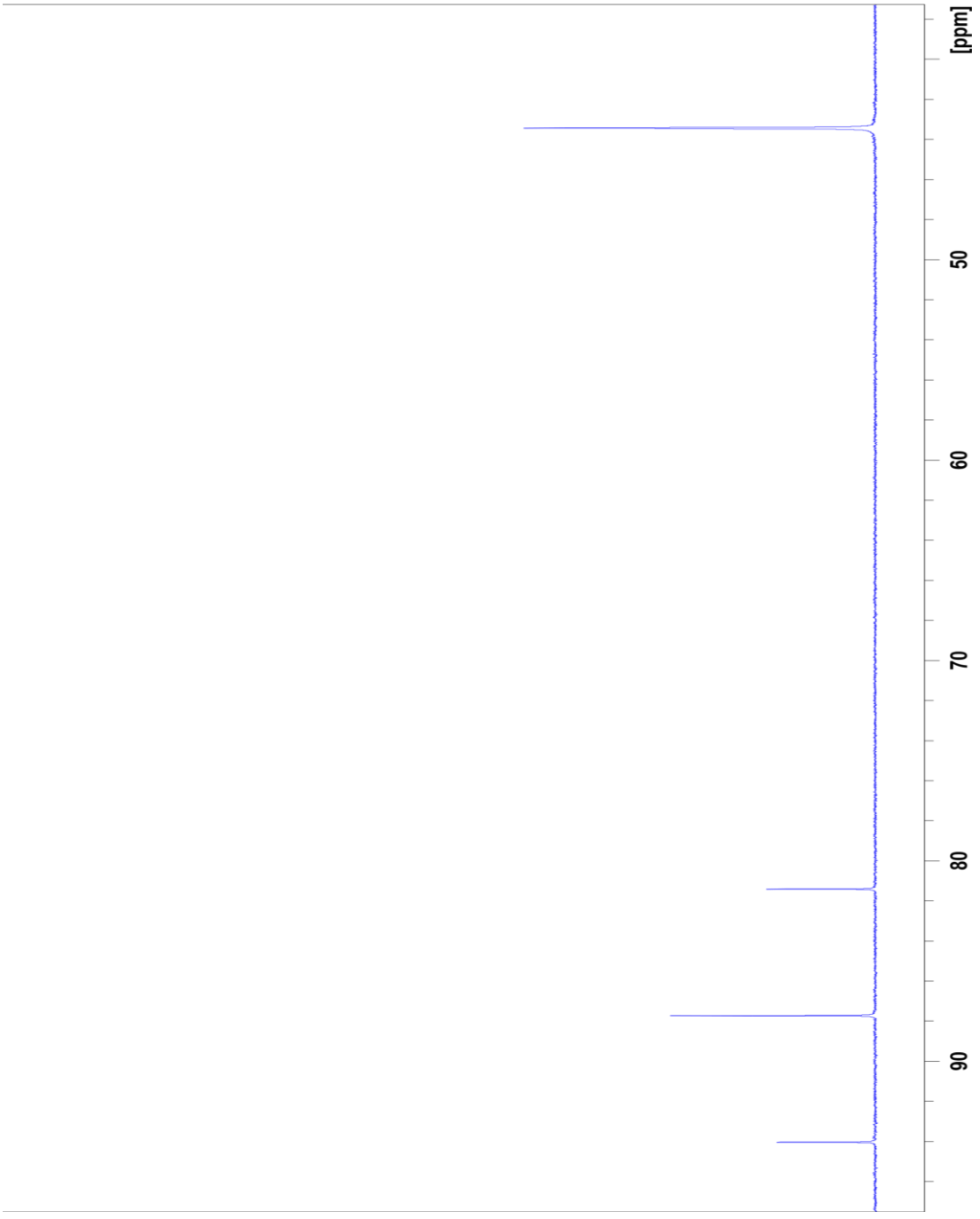

Figure S5.5: ^{19}F NMR spectrum of 2

Figure S5.6: ^{31}P NMR spectrum of 3

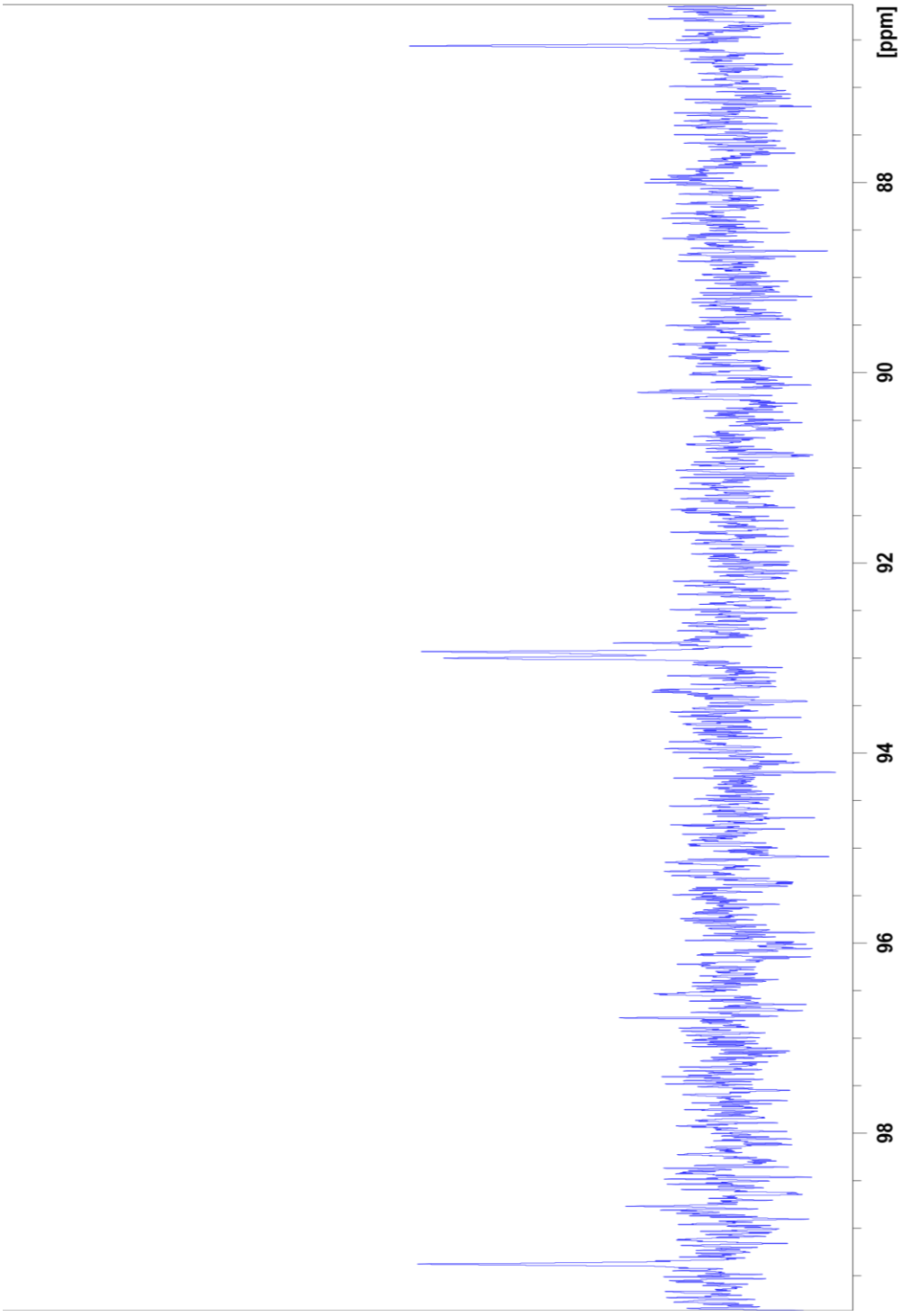

Figure S5.7: ^{19}F NMR spectrum of 3

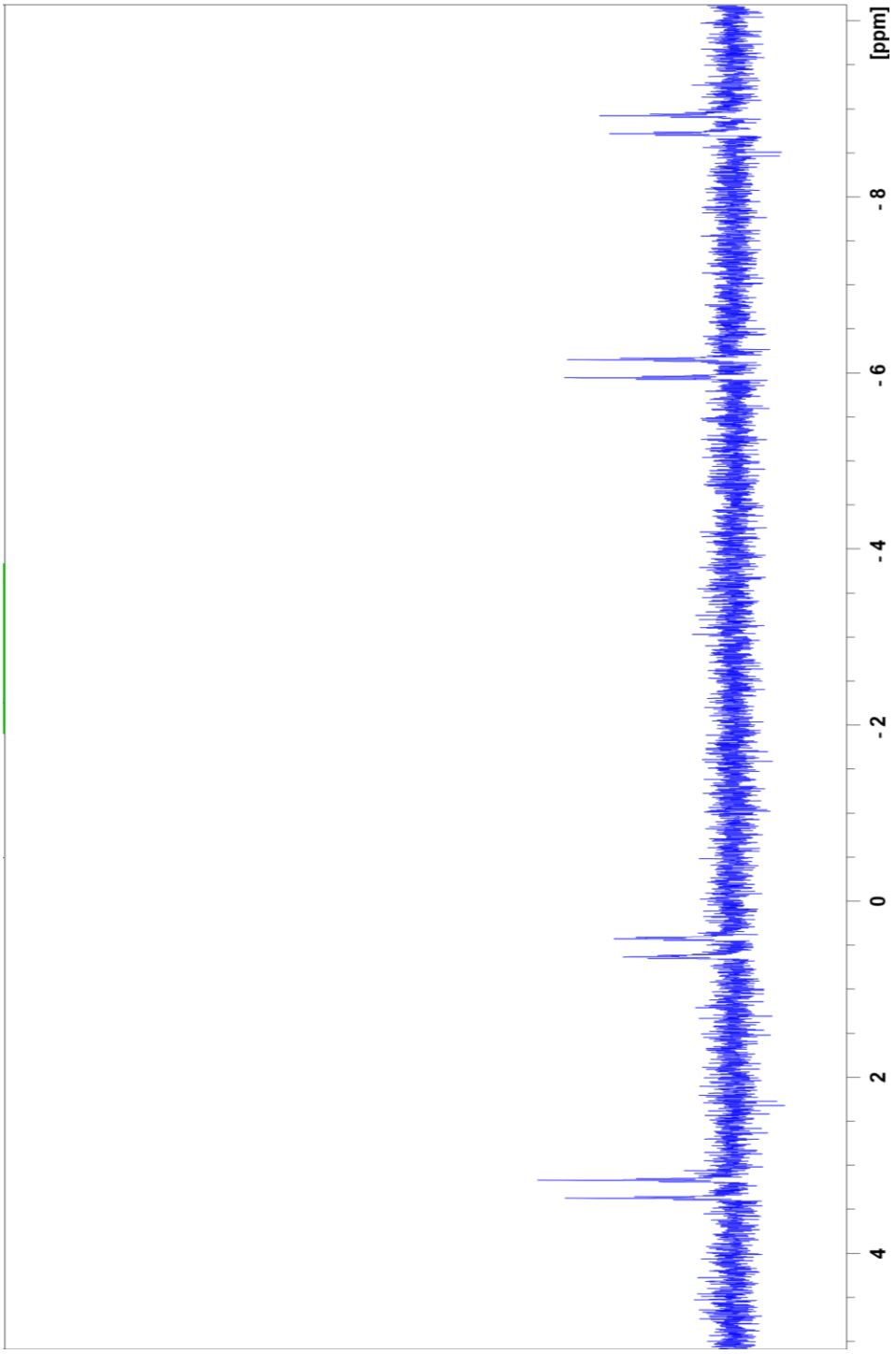

Figure S5.8: S_2PF_2 region in the ^{31}P NMR spectrum of 4

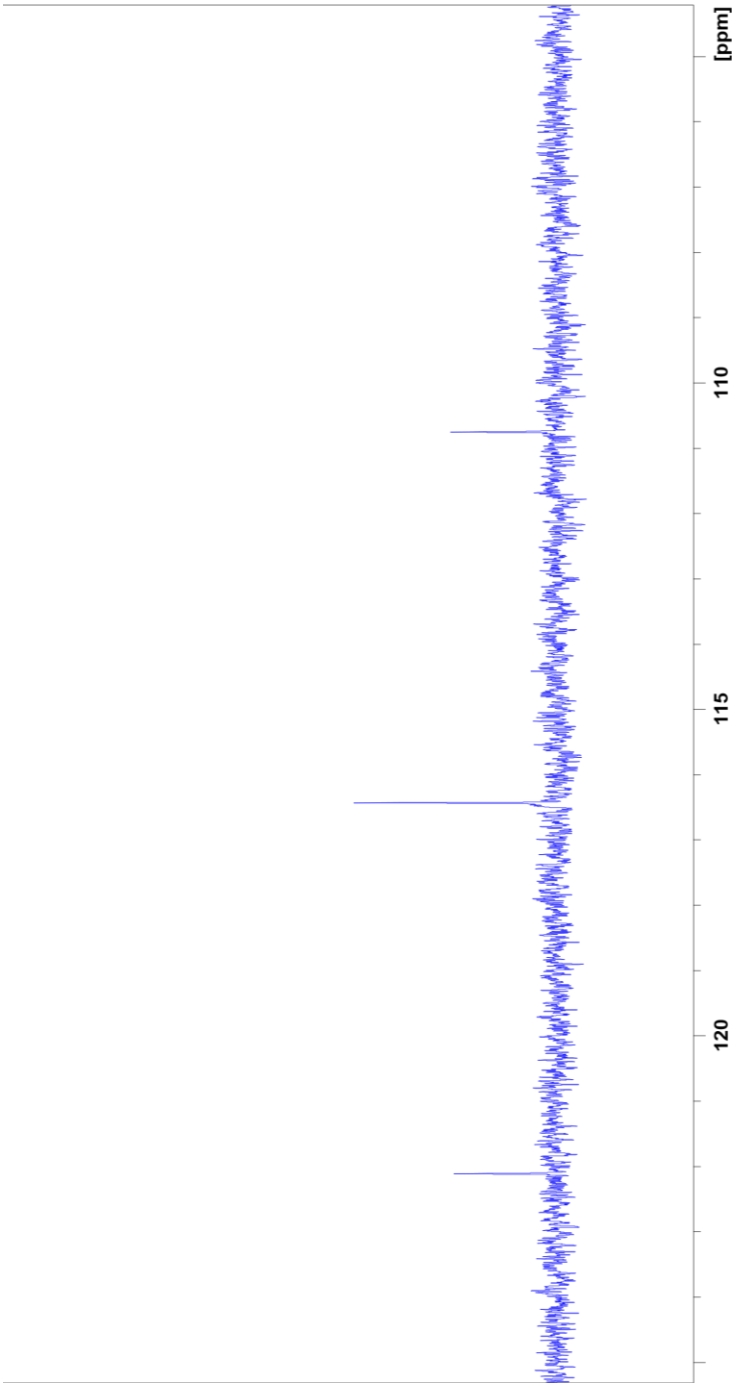

Figure S5.9: ^{31}P NMR spectrum of 5

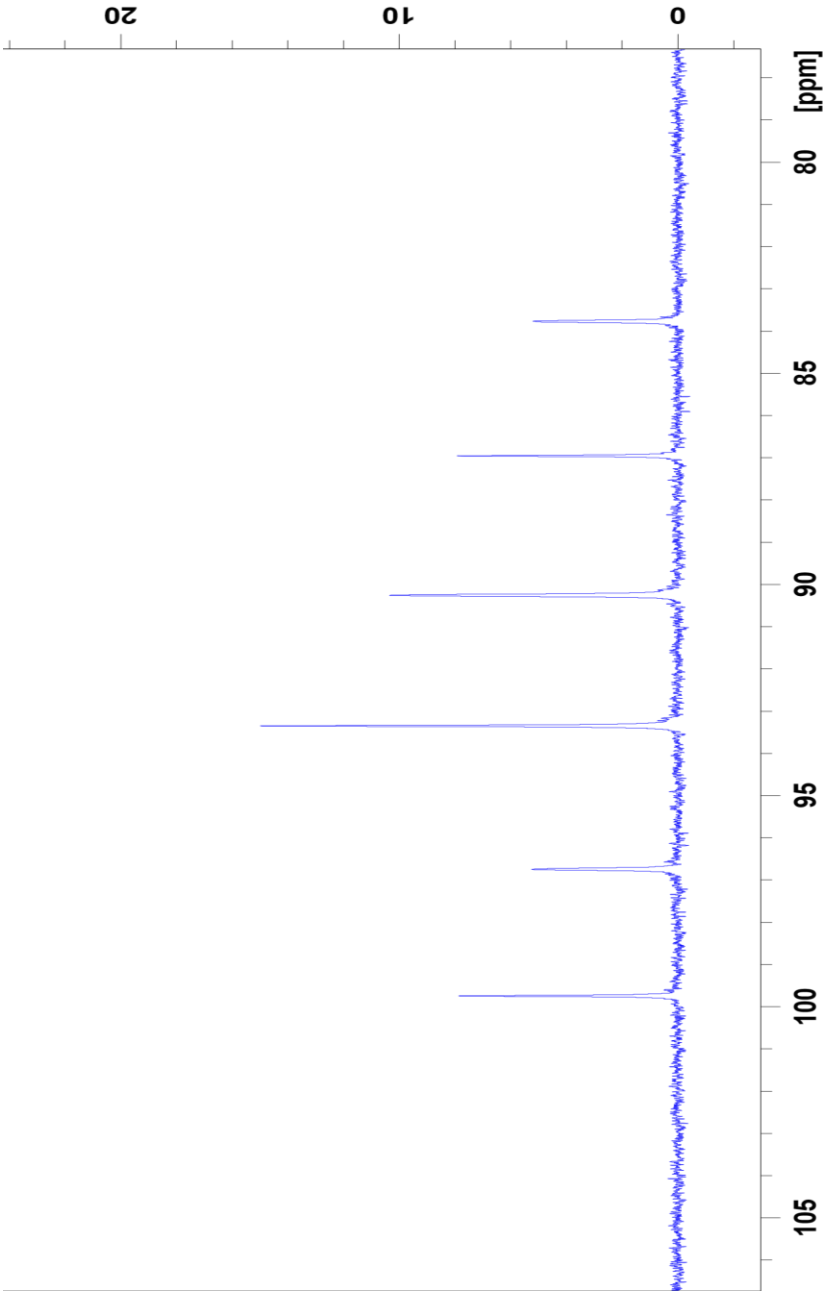

Figure S5.10: ^{19}F NMR spectrum of 5

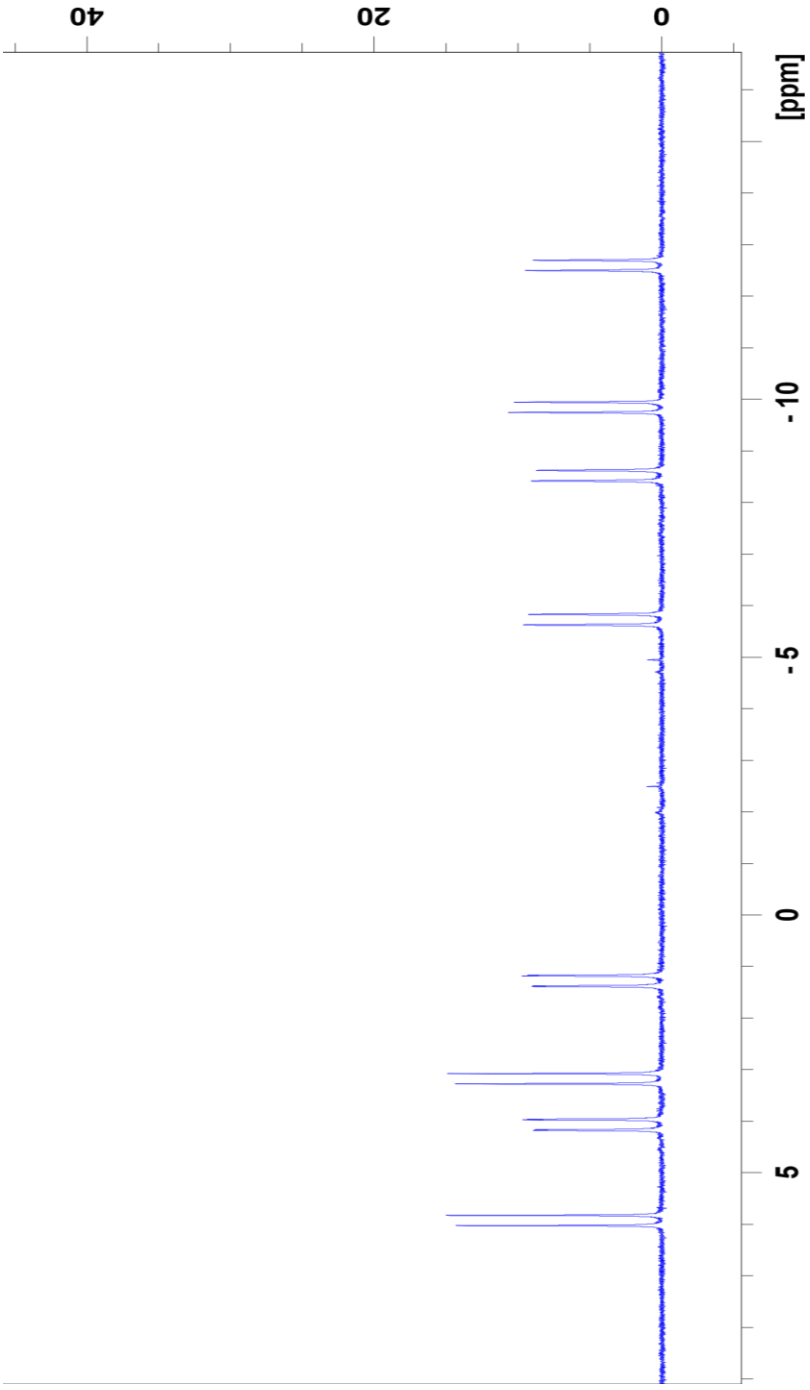

Figure S5.11: Ab-initio Calculated Geometries for $[NMe_4][F_2PS_2]$, $[N^nPr_4][F_2PS_2]$, and $Co(S_2PF_2)(CO)_3$.

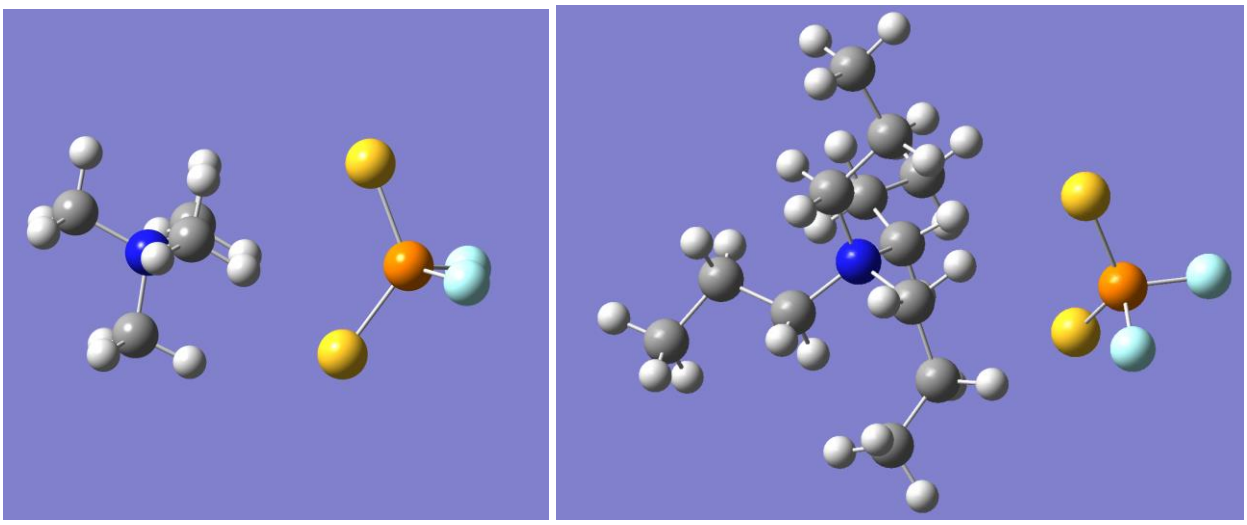

Two views of the hypothetical complex $Co(\eta^2\text{-}S_2PF_2)(CO)_3$. With a view down the Co-P axis on left and on right orthogonal to that axis.

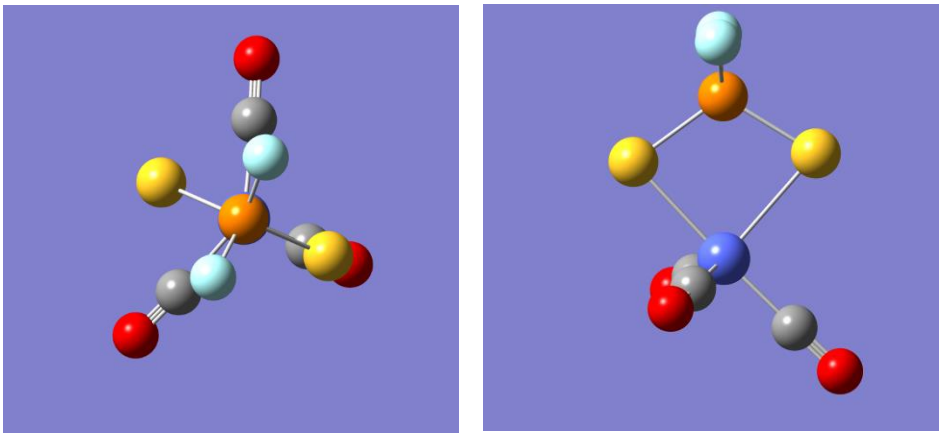

Density functional theory withB3LYP/cc-pvtz functionals/basis set used throughout. Metric data for these calculations are collected in Table 1.

APPENDIX E: Supplementary Data for Chapter 6

Table S6.1: Crystallographic information of the complexes

	$[N^nPr_4]_2[S_5P_2F_2]$	$[N^nPr_4]_2[Zn(S_5P_2F_2)_2]$	$[N^nPr_4]_4[Cu_8(S_3PF)_6]$	$[N^nPr_4]_4[Cd_3(S_5P_2F_2)_3(S_3PF)_2]$
Empirical Formula	$C_{24}H_{256}N_2F_2P_2S_5$	$C_{24}H_{54.36}F_4N_2P_4S_{10}Zn$	$C_{49}H_{112}Cu_8F_6N_4OP_6S_{18}$	$C_{48}H_{100}Cd_3F_8N_4P_8S_{21}$
Formula Weight	632.94	956.90	2158.64 g/mol	2143.53 g/mol
Crystal System	Monoclinic	Monoclinic	Triclinic	Triclinic
Space Group	$P2_1/n$	$P2_1$	P-1	P-1
a(Å)	18.217(5)	9.9122(11)	13.449(15)	13.880(4)
b(Å)	9.349(2)	13.7615(15)	13.683(16)	17.615(5)
c(Å)	22.237(6)	17.2710(19)	15.231(17)	21.875(7)
α(°)	90	90	67.731(14)	77.419(4)
β(°)	112.789(2)	92.851(2)	69.232(14)	78.528(4)
γ(°)	90	90	62.362(14)	68.821(4)
Volume($Å^3$)	3491.6(15)	2353.0(4)	2243.4	4825.0(3)
Density(g/cm^3)	1.204	1.351	1.598	1.475
Z	4	2	2	2
T(K)	571(2)	571(2)	571(2)	571(2)
Reflections collected	20817	26780	18551	18237
Independent reflections	3852	10303	6390	5319
Rint	0.0403	0.0360	0.0406	0.0438
Goodness-of-fit	1.009	0.988	1.081	1.108
R1	0.0350	0.0453	0.0345	0.0503
wR2	0.0464	0.1046	0.0890	0.1383
CCSD Number	2161074	2161076	2161075	2161077

Table S6.2: Comparison of bond lengths and angles of $[N^nPr_4]_2[S_5P_2F_2]$ and $[N^nPr_4]_2[S_5P_2(CN)_2]$

$[N^nPr_4]_2[S_5P_2F_2]$		$[N^nPr_4]_2[S_5P_2(CN)_2]$	
Bonds	Å	Bonds	Å
P-S (bridging)	2.1225(12)	P-S (bridging)	2.128(2)
	2.1078(11)		2.114(2)
P-S (terminal)	1.9513(13)	P-S (terminal)	1.937(2)
	1.9237(13)		1.954(2)
	1.9206(14)		1.946(3)
	1.9431(13)		1.943(2)

Angles	°	Angles	°
P-S-P	111.87(5)	P-S-P	110.5(1)
$S_{terminal}$-P-$S_{terminal}$	120.52(6)	$S_{terminal}$-P-$S_{terminal}$	122.9(1)
	121.18(6)		122.3(1)

Table S6.3: Selected average bond lengths, angles and chelate ring size of the $S_5P_2F_2$ anion in $[N^nPr_4]_2[S_5P_2F_2]$, $[N^nPr_4]_2[Zn(S_5P_2F_2)_2]$ and $[N^nPr_4]_4[Cd_3(S_5P_2F_2)_3(S_3PF)_2]$

$[N^nPr_4]_2[S_5P_2F_2]$		$[N^nPr_4]_2[Zn(S_5P_2F_2)_2]$		$[N^nPr_4]_4[Cd_3(S_5P_2F_2)_3(S_3PF)_2]$	
Bonds	Å	Bonds	Å	Bonds	Å
		Zn-S	2.330(2)	Cd-S	2.575(5)
P-F	1.578(2)	P-F	1.566(5)	P-F	1.578(8)
P-S (bridging)	2.1151(12)	P-S (bridging)	2.095(3)	P-S (bridging)	2.098(7)
P-S (terminal)	1.9342(13)	P-S (terminal)	1.972(3)	P-S(terminal)	1.955(7)
		P-S (coordinated)	1.909(4)	P-S (coordinated)	1.913(7)
Angles	°	Angles	°	Angles	°
		S-Zn-S	113.54(9)	S-Cd-S	102.12(18)
P-S-P	111.87(5)	P-S-P	110.70(12)	P-S-P	110.7(3)
		S(bridging)-P-S(coordinated)	113.42(13)	S(bridging)-P-S(coordinated)	114.70(5)
		Area	$Å^2$	Area	$Å^2$
		Chelate ring	11.611	Chelate ring	12.435

Table S6.4: Comparison of IR frequencies of $S_5P_2F_2$ and S_3PF of the complexes

	$[N^nPr_4]_2[Zn(S_5P_2F_2)_2]$	**$[N^nPr_4]_4[Cd_3(S_5P_2F_2)_3(S_3PF)_2]$**	**$[N^nPr_4]_4[Cu_8(S_3PF)_6]$**
$S_5P_2F_2$	532.93 622.08 695.35 789.79	532.63 627.61 697.15 789.19	N/A
S_3PF	N/A	562.0 597.27 698.15 756.12	552.76 594.82 698.36 755.79

Figure S6.1: Unit cell contents of $[N^nPr_4]_4[Cu_8(S_3PF)_6]$

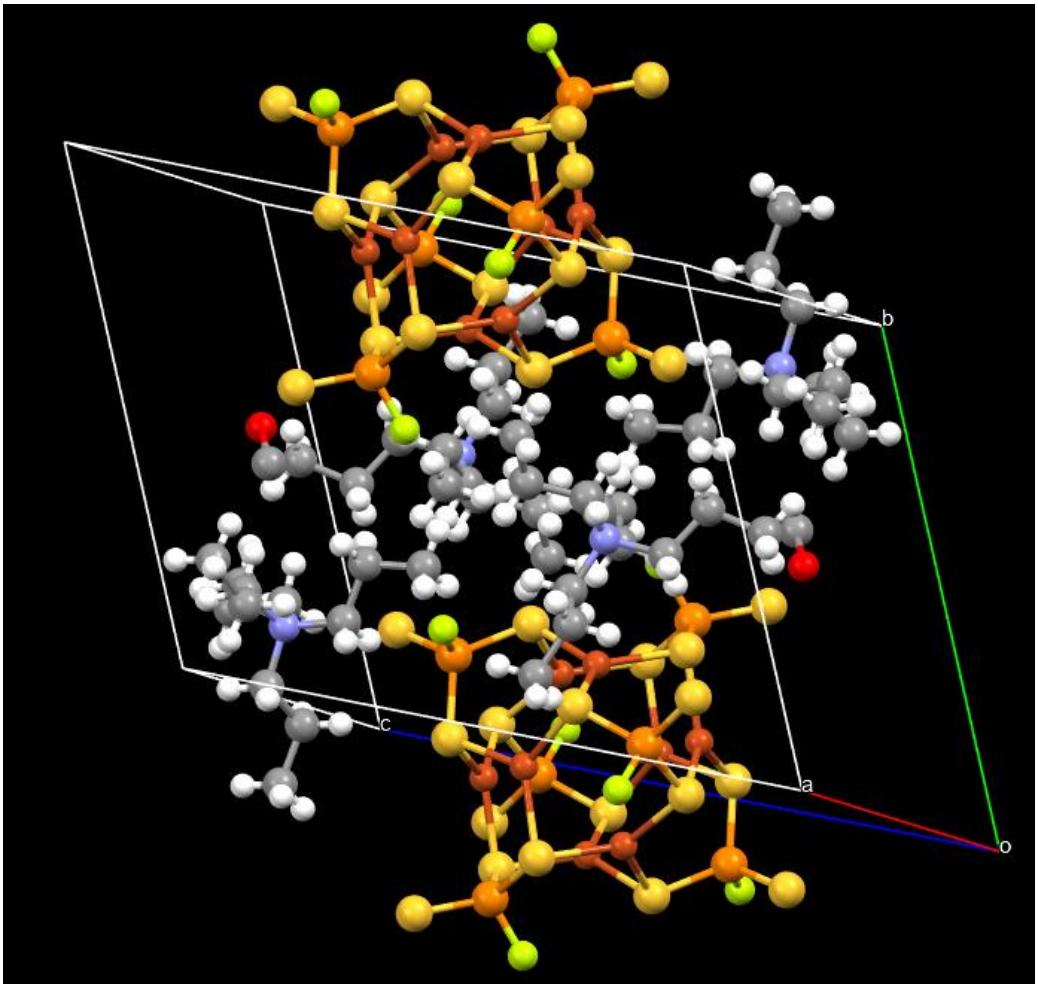

Figure S6.2: ^{31}P-NMR spectrum of $[N^nPr_4]_2[S_5P_2F_2]$

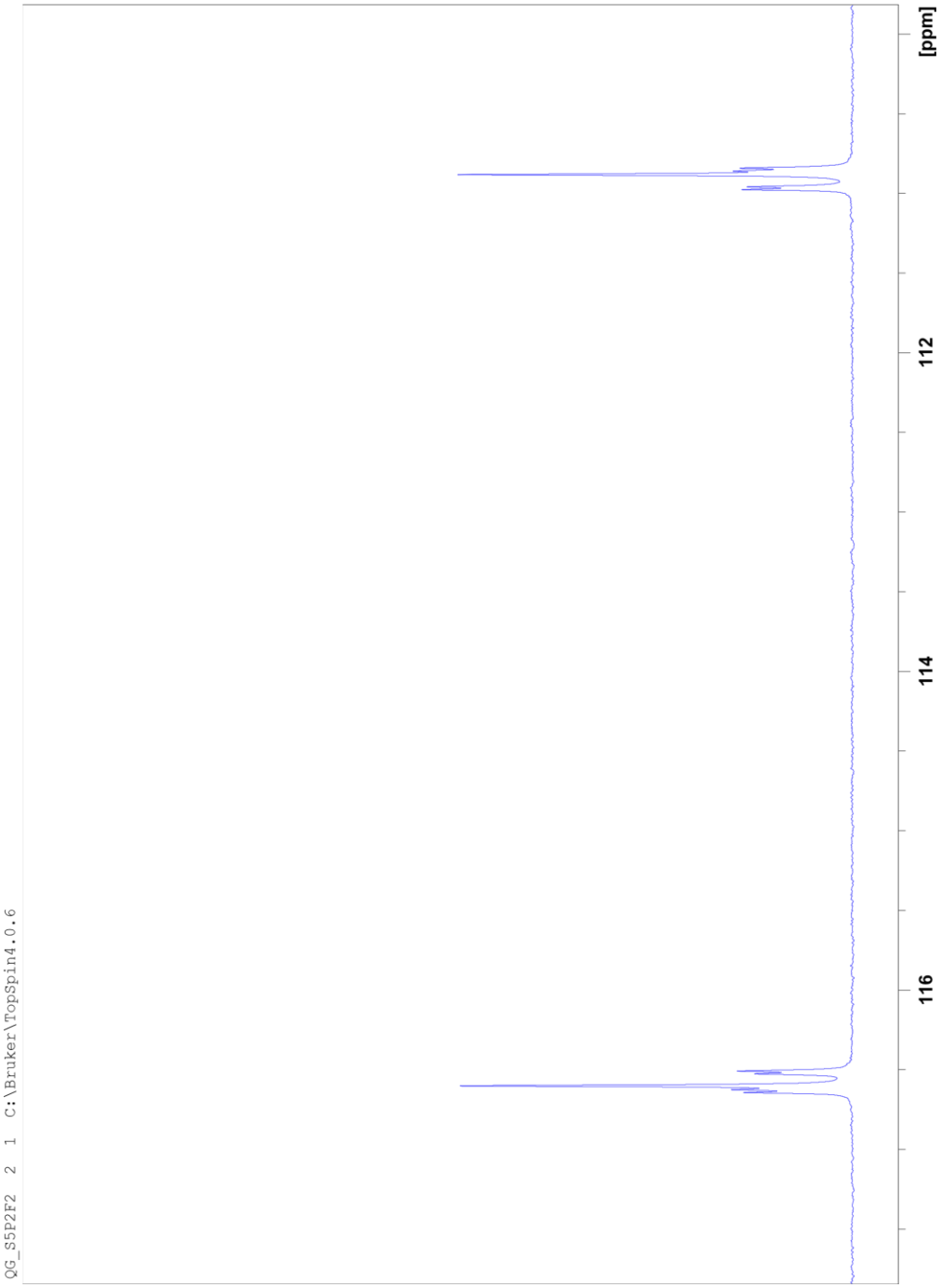

Figure S6.3: ^{19}F-NMR spectrum of $[N^nPr_4]_2[S_5P_2F_2]$

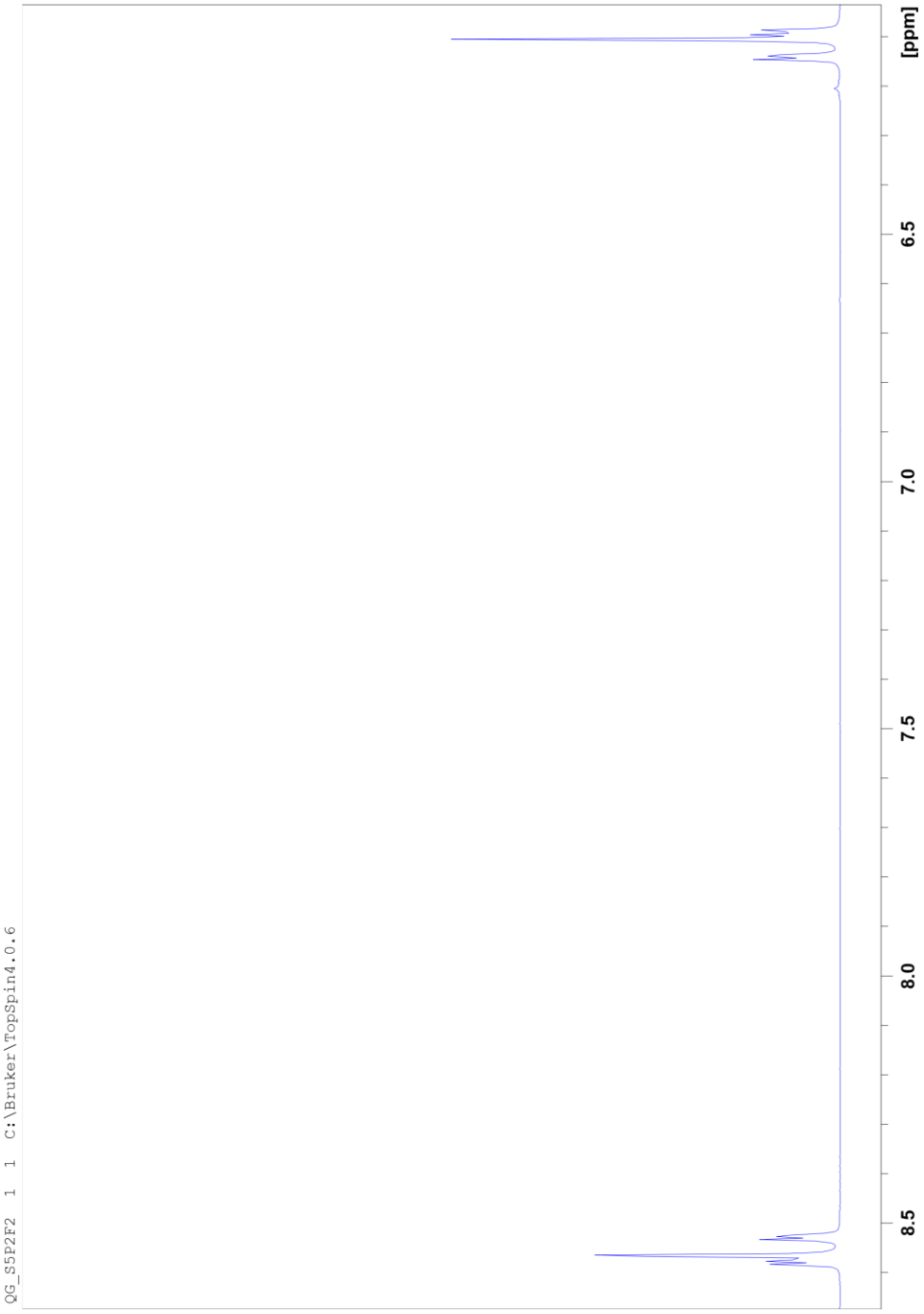

Figure S6.4: ^{31}P-NMR spectrum of $[N^nPr_4]_2[Zn(S_5P_2F_2)_2]$

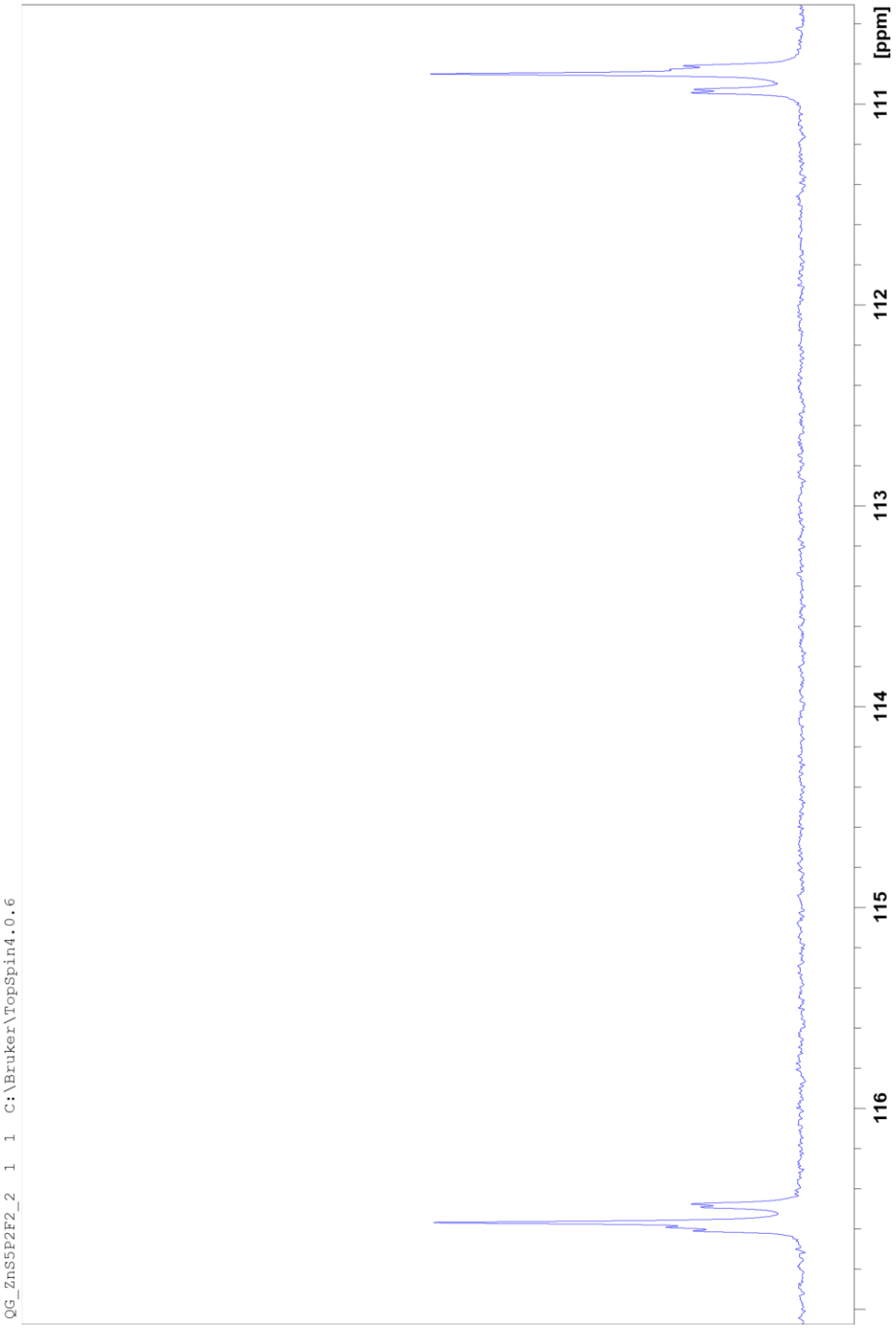

Figure S6.5: ^{19}F-NMR spectrum of $[N^nPr_4]_2[Zn(S_5P_2F_2)_2]$

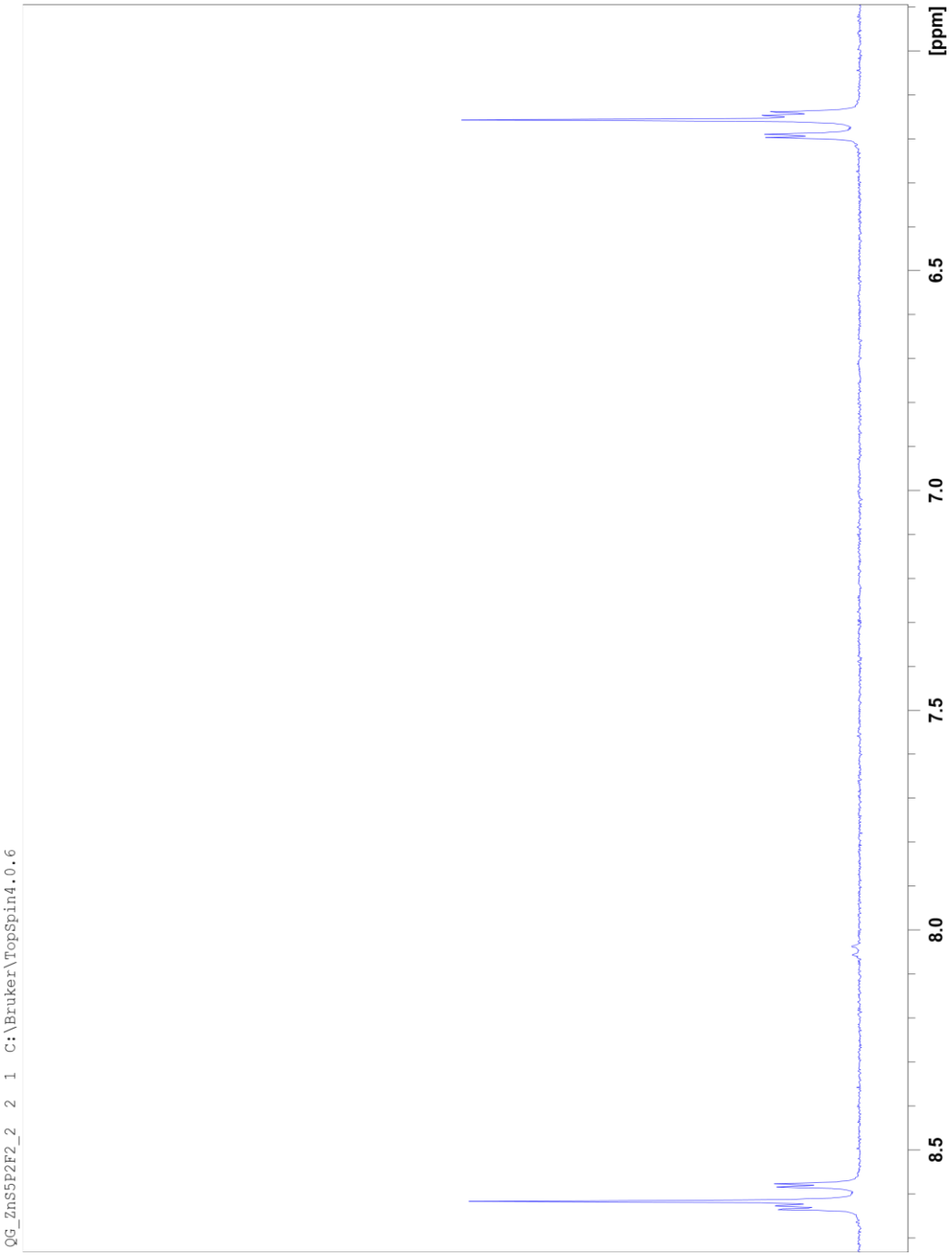

Figure S6.6: ^{31}P-NMR spectrum of $[N^nPr_4]_4[Cd_3(S_5P_2F_2)_3(S_3PF)_2]$

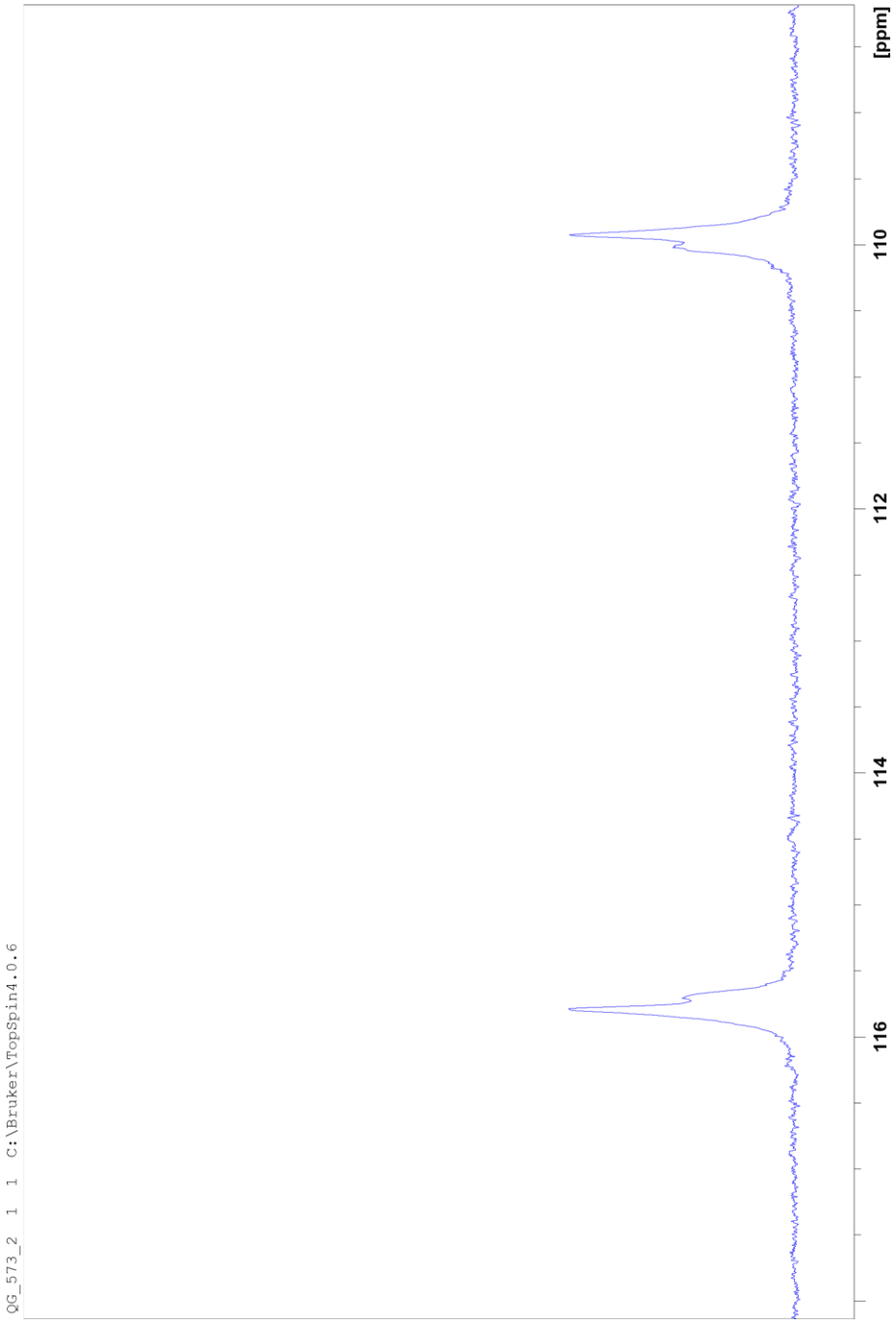

Figure S6.7: ^{19}F-NMR spectrum of $[N^nPr_4]_4[Cd_3(S_5P_2F_2)_3(S_3PF)_2]$

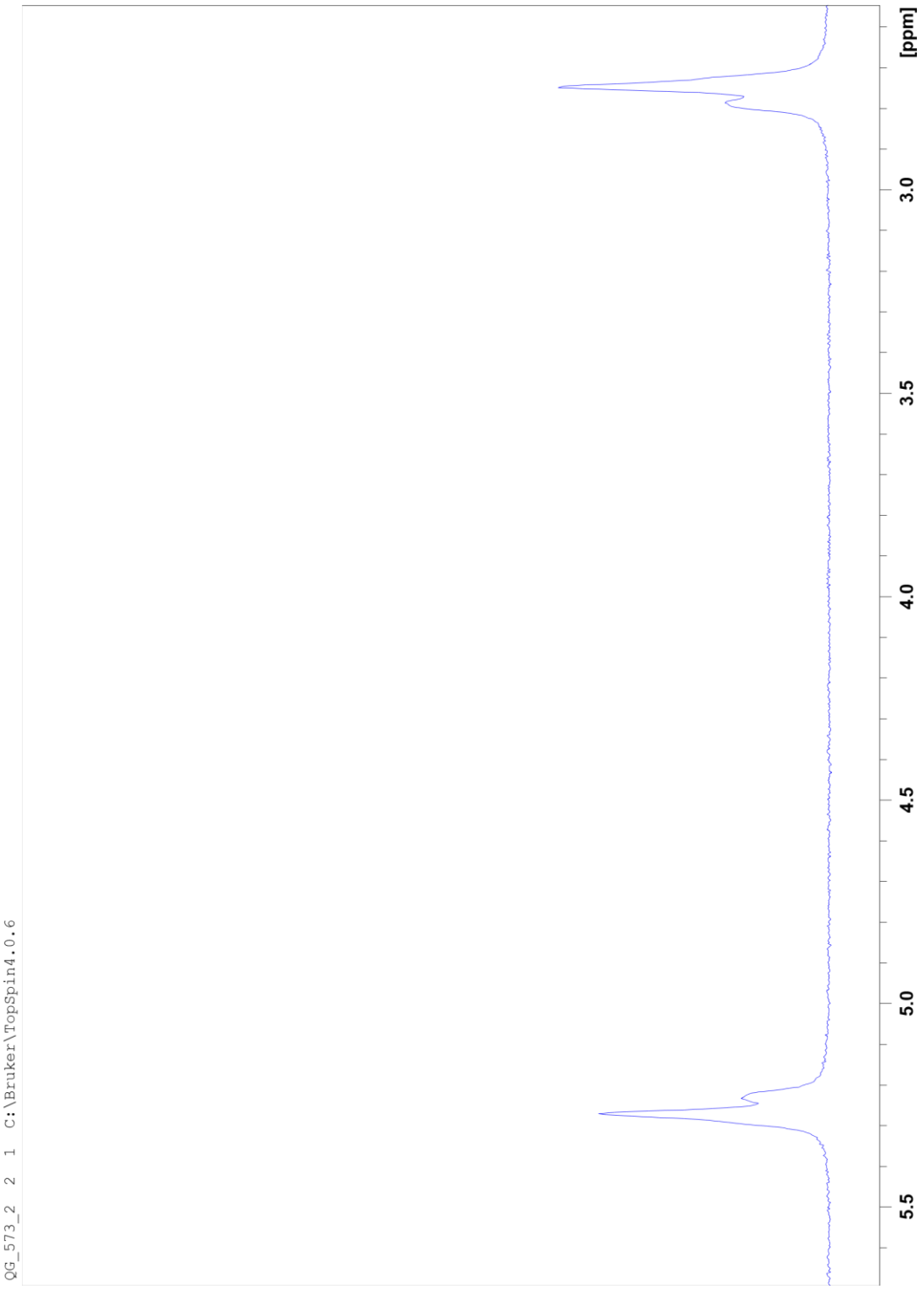

Figure S6.8: ^{31}P-NMR spectrum of $[N^nPr_4]_4[Cu_8(S_3PF)_6]$

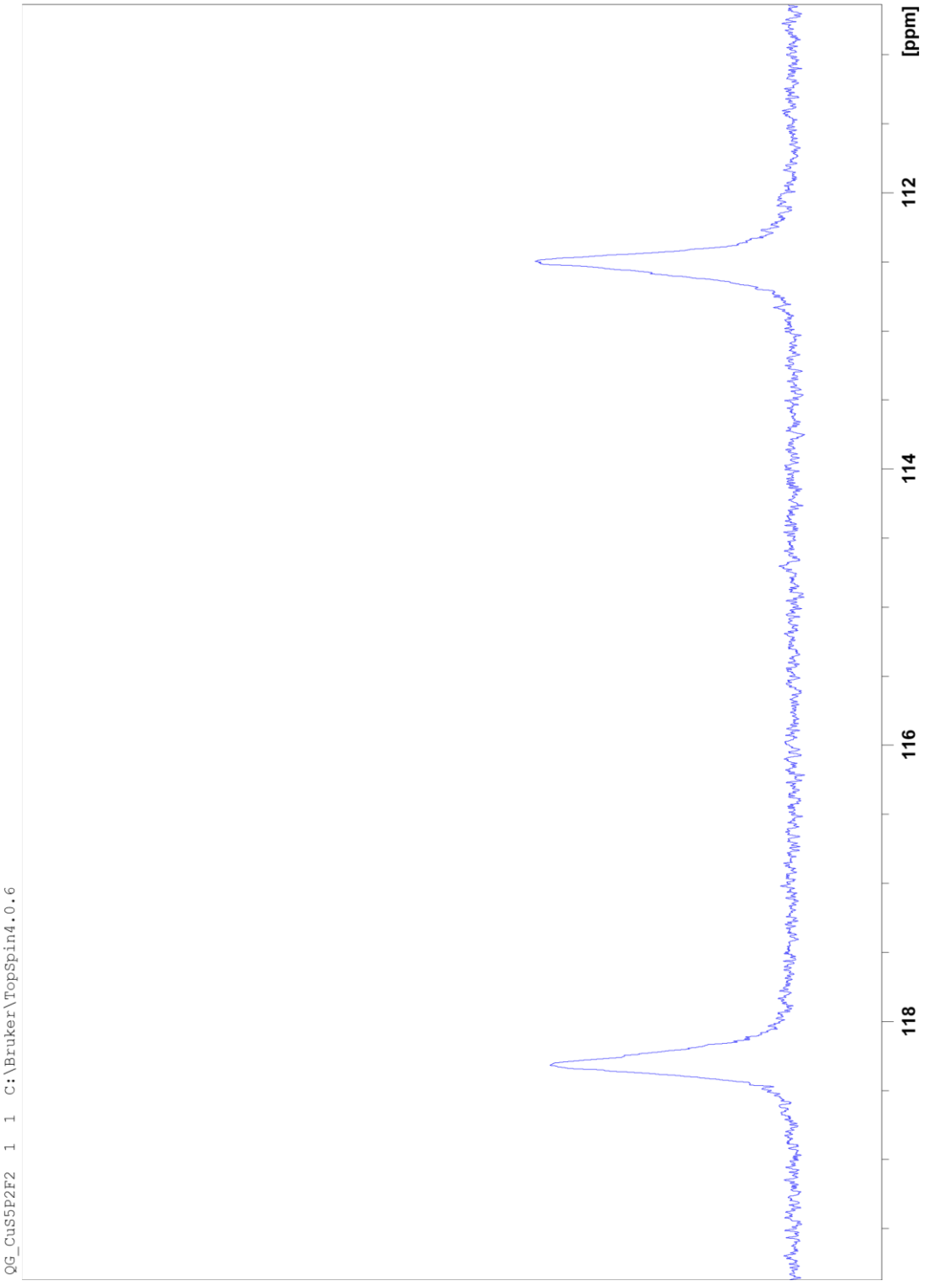

Figure S6.9: ^{19}F-NMR spectrum of $[N^nPr_4]_4[Cu_8(S_3PF)_6]$

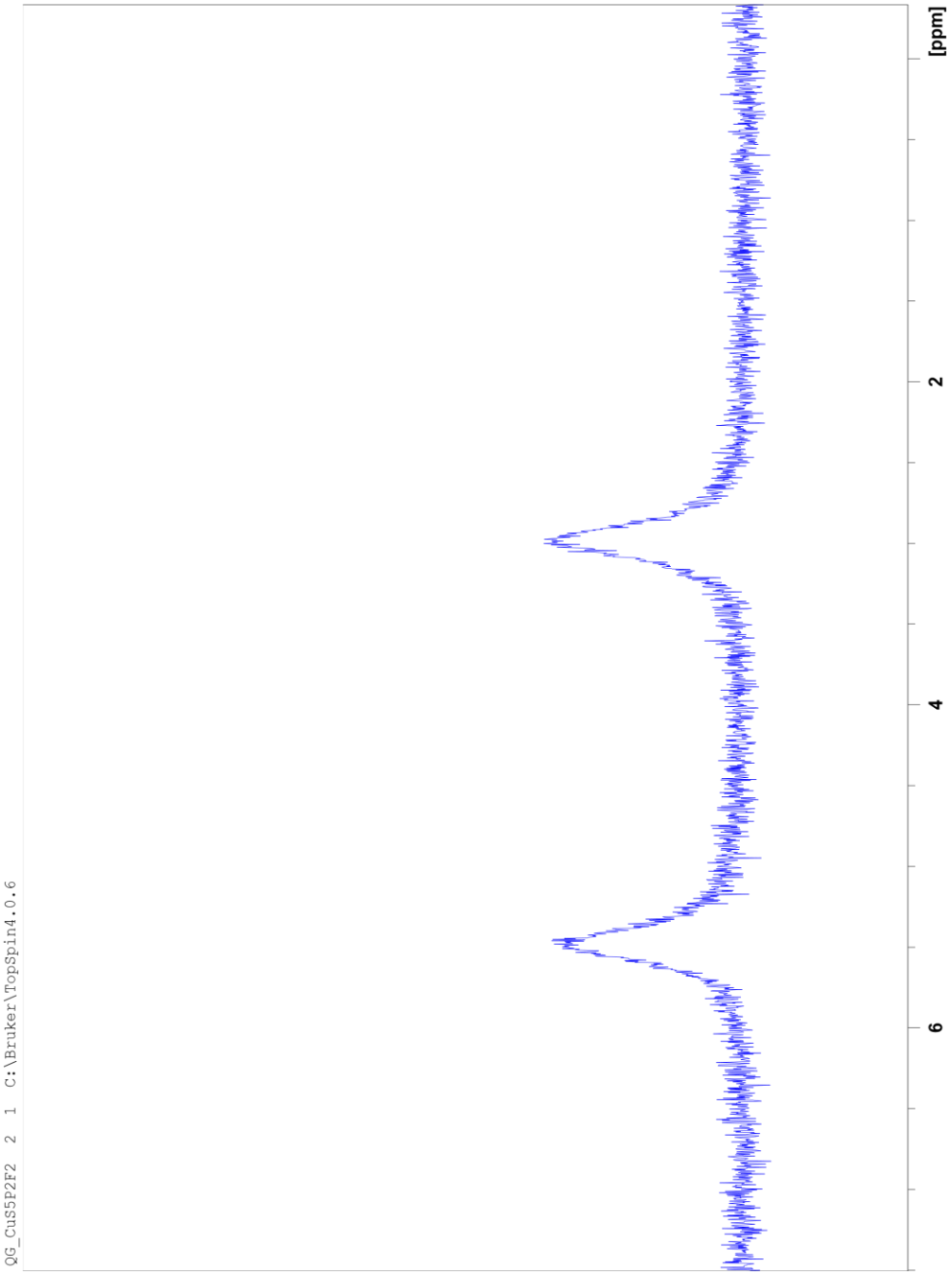

Figure S6.10: Geometric parameters of the Cu_8 core of $[Cu_8(S_3PF)_6]^{4-}$

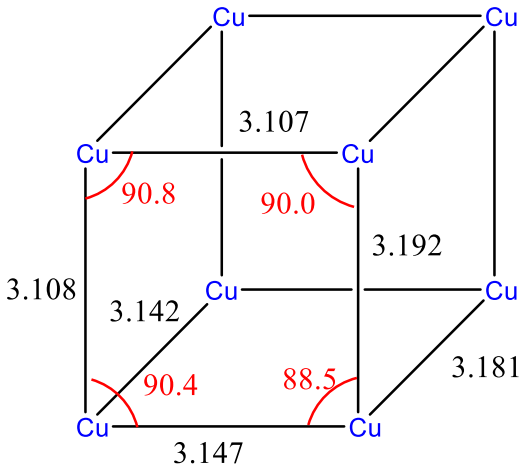

The geometry of the Cu_8 cube consisted in adjacent Cu-Cu separations averaging 3.142 Å and Cu-Cu-Cu angles varying between 88.7 ° and 91.5 °. Average diagonal distances of 4.449 Å within each face and 5.449 Å across the cube are observed. The volume of the cube was calculated to be 30.79 $Å^3$, in good agreement with other cubic cores in Cu_8S_{12} clusters reported previously. The Cu-S bond lengths averaged 2.244(3) Å, consistent with other reports of Cu(I)-S bonds in octanuclear complexes. S-Cu-S angles average 119.78(8) ° while Cu-S-Cu angles average 89.20(4) °. Coordination of each sulfur atom to two copper atoms results in large $S_{chelating}$-P-$S_{chelating}$ and low F-P-$S_{chelating}$ angles: these values respectively average to 116.38(10) ° and 100.96(17) °. Both values differ significantly from those found in the cadmium complex which average 114.2(3) ° and 104.2(3) °. The geometry of the terminal fluorine is much less affected: average P-F bonds respectively of and 1.592(4) Å as well as F-P-S angles of 109.19(13) ° were determined: these values average 1.596(11) Å and. The P-F bond lengths remain similar between both complexes with average lengths of 1.592(4) Å in $[Cu_8(S_3PF)_6]^{4-}$ and 1.597(11) Å in $[Cd_3(S_5P_2F_2)_3(S_3PF)_2]^{4-}$.

Figure S6.11: Isomers of $[Cu_8(S_3PF)_6]^{4-}$

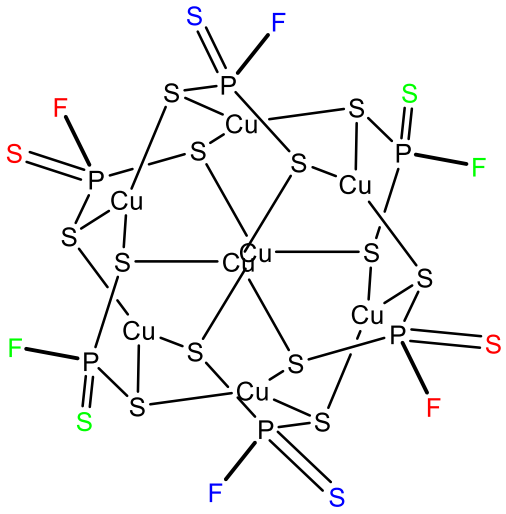

ttt

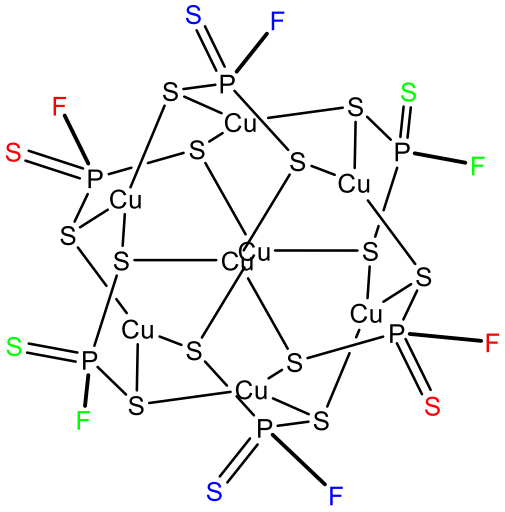

ccc

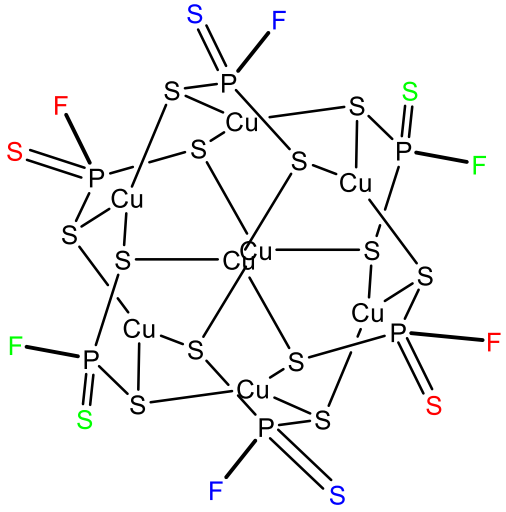

ttc

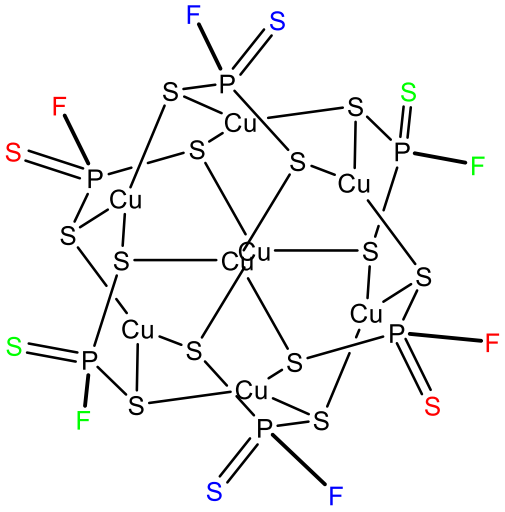

tcc

APPENDIX F: Supplementary Data for Chapter 7

Table S7.1: Crystallographic information of $[N^nPr_4]_2[Ni(S_3PF)_2]$, Ni(dpph)(S_3PF), Ni(dppe)(S_3PF) and [Ni(dpph)(S_2(SMe)PO)]

	$[N^nPr_4]_2[Ni(S_3PF)_2]$	Ni(dpph)(S_3PF)	Ni(dppe)(S_3PF)	[Ni(dpph)(S_2(SMe)PO)]
Empirical Formula	$C_{24}H_{56}F_2N_2NiP_2S_6$	$C_{30}H_{24}FNiP_3S_3$	$C_{26}H_{24}FNiP_3S_3$	$C_{31}H_{27}ONiP_3S_3$
Formula Weight	723.71	651.29	603.25	663.32
Crystal System	Triclinic	Monoclinic	Monoclinic	Monoclinic
Space Group	P-1	$P2_1/n$	$P2_1/n$	$P2_1/n$
a(Å)	9.5226(2)	9.5907(12)	12.047(14)	9.6300(16)
b(Å)	10.1047(2)	19.978(3)	19.02(2)	20.012(3)
c(Å)	10.6797(3)	15.5525(19)	12.139(14)	15.778(3)
α(°)	81.1970(10)	90	90	90
β(°)	66.7840(10)	92.003(2)	97.075(2)	91.082
γ(°)	78.9730(10)	90	90	90
Volume($Å^3$)	923.54(4)	2978.1(6)	2760.0(6)	3039.2(9)
Density(g/cm^3)	1.301	1.453	1.452	1.450
Z	2	4	4	4
T(K)	273(2)	571(2)	571(2)	571(2)
Reflections collected	14500	19621	14070	22237
Independent reflections	3639	3768	2926	5401
Rint	0.0691	0.0374	0.0776	0.1683
Goodness-of-fit	1.051	1.164	1.008	0.957
R1	0.0563	0.0619	0.0686	0.0569
wR2	0.1505	0.1322	0.1877	0.1387
CCSD Number				

Table S7.2: Crystallographic information of $Pd(PPh_3)_2(S_3PF)$, $Pt(PPh_3)_2(S_3PF)$ and $Pt(PPh_2Me)_2(S_3PF)$

	$Pd(PPh_3)_2(S_3PF)$	**$Pt(PPh_3)_2(S_3PF)$**	**$Pt(PPh_2Me)_2(S_3PF)$**
Empirical Formula	$C_{36}H_{30}FP_3PdS_3$	$C_{36}H_{30}FP_3PtS_3$	$C_{26}H_{26}FP_3PtS_3$
Formula Weight	777.09	865.78	741.65
Crystal System	Orthorhombic	Orthorhombic	Orthorhombic
Space Group	Pbca	Pbca	Pbca
a(Å)	17.046(4)	17.0272(16)	17.9523(12)
b(Å)	16.063(4)	16.0180(15)	16.6577(11)
c(Å)	25.288(6)	25.308(3)	38.327(3)
α(°)	90	90	90
β(°)	90	90	90
γ(°)	90	90	90
Volume($Å^3$)	6924.3(3)	6902.5(11)	11461.5(13)
Density(g/cm^3)	1.491	1.666	1.719
Z	8	8	16
T(K)	571(2)	571(2)	571(2)
Reflections collected	9102	27948	35869
Independent reflections	1478	3241	6783
Rint	0.0686	0.1036	0.0698
Goodness-of-fit	1.111	1.170	1.286
R1	0.0398	0.0471	0.0596
wR2	0.0887	0.1239	0.1198
CCSD Number			

Table S7.3: Comparison of structural features of Ni, Pd and Pt complexes of S_3PF

Ni(dppe)(S_3PF)		Ni(dpph)(S_3PF)		Pd(PPh_3)(S_3PF)		Pt(PPh_3)$_2$(S_3PF)		Pt(PPh_2Me)$_2$(S_3PF)	
Bonds	Å	Bonds	Å	Bonds	Å	Bonds	Å	Bonds	Å
Ni-P	2.157(3) 2.161(3)	Ni-P	2.1511(19) 2.1536(19)	Pd-P	2.299(4) 2.324(4)	Pt-P	2.266(4) 2.295(4)	Pt-P	2.280(4) 2.264(3) 2.272(4) 2.267(4)
Ni-S	2.211(3) 2.227(3)	Ni-S	2.207(2) 2.212(2)	Pd-S	2.346(3) 2.347(4)	Pt-S	2.359(4) 2.359(4)	Pt-S	2.384(4) 2.351(3) 2.358(4) 2.351(4)
P-S (terminal)	1.843(10) 1.900(5)	P-S (terminal)	1.812(7) 1.846(5)	P-S (terminal)	1.858(6)	P-S (terminal)	1.878(8)	P-S (terminal)	1.917(3) 1.98(3) 1.894(8) 1.78(5)
P-S (coordinated)	2.035(3) 2.021(4)	P-S (coordinated)	2.010(3) 2.015(3)	P-S (coordinated)	2.028(5) 2.006(5)	P-S (coordinated)	2.016(6) 2.038(5)	P-S (coordinated)	2.033(5) 2.042(5) 2.037(6) 2.033(6)
P-F	1.626(10) 1.658(16)	P-F	1.676(7) 1.789(15)	P-F	1.696(8)	P-F	1.641(10)	P-F	1.593(12) 1.57(4) 1.644(13) 1.68(2)

Angles	°	Angles	°	Angles	°	Angles	°	Angles	°
S-Ni-S	88.43(9)	S-Ni-S	87.60(8)	S-Pd-S	82.48(12)	S-Pt-S	82.56(14)	S-Pt-S	82.56(13) 82.84(14)
P-Ni-P	87.31(8)	P-Ni-P	88.81(7)	P-Pd-P	99.70(15)	P-Pt-P	99.90(13)	P-Pt-P	96.09(13) 95.41(14)
S-P-S	99.50(12)	S-P-S	98.94(11)	S-P-S	100.2(2)	S-P-S	100.3(2)	S-P-S	100.1(2) 99.9(2)
F-P-S	107.3(6) 107.5(10)	F-P-S	106.5(3) 96.9(8)	F-P-S	102.7(4)	F-P-S	107.5(4)	F-P-S	109.0(2) 107.0(7) 103.0(2) 104.9(7)

Table S7.4: Crystallographic information of [(cymene)Ru(S_3PF)]$_2$

	[(cymene)Ru(S_3PF)]$_2$
Empirical Formula	$C_{20}H_{28}F_2P_2Ru_2S_6$
Formula Weight	762.86
Crystal System	Triclinic
Space Group	P-1
a(Å)	8.425(4)
b(Å)	8.772(4)
c(Å)	10.704(5)(5)
α(°)	88.994(6)
β(°)	72.958(5)
γ(°)	67.499(5)
Volume(Å^3)	694.7(5)
Density(g/cm^3)	1.823
Z	1
T(K)	571(2)
Reflections collected	6868
Independent reflections	2557
Rint	0.0315
Goodness-of-fit	1.054
R1	0.0315
wR2	0.0665
CCSD Number	

Figure S7.1: ^{31}P-NMR spectrum of $[N^nPr_4)_2[Ni(S_3PF)_2]$

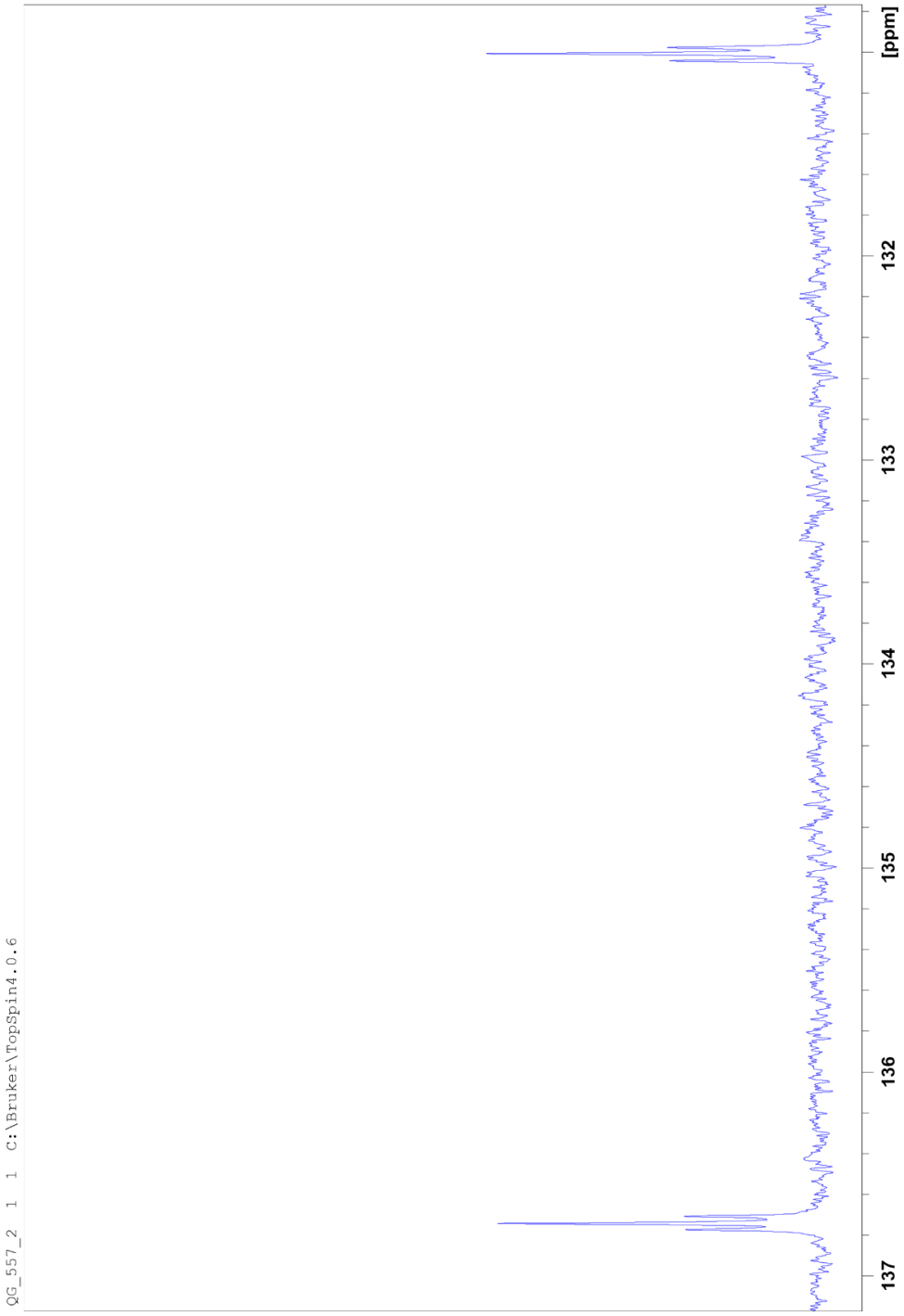

Figure S7.2: ^{19}F-NMR spectrum of $[N^nPr_4)_2[Ni(S_3PF)_2]$

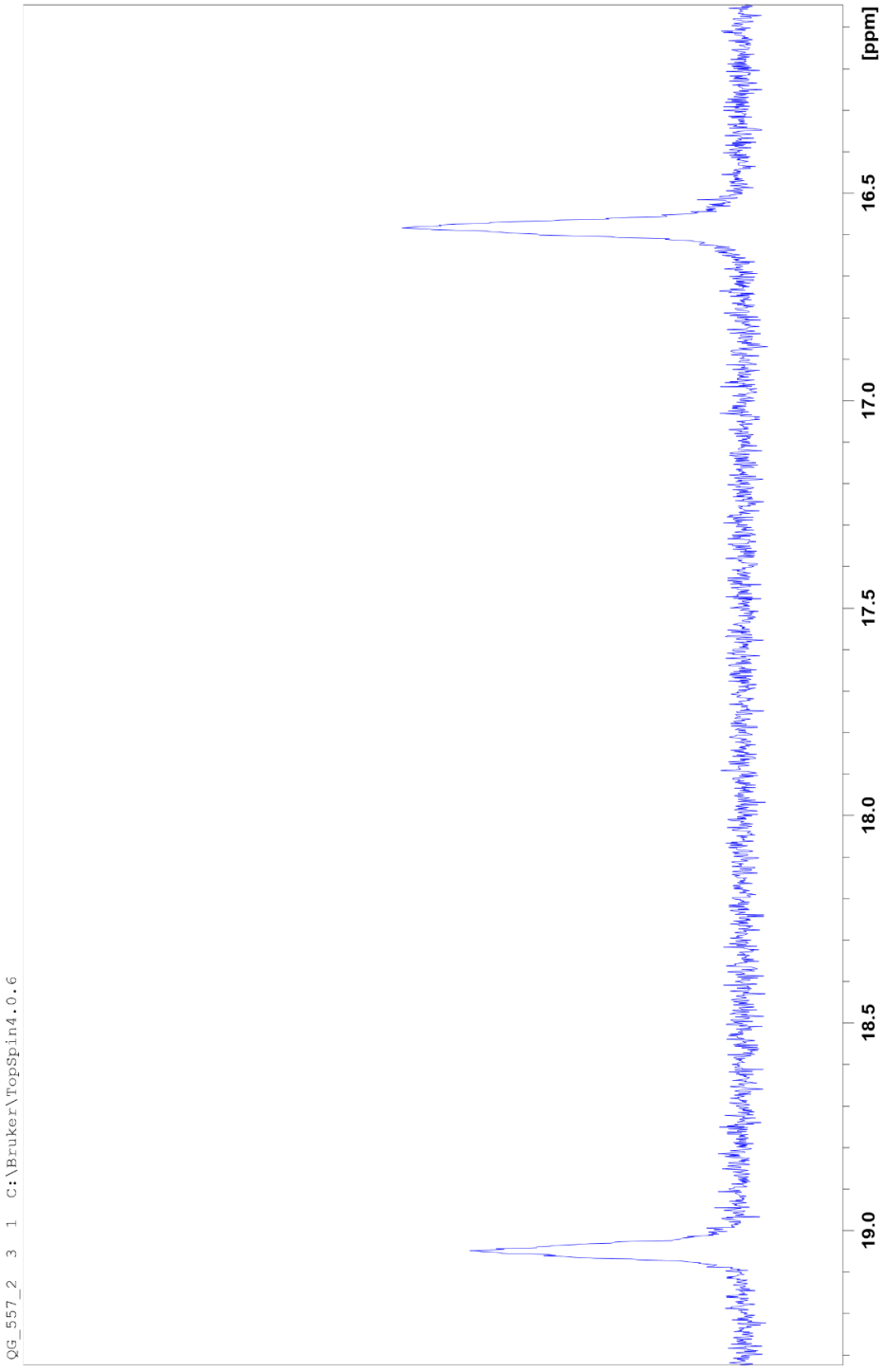

Figure S7.3: ^{31}P-NMR spectrum of Ni(dppe)(S_3PF)

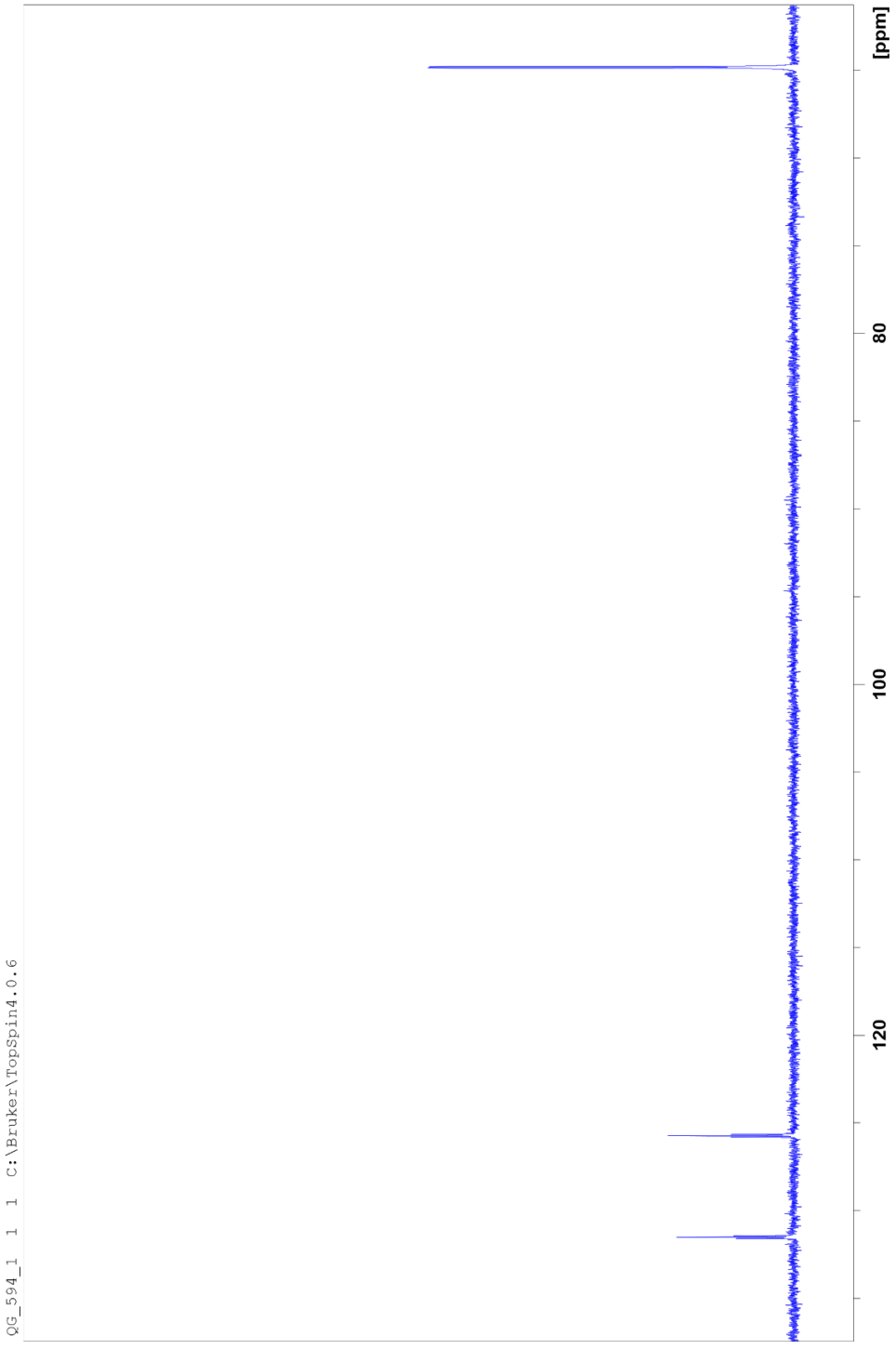

Figure S7.4: ^{19}F-NMR spectrum of Ni(dppe)(S_3PF)

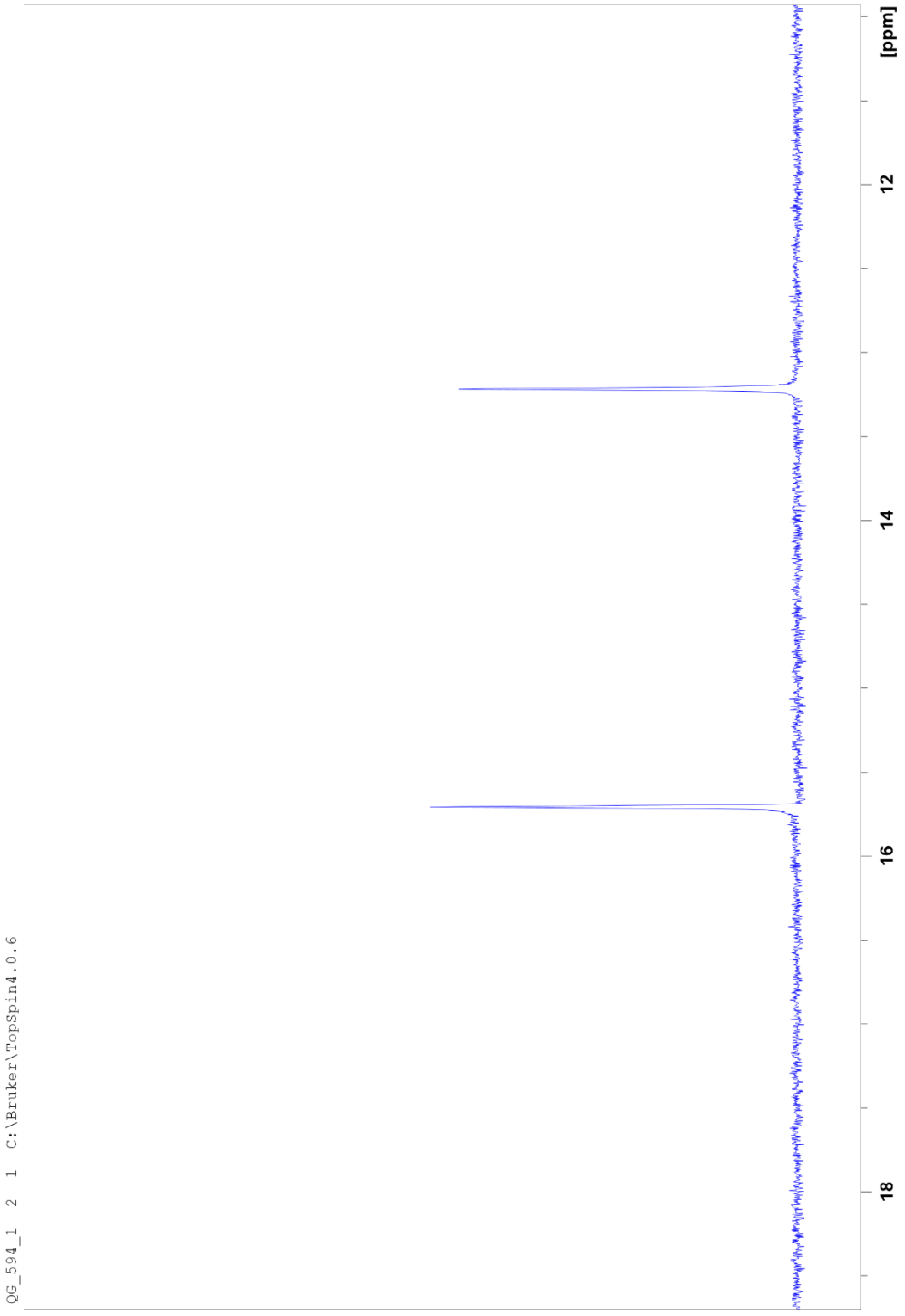

Figure S7.5: ^{31}P-NMR spectrum of Ni(dpph)(S_3PF)

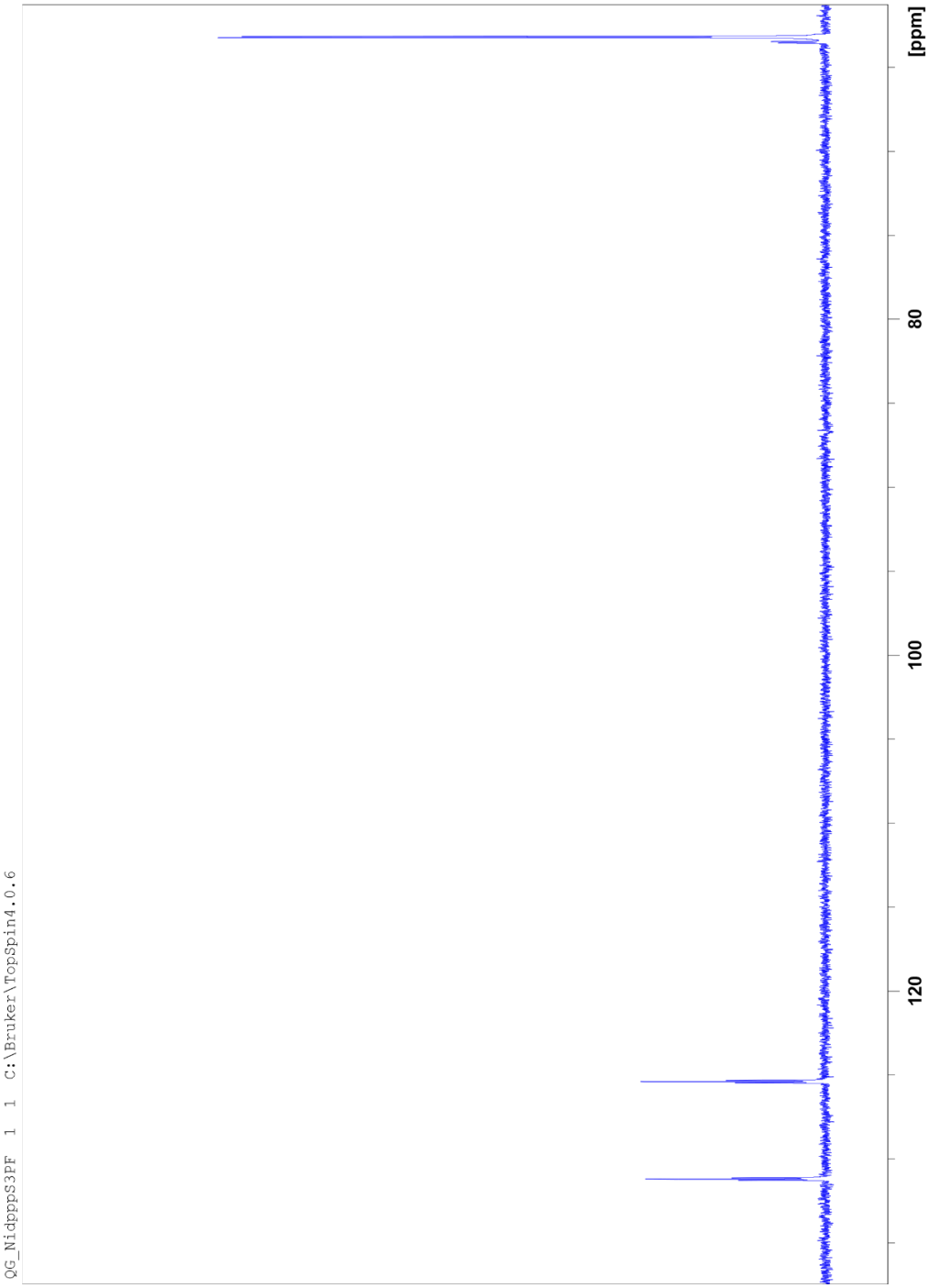

Figure S7.6: ^{19}F-NMR spectrum of Ni(dpph)(S_3PF)

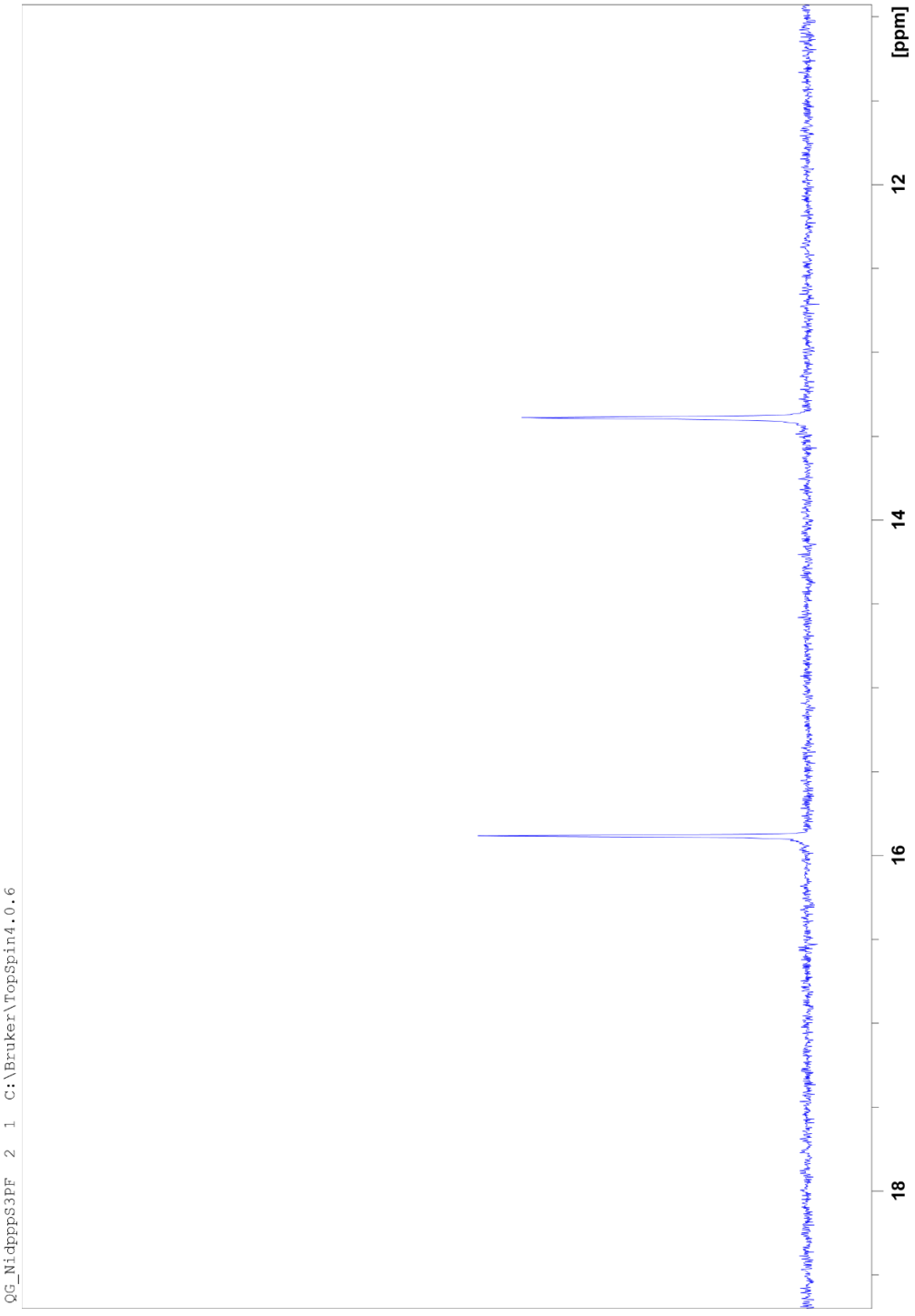

Figure S7.7: ^{31}P-NMR spectrum of $Ni_2(dppe)_2(S_3PF)(S_2POF)$

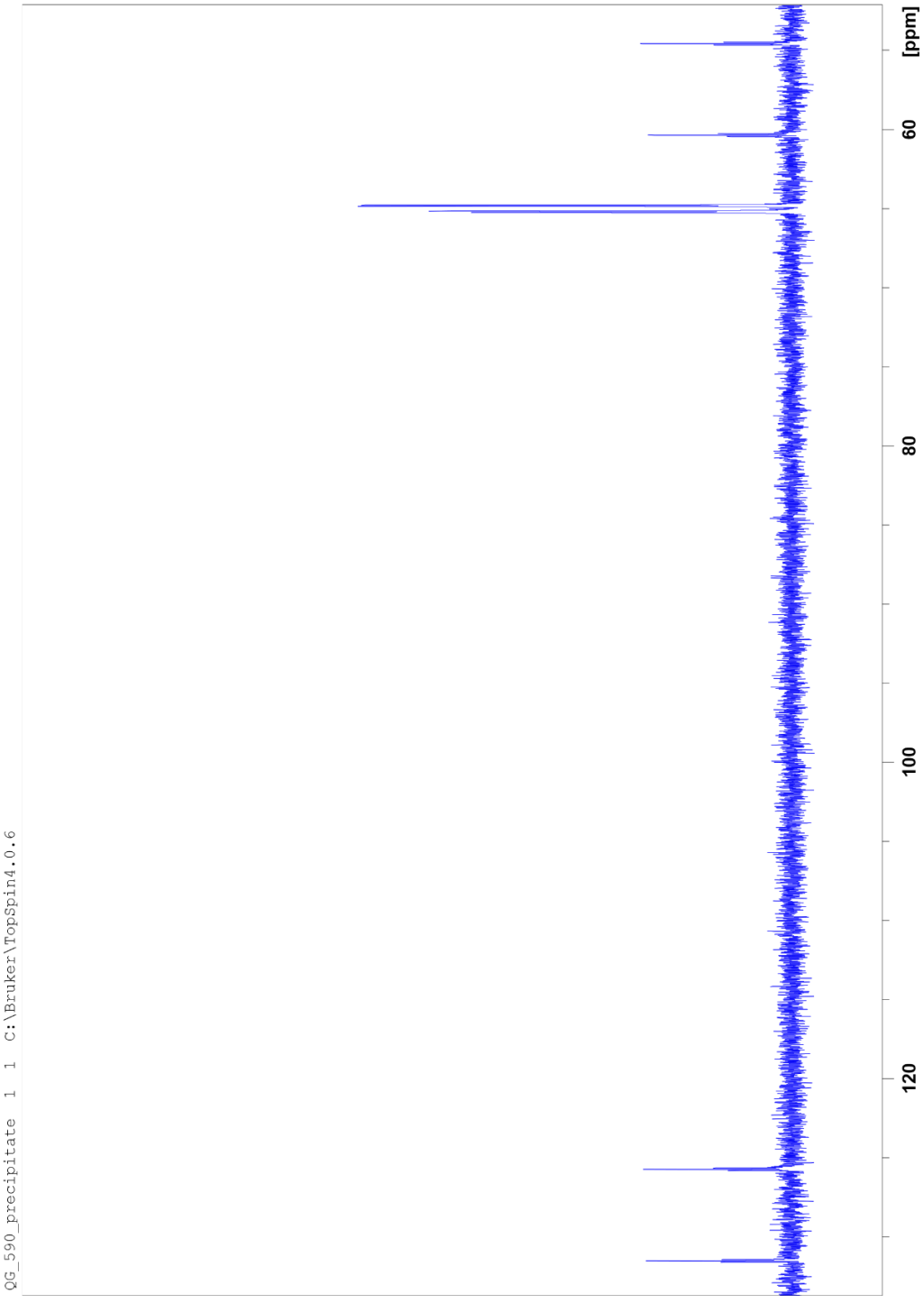

Figure S7.8: ^{19}F-NMR spectrum of $Ni_2(dppe)_2(S_3PF)(S_2POF)$